Experimentelle Physik

Light Control and Solar Power Conversion by Organic Optoelectronic Assemblies

Inaugural-Dissertation

zur Erlangung des Doktorgrades

der Naturwissenschaften im Fachbereich Physik

der Mathematisch-Naturwissenschaftlichen Fakultät

der Westfälischen Wilhelms-Universität Münster

vorgelegt von

Thomas Schemme

aus Mettingen

– März 2019 –

Contents

1 Introduction – What it's all about and why

Nowadays, our daily life would be almost unimaginable without plastics. In numerous applications, plastics have displaced materials that are typically employed in this field. While typical storage containers for food were commonly made of wood or clay for several thousand years, lightweight and almost indestructible plastic boxes have taken their place. Also in the vehicle or construction industry, plastics have been very successful in partially replacing metal or wood. In clothing, plastic fibers are added to common materials such as cotton or are even solely used for clothes with a special function. One of the most prominent representative of this type of clothing is the nylon stocking.

In all those fields, different kinds of plastics are applied. Strongly depending on the usage, plastics can be hard and brittle or soft and elastic or a different combination of these properties. The multiplicity of plastics allows adaption to almost any specific need. Its ductility and versatile processing procedures guarantee that shapes that are difficult to form with other materials are easily prepared from a suited plastic. There are many transparent materials like poly(methyl methacrylate) (PMMA) or polyethylene terephthalate (PET). The former is more commonly known as acrylic glass or by the trade name "Plexiglas". It is typically used as a replacement for glass in windows or other applications where specific properties of glass are not needed but the focus is set more to lightweight. PET is in turn the material most plastic bottles are made of. In addition, there are also many colorful plastic materials and the transparent ones can be easily colorized by an appropriate dye.

These examples clearly demonstrate the intersection of our daily life with plastic components. Another attribute that is typically in one's mind when thinking about plastic is its electrically insulating character. Most of the insulators put around electric wires are members of the plastic family. Anyhow, the first conductive polymer, i.e., polyaniline (PANI), was discovered in the 19th century by Letheby [1]. But, due to its low conductivity, it was not considered to be conductive but rather used as a dye material. More than 100 yeas later, the discovery of polymer doping in case of polyacetylene (PA) by C. K. Chiang et al. [2] brought a massive boost to research on so-called synthetic metals, i.e., conductive polymers and molecules [3]. To be more precise, the developed materials do not have necessarily a metallic conductivity as the declaration "synthetic metal" would suggest but there are also synthetic semiconductors. Especially this latter kind has attracted much attention during the last $2-3$ decades because their evolution allowed to achieve conductive properties that are close to some inorganic semiconductors. Consequently, as in the other fields where plastic materials are applied, also the conductive ones are considered to be candidates to replace inorganic semiconductors in multiple areas. Consequently, to understand the working principle of conductive organic media, they are introduced in part I of this thesis. In detail, this part explains what organic materials are, how they are composed and especially how excitation and charge transfer in organic materials work.

Two possible application of conductive organic media are introduced in parts II and III of this thesis, namely photorefractive materials and photovoltaic cells. While the former are already superior to inorganic photorefractive crystals in some use cases [4], organic solar cells are still lacking power conversion efficiencies that are competitive to their inorganic counterparts [5].

Organic photorefractive media are either considered to act as holographic data storages, optical switches [6], or as material for holographic three-dimensional (3D) displays [4, 7]. While the dynamics, i.e., the speed of the photorefractive response, might be of minor impact in the storage case[1], this totally changes for switches in optical circuits or displays. Here, the response times have to be significantly faster. To achieve higher photorefractive speeds, the material or material configuration has to be changed and optimized. Within this thesis, components of so-called photorefractive polymer composites are exchanged with ones that provide a higher light sensitivity and conductivity and thus should be the basis of better performing compositions. The concept of photorefractive compositions is not new and been studied for more than twenty years [8–15]. The beneficial aspect of this approach of photorefractive media is the adaptability to the specific needs. Instead of changing a material that provides the whole photorefractive functionality, single components can be replaced to optimize the composition for a certain application. Assuming at least three main components of such a compound, all of these can be exchanged to either improve or modify the functionality. While the operating wavelength is defined by the employed dye, predictions regarding the overall performance of a changed composition are very difficult. Additionally, there is also no standard recipe that allows to simply replace one component with another. As a consequence, detailed studies on new materials and their influence on the performance of the photorefractive compositions are needed. In part II of this thesis, the components that are responsible for charge generation and transport of a well established composition [16] are exchanged. Novel dye materials based on perylene bisimides as well as a more efficient charge transporting agent are incorporated. The resulting compounds are analyzed regarding their functionality and performance. Finally, the obtained data are evaluated and flaws are discussed. Sample preparation and characterization and the interpretation of results was partially performed with the support by Dipl. Phys. Katharina Ditte and B.Sc. Evgenij Travkin.

Organic solar cells or, more specific, organic photovoltaic cells convert sunlight into electrical energy and thus contribute to dogmatic change from burning fossil fuels to renewable energy that is based on sunlight impinging on the earth's surface. While other techniques such as hydroelectric power stations or wind engines have limited areas where they can be applied, photovoltaics is almost unlimited regarding its place of application. The only need is direct or indirect sunlight that shines on the surface of the cell. If classical photovoltaic cells are considered, it is obvious, that their area of application is also limited. Mainly due to the thickness of the single modules, independent from the underlying technology, e.g., single crystalline, polycrystalline, etc., they can only be applied at places where the actual weight does not matter. Consequently, they are typically put onto roofs that have to be stable enough, or fields. However due to these

---

1   This is the case if holographic media are considered to be applied for long-term storage where writing and access times play only a minor role.

limitations there is much space left that is reached by large amounts of sunlight but energy conversion via this kind of solar cell is impossible. At this point, organic solar cells come into play because they are capable to fill the niche due to the possibility to be fabricated foil based and thus to be flexible and lightweight. This in turn does not only enable application on fronts of buildings but also on any curved surfaces, cars, or even on hand-held devices like smartphones.

Another interesting aspect of organic solar cells (OSCs) is their tunability of the absorption and thus the capability to tailor the cells to a specific need. One approach that has to be mentioned in this context are energy-converting windows that only absorb the invisible parts of the light that are not needed to illuminate the room, i.e, ultraviolet (UV) and infrared light [17, 18]. As a result, even more space could be used for energy conversion while simultaneously reducing annealing of rooms by infrared light.

As already mentioned, the power conversion efficiency of OSCs is still below silicon-based cells but if OSCs are not considered as a replacement but rather as an supplement, efficiencies in the $5-10\,\%$-range can have a significant impact because of the coverage of additional space. Anyhow, the cells that are present today are still not ideal and thus major optimizations regarding their efficiencies are possible. To perform such optimizations, there exist several approaches. Besides the application of novel tailored materials that absorb and convert light, also the general design of the cell is of importance. Starting with the absorbing part of the cell that typically consists of two materials – a donor and an acceptor [19–21]. The material choice has to be performed considering at least two aspects. While the first one is the desired absorption regime, the second one is the energetic matching of both materials to each other. Consequently, it is almost impossible to combine arbitrary organic semiconductors to form an organic solar cell because it is unlikely that it will provide a significant power conversion efficiency. In addition to to the criteria mentioned previously, development of organic solar cells means cell fabrication and testing. The reason for testing is that materials that seem to fit perfectly to each other must not necessarily work because the recipe is not optimized or other effects hamper the energy conversion process. In part III of the thesis, the application and testing of different novel perylene bisimide acceptor materials in air-processed bulk-heterojunction solar cells is treated. While the main focus is set on these acceptors, also the donor materials are varied. The difficulty here is the processing under ambient conditions because several materials are sensitive to moisture and oxygen [22]. Solar cell processing and characterization was partially carried out together with B.Sc. Thomas Kohne and B.Sc. Martin Unland Elorrieta.

Another design aspect is the field of light management whose scope is set on efficient coupling of light into the cell and subsequent light trapping inside the cell, i.e., avoiding losses due to outcoupling, as well as optimizing the cell geometry [23–30]. The latter is possible because the absorbing layer is usually not able to absorb the whole light of the full wavelength range while it is passed for the first time. So, the optical path has to be artificially elongated by diffraction or even by achieving multiple reflections of light within the cell. This goal can be achieved via incorporation of light redistributing elements into the cell. These can be located either at the bottom [31] or at the top of the cell [31] or at both faces. While the pattern at the bottom is often combined with the reflectign back electrode, the pattern at the front face can be placed on top of

the cell or combined with the transparent front electrode. If the latter is chosen, the pattern can increase the light redistribution but has less impact on the other aspect that is mentioned ealier: coupling of light into the cell. For this purpose, the front surface can be patterned of transparent gratings are set on top of the cell. This type of light management has the beneficial aspect that reflections from the surface can be reduced and additionally light can be diffracted and thus redistributed in the cell. Here, usually completely random patterns are realized via etching [32], but also simple one-dimensional (1D) or two-dimensional (2D) structures are generated via different means [31, 33, 34]. While randomized patterns still carry the drawback that they also can backscatter light, the 1D or 2D structures possess a high angle selectivity due to their regular shape and periodicity because most of them are sinusoidal, blazed, or consist of pyramids or cones [31].

Part IV of this thesis focuses the development of optically-induced surface-relief grating that can be employed as light-harvesting patterns on top of solar cells. The reliefs are inscribed into azopolymers that are also plastics but the ones that are employed here, are insulators. The approach of azopolymer patterning is very similar to the one by [31] but with the advantage of being able to produce structures of almost any shape. The great advantage of this ansatz is its diversity. On the one hand it allows for rapid prototyping of different patterns within several hours without the need of costly mask fabrication. On the other hand, the flexibility to realize almost any shape allows to create patterns that are located in the intermediate region between being totally regular and periodic, and random patterns. Especially this possibility allows to generate light harvesting geometries that possibly overcome the detrimental effect of the previously described cases and in turn combines their advantages. While the azopolymer itself acts as a template material that can form surface reliefs due to illumination, the obtained patterns are transferred into a poly(dimethylsiloxane) (PDMS). The resulting transparent films carry the relief and can be easily attached onto solar cell or used as in arbitrary applications. The previously prepared azopolymer master is not destroyed by the transfer process and can be reused for another transfer. The fabrication of surface reliefs by two-beam interference, their transfer into PDMS, and their characterization was performed together with M.Sc José María Miranda Muñoz.

The light redistributing mechanism on top of solar cells is diffraction and thus it is crucial to generate patterns that suit the specific needs regarding feature size. In order to determine the light redistribution capabilities of different patterns types, theoretical modeling is employed. The simulation volume that is chosen consists of a patterned PDMS film on top of a glass substrate. An finite-difference time-domain (FDTD) simulation allows to analyze the influence of the structure on the impinging illumination and subsequently the redistributed light field at the end of the volume is visualized and evaluated. The obtained data allows to compare the different patterns and provides an informative basis for the further pattern development.

Part I

Light-sensitive functional organic materials

In order to understand the following part of this work that focuses on the concepts of light sensitive functional organic molecules, a short clarification of the field of organic chemistry has to be given, because the term "organic" very often leads to some confusion. This occurs, if people confuse the term "organic" from organic food, where it refers to a special way of farming that avoids pesticides and has some other specifics, with the "organic" in organic chemistry. Referring to the internet encyclopedia Wikipedia, organic chemistry ...

> "... is a chemistry subdiscipline involving the scientific study of the structure, properties, and reactions of organic compounds and organic materials, i.e., matter in its various forms that contain carbon atoms" [35].

Therefore, organic chemistry is not necessarily environmentally friendly. Depending on the components employed during synthesis, processing, and postprocessing, organic chemistry can produce substances that are very harmful to the environment. More precisely, besides several other poisonous organic materials or venoms, the twelve components known as the "dirty dozen" that are defined by the Stockholm Convention on Persistent Organic Pollutants are probably the most prominent examples for the fact, that there is also a "dark side" of organic chemistry [36].

In the following chapters a basic description of relevant properties of organic materials will be given. At the beginning formation of molecules, bonding, resulting energy levels, excitation mechanisms, transport of energy and charges are described. At the end some prominent representatives of the donor and acceptor families will be shortly introduced.

2 Organic molecules

2.1 Formation of organic molecules and bonding

The basis of every organic compound is the carbon atom C. The "basic" electron configuration of carbon is the following: two in the $1s$ orbital, two in the 2s orbital, and the last two electrons are distributed on the $2p_x$, $2p_y$, $2p_z$ states. Due to the small energy splitting between the $2s$ and the $2p$ state of about $4\,\mathrm{eV}$, an electron can be excited from $2s$ to $2p$, and thus in presence of other atoms like hydrogen the splitting can be compensated leading to degenerated $2s$ and $2p$ states [37].

Considering that one of the simplest organic compounds is methane (**1** in scheme 2.1), CH_4, it becomes clear, that there has to be a mechanism for carbon to bound to more than two partners, as it would be expected from the number of its valence electrons in the $2p$ orbitals. Carbon, like every other element, tends to follow the octet rule, i.e., achieve a noble gas configuration. By exploitation of the previously mentioned degeneration of the $2s$ and $2p$ states, the carbon is capable to form four so-called sp^3 hybrid orbitals from the $2s$, $2p_x$, $2p_y$, and $2p_z$ states. Theses hybrid orbitals are oriented in a tetrahedral formation with an edge central angle of $\theta_{orb} = 2\arctan\left(\sqrt{2}\right) \approx 109.47°$. The resulting bonds with the hydrogen atoms are so-called σ bonds consisting of two electrons in the overlapping sp^3(C)-s(H) orbital shared between C and H [21]. In case that only carbon atoms are bound under exploitation of the sp^3 hybrid orbitals, diamond is formed. But this type of bonding is not limited to carbon. Also several other materials that provide semiconducting properties such as crystalline silicon possess the same tetrahedral structure. All these materials have in common that they are very stable and provide semiconducting properties due to their band structure and high delocalization of additionally inserted electrons [21].

To get an idea of the energies that can be attributed to these orbitals, the quantum-mechanical picture has to be taken into account. As an approximation, the bonds between the atoms can be described as linear combinations of the single-atom orbitals (LCAO method) [21, 38–40]. These linear combinations possess split energy eigenvalues. In dependence on the phase of the overlapping wavefunctions ϕ, bonding or antibonding states Ψ are formed. Due to the fact that antibonding states typically have higher energies, the bonding states are occupied first.

Example materials where the carbon is only bound to three neighboring atoms are ethene (C_2H_4) and benzene (C_6H_6) (**2** and **3** in scheme 2.1). To achieve such structures, a different orbital configuration exists. Alternatively to the sp^3 hybridization, this is an sp^2 hybridization. In this case, only the p_x and p_y orbitals combined with one s orbital form three sp^2 orbitals. The p_z orbitals remain perpendicularly oriented to the planar sp^2 orbitals. The angle between the three sp^2 orbitals is $\theta_{orb} = 120°$, therefore representing a triangular orientation. If the residual p_z orbitals from neighboring atoms overlap, they contribute to a so-called π bond, that is out of plane of the σ bonds [41].
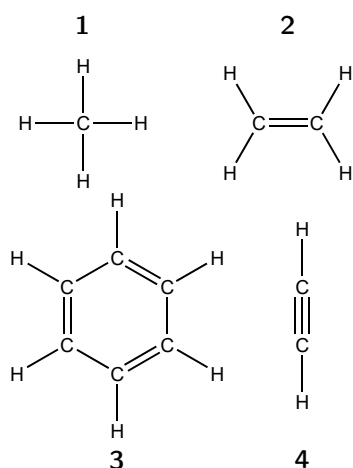
Scheme 2.1: Structural formula of hydrocarbon compounds with different covalent bonds and hybridization of the *s* and *p* orbitals. An sp^3 hybridization represented by methane **1**, in ethene **2** and benzene **3** carbon atoms are sp^2 hybridized, while in acetylene **4** an sp hybridization is existent.

If both, σ and π bonds occur, they form the well-known double bond. Due to the fact that the π bond can only be build up with one of the neighboring carbon atoms, two resonant configurations of benzene are possible. None of both mesomeric realizations is preferred over the other. The reason for this behavior lies in the symmetry of the ring structure. The consequence can also be found in the bond lengths that are equal for all single and double bonds on the ring [21, 37].

In dependence of the linear combination of the wavefunctions, also π bonds can be bonding π or antibonding π^*. In benzene, the six overlapping wavefunctions result in three bonding and antibonding orbitals, respectively. The energy of every orbital again strongly depends on the phase overlap resulting in the occupation of the three lower bonding orbitals by the six electrons while the antibonding orbitals remain unoccupied. This population of the orbitals is valid for the ground state of the molecule. Therefore, the highest occupied molecular orbital (HOMO) corresponds to the highest π orbital while the lowest unoccupied molecular orbital (LUMO) is represented by the lowest π^* orbital. These two states are of importance if excitation, especially optical excitation, is taken into account because the energetic distance of these two levels determines the energy, e.g., a photon has to bring a molecule into an excited state. For benzene, this energy is approximately 6 eV, i.e., around a wavelength of 200 nm [42]. To complete the list of hybrid orbital configurations of carbon, also an example for a sp hybridization is given. Ethyne (C_2H_2, **4** in scheme 2.1), or better known under its trivial name acetylene, is formed.

The basic building blocks of typical organic semiconductors are hydrocarbon molecules. Compared to the previously mentioned ring structures, the strength of the bonds of linear structures are weak. In turn ring structures, that are also called aromatic compounds, possess a higher bonding strength. Additionally to their stability, also their extended π-system plays a very crucial role because it significantly enhances the charge transfer capabilities due to the high delocalization of the π electrons. These effects are strongly enhanced if the aromatic ring system is extended by bonding several rings to each other leading to a further spreading of the single energy levels and larger delocalization of the π-system. Another effect is the reduction of the HOMO-LUMO distance resulting in an absorption shift to longer wavelengths. An explanation of this relation can be given if the electron in the π-system is considered as a particle in a box [43]. Here, the box size

corresponds to the size of the π-system. By exploiting this approach and solving the corresponding Schrödinger equation, it becomes evidently clear, that a larger π-system leads to a reduced separation of HOMO and LUMO levels and therefore the size of the π-system becomes a setscrew to adjust optical absorption [21, 43].

This behavior is not limited to aromatic compounds. Chains that are build-up from several hydrocarbon groups with alternating single and double bonds, so-called conjugated bonds, also possess a π-system that is extended along the chain. In addition, also a dependence of the HOMO-LUMO distance on the chain length exists. These chains of $(CH)_n$, starting from oligomers like $=C-C=C-$ or its equivalent $-C=C-C=$ go up to long chains that form the polymer polyacetylene (PA). Typically, such a chain consists of tens to hundreds of monomeric units. In fact, doped PA was the first discovered conductive polymer. In 1976, a group around Alan J. Heeger, Alan MacDiarmid, and Hideki Shirakawa observed that the conductivity of PA is significantly enhanced when it is doped with halogens [2, 44]. Due to this discovery, the three were awarded with the nobel prize in chemistry in 2000 [45]. Up to now, several other conductive polymers have been synthesized. Most of them are not purely consisting of hydrocarbons but they are functionalized to adapt them to the specific needs of their intended use.

The electron distribution on the molecular orbitals has to obey the Pauli principle connoting that there cannot be two or more electrons in an atom that occupy the same quantum state simultaneously, i.e., that coincide in all four quantum numbers: the principal quantum number n, the orbital quantum number l, the magnetical quantum number m_l, and the spin quantum number m_s [46]. As a result of this occupation rule for the electrons, the Aufbau principle by Bohr [47], and Hund's rules [41, 48, 49], the electronic configuration of a molecule can be described. The occupation of the molecular orbitals does not only depend on the number of electrons available. Energy within the molecule also plays an important role. Due to energy insertion resulting in excitation of different configurations the molecule can be set into different states. Besides singlet states, also states with higher spin multiplicity

$$\text{multiplicity} = 2S + 1, \quad S = \left| \sum_i s_i \right| \tag{2.1}$$

exist [21]. Particularly, besides singlet states, triplet states are from major interest, especially when molecules are excited electrically as it is the case for organic light emitting diodes (OLEDs). Due to the occurrence of the triplet and singlet states, three quarters of the injected charge carriers get into triplet states while the residual quarter forms a singlet state. The problem with the formation of triplet states in this context is, that relaxation to the ground state, that is typically singlet, is forbidden due to spin conservation. Issues that might occur during charge and energy transfer in combination with the presence of triplet states are discussed in section 2.2.

2.2 Optical excitation and relaxation of organic molecules

In analogy to absorption and emission in inorganic materials, these processes also occur in organic molecules. In figure 2.1, some examples of possible transitions (allowed

and spin-forbidden ones) within one molecule are given. Allowed transitions typically start and end in a singlet or triplet state (solid horizontal lines), respectively. These processes are denoted by solid arrows within the image. Most common is absorption where photons that carry sufficient energy excite the molecule from the singlet ground state (S_0) or a slightly higher vibronic level (dotted horizontal lines) to an excited state (S_1 or S_2) or one of its vibronic levels. If only the S levels themselves are considered, absorption and emission spectra would consist of individual sharp lines resulting from these transitions. But, due to the existence of vibronic levels additional excitation and relaxation pathways are possible resulting in additional peaks. The vibrational levels are themselves superimposed by translational and rotational levels. The energy splitting of these manifolds is comparably small (a few meV) and therefore not illustrated separately. Furthermore, peaks in typical emission and absorption spectra are not sharp and can be hardly distinguished because of several effects that cause broadening of the spectral lines. Among others, the most important effects are natural broadening, i.e., due to the uncertainty principle, states with a short lifetime have broad spectra, Doppler broadening, as well as pressure broadening [50].
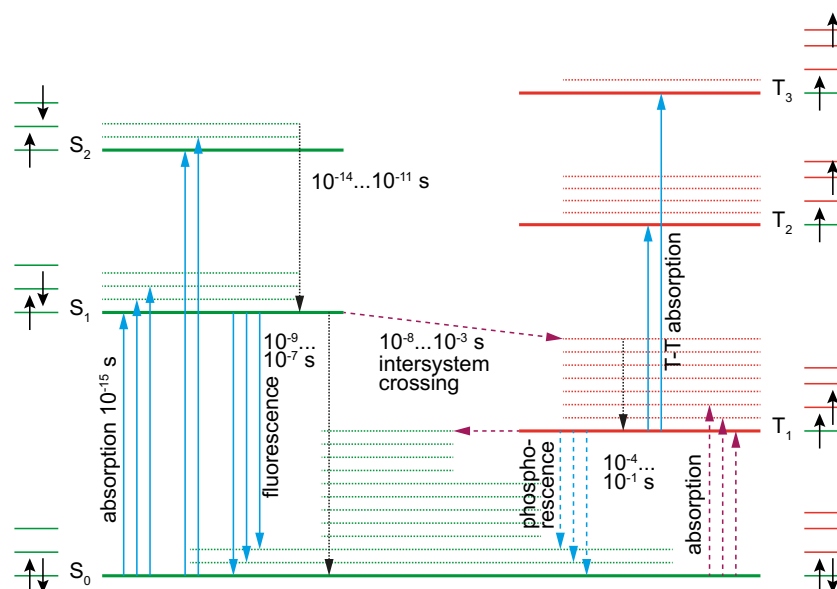
Figure 2.1: Jablonski diagram of excitation and relaxation processes for singlet (S) and triplet (T) states in organic molecules. Solid horizontal lines represent different energy levels, while the dotted ones represent vibrational levels. Solid arrows illustrate some of the possible optical transitions from S to S or T to T state. Spin-forbidden transitions from S to T or T to S are depicted by dashed arrows. Finally, the dotted arrows mark non-radiative internal conversion processes. Typical timescales for the corresponding processes are indicated by the numbers. Inspired by reference [21].

Besides excitation from a ground state to an higher singlet state, also triplet (T) to T transitions via absorption are possible. Disexciation can follow several routes within one molecule. The process(es) involved strongly depend(s) on the multiplicity of the excited state. The first one, the so-called internal conversion process is depicted by dotted arrows and typically occurs during relaxation from a higher energetic level to a lower S or T level of the same multiplicity. Relaxation by internal conversion occurs

without emission of photons. Kasha's rule states that optical emission starts from the lowest excited state of a given multiplicity [51]. The consequence of this principle is that prior to any radiating process there is typically internal conversion to bring the excited molecule to the lowest excited state. The differences of the radiating processes, namely fluorescence and phosphorescence, are their starting points and the time within they typically occur. Fluorescence (solid arrows, downwards) is the S_1 to S_0 transition, while phosphorescence (dashed arrows, downwards) describes the T_1 to S_0 relaxation. Due to the change of multiplicity and thus its spin-forbidden nature, phosphorescence is much more unlikely to occur than fluorescence and therefore the relaxation times are much longer. Another mechanism, illustrated by dashed horizontal arrows, is intersystem crossing. Similar to phosphorescence, this radiationless process enables an excited state to undergo a transition from singlet to triplet or vice versa. Because of its spin-forbidden nature, these processes are rather slow and the probability to occur is also very low (cf. figure 2.1).

As mentioned earlier, in OLEDs 75 % of all electrons get into a triplet state. Therefore, the development of triplet-harvesting metal complexes based on platinum, iridium, or some other transition metals is one crucial aspect in OLED development because it enables electron-to-photon conversion efficiencies of up to 100 %. Within these complexes the transition from triplet to singlet states becomes possible due to spin-orbit coupling. This holds for intersystem crossing as well as phosphorescence [52]. In contrast to OLEDs, the formation of triplet states can also be desired. Especially if charges should be transported for comparably long distances without the risk of relaxation to the ground state, the formation of triplet states is highly desirable because they can significantly reduce charge recombination or relaxation. Concepts and ideas of triplet state exploitation in OSCs have been discussed by Rao et al. [53] and Chang et al. [54].

3 Energy and charge transport

Besides the fundamental processes of excitation and relaxation of organic molecules, there are also more mechanisms of importance. In order to understand how conductivity in an organic material is achieved, how energy and charges are transported, the underlying processes are introduced in the following sections and chapters. Further, also requirements of molecules to enable these processes are presented.

3.1 Energy levels, ionization potential and electron affinity

In general, materials that are considered as organic semiconductors behave on the macroscopic scale to some extend similar to their inorganic counterparts. They can also be subdivided into donors and acceptors whereat acceptor materials are electron (n-type) conducting and donors hole (p-type) conducting. This definition should not be mixed up with the terms that are typically employed when doping of inorganic semiconductors is described. In that context, typically the dopants themselves are called donors and acceptors, i.e., donors are n-type dopants because of their excess of electrons while acceptors are p-type dopants.

Whether an organic compound is a donor or an acceptor material, depends on its electron affinity and its ionization potential. If two materials are compared, the one with the higher electron affinity and ionization potential is the acceptor while the other one is the donor [55]. The terms electron affinity and ionization potential are defined in the following way:

Electron affinity (EA) denotes the energy that is released if a neutrally charged molecule gets an additional electron and therefore becomes an anion [56].

Ionization potential (IP) or ionization energy is the energy needed to remove an electron from a neutrally charged molecule [56].

Having the meaning of these energies in mind, they can be related to energies of HOMO ($E_{\mathrm{HOMO}} = -E_{\mathrm{IP}}$) and LUMO ($E_{\mathrm{LUMO}} = -E_{\mathrm{EA}}$) levels of a molecule. Extraction of a HOMO electron of an unexcited molecule would require the ionization energy while the addition of an electron to the uncharged molecules would free the energy that corresponds to the electron affinity. Unlike to inorganic materials, the optical transition is not simply $E_{\mathrm{opt}} = E_{\mathrm{IP}} - E_{\mathrm{EA}}$. Due to intramolecular interaction, the energy for an optical HOMO to LUMO transition can be much less (up to several eV). The intramolecular interactions are the so-called exchange interaction which is also responsible for the singlet-triplet splitting as well as the electron repulsion integral which is basically following Coulomb's law. A more detailed explanation can be found in references [21, 57]. In general, the difference between E_{opt} and $E_{\mathrm{IP}} - E_{\mathrm{EA}}$ decreases with rising molecular dimensions [21].

As stated before, there is a difference between the energy of an optical transition (excitation or relaxation) and the distance of the HOMO and LUMO levels. To avoid

confusion, the terms HOMO and LUMO will be strictly distinguished from optical transitions within this part of the thesis[1]. Therefore, if optical transitions (E_{opt}) are considered the states of the specific multiplicity will be employed while HOMO (IP) and LUMO (EA) are applied in their original sense. Consequently, the following definitions are introduced:

$$E_{\mathrm{opt,S}} = E_{\mathrm{S_0}} - E_{\mathrm{S_1}} \tag{3.1}$$

$$E_{\mathrm{opt,T}} = E_{\mathrm{S_0}} - E_{\mathrm{T_1}} \tag{3.2}$$

$$E_{\mathrm{IP,EA}} = E_{\mathrm{IP}} - E_{\mathrm{EA}} \tag{3.3}$$

If an optical transition is considered, equations (3.1) or, in the spin-forbidden case (3.2), have to be used while equation (3.3) is applied if energies that are related to charge transfer are taken into account.

   If the transition from a single molecule to a solid occurs, the positions of the energy levels change. Due to additional intermolecular interactions including polarization and charge shielding, the energies that are described by equations (3.1) to (3.3) are significantly reduced. In highly ordered crystals, the degenerate energy levels corresponding to IP and EA overlap and tend to form bands comparable to their inorganic counterparts. Due to the small overlap of the wavefunctions, the bands are relatively narrow. Contrary, in disordered films, that are typically amorphous, there is a Gaussian distribution of density of states for IP and EA, respectively [21]. Referring again on the difference between the energy needed for optical excitation, $E_{\mathrm{opt,S}}$, and $E_{\mathrm{IP,EA}}$, it can be considered as binding energy of the electron. An optically excited state called exciton is strongly bound to the molecule where it has been excited. The binding energy is typically in the range of several hundred meV and is therefore much higher than in inorganic semiconductors [58]. This difference can be explained by the lower dielectric constant of the organic materials [21]. Consequently, due to the strongly bound exciton, also called Frenkel exciton, the
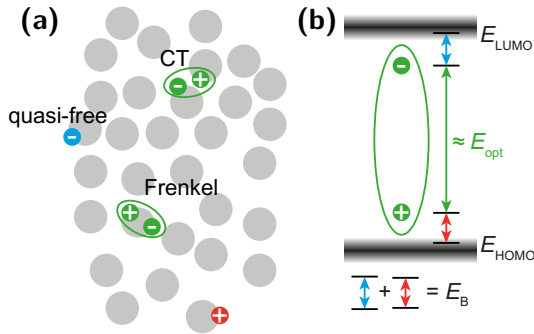
Figure 3.1: Part (a): Schematic representation of a Frenkel and a charge-transfer (CT) exciton in a disordered solid. Additionally, also free charges are depicted. Part (b): An exciton of energy E_{opt} with its binding energy E_{B} and the charge transfer levels E_{HOMO} and E_{LUMO}. Inspired by [21].

energy of an absorbed photon has not only to be large enough to excite the molecule but also should provide enough energy to overcome the binding energy of the exciton. If the photon energy is not large enough, the probability of exciton dissociation is strongly decreased as dissociation by thermal processes can be excluded. In figure 3.1 (a) two types of excitons are illustrated. The already introduced Frenkel exciton is located on a

---

1   Later in the other parts, the HOMO-to-LUMO distance is also applied for the energy a photon needs to excite a molecule as it is mainly applied in the literature.

single molecule, while the charge-transfer (CT) exciton is separated on two neighboring molecules, one keeping the electron, the other one the hole. Additionally, also quasi-free charges are depicted. Part (b) of figure 3.1 visualizes how a Frenkel exciton is bound to a molecule by its binding energy E_B. This energy consists of contributions acting on electron and hole, respectively. These contributions are the summed difference between the HOMO-LUMO distance and the optically induced energy of the exciton.

An exciton can either recombine, move to a different molecule, or separate into quasi-free charges. The recombination coincides with the previously described processes in figure 2.1. The other processes are described in the following sections 3.2 and 3.4.

3.2 Energy transfer

In general there are two fundamental processes for exciton-based energy transfer on a molecular scale. The processes namely Förster resonant energy transfer and Dexter transfer differ regarding their range and the type of excitons that are transferred. The following subsections give an explanation of the working principles of both procedures that are illustrated in figure 3.2 [21].

(a) Förster energy transfer   **(b)** Dexter energy transfer
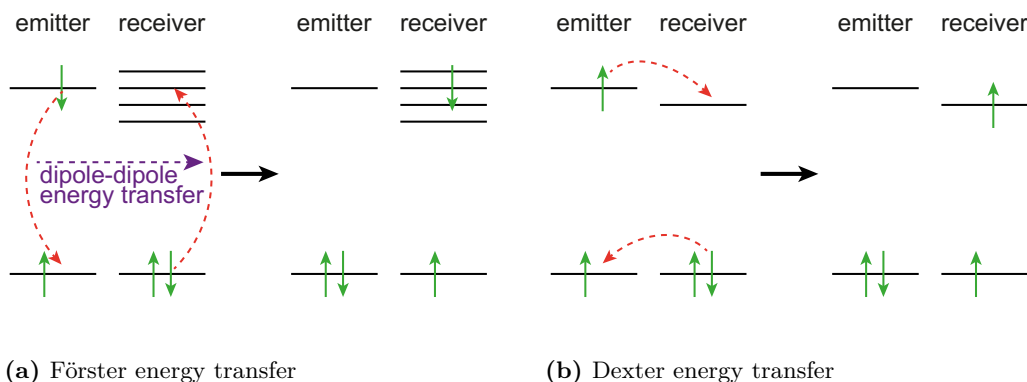
Figure 3.2: Visualization of Förster and Dexter energy transfer processes. In both processes energy is transferred from the left emitter molecule to the right receiver molecule. Inspired by [21].

3.2.1 Förster resonant energy transfer

The Förster resonant energy transfer (FRET) in subfigure 3.2(a) is based on dipole-dipole interactions of a molecule carrying an exciton with another molecule that is close enough [56, 59]. As illustrated in the figure, the electron of the originally excited molecule relaxes while an electron in the receiver molecule is excited. In order to get the FRET working, there has to be some spectral overlap of emission and absorption spectra of the emitting and receiving molecules. This overlap ensures that the transferred energy "fits" to the energy level structure of the receiving molecule. Due to the spin-conserving nature of this process within the molecules involved, only singlet-singlet transfer is allowed. Under certain preconditions that refer to the fluorescence and absorption properties of the emitter and receiver, also other transitions are possible [52]. The rate constant k_T^{dd} for

FRET with its dipole-dipole interaction is

$$k_T^{dd} = k_D \left(\frac{R_0}{r}\right)^6 = \frac{1}{\tau_D^0} \left(\frac{R_0}{r}\right)^6 , \tag{3.4}$$

where k_D is the emission rate constant of the emitter and τ_D^0 is its lifetime in the absence of transfer, r is the distance between emitter and receiver (assumed to be constant during lifetime of the emitter), and R_0 is the critical distance or also called Förster radius, i.e., the distance at which transfer and spontaneous decay of the excited emitter are equally probable to occur ($k_T = k_D$). Förster radii R_0 are in the $15-60$ Å range for common materials. and typical distances that can be bridged by FRET are up to $10\,\mathrm{nm}$ [52]. Consequently, longer transport paths have to be bridged by a cascade of FRET processes or they have to be maintained by the following process that is based on emission and absorption.

As an alternative to FRET, the exciton can recombine, emit one photon which in turn can be absorbed by another molecule, and thus energy can be transferred even over longer distances. This latter process is effective at distances that are typically longer than half the wavelength of the emitted photon.

3.2.2 Dexter transfer

The Dexter energy transfer is based on exchange of electrons and is illustrated in subfigure 3.2(b) [56, 60]. During the process, the excited electron from the emitter molecule is transferred to the receiver molecule while an electron from the ground state of the receiver (or the hole from the emitter) is transmitted to the ground state of the emitter (receiver). The rate constant for the Dexter electron-exchange energy transfer is

$$k_T^{ex} = \frac{2\pi}{h} K J' \exp\left(-2r/L\right), \tag{3.5}$$

where K is a constant, J' is the overlap integral, and L the average Bohr radius [52]. Here, the transfer mechanism is not resonant but is based on the overlap of orbitals of neighboring molecules. Because of this criterion, Dexter energy transfer only works on short distances up to $1-2\,\mathrm{nm}$ [21]. Due to the fact that the spin of the whole receiver-emitter system is conserved and not only for the single molecule, this process also allows transfer from triplet to triplet states.

3.3 Charge separation

A crucial process in all organic materials that provide photoconductivity is charge separation. During this process, the bound exciton is split up into two separate charges – an electron and a hole. The excited state, the exciton, can either be located on the donor or the acceptor molecule. In order to separate an exciton, the binding energy has to be overcome. As stated in section 3.1, the binding energy of the exciton can be several hundreds of meV and therefore thermal-driven separation at room temperature is almost impossible because the thermal energy $E_{\mathrm{therm}} = kT$ at $T = 300\,\mathrm{K}$ is only about $26\,\mathrm{meV}$.

Due to this restriction, another mechanism has to be enabled to separate the exciton.

In a typical configuration where organic photoconductivity is applied, it is based on a mixture of different donor and acceptor materials. Ideally, these materials differ regarding the position of the energy of their molecular orbitals. This means the LUMO of the acceptor should be located energetically lower than the LUMO of the donor. The same holds also for the HOMO levels. If the difference in energy is large enough, this potential is the driving force to separate the exciton and therefore the charges [61]. Of course, also applied electric fields can assist to separate charges.

3.4 Charge transport processes

The energetic landscape within an organic semiconductor can either be band-like and therefore similar to its inorganic counterparts or disordered as in a thin amorphous film. Especially in the latter case, charge-transfer processes in organic solids are mainly considered to be based on a mechanism called hopping. The term hopping has to be understood figuratively. Electrons (or holes) jump from the LUMO of one molecule to the LUMO of another. Within a molecule, the charge carrier is delocalized in the π-system.

There exist several theoretical models that describe charge transfer in organic solids. On one side, there is the famous Marcus theory [62] by Rudolph Arthur Marcus (Nobel Prize in Chemistry in 1992) and on the other side is the Miller-Abrahams formalism [63] to describe hopping rates of charge carriers. During the years, both ideas have been applied to the so-called Gaussian disorder model (GDM) or Bässler model [64–66] that was introduced by Heinz Bässler. Originally, Bässler chose the Miller-Abrahams hopping rate, but over the years it turned out that it was not capable to well describe all effects. Especially, polaronic contributions were neglected. This was the reason why others applied Marcus theory to the GDM and achieved far better results [67].

Hopping rate probabilities [21] in Marcus theory are described by

$$\nu_{ij} = \frac{|I_{ij}|^2}{\hbar} \sqrt{\frac{\pi}{\lambda k_B T}} \exp\left(-\frac{(\Delta G_0 + \lambda)^2}{4\lambda k_B T}\right) \tag{3.6}$$

and in Miller-Abrahams formalism by

$$\nu_{ij} = \nu_0 \exp\left(-2\gamma \Delta R_{ij}\right) \cdot \begin{cases} \exp\left(-\frac{E_j - E_i}{k_B T}\right); & E_j > E_i \\ 1; & E_j < E_i. \end{cases} \tag{3.7}$$

The term I_{ij} describes the electronic coupling, depends on the orbital overlap, and therefore strongly depends on the distance of the molecules (typ. exponentially). The Planck constant in its reduced form is given by $\hbar$, while k_B denotes the Boltzmann constant, and T the temperature. The difference of Gibbs' free energy of receiver and emitter at their minimum position is represented by ΔG_0 and λ is the so-called reorganization energy that is the amount of energy that is needed to convert the nuclear configuration of the products into the configuration of the educts without electron transfer [21]. Changes in the local dielectric properties are responsible for it. Two main

contributions have been identified by Marcus. The first one is a change in inner shell vibrational modes and the second results from solvent effects that are caused by the polarizability of the local environment. In equation (3.7), the ΔR_{ij} is the distance of the sites of the molecules, therefore, the first exponential term denotes the wave function overlap and the tunneling probability of the charge carrier. The quantity γ is the wave function decay parameter in the order of $10^{10}\,\mathrm{m}^{-1}$. The prefactor ν_0 is the attempt frequency of an electron trying a jump and is typically in the range of $10^{13}\,\mathrm{s}^{-1}$. Due to the magnitude of these parameters, a ΔR_{ij} of about $1\,\mathrm{nm}$ results in approximately 10 downward jumps per millisecond while a ΔR_{ij} of about $0.5\,\mathrm{nm}$ yields ca. 1 jump per nanosecond. This small change clearly shows the sensitivity on the site distance. In turn, an upward jump additionally depends on a Boltzmann factor with an energy offset that corresponds to the energy difference of the two sites E_j and E_i. Again, this difference is just ΔG_0 from equation (3.6) and typically larger than $k_\mathrm{B}T$. Therefore, the Miller-Abrahams formalism is just a simplified version of the Marcus theory as it is lacking the reorganization energy λ that respects polarization effects that may occur due to charging and discharging of a molecule [21].

Within the Gaussian disorder model, all sites where a charge carrier can jump to are considered to follow a Gaussian distribution. In other words, the density of states (DOS) has the Gaussian shape

$$g(E) = \frac{N_\mathrm{sit}}{\sqrt{2\pi}\sigma} \exp\left(-\frac{(E-E_0)^2}{2\sigma^2}\right). \tag{3.8}$$

Here, E_0 denotes the center of the DOS, σ is the width of the distribution, and N_sit is the density of available hopping sites.

Disorder itself is split into two contributions: so-called diagonal disorder that is due to the Gaussian distribution of the energy levels of the sites, and off-diagonal disorder that results from different site-to-site distances (R_{ij} in the Miller-Abrahams formalism) also following a Gaussian distribution. As mentioned above, the originally applied hopping rate within the GDM was the one from the Miller-Abrahams formalism. Therefore, it will be employed here as well to explain the GDM.

Within the model, an externally applied electric field F causes a driving force for charge carriers and can also enable jumps from one site to a site of higher energy by reduction of the energy $E_j - E_i$. In turn, jumps downward in energy are not influenced because the changed energetic relation $E_j - E_i = E_j^0 - E_i^0 - eF|\mathbf{r}_j - \mathbf{r}_i|$, where a constant field between $\mathbf{r}_j$ and $\mathbf{r}_i$ is assumed, has only impact on the first case of equation (3.7). Additionally, as the hopping rate, the probability for a jump of a charge carrier from site i to j is of interest. This probability is defined as quotient of the hopping rate by the total jump probability including all eligible destination sites j' in the neighborhood of i:

$$p_{ij} = \frac{\nu_{ij}}{\sum_{j',j'\neq i}\nu_{ij'}} \ . \tag{3.9}$$

In order to study the charge carriers' behavior within the DOS and the hopping process, Monte Carlo simulations were carried out by Bässler and coworkers. Single charge carriers are placed in a simulation volume of $70\times70\times70$ lattice sites (restricted by simulation time and computational capabilities in 1993) and consequently the carriers perform a random

walk through this landscape with Gaussian disorder. Assuming an averaged distance of $0.6\,\text{nm}$, the dimensions are $42 \times 42 \times 42\,\text{nm}^3$. The simulation volume itself is virtually extended by application of periodic boundary conditions. Therefore, random walks for almost arbitrary distances can be simulated in spite of computational restrictions.

Bässler's simulations led to a relaxation of the charge carriers to a Gaussian equilibrium distribution around a position E_0^{relax} that is lower than E_0 which is the center of the Gaussian distribution of the DOS. The resulting relation is

$$E_0^{\text{relax}} = E_0 - \frac{\sigma^2}{k_{\text{B}}T}. \tag{3.10}$$

Assuming a width of the DOS of about $50\,\text{meV}$ that is approximately twice the thermal energy at room temperature, the resulting position of E_0^{relax} is about $100\,\text{meV}$ below E_0. Due to the fact that the shape of the DOS is Gaussian, the probability of trapping in lower energetic states rises. Depending on the depth of the trap, a thermally induced reactivation of the charges carrier is possible. If the trap is too deep, only an additional driving force like optical excitation allows to detrap the charge carrier [14]. Therefore, typically a difference is made between a shallow trap that allows detrapping via thermal activation and deep traps where thermal detrapping is significantly reduced but still possible. The energetic landscape has also a strong impact on the mobility of charge carriers. Based on their Monte-Carlo simulations, Bässler and coworkers established the following equation to derive the mobility μ dependent on temperature T, diagonal σ and off-diagonal disorder Σ, and electric field F [65, 68]:

$$\mu(\sigma, \Sigma, F, T) = \mu_0 \exp\left(-\left(\frac{2\sigma}{3k_{\text{B}}T}\right)^2\right) \cdot \begin{cases} \exp\left(C \cdot \left(\left(\frac{\sigma}{k_{\text{B}}T}\right)^2 - \Sigma^2\right)\sqrt{F}\right); & \Sigma \geq 1.5 \\ \exp\left(C \cdot \left(\left(\frac{\sigma}{k_{\text{B}}T}\right)^2 - 2.25\right)\sqrt{F}\right); & \Sigma < 1.5 \end{cases} \tag{3.11}$$

Due to the empirical nature of the equation that is only based on fitting of selected analytical equations to the simulation results, also the constant C is empirical. Its value is $C = 2.9 \times 10^{-4}\,\sqrt{\text{cm/V}}$ for the above mentioned site distance of $0.6\,\text{nm}$. Equation (3.11) clearly illustrates the dependence of the mobility μ on the temperature within organic solids. Higher temperatures and thus a higher thermal activation energy allow for better detrapping and therefore enhanced charge transfer. Additionally, the influence of both disorder contributions becomes clear. A specialty occurs if the off-diagonal disorder becomes larger than the diagonal disorder contribution divided by thermal activation energy $\hat{\sigma} = \sigma/k_{\text{B}}T$. In this case, the argument of the second exponential term becomes negative and leads to a reduced mobility of the charge carriers if the electric field is strong. Figuratively, this means that the diagonal disorder hinders a jump of charge carriers along the direction of the electric field (assuming that charge carriers move along the electric field). In turn, the electric field inhibits a backwards jump that might result in a route of the charge carrier that is more favorable. In this case, the direct path of the charge carrier is costlier due to the positional disorder, and movement along the longer path including backjumps would have a higher probability for the charge carrier to reach the destination [68].

In general, charge carriers behave as predicted by the Poole-Frenkel effect [69, 70] that also describes the dependence of charge carrier mobility on the root of the applied external field. This similarity does not necessarily imply that it is equal. The Poole-Frenkel effect considers a quasi-free electron in the Coulomb potential of a positively charged state [21] resulting in long-range distance transport at electric field of typical strengths $(10^5 - 10^6 \, \mathrm{V \, cm^{-1}})$ compared to hopping transfer described within the GDM. Therefore, if the distances that occur during hopping transfer are assumed, the reduction of the potential barrier that is caused by the electric field is much lower than in the Poole-Frenkel case. However, in organic solids, the Poole-Frenkel effect is not applicable for hopping transport in the general case.

Due to diversity of organic materials employed in organic electronics, it is hard to find a model that describes properly their behavior regarding conduction in every case. Parameters such as concentration, molecular orientation, solvent that is employed for processing, and several more influence charge transport. There are also chemical influences like substituents and side chains that also have direct impact on optical and electronic characteristics plus indirect impact via influence on morphology. Since Bässler's model, several modifications and improvements were suggested. Especially the off-diagonal or spatial disorder is considered to have a non-Gaussian shape. Further issues address the influence of neighboring carriers on each other. Particularly if one site is occupied, the energy level of the other site may be influenced and therefore a model that considers only single charges that move within an energy landscape underestimates these influences. As a result, models have to be permanently optimized and fitted to the specific situation. As the available computational power rises over the years, more adequate models allow to better mimic the behavior of the real organic materials.

4 Common representative molecules

Since the first discovery of conductive organic materials much effort has been invested to drive research and synthesis towards more efficient charge transport and high mobilities. While charge transfer is of utmost importance considering devices such as organic field effect transistors (OFETs) [71], light absorption and accordingly emission come into play if OLEDs, organic light emitting transistors (OLETs), and OSCs [72] are contemplated. Especially in the latter cases fine tuning of the single properties is needed because improvement of charge transport may be detrimental to absorption/emission and vice versa. The permanent enhancements have led to some material families that prove to be very promising and provide highly efficient charge transfer combined with outstanding light-matter interaction. In the following sections, some of these families separated by their typical application – donor or acceptor – will be introduced.

4.1 Donors

Donors are hole conducting materials that are capable of give an electron after excitation to an acceptor molecule.

An example for a small-molecule donor, the compound **5**, N,N'-Bis(3-methylphenyl)-N,N'-diphenylbenzidine (TPD)[1], is displayed in scheme 4.1. TPD is transparent and provides proper conductivity when an electric field is applied. Due to the tendency of aggregation, it is typically combined with some host polymer such as polystyrene (PS) and therefore acts as a dopant [73, 74]. TPD is highly soluble in chloroform and non polar organic solvents. Over the years, also derivatives have been developed and successfully tested [75]. Today, there are also many other small molecule donors, e.g., phthalocyanine (Pc) derivatives are probably among the most common small molecule donors for OSCs.

In this thesis, most of the employed donors are polymers. The first one is the transparent poly(9-vinylcarbazole) (PVK) **6** in scheme 4.1 that is employed in photorefractive composites [76, 77]. Here, charge carriers are delocalized in the carbazole unit that is connected to the polyvinyl backbone. Due to the fact that polyvinyl is not conjugated, charge transfer is provided via hopping from one carbazole unit to the next [78]. In contrast to PVK, most of the other donor polymers are conjugated. Starting with the most prominent, poly(3-hexylthiophene-2,5-diyl) (P3HT),

---

1 The abbreviation TPD is also employed in other compounds where TPD denotes completely different molecules or parts of molecules. This issue, ambiguity of abbreviated names of molecules can lead to confusion if an abbreviated name is used in different research communities and the abbreviation is defined for different materials. Therefore, within this work, all abbreviated names of molecules are introduced in combination with their full length name regarding to the International Union of Pure and Applied Chemistry (IUPAC). In addition to the position within the text, the compounds are also listed within the list of acronyms.

7, that has been the workhorse on the donor side during the last years in organic solar cell research [79] and also was the prime father and pioneer of most of the present thiophene-based donor polymers. Two prominent descendants of P3HTs are the copolymers poly[(4,8-bis-(2-ethylhexyloxy)-benzo(1,2-b:4,5-b')dithiophene)-2,6-diyl-alt-(4-(2-ethylhexyl)-3-fluorothieno[3,4-b]thiophene-)-2-carboxylate-2-6-diyl)] (PTB7), **10**, and poly[(2,6-Bis(trimethyltin)-4,8-bis(5-(2-ethylhexyl)thiophen-2-yl)benzo[1,2-b:4,5-b']-dithiophene)] (PBDTTT-C-T), **11**. These, among others like poly[N-9'-heptadecanyl-2,7-carbazole-alt-5,5-(4',7'-di-2-thienyl-2',1',3'-benzothiadiazole)] (PCDTBT), a copolymer of carbazole and thiophene, and their derivatives are typical representative polymers that are employed as donors today. The poly(p-phenylene vinylene) (PPV), **8**, and its derivative poly[2-methoxy-5-(2-ethylhexyloxy)-1,4-phenylenevinylene] (MEH-PPV), **9**, can be seen as intermediate donors that possess a conjugated structure but do not contain thiophene derivatives or sulfur at all. Except TPD and PVK, all are completely conjugated and thus the hopping mechanism only comes into play if charges move from one polymer chain to another.
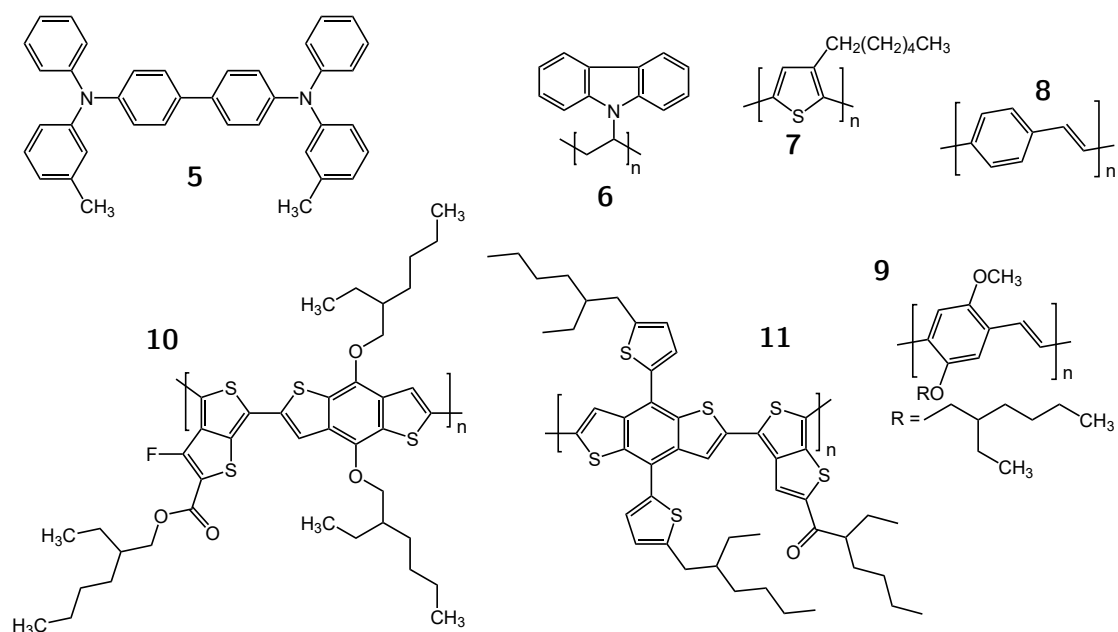
Scheme 4.1: Some representative molecules and polymers that are employed within organic optoelectronics: Small molecule TPD **5**, carbazole-based polymer PVK **6**, P3HT **7**, most-common thiophene derivative for organic solar cells, PPV **8**, a conductive and electroluminescent polymer that is also precursor for several other derivatives, PBDTTT-C-T **11** and PTB7 **10** are copolymers and more recent thiophene derivatives that provide higher efficiencies than P3HT, MEH-PPV **9** is a modified PPV.

4.2 Acceptors

Acceptors in organic optoelectronics are typically small molecules. The most common compounds are based on the famous buckminsterfullerene C_{60}, **12** in scheme 4.2, that is also called "buckyball". This molecule has the shape of a football (truncated icosahedron) and therefore consists of 60 carbon atoms that form 12 pentagons and 20 hexagons. The

molecule is completely conjugated and thus allows charges to be completely delocalized all over the surface. The variation with 70 carbon atoms is slightly elongated, has the shape of a rugby ball and consists of 25 hexagons and 12 pentagons. C_{60} and C_{70} as well as their derivatives are well-established in organic solar cell research. If solubility is needed for processing, the fullerenes are typically functionalized with groups that enhance the compatibility with common solvents. Examples are phenyl-C_{61}-butyric acid methyl ester (PCBM) (**13**) and 1',1'',4',4''-tetrahydro-di[1,4]methanonaphthaleno[5,6]fullerene-C_{60} (ICBA) (**14**). Both are highly soluble and provide good performance in bulk-heterojunction solar cells [80].
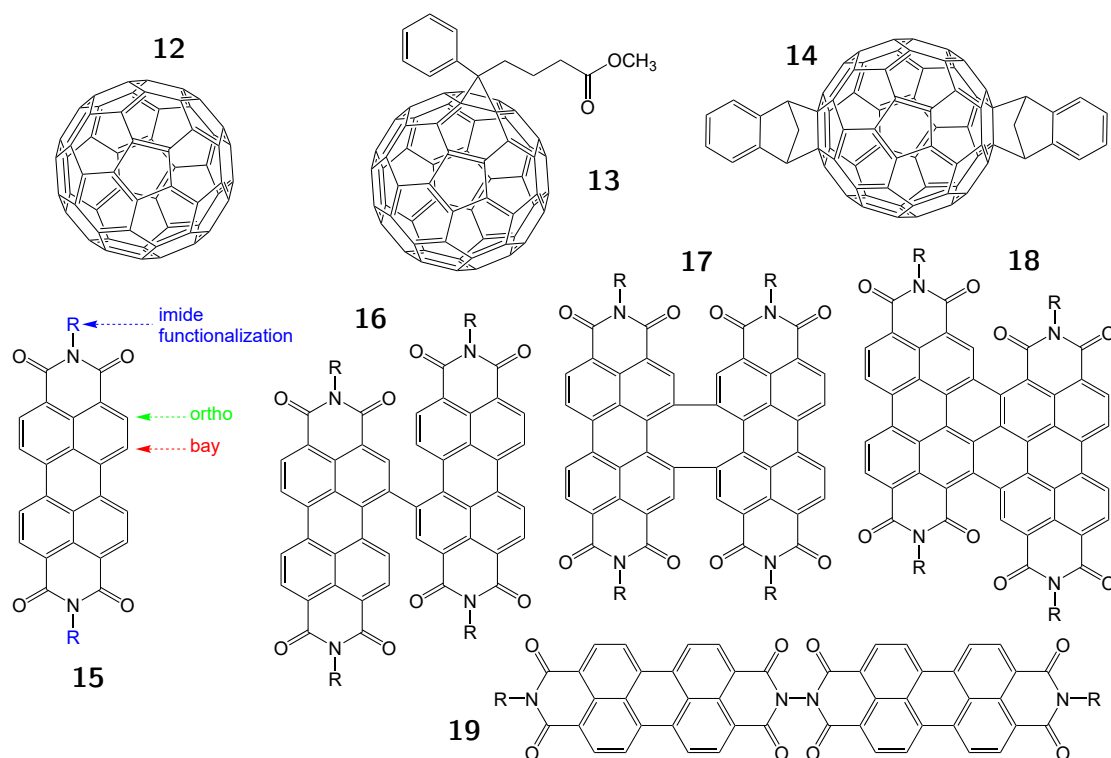
Scheme 4.2: Some representative acceptor molecules that are employed in organic optoelectronics: Within the fullerene familiy, C_{60}, **12**, PCBM, **13**, and ICBA, **14** and their C_{70} counterparts are most common. Non-fullerene alternatives are often based on perylene derivatives such as perylene bisimide (PBI), **15**. Additionally, PBIs can be dimerized resulting in different diperylene bisimides (diPBIs) like the singly-linked **16**, doubly-linked **17**, triply-linked **18**, and imide-linked **19**.

Due to some disadvantageous properties of fullerenes, especially their comparably low absorption in the spectral region of high sunlight intensities, research on non-fullerene acceptors has emerged during the last years [81]. Although already known for some time to be good and strong absorbing materials and also for being capable to perform light to electricity conversion, perylene derivatives were neglected for some time. Among several variations of derivatives, PBIs or also known as perylene diimides (PDIs) (**15**) have turned out to be very promising candidates to replace fullerenes. With their flat core similar to graphene, their broad functionalizability, and connectability to dimers, or higher oligomers, PBIs possess a higher flexibility and optimizability than many other families of molecules. Several possible variations of dimers have been realized and tested regarding

their applicability in organic electronics. While the singly-linked **16** and **19** variations provide outstanding performance in organic solar cells [82, 83], the doubly- **17** and triply-linked **18** compounds perform much less. Instead, the triply-linked derivative is a successful charge transfer agent in OFETs and highly efficient sensitizer in photorefractive composites [74, 76]. Typically, PBIs offer multiple positions for functionalization and thus for changing their solubility and optical properties. While groups added in the imide position (cf. **15**) change the solubility, other atoms or molecules in the bay position (cf. **15**) shift the energy levels and thus allow for tuning of the absorption properties.

As already demonstrated in the case of donors, also most of the common acceptor molecules have a conjugated structure. Additionally to the obvious reason that are grounded in improved charge transfer, acceptors are typically strong absorbing materials. The relation between conjugated materials and their application as chromophores (or dyes) was first described by Otto Nikolaus Witt, Russian, Swiss, and German chemist in 1876 [84, 85]. He made the following conclusion:

> "Die Farbstoffnatur aromatischer Körper ist bedingt durch die gleichzeitige Anwe-
> senheit einer farbstoffgebenden und einer salzbildenden Gruppe."

This German sentence says: "The origin of the dye-character of aromatic compounds calls for a simultaneous presence of a chromophore and a salt-producing unit." In general, Witt's assumptions are not limited to aromatic compounds but also valid for other types of conjugated materials.

However, the list of acceptors that are introduced in this section as well as the list of donors that have been introduced in section 4.1 make no claim of being complete. Instead, they aim to illustrate some material classes and to show that conjugation of organic materials plays a very important role in the field of organic optoelectronics. More detailed information on perylene derivatives are given in the respective section 10.1.

The following parts focus on applications of different organic materials. Parts II and III treat photorefractive polymer composites and organic solar cells, respectively. In both systems, mixtures of donor and acceptor materials are employed to act as a charge generating and transporting system. The azopolymers employed in part IV are not conductive but they are also excited optically.

Part II

Photorefractive polymer composites

Within this part, organic photorefractive (PR) composites are introduced. The focus is set on material synthesis as well as characterization. The term photorefractive is composed of the terms photon and refraction, i.e., it describes a light-induced change of the refractive index within a material. PR materials have been intensely studied during the last five decades [86–92]. The most prominent ones are inorganic crystals like lithium niobate (LiNbO$_3$), strontium barium niobate, Sr$_x$Ba$_{1-x}$Nb$_2$O$_6$ for $0.32 \leq x \leq 0.82$ (SBN), or barium titanate (BaTiO$_3$) [89]. These have been employed for experiments on holographic data storage, optical switching, optical phase conjugation, and as a platform for optical induction of photonic lattices [93–97].

With the advent of conductive organic materials also the development of photorefractive organic materials started. Several approaches to realize organic PR materials have been developed [11, 14, 15, 98, 99]. Besides organic amorphous glasses, fully functionalized polymers, polymer-dispersed liquid crystals, and other liquid crystal containing organics, the approach of organic photorefractive polymer composites has turned out to be very promising. This approach enables an ideal tunability of photorefractive speed, absorption, gain coefficient, and therefore offers the possibility to tailor the composition to the specific needs of an application [14].

In the next chapters and sections, the working principle of PR materials in general, followed by specific differences for organic photorefractives will be introduced. Subsequent, the synthesis or rather mixing of the components will be illustrated. Afterwards, the photophysical characterization process to determine the PR performance of the composites is presented, and results of newly developed compounds are displayed. The findings will especially illuminate the influence of non-fullerene sensitizers that are based on PBIs and especially diPBI. At last, also the influence of a different charge-transporting agent within the composites is studied.

5 Fundamentals of photorefractive properties in organic media

The photorefractive effect describes a light-induced refractive index change in a material [86]. In turn, this behavior can be exploited to influence light that propagates through such a compound. As mentioned in the introduction of the thesis, several materials possess the capability to store the varied refractive-index distribution. Consequently, they can be employed as storage media for data. In a different case, if the index modification is in the millisecond regime or even faster, optical switching or holographic displays become possible.

Due to the fact that the PR effect itself is based on two subprocesses, i.e., photoconductivity and the electro-optic (EO) effect, a photorefractive material has to provide both of them. While several inorganic crystals have inherent PR capabilities, this is typically not the case for organic media. Consequently, organic media have to be synthesized to provide the desired functionality. In order to understand the origin of each of the underlying subprocesses, they are explained in the following sections.

5.1 Photoconductivity

Photoconductivity describes a significant enhancement of a materials' conductivity that is caused by irradiation with light. While several semiconducting materials already provide conductivity to some extent without need of illumination, others only provide poor conductivity and thus are close to insulators.

Photoconductivity in a conventional semiconductor can be explained by employing the band model. Photons excite electrons from the valence band (VB) to the conduction band (CB). Within the CB, the electron is mobile and can freely move until it recombines with a hole or becomes extracted. The processes strongly depend on the material itself, e.g., the absorbed wavelengths depend on the CB-VB distance. Typically, most materials are not perfectly pure at all because they possess impurities due to the manufacturing process, or they are specifically doped with other materials. Both types of impurities lead to additional energy levels in the energy diagram. These levels are also called defect sites and can act as trapping sites for charge carriers. Thus, the distance between CB and the level of the defect site defines another wavelengths that is absorbed. In turn, recombination depends on the number of defect sites that cause a certain degree of localization of the charge carrier and therefore enable higher recombination rates.

In addition to absorption, the other crucial aspect of photoconductivity is charge carrier mobility. The higher the mobility and absorption the higher is the output of photo-generated charge carriers. Mobility itself is also strongly influenced by defect sites that cause trapping of charge carriers. The movement of trapped charge carriers' is hampered until they are detrapped. Therefore, more defects will obviously reduce the charge carriers' mobility.

Contrary to inorganic semiconductors, photoconductivity in organic PR media is slightly different. Due to the nature of the compositions that are typically realized by a dye acting as an acceptor and a transparent donor, holes are mobile while electrons are bound to a dye molecule. A schematic representation of the charge transfer including trapping and detrapping is illustrated in figure 5.1. An electron in a sensitizer molecule
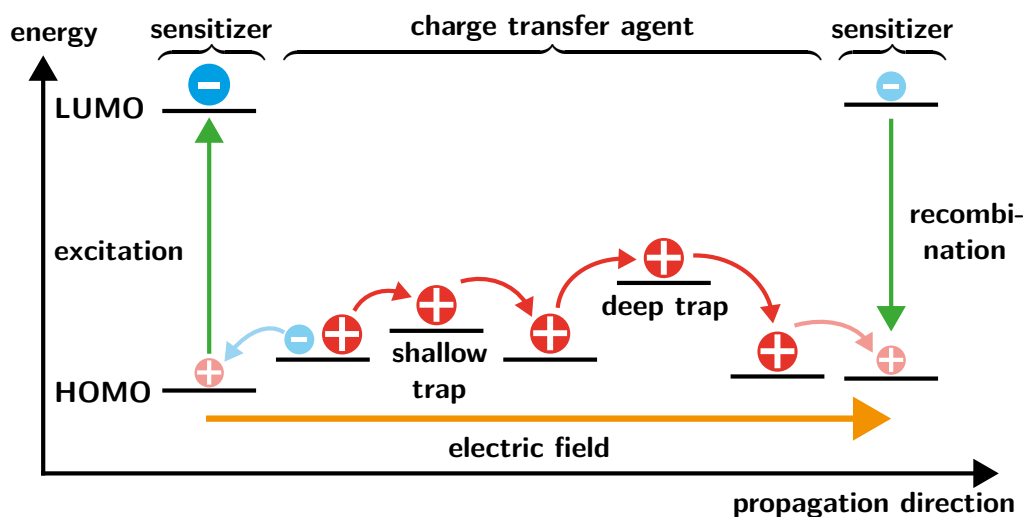
Figure 5.1: Schematic representation of the charge carrier movement in an organic photorefractive material. Excitation and recombination occurs at sensitizer sites while charges are transported by the charge-transporting agent (CTA) and driven by the applied electric field. The smaller carriers with enhanced transparency indicate exciton separation and formation, respectively.

is excited from the HOMO to the LUMO level. This excited state is called exciton. The applied electric field leads to exciton separation, and consequently, due to the low dye density, the electron remains bound to the molecule. In turn, the remaining hole is filled by an electron from a charge-transporting agent (CTA) molecule. Subsequently, the hole moves through the CTA and is driven by the applied electric field. On its way, trapping in shallow or deep traps may occur. The difference between both types of traps is the detrapping probability. While the holes in shallow traps are easily thermally detrapped, the probability is about one order of magnitude smaller for deep traps [14]. Finally, if the mobile hole are not extracted at an electrode, it may form a new exciton with an electron that is bound in a sensitizer molecule. If not separated again, this exciton recombines.

In PR materials, a compromise between the number of defect or trapping sites and charge carrier mobility has to be found. While high mobilities enable a fast redistribution of excited charge carriers, the trapping sites are desired to get an inhomogeneous spatial distribution of charge carriers that in turn influence the refractive index of the material. The underlying mechanism that finally leads to the refractive index change is the so-called electro-optic effect. While inorganic PR materials possess inherent electro-optic features, in most cases they have to be added by separate components in the organic photorefractive species. In the following section, the basics of the electro-optic effect will be introduced and differences between organic and inorganic will be enlightened.

5.2 Electro-optic effect

5.2.1 Short introduction into nonlinear optics

Typically, a materials' response to an electric field is linearly dependent on the magnitude of the field. In case of strong fields that overcome the internal fields, as it is the case when lasers are employed as light source, the response can shift to a nonlinear regime. This nonlinear response is described by an expansion of the field-dependent susceptibility [100]

$$\chi(E) = \chi_{\mathrm{L}} + \chi^{(2)} E + \chi^{(3)} EE + \dots \ . \tag{5.1}$$

Here, χ_{L} describes the linear part of the total optical susceptibility $\chi(E)$, while $\chi^{(2)}$ and $\chi^{(3)}$ are higher order terms, namely the second- and third-order susceptibilities. Because of the relation between material polarization, susceptibility, and electric field $P(r,t) = \varepsilon_0 \chi E(r,t)$, the nonlinear behavior of the second has also an influence on the polarization that becomes

$$P(E) = \varepsilon_0 \chi_{\mathrm{L}} E + \varepsilon_0 \chi^{(2)} EE + \varepsilon_0 \chi^{(3)} EEE + \dots \ . \tag{5.2}$$

Analogous to the susceptibility, the second and the third terms of equation (5.2) correspond to the second- and third order contributions of the polarization. These terms that correct the polarization in case of high electric fields are the basis to explain several effects of nonlinear optics of second- or third order, respectively. The most common examples are the generation of higher harmonics (frequency conversion processes), optical rectification, or a refractive index change.

While all materials have a non-zero $\chi^{(3)}$ and therefore third-order nonlinear processes exist in every medium, this does not hold for second-order processes. These are limited to compounds that possess no inversion symmetry, i.e., that are not centrosymmetric. The reason for the necessity of lacking inversion symmetry becomes obvious if the induced polarization of two electric fields of equal amplitude that are oriented in opposite directions is considered. The susceptibility contributions would sum up to zero, i.e., $\chi^{(2)} = 0$. Having this in mind, one can easily conclude that symmetry considerations of the employed material are essential if nonlinear $\chi^{(2)}$ processes are desired. As a consequence, photorefractive materials whose refractive index change due to the electro-optic effect is based on a $\chi^{(2)}$ effect have to be noncentrosymmetric [100]. Anisotropy in general is not a sufficient criterion for noncentrosymmetry because molecules can still be aligned antiparallelly and therefore centrosymmetrically. This symmetry can be broken up by a parallel alignment of the molecules, e.g., by poling with an electric field.

The necessity for $\chi^{(2)}$-media to be anisotropic requires that $\chi^{(2)}$ itself is not a simple constant but a tensor of rank 3 with 27 components. In general, $\chi^{(n)}$ are tensors of rank $n + 1$ with 3^{n+1} components. Typically, to reduce complexity, several assumptions and simplifications are made. One of the most common is the application of group theory to contract components that are equal. This is possible since there are other symmetries that can be exploited apart from the lacking inversion symmetry. Additionally, if the medium is lossless, i.e., the imaginary part of the complex susceptibility vanishes, full permutation

symmetry exists. Further, if the nonlinear interaction of the involved wavelengths is far from resonance, the dispersion of the optical response can be ignored. Now, all Cartesian indices of the susceptibility can be permuted without changing the frequencies while the tensor elements stay the same. This approximation is called Kleinman symmetry and is typically applied to describe electro-optic media [100].

A Fourier transform of the $P(t) = \chi(t)E(t)$-relation with respect to $\chi^{(2)}$ gives the expression

$$P_i(\omega_n + \omega_m) = \varepsilon_0 D \sum_{jk} \chi_{ijk}^{(2)}(\omega_n + \omega_m; \omega_n, \omega_m) E_j(\omega_n) E_k(\omega_m) \tag{5.3}$$

where the indices i,j,k refer to the Cartesian components of the fields. D is the so-called degeneracy factor that represents the number of distinct permutations of the frequencies ω_n and ω_m [100]. The first argument of the susceptibility term in equation (5.3) denotes the specific nonlinear process. In case of second harmonic generation, this term would be 2ω. The second and third terms describe the frequencies of the two fields that contribute to the process. These frequencies are not limited to the optical range but can be very low or even zero. If this is the case, a zero-frequency field (d.c.) interacts via equation (5.3) with a field of an optical frequency, the effect of a refractive index modulation is described.

In general, the complex refractive index is defined as

$$n = \sqrt{\varepsilon_r \mu_r} \tag{5.4}$$

where ε_r is the permittivity and μ_r is the magnetic permeability. In nonmagnetic media, the latter typically equals 1 and the equation reduces to $n = \sqrt{\varepsilon_r}$. With $\varepsilon_r = 1 + \chi$ the connection between susceptibility and refractive index is made and is represented by the term [101]

$$n = \sqrt{1 + \chi} \; . \tag{5.5}$$

This relation provides the basis for the description of the (light) field-induced refractive index change used in the next section.

5.2.2 Field-dependent refractive index change

The electro-optic effect denotes the influence of an electric charge-density distribution on the refractive index of a material and therefore an impact on the optical properties. The effect itself can be split up in a linear part, the so-called Pockels effect, and a quadratic part, the Kerr effect. The notation linear and quadratic refer in this case to the linear and respectively quadratic dependence of the refractive index change on the electric field that result from a Taylor expansion (cf. equation (5.6) [101]:

$$n(E) = n + a_1 E + \frac{1}{2} a_2 E^2 + \dots \; . \tag{5.6}$$

Here, the coefficient n denotes the refractive index at zero field intensity $n = n(0)$, while $a_1 = (\mathrm{d}n/\mathrm{d}E)|_{E=0}$ and $a_2 = (\mathrm{d}^2 n/\mathrm{d}E^2)|_{E=0}$. Typically, the terms a_1 and a_2 are

rewritten to $r_{\text{Pock}} = -2a_1/n^3$ and $r_{\text{Kerr}} = -a_2/n^3$ that are known as the electro-optic coefficients. Now, equation (5.6) can be reformulated to

$$n(E) = n - \frac{1}{2}r_{\text{Pock}}n^3 E - \frac{1}{2}r_{\text{Kerr}}n^3 E^2 + \dots \; . \tag{5.7}$$

Based on this equation, the refractive index change $\Delta n = n - n(E)$ is just the sum of the linear and quadratic field terms of the Taylor expansion. Higher order terms are typically neglected because they are much smaller than the already mentioned ones [101].

5.2.3 Pockels effect

Depending on the medium that is employed, the coefficients r_{Pock} and r_{Kerr} control the influence of the linear and quadratic part of the refractive index change. In case of materials without an inversion symmetry like $LiNbO_3$, SBN, or other non-centrosymmetric compounds r_{Pock} provides a significant contribution of the linear part while the quadratic one can be neglected. This results in

$$\Delta n = \frac{1}{2}r_{\text{Pock}}n^3 E \tag{5.8}$$

and is called the Pockels effect, named after the German physicist Friedrich Pockels, while r_{Pock} is called Pockels coefficient or first electro-optic coefficient. Typical values of r_{Pock} are in the range of $10^{-12} - 10^{-10}\,\text{m V}^{-1}$ resulting in a refractive index change $\Delta n = 10^{-6} - 10^{-4}$ assuming an electric field of $E = 10^6\,\text{V m}^{-1}$ [101].

5.2.4 Kerr effect

In case of $r_{\text{Kerr}} \neq 0$, for the so-called Kerr coefficient or second electro-optic coefficient, the medium has to be centrosymmetric. For media like gases, liquids, and some crystals, this is valid. The resulting change of the refractive index

$$\Delta n = \frac{1}{2}r_{\text{Kerr}}n^3 E^2 \tag{5.9}$$

is called Kerr effect, named after the Scottish physicist John Kerr. Typical values of the Kerr coefficient are in the range $10^{-18} - 10^{-14}\,\text{m}^2\,\text{V}^{-2}$ in crystals and $10^{-22} - 10^{-19}\,\text{m}^2\,\text{V}^{-2}$ in liquids. For an applied electric field of $10^6\,\text{V m}^{-1}$, Δn is in the range of $10^{-6} - 10^{-2}$ in crystals and $10^{-10} - 10^{-7}$ in liquids [101].

5.2.5 Electro-optics in organic photorefractive materials

In organic photorefractive media, the functionality is to some part different to inorganic crystals. Besides the already mentioned differences that refer to charge transfer that is mainly performed by hopping and tunneling processes, also the electro-optic (EO) effect has a different working principle in organic media. The EO effect is not provided by a charge density distribution within a bulk material but by the sum of many little contributions that are provided by electro-optic molecules within an organic

PR compound. Figure 5.2 depicts the orientation of electro-optic molecules, here also
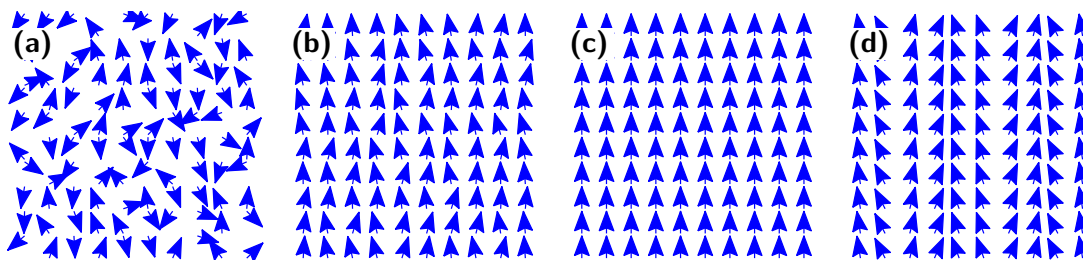
Figure 5.2: Schematic illustration of chromophore orientation. From left to right: Isotropic or random distribution **(a)**, weakly poled distribution **(b)**, strongly poled anisotropic distribution **(c)**, and anisotropic distribution with superimposed sinusoidal pattern **(d)**.

called chromophores, in different states. Subfigure **(a)** represents the isotropic phase where all units are randomly oriented. In this case, no centrosymmetric configuration is given, but in general, all contributions would sum up to $\chi^{(2)} = 0$ and therefore this configuration would not be electro-optic. In case **(b)**, an electric field is applied to the chromophores and this leads to an orientation of the molecules along the direction of the field. Depending on the strength of the field, randomness still holds (cf. **(b)**) or approximately vanishes and all chromophores are almost perfectly aligned along the strong field in **(c)**. In a photorefractive material, the redistributed charges lead to formation of a space-charge field E_{SC} that has the shape of the incident light field. Assuming a sinusoidal light field, the redistributed charges would induce a space-charge field of the same shape. If this E_{SC} is superimposed with the applied electric field E_{ext}, the resulting chromophore orientation corresponds to subfigure **(d)**.

In the previous sections, fundamental criteria for photorefractivity and desired properties that materials have to fulfill were introduced. Besides photoconductivity, electro-optic properties are desired. In organic photorefractives, the sum of contributions of several molecules give the response of the whole material. What is lacking until now are specific design criteria for a molecule to be electro-optic. Breaking down the macroscopic consideration of symmetry to a microscopic level, also the molecules themselves are not allowed to be centrosymmetric. Therefore, ways to break the symmetry have to be established. One possibility is the attachment of different groups to the ends of a conjugated system. These groups have to be different regarding their electron affinity thus one end of the molecule is acting as a donor while the other acts as an acceptor. These so-called push-pull molecules possess a dipole moment in their ground state and can be manipulated by an external electric field. The degree that describes the strength of this response, its polarizability, depends on the direction of the electric field with respect to the molecular orientation. In general, the charge flow towards the acceptor is strong while it is hindered towards the donor [100]. This asymmetry of the polarization leads to the desired strong second-order nonlinearity. Approximating the molecule by a dipole and assuming nonresonant conditions, the microscopic components of the expanded polarization can be written as

$$p_i = \mu_i + \sum_j \alpha_{ij} E_j + R^{(2)} \sum_{jk} \beta_{ijk} E_j E_k + R^{(3)} \sum_{jkl} \gamma_{ijkl} E_j E_k E_l + \dots \,, \qquad (5.10)$$

where α_{ij}, β_{ijk}, and γ_{ijkl} represent tensor elements while E_j, E_k, and E_l are components of the electric field [102]. The indices i, j, k, and l refer to Cartesian coordinates that are expressed in the frame of the molecule. The ground state dipole moment of the molecule is given by μ_i. Further, the complete tensors $\tilde{\alpha}$, $\tilde{\beta}$, and $\tilde{\gamma}$ that represent the linear polarizability, the first hyperpolarizability, and the second hyperpolarizability, respectively, can be directly related to macroscopic quantities. The tensor $\tilde{\beta}$ corresponds to $\chi^{(2)}$ while $\tilde{\gamma}$ is the equivalent of $\chi^{(3)}$ on the molecular scale. Analogous to D in equation (5.3), the $R^{(n)}$ represent degeneracy factors that are influenced by the nonlinear process and the frequencies that contribute to the process.

From equation (5.10) can be directly derived that not only $\tilde{\beta}$ has a strong impact on the overall polarization but also the ground state dipole moment μ. Therefore, molecules that exhibit a large μ and a strong first order hyperpolarizability are desired for organic photorefractives that provide high performance.

As already mentioned, $\tilde{\beta}$ corresponds to $\chi^{(2)}$. This connection can be made via the oriented gas model four basic assumptions [100]. The first assumption excludes coupling or reaction of the surrounding matrix with the chromophore units at the poling temperature. Therefore, the electro-optic molecules can freely rotate under the influence of the applied electric field. The second assumption expects that the chromophores have cylindrical symmetry and β_{zzz} is the only non-vanishing tensor element of the hyperpolarizability. The index z corresponds to the symmetry axis of the molecule. The third assumption refers to the permanent dipole moment of the molecule that has to be oriented along the z-axis. Finally, the fourth assumption requires non-interacting and independent chromophore molecules.

If Kleinman symmetry is applied, there are left only two independent tensor elements for poled polymers of $\chi^{(2)}$. These are $\chi^{(2)}_{ZZZ}$ and $\chi^{(2)}_{ZXX}$ where the indices Z and X refer to the macroscopic Cartesian coordinates. Introducing reasonable experimental restrictions regarding the magnitude of the dipole moment, the applied electric field, and the temperature, the tensor elements can be written as

$$\chi^{(2)}_{ZZZ} = N \frac{\mu^* E_p}{5 k_{\mathrm{B}} T} \beta^*_{zzz} \tag{5.11}$$

and

$$\chi^{(2)}_{ZXX} = N \frac{\mu^* E_p}{15 k_{\mathrm{B}} T} \beta^*_{zzz} \ . \tag{5.12}$$

Here, the relation $\chi^{(2)}_{ZXX} = \chi^{(2)}_{ZZZ}/3$ of the two components becomes directly obvious. The asterisk superscripts of μ^* and β^*_{zzz} indicate that theses values are corrected for local field effects of the surrounding matrix, while E_p describes the part of the applied poling field that is oriented along the Z axis. The terms k_{B} and T represent the Boltzmann constant and the temperature, respectively, while N is the density of the chromophores [100]. Again, as already highlighted by equation (5.10), the importance of the dipole moment of the chromophores is additionally displayed by equations (5.11) and (5.12) and therefore it has to be preferably large. This also holds for the first hyperpolarizability. Consequently, both parameters play a crucial role in chromophore design.

Another effect that occurs especially in organic photorefractive media whose glass transition temperature T_g is close to ambient temperature is the so-called orientational birefringence. Media with considerably high T_g are heated up for poling and then cooled down for operation. Therefore, they posses a permanent birefringence that is spatially uniform and plays an underpart in electro-optic modulation. In contrast, the birefringence of low-T_g media can be manipulated during normal electro-optic operation. This spatially-modulated birefringence is mainly induced by the spatially-modulated internal space-charge field. The refractive index changes in x- and z-direction can be expressed as [103]

$$\Delta n_z^{\mathrm{BR}} = \frac{1}{2n} \Delta \chi_{zz}^{(1,\mathrm{BR})} \quad \text{and} \tag{5.13}$$

$$\Delta n_x^{\mathrm{BR}} = -\frac{1}{4n} \Delta \chi_{zz}^{(1,\mathrm{BR})} \; . \tag{5.14}$$

Here, n is the unperturbed refractive index and $\Delta \chi_{zz}^{(1,\mathrm{BR})}$ is the change in the first-order optical susceptibility resulting from the poling-induced birefringence. The latter is quadratically dependent on the electric poling field E_p via

$$\Delta \chi_{zz}^{(1,\mathrm{BR})}(-\omega;\omega) = N(\alpha_{\parallel}^{(\omega)} - \alpha_{\perp}^{(\omega)}) \left(\frac{2}{45} \right) \left(\frac{\mu E_p}{k_{\mathrm{B}} T} \right)^2 \; . \tag{5.15}$$

This dependence is the reason why this effect is called orientational Kerr effect despite it does not depend on $\chi^{(3)}$.

5.3 Photorefractive effect

In this section, the interplay between photoconductivity and the electro-optic effect is explained in more detail and therefore a deeper understanding of the photorefractive effect is provided. A schematic representation of the subprocesses of the PR effect is given in figure 5.3. The crossing green arrows at the top indicate two interfering laser beams as an example for simple pattern generation. This interference is expressed in a sinusoidal light intensity distribution in **(a)**[1]. Within the material, the light causes a formation of excitons that are split up to positive and negative charge carriers. While, in case of organic photorefractives, the electrons remain immobile at the excited acceptor sites, the holes can be redistributed (cf. **(b)**). The redistribution processes are diffusion and drift whereas drift in an electric field is the dominating process for organic materials. Finally, trapping leads to a stop of the hole movement in regions with low light intensity, as depicted in **(c)**. Due to the separation of both types of charge carriers, a SCF is build up (step **(d)**). Finally, the electro-optic effect, mainly the Pockels effect, converts the SCF into a refractive index change. Compared to the incident light intensity pattern, the refractive index modulation is shifted by ϕ as can be observed in **(e)**. In case of drift dominated charge transfer, as it is the case for the organic photorefractive media within this thesis, the phase shift is $\phi = 90°$. As a direct consequence of the dephasing, incident

---

1   The abscissa only indicates the spatial component. Its position relative to the ordinate does not imply a negative intensity.
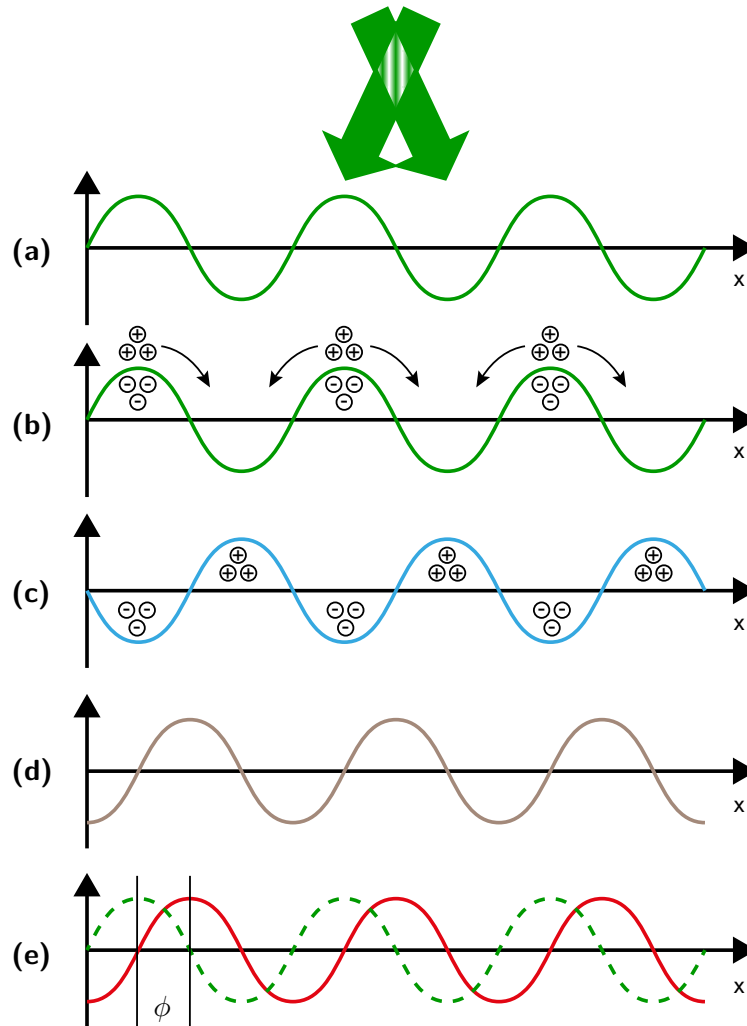
Figure 5.3: Illustration of the mechanisms of the photorefractive effect. The green arrows indicate two interfering laser beams that generate a sinusoidal light pattern represented by **(a)**. Part **(b)** shows the generation of charge carriers in regions with high light intensity and subsequent redistribution of the mobile holes that is completed by trapping of the holes in **(c)**. As a consequence, the space-charge field (SCF) in **(d)** is build up and leads to the refractive index pattern in **(e)**. The ϕ indicates the phase shift between incident light pattern and refractive index grating. The image is adapted from [102].

light beams interfere within the sample and thus energy transfer from one beam to the other occurs. The direction of the energy transfer depends on the direction of the phase shift with respect to the incident beams. Constructive interference leads to energy gain while destructive interference leads to energy loss [98, 103, 104].

This description of the fundamental PR effect lacks information about quantities of the space-charge field, optically induced refractive index change, as well as details of the photorefractive sample. The latter will be given in the next section while the other parameters as well as a further explanations regarding the characterization of the photorefractive effect are provided in section (6.3). There, a special focus will be set on the conditions that are enforced by sample size and geometry.

In the next section, the composition and preparation of PR composites are explained. Additionally, information about the employed sample design is provided.

5.4 Composition and sample layout

Photorefractive compositions discussed in this thesis are typically composed of three to four components. While the electro-optic unit, 4'-Pentyl-4-biphenylcarbonitrile (5CB) is kept in all compositions, the other components such as the acceptor, also called sensitizer, and the donor (or CTA) are varied. As a reference system, the composition PCBM:PVK:5CB is chosen. First studies on this system were made by Zhang et al. [16] (with $(C_{60}\text{-}I_h)[5,6]$fullerene (C_{60}) instead of PCBM) in 1998. The great advantages of this composition are the quite good photorefractive performance as well as its ease of fabrication due to commercially available ingredients.

In a first step, the influence of the sensitizer that is responsible for light absorption and thus the operating wavelength is studied. Besides the absorption, the dye is additionally crucial for the photoconductivity because it determines the number of photons that are converted to charge carriers. To check how large this impact is, PCBM is replaced by diPBI, more precisely triply-linked 12C-4CldiPBI[1] with chlorine atoms in the bay position and dodecyl chains in the imide positions, respectively. In a subsequent step, the CTA is replaced by TPD doped polysterene to further boost the performance. The sensitizers as well as the CTAs have been introduced in chapter 4, schemes 4.2 and 4.1. Additionally, more details about diPBI can be found in section 10.1.

5.4.1 5CB

The so far missing component, the electro-optic unit, is 5CB and depicted in scheme 5.1. The nematic liquid crystal 5CB was first synthesized by Gray et al. at the University of Hull in 1972 [105]. Its design is based on the previously introduced concept of a push-pull molecule consisting of a conjugated part connecting a polar cyano group with a nonpolar pentyl tail [106]. Consequently it possesses a large dipole moment and thus can be easily poled via application of an electric field. This poling breaks the centrosymmetry and thus allowing for high electro-optic coefficients and large refractive index changes due to

---

1 Although later denoted as tdiPBI, in this part it is mostly referred as diPBI.
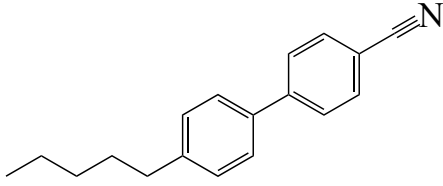
Scheme 5.1: Chemical structure of a molecule of the nematic liquid crystal 5CB.

the Pockels effect. 5CB itself is transparent over a wide spectral range and therefore does not influence the overall light intensity via absorption. Its melting temperature is at $T_{\text{melt}} = 22.5\,°\text{C}$ and its nematic clearing point $T_{\text{NC}} = 35.0\,°\text{C}$. This allows for good liquid crystal operation at room temperature and slightly above. The inventors of 5CB have shown that it is operational in a supercooled state and therefore allows for an even broader operational window than the $T_{\text{NC}} - T_{\text{melt}}$ difference [105].

Due to its liquid crystal character and its low T_{melt}, 5CB also reduces the T_{g} of an photorefractive composite and therefore supersedes the need for an plasticizing agent that is typically comprised in organic PR compounds. Plasticizers are employed to reduce the viscosity of PR composites. Without it, the chromophores would not be able to be reoriented via external and internal electric fields. Due to the fact that 5CB acts as an electro-optic moiety and plasticizer at once, no special plasticizers are used in this work, so they are not explained in more detail. Further information can be found in several reviews and books on organic photorefractive materials [11, 14, 15, 100].

Relevant parameters of 5CB for its PR performance are the dipole moment μ_{5CB}, the polarizability α_{5CB}, the anisotropic polarizability $\Delta\alpha_{\text{5CB}} = \alpha_{\parallel} - \alpha_{\perp}$, and the first hyperpolarizability β. The dipole moment has been determined to be $\mu_{\text{5CB}} = 4.76\,\text{D} = 15.9 \times 10^{-30}\,\text{C m}$ [107, 108]. Data regarding the average polarizability $\bar{\alpha}_{\text{5CB}}$ and the anisotropic polarizability vary within the literature. While Dunmur et al. [107] state $\bar{\alpha}_{\text{5CB}} = 37.5 \times 10^{-40}\,\text{C}^2\,\text{m}^2\,\text{J}^{-1}$ and $\Delta\alpha_{\text{5CB}} = 19.4 \times 10^{-40}\,\text{C}^2\,\text{m}^2\,\text{J}^{-1}$, Clark et al. [109] provide the full tensor

$$\alpha_{\text{5CB}} = \begin{pmatrix} 66.15 & -2.65 & -0.90 \\ -2.65 & 26.67 & -2.07 \\ -0.90 & -2.07 & 27.64 \end{pmatrix}$$

in electro static units (esu). Taking polarizability conversion factors from Cox et al. [110] (see also A.1), the average is simply calculated by $\bar{\alpha}_{\text{5CB}} = \text{tr}\,(\alpha_{\text{5CB}})/3 = 40.15 \times 10^{-24}\,\text{cm}^3 = 44.7 \times 10^{-40}\,\text{C}^2\,\text{m}^2\,\text{J}^{-1}$ of the polarizability, where the operator tr denotes the trace of the tensor [109]. Additionally, the average polarizability can be calculated from the diagonalized tensor α_{5CB} and the relations $\alpha_{xx} > \alpha_{yy}$ and $\alpha_{yy} \approx \alpha_{zz}$ while $\Delta\alpha_{\text{5CB}} = \alpha_{xx} - \alpha_{yy}$. The first relations assume that the conjugated system is oriented along the x-direction. Due to the fact that α_{yy} and α_{zz} cannot be clearly distinguished, $\Delta\alpha_{\text{5CB}}$ has to be in the range between $\alpha_{xx} - \alpha_{yy}$ and $\alpha_{xx} - \alpha_{zz}$ resulting in the range $\Delta\alpha_{\text{5CB}} = 41.3 \times 10^{-40} - 46.2 \times 10^{-40}\,\text{C}^2\,\text{m}^2\,\text{J}^{-1}$. Tensor diagonalization is performed employing MATLAB's *eig*-function [111]. The $\Delta\alpha_{\text{5CB}}$ based on [109] is more than twice as large as the one reported by [107]. Subsequent studies of further publications [108, 112] reveal that calculated data for polarizability and polarizability anisotropy vary to some extent and only coincide in a few cases. Obviously, differences originate from different approaches that have been employed for calculation while others

are caused by the dispersive behavior of these parameters. Finally, the data reported for $\Delta\alpha_{5CB}$ in different articles are within the range that results from the values from Clark et al. and Dunmur et al.

Studies on the hyperpolarizability that is from importance for the Pockels effect were carried out by Risser et al. [113]. Besides the expected dispersive behavior of these parameters, they found a significant influence of the twist between the phenyl rings and thus of the conjugated system that constrains the electronic system. If the system is twisted by 90°, first and second hyperpolarizability are minimized, whereas the maximum values are reached at 0° and 180°, respectively. Considering minimum energy conformation, a twist angle of 40.14° has proven to be the optimum which is in coincidence with experimental values.

For twist angles in the range $0-90°$, the first hyperpolarizability under static conditions varies between $2.672 \times 10^{-50}\,\mathrm{C^3\,m^3\,J^{-2}}$ for the non-twisted case and $0.965 \times 10^{-50}\,\mathrm{C^3\,m^3\,J^{-2}}$ in the fully-twisted case. Considering a twist angle of 40.14°, β is in the range of $2.041 \times 10^{-50} - 3.897 \times 10^{-50}\,\mathrm{C^3\,m^3\,J^{-2}}$ for the energy range $0-1.2\,\mathrm{eV}$ [113].

Compared to other electro-optic moieties like disperse red (DR) or 2,5-dimethyl-4-(p-nitrophenylazo)anisole (DMNPAA) [114] that are employed within photorefractive polymers, the dipole moment as well as the first hyperpolarizability of 5CB are rather low and there are several other materials that provide larger coefficients but the great advantage of 5CB is its ease of application and availability.

5.4.2 Fabrication of photorefractive samples

In the context of this thesis, a photorefractive sample consists of two glass slides coated with indium tin oxide (ITO) that sandwich the composite material. In more detail, several aspects that have a large impact on overall sample performance and characterization have to be considered. First, the area and consequently the volume of the photorefractive material within the sample have to be fixed. This is realized by a tailored electrode design and fixed electrode spacings.

The employed substrates from *Präzisions Glas & Optik GmbH, Iserlohn* are coated with a 25 nm silicon dioxide (SiO_2) passivation layer, a 100 nm ITO layer, and possess a resulting sheet resistance of $20\,\Omega$. In order to generate the shape of the electrode that is depicted in figure 5.4, the area where ITO should remain is covered with tape[1]. Subsequently, the substrates are given to diluted hydrochloric acid[2] and etched for about $1-2$ hours until ITO as well as passivation layer are completely removed in the unmasked area.

5.4.2.1 Electrode patterning and sample layout

The electrode layout in figure 5.4 ensures a fixed circular area of $3.5^2 \times \pi\,\mathrm{mm^2}$ if two substrates with opposing directions of electrodes are employed to sandwich PR composites

---

1   Structured with a cutting plotter
2   Mixture of water and hydrochloric acid (37 %) in a volume ratio of 1:1.

and spacer foil. A schematic representation (not true to scale) of a prepared sample is given in figure 5.5. The scheme is split into two views whereof the upper part displays
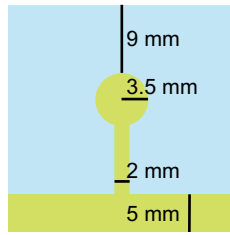
Figure 5.4: Schematic representation of a glass substrate with a structured ITO electrode (yellowish part). The overall dimensions are $30.0 \times 30.0 \times 0.7\,mm^3$. All dimensions of the electrode are chosen to result in a perfectly opposing circular pair of electrodes and two 5 mm electrode stripes on both sides for electric connections.

the profile of the assembled sample while the lower part is the top (or bottom) view. It can be clearly seen that the circular parts of the electrodes form a circular electrode pair while there are no other overlapping electrode parts. Further, the circular parts of both electrodes are separated by the PR composite. To avoid short circuits in this region, it is important that the diameter of the PR material is larger than the diameter of the electrodes. Due to the electrode layout, there are ITO-coated stripes on both sides of the sample that are employed to realize electric connections. For this purpose, conductive copper tape is attached to these regions and enables good connections to a high voltage source as well as metrology.
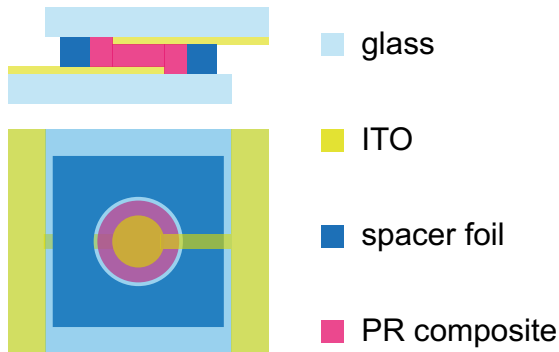
Figure 5.5: Scheme of profile and top view (not true to scale) of an assembled PR sample. The PR composite (purple) is sandwiched between two glass substrates (light blue) with structured electrodes (yellowish). The spacing of the electrodes is adjusted by the spacer foil (dark blue). The illustration of the SiO_2 passivation layer is omitted.

5.4.2.2 Synthesis of photorefractive compositions

Another step in PR sample fabrication is the preparation of the composite itself. Except of the nonlinear liquid crystal (LC) employed for the electro-optic functionality, all components are powders and thus need to be dissolved prior to mixing. Dissolving is essential because of the difficulty of weighing in the sub-mg regime. Especially if the sensitizing material is considered, weighing the exact amount of it would not work. Therefore, solutions with a defined concentration of sensitizer and CTA are prepared, respectively, and subsequently mixed in the desired ratio. This ratio is based on the composition by Zhang et al. [16], i.e., PVK:5CB:C_{60} 59.8:40.0:0.2 wt%. In order enhance solubility of the sensitizer in common solvents (here: chloroform ($CHCl_3$)), C_{60} is replaced by its derivative PCBM while the mass ratio is kept the same. Converting the values to a molar ratio gives 0.983:98.882:0.135 mol% if the molecular weight (M) listed in table A.1 in appendix A.2 are applied. Based on this molar ratio, the desired quantities for compositions made of other materials can be easily calculated. In a first step, the influence of the sensitizer on the PR performance is tested. To do so, PCBM is

replaced by diPBI and crucial parameters such as photorefractive gain as well as speed (cf. subsection 6.3.1) are determined [76, 77]. In a second step, the charge-transfer agent PVK is replaced by the monomeric TPD. Due to processing difficulties and crystallization of the prepared samples, PS is added to the composition to act as a polymeric matrix for TPD. While a weight ratio of 50.0:50.0 wt% (TPD:PS) still tends to crystallization, this is omitted in a 20.0:80.0 wt% relation and thus this ratio is chosen to replace PVK while the weight amount of CTA in the composition is kept.

In order to compare the performance of different sensitizers as well as charge-transfer agents, the compositions described in table 5.1 are adjusted to provide the same absorption coefficient α (cf. equation (6.2)) at 532 nm. Due to this requirement, amounts of sensitizer vary significantly between the PCBM and diPBI containing samples [74, 76]. Additionally, this has a small impact on the amounts of CTA and chromophores. The differences between the molar amounts of PVK and TPD:PS containing samples originate from the different molar weights of the components. The data provided in table 5.1 are calculated assuming the averaged weights of the polymer chains. If the weights of single molecules would be assumed, the molar composition would scale completely different.

Table 5.1: Photorefractive compositions that provide the same absorption at 532 nm. The name of the composites results from the CTA and the sensitizer in the following way: <first_letter_of_CTA>-<first_letter_of_sensitizer>. All values are given in wt% and mol % in which the average molecular weight of the polymer chains regarding table A.1 is applied.

		P-P	P-D	T-P	T-D
PVK	wt%	59.690	59.797	–	–
	mol %	0.979	0.980	–	–
TPD	wt%	–	–	11.938	11.959
	mol %	–	–	12.528	12.542
PS	wt%	–	–	47.752	47.838
	mol %	–	–	0.129	0.130
5CB	wt%	40.111	40.184	40.111	40.184
	mol %	98.887	99.013	87.224	87.321
PCBM	wt%	0.199	–	0.199	–
	mol %	0.134	–	0.118	–
diPBI	wt%	–	0.019	–	0.019
	mol %	–	0.007	–	0.007

As previously mentioned, for the sake of handling sensitizer solutions at concentrations of $c_{\text{PCBM}} = 10\,\text{mg}\,\text{ml}^{-1}$ for PCBM and $c_{\text{diPBI}} = 1.75\,\text{mg}\,\text{ml}^{-1}$ for diPBI are prepared in CHCl$_3$, respectively. Depending on the desired composition, the needed amount of sensitizer solution is added to the other components. The amounts of PVK, TPD, and PS are large enough to be weighed directly without the preparation of an intermediate CTA

solution. However, in case of TPD and PS, they are dissolved in a sufficient volume[1] of CHCl$_3$ to increase the mixing. Subsequent evaporation of the solvent at 70 °C for 30 min in a drying oven ensures that the solvent employed during premixing has no impact on the total solvent amount during the mixing process of the final composite.

After the sensitizer solution and TPD:PS are prepared, the mixing process is as follows: 30 mg CTA, 20 µL 5CB, and the needed amount of sensitizer solution are solved in 200 µL CHCl$_3$. Ultrasonication assists the solvation and mixing process, and finally leads to a viscous substance. In order to get a homogenized composition and to avoid entrapped air in the samples that would lead to short circuits during operation, the composite is stored in a refrigerator overnight.

5.4.2.3 Assembly of the samples and melt-pressing

The sample-assembly process starts with pipetting the composite onto one of the prepared substrates until total coverage of the circular part of the electrode. During this process, care has to be taken to avoid undesired air bubbles within the composite. Subsequently, the sample is dried at ambient air for 20 min to let the major part of the solvent evaporate. In a next step, the composite is further dried in a drying oven at 50 °C for about 4 h. The temperature is chosen considerably low (compared to the boiling point of CHCl$_3$ at 62 °C) to prevent the solvent from boiling and thus inducing solvent bubbles within the sample. Depending on the behavior of the composition, it might be necessary to just put a small amount of composites onto the electrode, let the solvent evaporate, dry it in the oven (for about one hour), and repeat the process until the terminal amount of material has been applied. This procedure is chosen, if application of the whole composite in one step leads to a large amount of gas bubbles within the composite. Afterwards, the sample is annealed up to 90 °C and, in case that there are no air bubbles, the spacer foil of 50 µm thickness is inserted and the second electrode is set on top of the composite as illustrated by figure 5.5. The composite is now rather fluid and thus the electrodes tighten themselves to the defined thickness of the spacer foil. Due to the procedure of this last step, it is called melt-pressing. At last, after about one hour in the oven, the finalized sample is cooled down to room temperature slowly.

---

1   The exact amount of solvent is not of importance because the whole solvent is evaporated prior to further processing.

6 Photophysical characterization

The photophysical performance, i.e., the light-matter-light interaction of photorefractive composites has to be determined by different means. Splitting the characterization into different parts, where every technique addresses single aspects of the photorefractive process enables to clearly attribute the changes of the PR performance to the variations of the composition. As the main focus of this part of the thesis is the exchange of sensitizer and charge-transfer agent, the determination of the influence of both on the PR processes is of largest impact. Therefore, characterization starts with the examination of the absorption properties, followed by exploration of the photocurrent generation. Due to the fact that the electro-optic unit is kept, an extensive study is omitted here but was reported in [76]. Finally, the photorefractive behavior is studied and the gain during so-called two-beam coupling is determined.

6.1 UV/Vis spectroscopy

UV/Vis spectroscopy is one of the most important techniques during photophysical characterization of compounds. It enables to study in detail the transmittance and subsequently the absorption properties and thus also allows to determine the HOMO to LUMO distance of organic materials. In contrast, identification of the absolute energy of these levels needs additional techniques to determine at least one of the absolute energy values. Besides theoretical modeling, cyclic voltammetry has proven to be a method of choice [115].

Additionally, UV/Vis spectroscopy is a convenient tool for the determination of structural parameters of molecules [116], thickness analysis of thin films, as well as substance concentration in liquids. For the latter, typically the Beer-Lambert law [117] is applied. It relates the quantities absorbance A, concentration c, typically in $\mathrm{mol\,L^{-1}}$, ratio of transmitted to incident intensity I/I_0, propagation length through the absorbing medium l in m, and the molar extinction coefficient ε in $\mathrm{m^2\,mol^{-1}}$ to:

$$A = -\log_{10}\frac{I}{I_0} = \varepsilon \cdot c \cdot l \ . \tag{6.1}$$

The often employed absorption coefficient $\alpha = 1/l \cdot \ln I_0/I$, typically given for several media, can be directly related to concentration and molar extinction via equation (6.1) to be

$$\alpha = \varepsilon \cdot c \cdot \ln 10 \ . \tag{6.2}$$

The factor $\ln 10$ originates from the decadic definition of A and ε in the Beer-Lambert law. In contrast to definition provided here, A is also found in a Napierian version and thus attention has to be paid to not mix them up. In this work, the decadic definition is

continuously used.

Figure 6.1 provides normalized absorption spectra of the sensitizer materials employed in the photorefractive composites. The significant difference between PCBM and diPBI
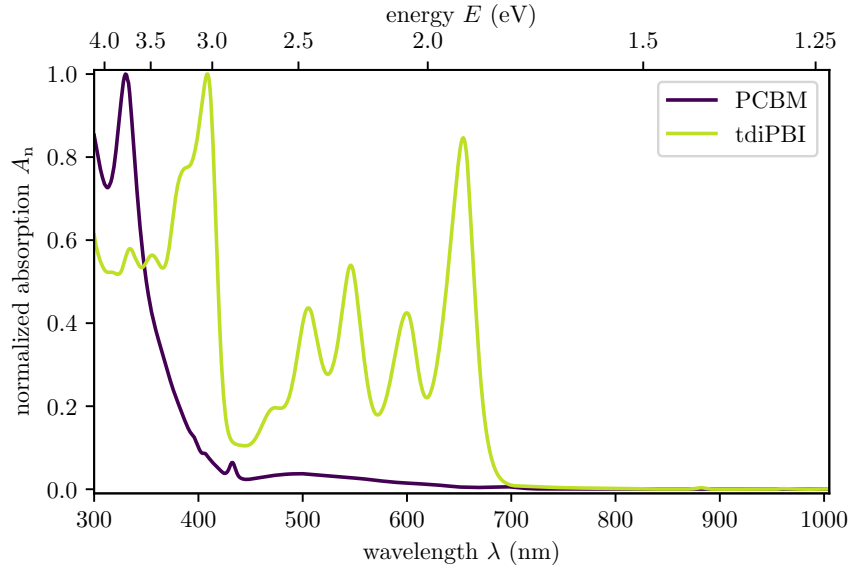
Figure 6.1: UV/Vis spectra of the employed sensitizers PCBM and diPBI in chloroform. The data are a subset of the data in figure 10.6.

becomes obvious. While PCBM provides strong absorption in the UV to blue region of the spectrum, diPBI additionally absorbs in the green and red region. Further, the magnitude of PCBM's curve is significantly dropping with increasing wavelength. Based on the single absorption spectra, the spectra of the PR composites in figure 6.2 have a shape that is dominated by the characteristics of the sensitizers and no additional features induced by absorbing charge-transfer states are observed. Considering the reference spectra P-0 corresponding to PVK:5CB and T-0 corresponding to PS:TPD:5CB, the fact that absorption is only due to the sensitizers becomes evident. Originally, the sensitizer amounts are calculated to provide the same absorbance at $\lambda = 532\,\text{nm}$ in all samples. However, because of the very tiny amounts of dyes to be used, slight variances lead to the relative shift of the spectra to each other. Additionally, there is a large difference of the PCBM containing samples (P-P and T-P) in the blue part of the spectrum. Contrary to the T-P sample, the P-P sample provides a much higher absorption that cannot be directly related to the changed CTA since both reference spectra are similar. Consequently, this difference might have a completely different reason because the absorption of PCBM does not rise to this extent in this wavelength range. An explanation might be the formation of an absorptive state between both materials but this cannot be deduced from the energy levels in figure 6.3. Such an absorptive charge-transfer state would form between the HOMO of the donor and the LUMO of the acceptor. Thus, the energy difference of the charge-transfer state

$$\Delta E_{\text{CT}} = E_{\text{IP,D}} - E_{\text{EA,A}} - J \tag{6.3}$$
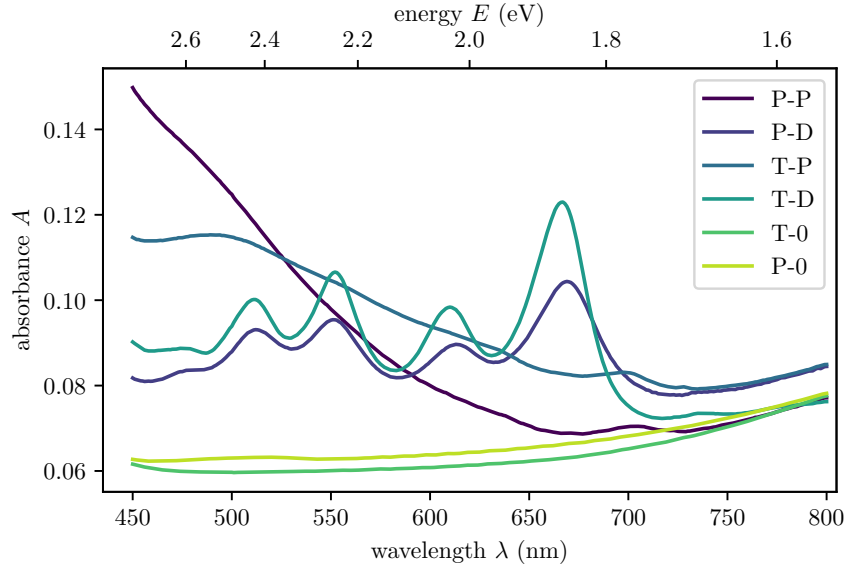
Figure 6.2: UV/Vis spectra of representatives of the realized PR samples and reference spectra of compositions without dyes. Here, P-0 corresponds to PVK:5CB and T-0 to PS:TPD:5CB.
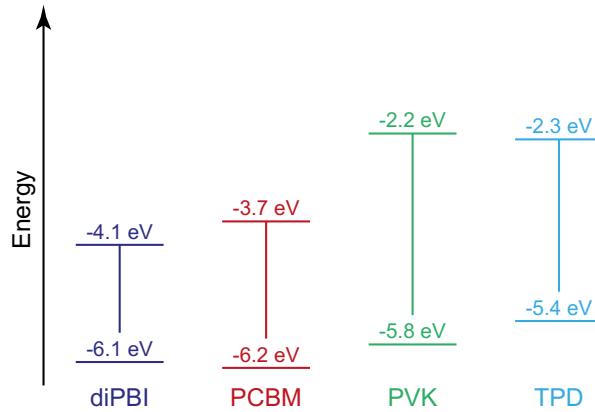
Figure 6.3: Energy diagram of sensitizers and CTAs employed in PR composites [118–120].

would be too low to explain strong absorption in the blue region [121]. Here, $E_{\text{IP,D}}$ is the ionization potential of the donor, $E_{\text{EA,A}}$ is the electron affinity of the acceptor, and J is the electrostatic interaction between the ions formed by electron transfer. Consequently, to find the origin of the different absorption rates of the T-P and P-P samples in the blue part of the spectrum, a more specific analysis has to be carried out. As the operating wavelength is $\lambda = 532\,\text{nm}$, the difference is considered of less importance for the further characterization and thus a more detailed study is omitted.

The absorption peaks introduced by the perylene derivatives enable broadband usage of the composites over the whole visible range while PCBM is limited to the blue and green regions with comparably low performance in the latter.

6.2 Photocurrent spectroscopy

The technique called photocurrent spectroscopy is employed to study the process that includes absorption and the processes that directly succeed: generation of charge carriers and their transport. While UV/Vis spectroscopy is only capable to analyze the amount of absorbed photons, it is important to determine how many photons are converted into mobile charge carriers and finally contribute to charge transfer and charge redistribution due to trapping. This conversion efficiency is a direct measure for the quality of the charge-generating composition.

Photoconductivity σ_{ph} itself is the light induced part of the total conductivity σ_{tot} minus the dark conductivity σ_{dark} [122]:

$$\sigma_{\mathrm{tot}} - \sigma_{\mathrm{dark}} = \sigma_{\mathrm{ph}} = ne\mu(E) = \underbrace{\Phi(E)\frac{I\alpha_{\mathrm{abs}}\tau}{h\nu}}_{\text{charge generation}} \cdot \underbrace{e\mu(E)}_{\text{mobility}} \ . \tag{6.4}$$

Here, n is the number density of free charges, e the elementary charge, μ the charge carriers' mobility, Φ the photogeneration efficiency, I the incident light intensity, α_{abs} the absorption coefficient, τ the lifetime of photogenerated carriers, h Planck's constant, and ν the optical frequency.

Obviously, the right part of equation (6.4) can be split up into two contributions. One is responsible for charge generation whereas the other describes the mobility part, i.e., charge transfer. Looking at the intrinsic parameters of a material, large photoconductivities are governed by large photo charge generation efficiencies, strong absorption and high carrier lifetimes in the charge generation part as well as high charge carrier mobilities. While Φ is strongly dependent on the electric field, it can also be enhanced by choosing material compositions that efficiently separate electrons and holes and avoid geminate recombination [122]. In turn, the number of absorbed photons that can be converted depends on α_{abs} that is dependent on the amount of applied sensitizer. While an enhancement of these parameters would be beneficial on the photorefractive effect, the improvement of charge carrier lifetime τ and mobility μ might be detrimental if it arises from a reduction of trapping sites because these are essential for the photorefractive effect. As an alternative to trapping site reduction, large electric fields E increase the mobility of the charge carriers. Therefore high electric fields are desirable because they enhance mobility as well as charge generation efficiency and thus photoconductivity. Indeed, strong E are typical in organic photorefractive media and they reach several tens of $\mathrm{V\,\mu m^{-1}}$. Compared to the electric breakdown voltage in air that is about $3.3\,\mathrm{V\,\mu m^{-1}}$ [123], these fields are several times stronger. Additionally, this fact explains why it is so important during sample preparation that the whole electrodes are covered with the PR compound. On the other side, strong electric fields have higher demands for operation safety and thus are not beneficial and preferable at all.

6.2.1 Spectroscopy technique

In order to determine the photoconductivity of the PR composites, two measurements are needed: one to record the dark current and one to obtain the overall current

under homogeneous illumination. For this purpose, the setup illustrated in figure 6.4 is employed. It can be separated into an illumination part and a metrology part. The illumination part consists of a frequency-doubled cw Nd:YAG laser (**Laser**, *Coherent,*
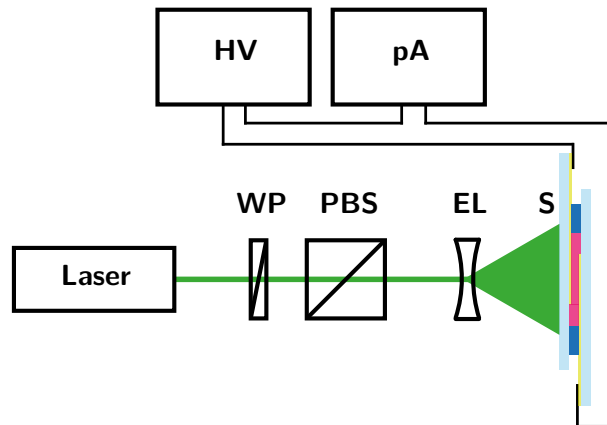
Figure 6.4: Photocurrent spectroscopy setup consisting of frequency-doubled Nd:YAG laser (**Laser**), an intensity control system made of a waveplate and a polarizing beam splitter (**WP** & **PBS**), a biconcave expansion lens (**EL**) for homogeneous sample illumination, sample (**S**), and the metrology part consisting of a high voltage source (**HV**) and a picoammeter (**pA**).

model Compass 315-100) operating at 532 nm, an intensity control system realized by a half-wave plate (**WP**) for polarization rotation combined with a polarizing beam splitter (**PBS**), and a biconcave expansion lens (**EL**) for homogeneous illumination of the sample (**S**). The metrology part is employed to apply high voltage to the sample and measure dark- and total current in the circuit. Thus, it consists of a high voltage source (**HV**, *Heinzinger, model LNC 10000-5 neg*) and a picoammeter (**pA**, *Keithley, model 6485*). Additionally, the setup includes a shutter that is used for beam blocking during the measurements of the dark current. Together with the metrology part, the shutter is computer-controlled allowing automated measurements.

As stated above in equation (6.4), photoconductivity is the difference between the total conductivity and the dark conductivity. Thus, to calculate the photoconductivity, total conductivity and dark conductivity have to be determined by two separate measurements. The relation between conductivity σ, electric field E, and current j is

$$\sigma = \frac{J}{E} = \frac{j}{A \cdot E} \ , \tag{6.5}$$

in which J is the current density and A is the area of the composite that is covered by the electrodes [124]. Based on equations (6.4) and (6.5), the photoconductivity can be determined from investigations on total current and dark current. Thus, a routine for the field-dependent characterization procedure is established that includes the following steps:

1. Slowly set the applied external field to the first value.

2. Wait for 120 s to equilibrate the charges within the sample and afterwards start the measurement.

3. Open the shutter after 10 s. This results in an illuminated sample.

4. Measurement of the photocurrent for 110 s. Close the shutter.

5. Stop the measurement of the decaying current after another 30 s of tracking.

6. Set the field to the next value and repeat steps 2 to 6 until the current of the maximum field is determined.

In order to compare the results with quantities that have been achieved under different experimental conditions, i.e., different light intensities, the auxiliary quantity S is introduced. S denotes the so-called photoconductivity efficiency and is obtained by normalization to the light intensity, hence

$$S = \frac{\sigma_{\mathrm{ph}}}{I} \ . \tag{6.6}$$

Additionally, to compare different material compositions, it is from interest how many charges are generated per absorbed photon. Therefore the internal photocurrent efficiency is calculated via equations (2) and (15) from Däubler et al. [125]:

$$\phi_{\mathrm{int}} = \frac{SEh\nu}{e\alpha d} = \frac{\sigma_{\mathrm{ph}}Eh\nu}{e\alpha d I} \ . \tag{6.7}$$

The quantities in this equation correspond to the ones already named in equation (6.4). Therefore, it is obvious that the Φ from equation (6.4) is very similar (but not identical) to the ϕ_{int} defined here.

6.2.2 Influence of different components on photocurrent

Figure 6.5 illustrates the temporal behavior of the field-dependent photocurrent. The applied electric fields E_{ext} are varied in the measurements between $10-30\,\mathrm{V}\,\text{µm}^{-1}$ with $\Delta E_{\mathrm{ext}} = 2\,\mathrm{V}\,\text{µm}^{-1}$. Data have been gained by the routine described above and the dark current is already subtracted (mean value of current during the first 10 s). It can be clearly observed that the photocurrent rises instantaneously when the shutter is opened at $t = 10\,\mathrm{s}$. After reaching a maximum value, j_{ph} decays until it reaches an almost static value at $t = 115\,\mathrm{s}$ to 120 s. This steady state is more or less pronounced and depends on the sample composition. In case of a T-D sample, the current is still decaying at the end of the illumination. In other samples, such as P-D, j_{ph} is already constant after a few seconds of illumination. After the shutter is closed at $t = 120\,\mathrm{s}$, a sharp edge indicates the stop of the photocurrent generation and the sample relaxes with a slightly negative current. Due to the fact that the falling edge (when the shutter is closed) of the photocurrent occurs for all electric fields that have been applied, the mobility of the holes is considered to be field-independent (for the field range that has been tested). Otherwise, the process of the decaying photocurrent might be less rapid for lower electric fields. Therefore, the photocurrent is considered to be only field-dependent in the charge generation term of equation (6.4).

Based on these curves, field-dependent conductivities of the samples are calculated. The dark conductivity is calculated from the mean value of the current in the first 10 s, while the photoconductivity is computed from the mean values of the (static)
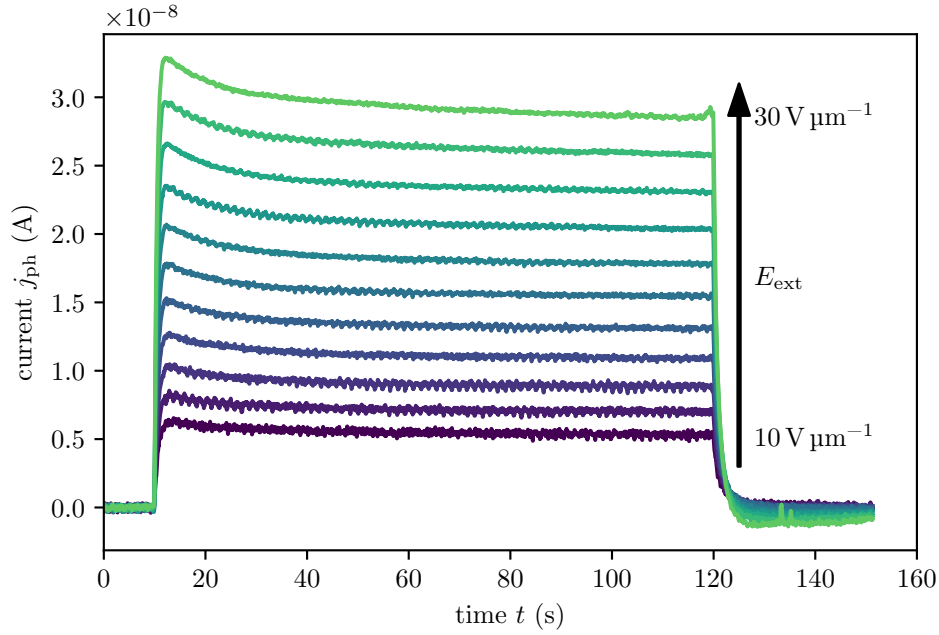
Figure 6.5: Temporal development of electric field-dependent photocurrent measurements of a T-D sample. The dark current (mean value of current in the first $10\,\mathrm{s}$) is subtracted, electric fields are in the range $E_{\mathrm{ext}} = 10 - 30\,\mathrm{V\,\mu m^{-1}}$ with a step width of $\Delta E_{\mathrm{ext}} = 2\,\mathrm{V\,\mu m^{-1}}$.

photocurrent of the last $1\,\mathrm{s}$ before closing the shutter. Figure 6.6 depicts the dark- and photoconductivities ($\sigma_{\mathrm{d,x}}$ and $\sigma_{\mathrm{ph,x}}$) of the T-D and P-D samples in dependence on the electric field. For sake of visualization, the conductivity axis has a logarithmic scale. There are several remarkable effects in this figure. The first one refers to the relation in which the conductivity increases with the electric field. This behavior is valid for $\sigma_{\mathrm{d,T\text{-}D}}$, $\sigma_{\mathrm{ph,T\text{-}D}}$, and $\sigma_{\mathrm{ph,P\text{-}D}}$. In turn, $\sigma_{\mathrm{d,P\text{-}D}}$ is only slightly growing and thus seems to be constant and completely independent from the applied field. The second effect refers to the observations in which the dark conductivity $\sigma_{\mathrm{d,P\text{-}D}}$ in the P-D sample is larger than the photoconductivity $\sigma_{\mathrm{ph,P\text{-}D}}$ while both conductivities of the P-D sample remain lower than the ones of the T-D sample. An explanation of this behavior is given by the energy diagram in figure 6.3. Here, the distance between the HOMO levels of diPBI and TPD is larger than between diPBI and PVK resulting in a larger intrinsic driving force for charge separation. Additionally, the difference for diPBI and PVK is only $0.3\,\mathrm{eV}$ and thus is close to the lower limit for charge separation that is given for organic solar cells [126]. Considering the internal photocurrent efficiency ϕ_{int} (cf. equation (6.7)) in figure 6.7, this assumption is also supported. Here, the slightly different absorption coefficients are not longer of importance because ϕ_{int} represents the number of charges per absorbed photon and therefore allows for a direct comparison of differently absorbing samples. The internal photocurrent efficiency for the T-D sample is more than an order of magnitude larger than the one of the P-D sample. This leads to the conclusion that TPD in general is a better charge transfer agent than PVK.

In turn, it was already mentioned that the dark conductivity of the T-D sample is not independent of the applied electric field. The determination of the origin of the dark
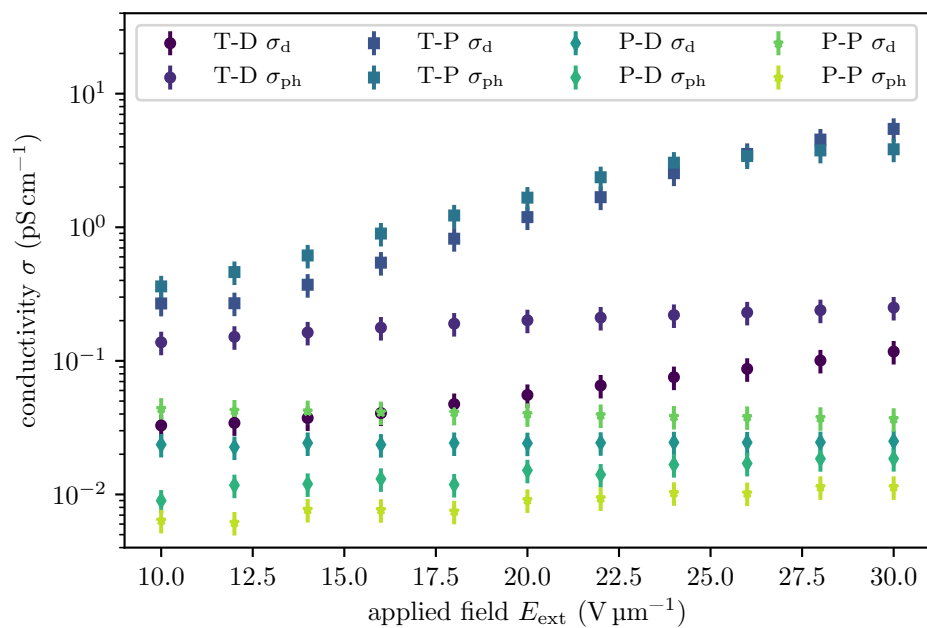
Figure 6.6: Dark- and photoconductivity of T-D, P-D, T-P, and T-D samples in dependence on the applied electric field.
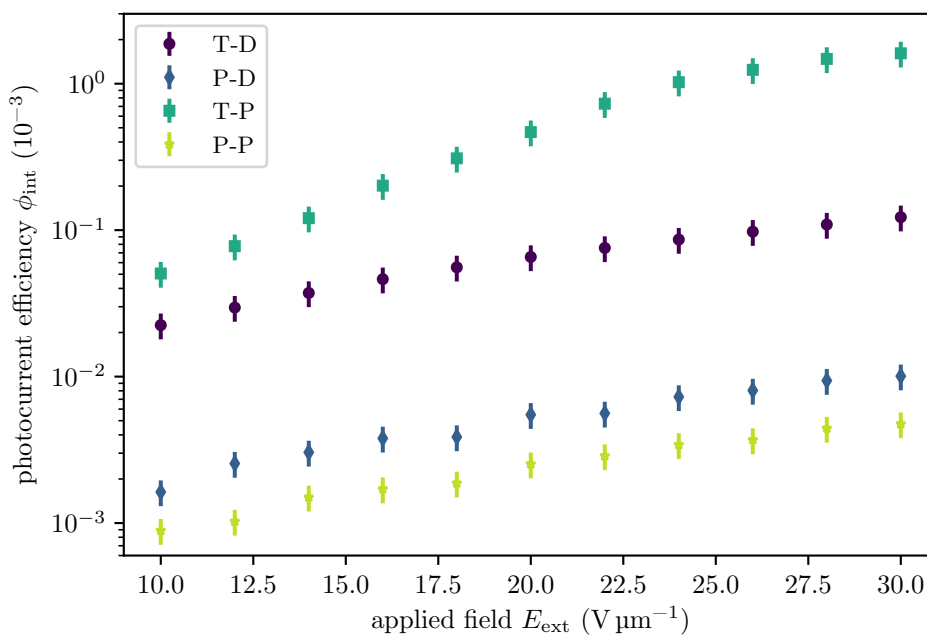
Figure 6.7: Internal photocurrent efficiency of the different compositions in dependence on the applied electric field.

current is rather complicated. Regarding to Ostroverkhova et al. [127], there are two possibilities to generate dark current: injection from the electrodes or generation in the bulk material. While the latter can be electronic or ionic, the injected current can be either space-charge field-limited or emission-limited. In order to determine the exact reason for the large dark currents, further measurements considering several parameters such as temperature, electric field, work function of the ITO electrodes, etc. are needed [127].

In this work the research focus is set onto the attempt to replace PVK by TPD:PS within PR composites. Thus, deep insights on the origins of high dark currents are not needed at all. In fact, it is sufficient to understand that a low trap density combined with a low depth of traps is an explanation for high conductivities and in turn would have a large impact onto the photorefractive performance. This behavior is studied in section 6.3

6.2.3 Transient development of dark conductivity and internal photocurrent efficiency

In order to study the behavior of the realized samples on multiple poling as well as repeated illumination, the conductivities are determined several times. The dark conductivity σ_d is given in figure 6.8 while the corresponding internal photocurrent efficiencies are provided in figure 6.9. Due to the measurement routine, the time between two data points of consecutive electric fields is $4.5\,\mathrm{min}$ resulting in a time frame of $60.5\,\mathrm{min}$ for a field range between $10-30\,\mathrm{V\,\mu m^{-1}}$. Figure 6.8 clearly illustrate that the dark conductivity dramatically drops during the first measurement and then remains rather constant through each of the following sequences while there is a slight drop from sequence to sequence. In case of the TPD containing samples (figures 6.8(a) and 6.8(b)), there is a weak field dependence of σ_d whereas this is not the case for the PVK-based samples (figures 6.8(c) and 6.8(d)).

A different behavior is observed in figure 6.9 and its subfigures in case of the internal photocurrent efficiency. Here, the transient change is less prominent except for the P-D sample in figure 6.9(c). Here, a dramatic decrease of the photoconductivity and consequently of the internal photocurrent efficiency is observed. In case of the T-P sample, ϕ_{int} remains almost constant for the repeated measurements. Additionally, the first sequences of the T-D, T-P, and P-P samples provide artifacts, i.e., larger deviations from the other values that do not occur in the subsequent measurements. These artifacts might originate from slight variances of the overall conductivity during the first sequence. Although not coinciding completely with the changes in the dark conductivity, instabilities in the conductivity at all might cause these artifacts.

To make the temporal dependence clearer, the measurements of σ_d and ϕ_{int} at $E_{\mathrm{ext}} = 30\,\mathrm{V\,\mu m^{-1}}$ are depicted in figure 6.10. Here, it becomes clearly visible that in any case the dark conductivity decreases over time. This effect is more pronounced for the TPD containing samples while PVK containing samples seem to be more stable regarding their dark conductivity. Nevertheless, σ_d of P-P and P-D is always smaller than of T-D and T-P.

A different picture can be observed if the internal photocurrent efficiency is considered. Here, the TPD containing samples present almost constant data while the performance
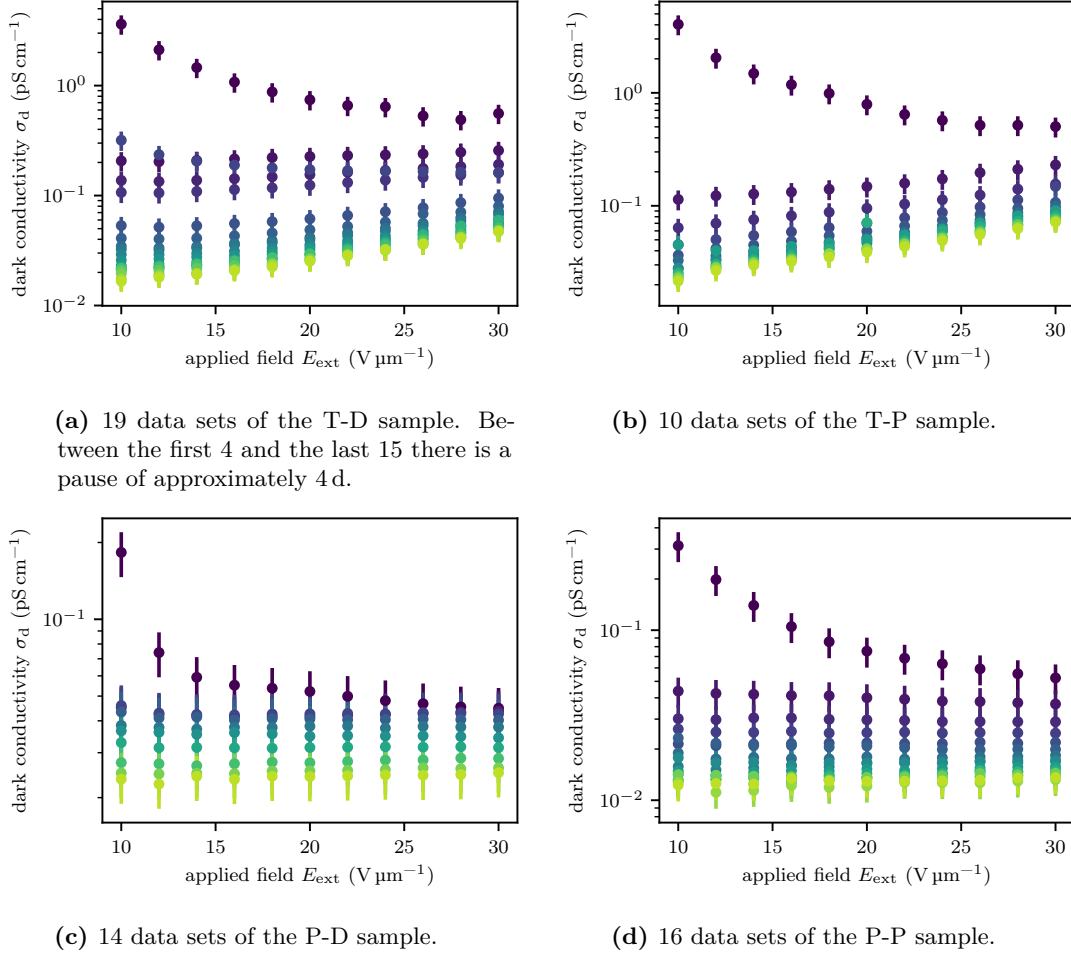
(a) 19 data sets of the T-D sample. Between the first 4 and the last 15 there is a pause of approximately 4 d.

(b) 10 data sets of the T-P sample.

(c) 14 data sets of the P-D sample.

(d) 16 data sets of the P-P sample.

Figure 6.8: Transient development of the dark conductivities σ_d for T-D, T-P, P-D, and P-P samples. The chronological sequence is color coded from dark to bright.

of PVK containing samples significantly drops over time. Consequently, putting the results from figure 6.10 together, the contrast between photo- and dark conductivity of TPD containing samples increases over time whereas it decreases or remains more or less constant for their PVK counterparts. The latter seem to suffer from an aging effect that reduces the overall conductivity and probably would finally lead to non-functional samples. On the other side, the behavior of T-D and T-P samples is highly desirable because a lowering of the dark conductivity reduces charge movement in non-illuminated sample areas while keeping the photoresponsivity and thus might lead to an enhanced photorefractive performance.

Based on this finding, a special treatment of TPD containing samples should be considered to maximize the contrast between photo- and dark conductivity. Whether a long-term poling over several hours is sufficient or the samples should be illuminated during this poling process still needs to be found out. The underlying effects have to be analyzed in more detail. It is obvious that only processes that contribute to the dark conductivity are influenced. These may be thermally activated charge carriers that can be drawn by the external field. Another explanation are ionic contributions

(a) 19 data sets of the T-D sample. Between the first 4 and the last 15 there is a pause of approximately 4 d.

(b) 14 data sets of the T-P sample.

(c) 10 data sets of the P-D sample.

(d) 16 data sets of the P-P sample.
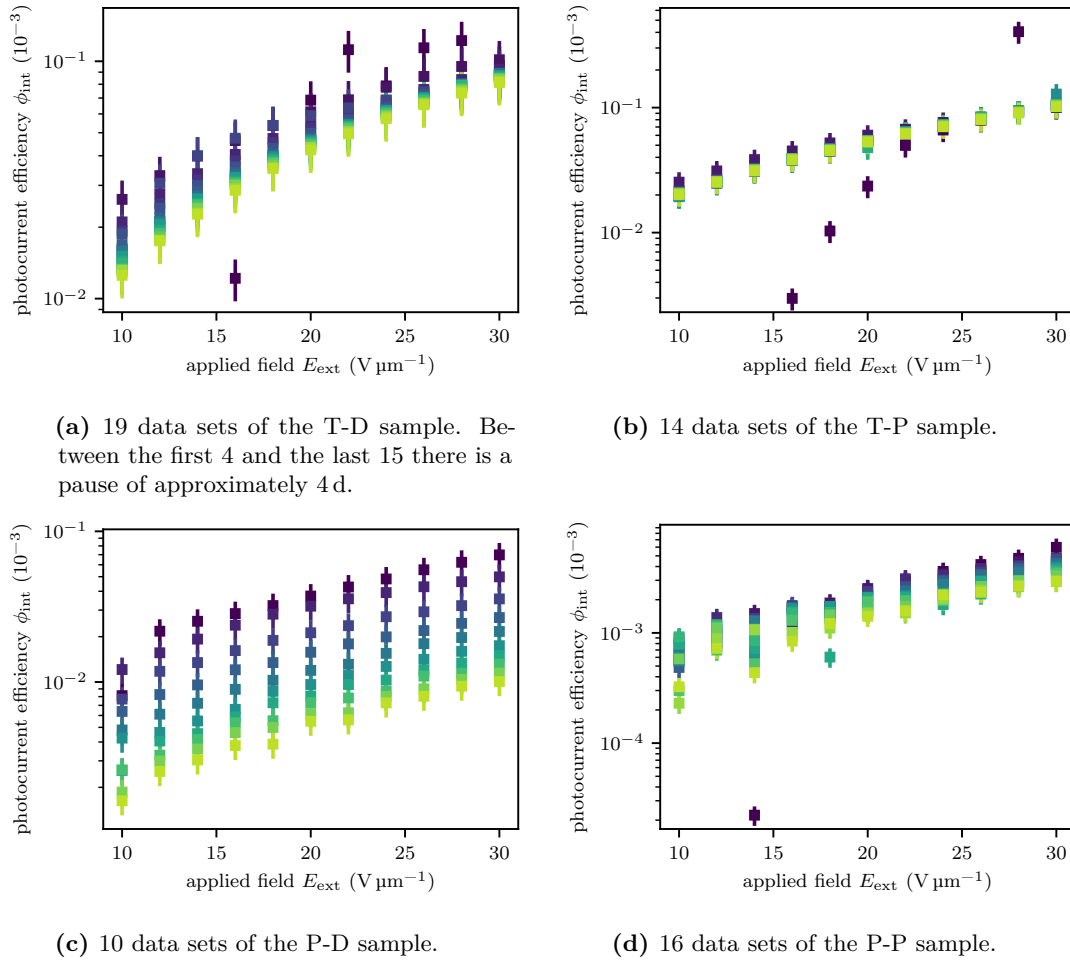
Figure 6.9: Transient development of the internal photocurrent efficiency ϕ_{int} for T-D, T-P, P-D, and P-P samples. The chronological sequence is color coded from dark to bright.
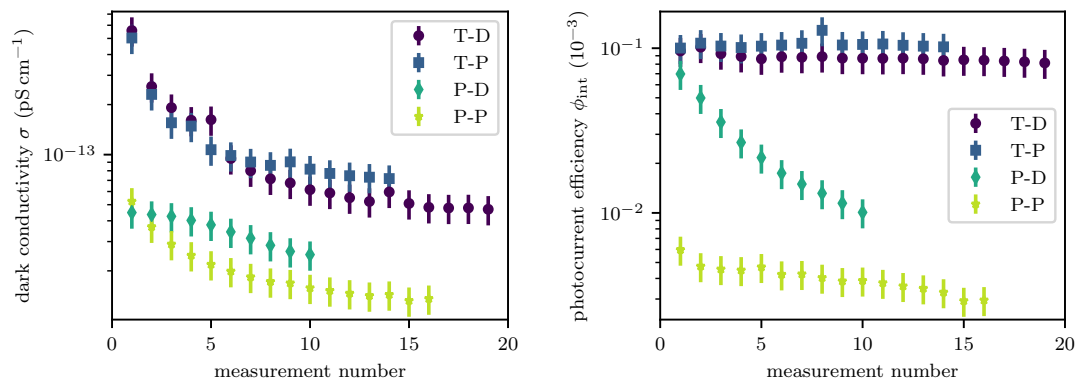
Figure 6.10: Dark conductivity and internal photocurrent efficiency at an applied field of $E_{\mathrm{ext}} = 30\,\mathrm{V\,\mu m^{-1}}$

that may be part of conformational change of the material that has no impact onto the photoconductivity.

The influence of the materials themselves is not quite clear so far. While the ratio of PS:TPD is fixed because of stability considerations regarding a tendency to crystallization, there is no dependence on the TPD content so far. Consequently, the impact of the actual TPD amount remains unclear and further studies should be carried out with further reduced TPD content.

Setting the focus to the influence of the sensitizer, the opposite behavior depending on the charge-transporting agent is employed. While diPBI is superior to PCBM if PVK is the charge transporter, this is reversed for the PS:TPD combination. Possible explanations for this characteristics originate from intermolecular interaction between sensitizer and charge transporter. Here, energetic consideration should not play a large role in this context because HOMO levels of diPBI and PCBM are only slightly different (cf. figure 6.3). Consequently, besides ideally matching energy levels, there are other crucial material properties that have to be considered and analyzed. One of these is the orientation of molecules to each other. While it is known that perylene bisimide derivatives tend to stacking [128], this is not the case for PCBM. Due to the low content of sensitizer, stacking of diPBI occur but the clusters are not very large. Additionally, TPD crystallizes, which is why PS has been introduced. If both materials form their own homogeneous clusters, charge separation is inhibited to a large extent. Consequently the photocurrent efficiency is low because excitons are not efficiently dissociated. In contrast, the conductivity, especially the dark conductivity can still be high because highly ordered material packing modes are very beneficial for charge transfer itself.

In order to characterize the effects that hinder the photoconductivity in PS:TPD, especially if diPBI is employed, studies on the molecular scale have to be performed. These could be experimental techniques such as high-resolution atomic force microscopy (AFM) or scanning tunneling microscopy (STM) techniques supported by theoretical modeling. The latter would help to understand the experimental findings or could be employed solely to provide further suggestions for optimization routes.

6.3 Two-beam coupling

To check if a material is photorefractive, not only the two conditions – photoconductive and electro-optic – have to be fulfilled but the material has to be tested regarding photorefractivity directly. One experiment to prove the photorefractive functionality is the so-called two-beam coupling. It is one of the methods of choice to determine whether a material is photorefractive or not. In this experiment, two laser beams are adjusted to intersect within the sample volume. If the polarization of the beams coincides, a sinusoidal light-intensity pattern is formed in the region of the intersection. As described in section 5.3, the sinusoidal intensity distribution is converted into a refractive index grating that is spatially shifted with respect to the incident light pattern. Diffraction, combined with constructive interference finally leads to an energy transfer resulting in a beam with decreased and one with increased intensity.

6.3.1 Setup and fundamentals

In a typical two-beam-coupling setup, the grating vector $\vec{K}$ of the light pattern is oriented parallel to the c-axis of a photorefractive crystal. In a PR composite there is no c-axis. Instead, the poled chromophores, here 5CB, are aligned along the direction of the applied field and thus this poling direction can be considered as the c-axis and the direction that excited charges move along. Consequently, charges that were excited by light only move more or less parallel to the electric field and thus overlap between $\vec{K}$ and $\vec{E}_{ext}$ is needed, i.e., $\vec{K} \not\parallel \vec{E}_{ext}$, in order to redistribute the charges and achieve the buildup of a refractive index grating. This overlap is realized by the so-called tilted-sample geometry [98]. A schematic representation of the impinging beams is given in figure 6.11. Here, two laser beams with same intensity illuminate the sample with angles of incidence of $\alpha = 40°$ (beam **B1**) and $\beta = 60°$ (beam **B2**) with respect to the sample normal. Within
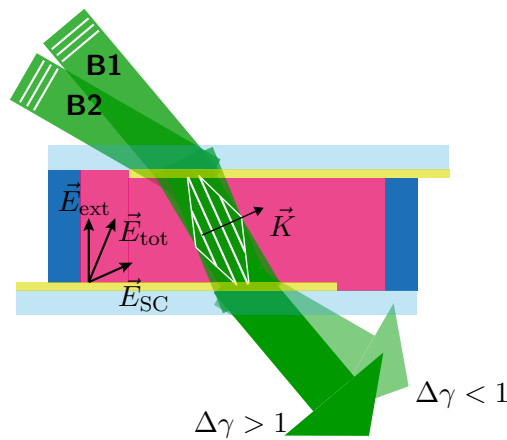
Figure 6.11: Schematic representation of two-beam coupling in a photorefractive composite in the tilted geometry. Here, **B1** and **B2** are the incident beams, $\vec{E}_{ext}$ denotes the applied field, $\vec{E}_{SC}$ the space-charge field, $\vec{E}_{tot}$ the total field, and $\vec{K}$ the wave vector of the interference pattern. The quantity $\Delta\gamma$ describes the gain of the respective beam.

the sample, refraction leads to different internal angles of the beams. Applying Snell's law and assuming that the refractive index of the composition is about $n_{comp} = 1.7$ the internal angles are calculated to be $\alpha_{int} = 22.2°$ and $\beta_{int} = 30.6°$. The assumption of the composite's refractive index seems reasonable because the major part of it consists of the charge-transporting agent and with $n_{PVK} = 1.67 - 1.70$ [129, 130], $n_{TPD} = 1.75$ [131], and $n_{PS} = 1.60$ [132, 133]. Thus $n_{comp} = 1.7$ seems to be close to the proper index and therefore a reasonable approximation, for both, TPD and PVK containing samples. The orientation of the contributing electric fields $\vec{E}_{ext}$, $\vec{E}_{SC}$, and the resulting total field $\vec{E}_{tot}$ is schematically given by the arrows in the scheme. The grating vector of the sinusoidal intensity pattern is indicated by $\vec{K}$. Finally, as a consequence of the two-beam coupling effect one of the transmitted beams loses intensity while the other one gains intensity. In addition, this is indicated by the gain $\Delta\gamma$ of the respective beam. Figure 6.12 illustrates the employed experimental setup. The beam of a frequency-doubled Nd:YAG laser (**laser**) operating at $\lambda = 532\,\text{nm}$ is split up into two arms **B1** and **B2** by a polarizing beam splitter (**PBS**). The splitting ratio can be adjusted by a half-wave plate (**WP**)
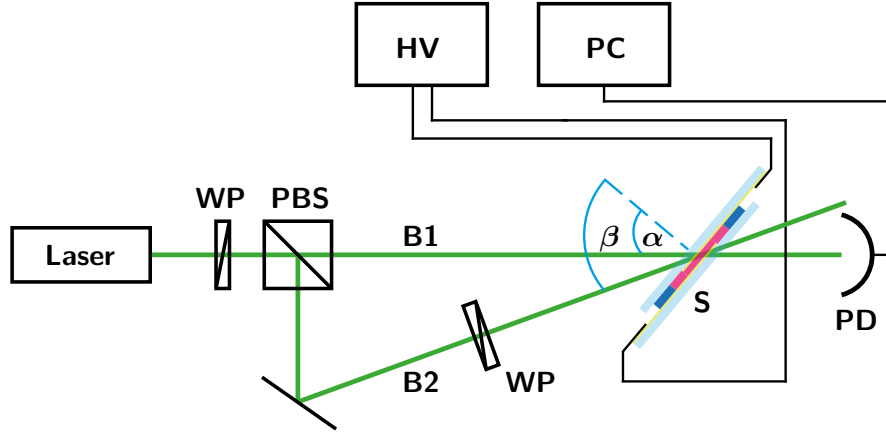
Figure 6.12: Schematic representation of the two-beam coupling experiment. The beam of a laser (**Laser**) is split up by a polarizing beam splitter (**PBS**) into the arms **B1** and **B2**. The splitting ratio is adjusted by a half-wave plate **WP** in front of the beam splitter. The second waveplate in arm **B2** adjusts the beam polarization to be coincident with the polarization of **B1**. A photodiode detects the power of the transmitted part of **B1**. Data is collected by a computer **PC**. The high-voltage source is indicated by **HV**. The angles of the incident beams with respect to the sample (**S**) normal are given by α and β.

in front of the beam splitter. In order to adjust the polarization of arm **B2**, a second half-wave plate is inserted into this arm. Consequently, both beams are p-polarized. The sample (cf. figure 6.11) is indicated by **S**. As described before, beams of both arms illuminate the sample in specific angles indicated by α and β. The resulting gain (or attenuation) of one beam is recorded with a photodiode (**PD**) that is connected via an amplifier to a computer (**PC**). The computer is additionally employed to control the high voltage applied via a high-voltage source (**HV**) as well as to run the automated measurement routine.

The orientation of the electric field is chosen in a way that the negative electrode is on the side where the illuminating beams impinge. This configuration is desired to avoid beam fanning, reported by Grunnet-Jepsen et al. [134]. Consequently, beam **B1** gets gain whereas **B2** is attenuated.

The characterization routine works the following way:

1. Slowly set the applied external field to the first value.

2. Wait for 60 s to let the charges within the sample equilibrate and afterwards start the measurement. Only one beam (**B1**) is illuminating the sample.

3. Open the shutter of beam **B2** after 5 s. An interference pattern in the sample forms.

4. Measurement of the gained transmitted beam **B1** for 40 s. Close the shutter of beam **B2**.

5. Stop the measurement of the decaying signal after another 15 s of tracking.

6. Set the field to the next value and repeat steps 2 to 6 until the current of the maximum field is determined.

Based on the internal angles α_{int}, β_{int}, and the refractive index n given above, the grating spacing within the sample can be calculated via [14]

$$\Lambda = \frac{\lambda}{2n \sin\left(0.5(\alpha_{\text{int}} - \beta_{\text{int}})\right)} \tag{6.8}$$

to be $\Lambda \approx 2.1\,\mu\text{m}$. This grating spacing is important, if the resulting grating is categorized to be either in the so-called Bragg regime (thick grating) or in the Raman-Nath regime (thin grating). To distinguish both, the quality factor Q is defined by [135, 136]:

$$Q = \frac{2\pi\lambda d}{n\Lambda^2} \ . \tag{6.9}$$

Here, the thickness of the grating d is assumed to be as great as the sample thickness of $50\,\mu\text{m}$. This results in $Q \approx 22$ and therefore, if the criteria for thick gratings $Q \gg 1$ or alternatively the ones by M. Moharam et al. [136] are applied, the grating is a thick one. This finding coincides with the observations that are made during the experimental characterization because only the fundamental beams could be observed. Another consequence of these findings is that the induced refractive-index grating and the probing beam are automatically matched regarding the Bragg condition.

The mathematical description of the resulting intensity interference pattern generated by two coherent plane waves of equal polarization is expressed in the following way [101]:

$$I_{\text{res}}(x) = I_1 + I_2 + 2\sqrt{I_1 I_2} \cos\left(\frac{2\pi x}{\Lambda}\right) \ . \tag{6.10}$$

Again, Λ is the spacing of the fringes of the grating, that can be expressed via the wave vector of the grating $\left|\vec{K}\right| = 2\pi/\Lambda$. Here, the x-direction is oriented parallel the plane that is spanned by the incident beams and normal to the propagation direction.

The evolution of the single beams in the sample are described by the wave equation and the assumption that beams impinge from the same side and are only variant in the z-direction. Under exploitation of the slowly varying envelope approximation this leads to the coupled differential equations [137]

$$\frac{\partial I_1}{\partial z} = -\Gamma \frac{I_1 I_2}{I_1 + I_2} - \alpha I_1 \quad \text{and} \tag{6.11}$$

$$\frac{\partial I_2}{\partial z} = \Gamma \frac{I_1 I_2}{I_1 + I_2} - \alpha I_2 \ , \tag{6.12}$$

where Γ denotes the gain coefficient and α the absorption within the sample. Additionally, z is the direction of propagation. The gain coefficient is defined the following way:

$$\Gamma = \frac{2\pi n_1}{\lambda \cos\left(\psi/2\right)} \sin\phi \ . \tag{6.13}$$

Here, ϕ denotes the relative phase between the two incident beams, ψ is the angle between the beams. Further n_1 is a real, positive number, and depends on the grating spacing, its direction, and on the electro-optic coefficient of the medium [137]. In several

publications, the gain coefficient is rewritten to

$$\Gamma = \frac{4\pi}{\lambda} \frac{\Delta n}{m} \sin\phi \ . \tag{6.14}$$

In the equation, Δn is taken from equation (5.8) or, in case of compositions with low T_g, rather from equation (5.13) and the modulation ratio is $m = 2\sqrt{\beta_\mathrm{p}}/(1 + \beta_\mathrm{p})$ where $\beta_\mathrm{p} = I_2/I_1$ [14, 98]. Here, I_1 is the so-called signal beam that is gained while I_2 is attenuated. The angle dependence of Γ is shifted into the interaction length term $L = d/\cos\theta$ that occurs in the solution of equations (6.11) and (6.12). These solutions are

$$I_1(\text{out}) = \frac{I_0}{1 + \beta_\mathrm{p} \exp\left(-\Gamma L\right)} \quad \text{and} \tag{6.15}$$

$$I_2(\text{out}) = \frac{I_0 \beta_\mathrm{p}}{\beta_\mathrm{p} + \exp\left(\Gamma L\right)} \ , \tag{6.16}$$

where $I_0 = I_1 + I_2$ is the total intensity of the incident or leaving beam pairs, respectively [11, 14]. Other references such as K.-S. Lee [102] still include the angle dependence in Γ. The absorption terms are left out and, as stated before, L denotes the interaction length. Thus it corresponds to z, with the internal angle θ of the enhanced beam and the sample thickness d [14, 98, 137].

Based on the equations (6.15) and (6.16), a formula to calculate the gain coefficient Γ from measured intensities can be set up via $\Gamma = \ln(\beta_\mathrm{p} I_1(\text{out})/I_2(\text{out}))/L$ resulting in

$$\Gamma = \frac{\cos\theta}{d}[\ln\left(\gamma\beta_\mathrm{p}\right) - \ln\left(\beta_\mathrm{p} + 1 - \gamma\right)] \tag{6.17}$$

with the gain factor $\gamma = I_1(\text{out})/I_1(\text{in})$. While β_p as well as the angles of incident are typically adjusted before the measurement is started, γ is the only quantity that has to be determined by the routine described above. If the gain that is achieved by the two-beam coupling is larger than the absorption of the sample, net gain that is highly desirable for technical applications is achieved.

Considering equation (6.14), the strong dependence of the gain on the phase shift ϕ between light pattern and refractive index grating becomes obvious. While the gain vanishes if the light pattern and index grating coincide, it is maximized when the phase shift reaches $\phi = \pi/2$. Because the phase shift of the refractive index grating is the same compared to the space-charge field, the latter can be employed to determine the shift. The SCF is described by

$$E_\mathrm{SC} = |E_\mathrm{SC}| \exp\left(i\phi\right) \tag{6.18}$$

with amplitude $|E_\mathrm{SC}|$ and phase ϕ [102]. The amplitude of the SCF is described by

$$|E_\mathrm{SC}| = m \left(\frac{(E_0^2 + E_\mathrm{D}^2)}{(1 + E_\mathrm{D}/E_\mathrm{q})^2 + (E_0/E_\mathrm{q})^2} \right)^{1/2} \ , \tag{6.19}$$

where E_0 is the part of the external field that is projected along the grating vector $\vec{K}$,

E_D is the diffusion field that is neglected because PR composites are drift dominated [102]. The term E_q denotes the limiting space-charge field that strongly depends on the trap density N_{eff} within the composition. The diffusion field is given by

$$E_D = \frac{2\pi k_B T}{\Lambda e} \tag{6.20}$$

and the limiting space-charge field by

$$E_q = \frac{2\Lambda e N_{eff}}{\varepsilon_{dc}} \; , \tag{6.21}$$

where ε_{dc} represents the low-frequency dielectric constant. Finally, the phase shift can be calculated by

$$\phi = \arctan\left[\frac{E_D}{E_0}\left(1 + \frac{E_D}{E_q} + \frac{E_0^2}{E_D E_q}\right)\right], \, E_0 \neq 0 \, , \tag{6.22}$$

and $\phi = \pi/2$ if $E_0 = 0$ [102]. Experimentally, the phase shift can be determined by via translation of the index grating with respect to the light pattern. This can be realized by sample movement or by a shift of the relative phase of the two incident beams, thus moving the interference pattern along the x-direction [14].

6.3.2 Two-beam coupling performance of the realized compositions

Figure 6.13 exemplarily illustrates the time-dependent data (1000 samples/s) of the gain factor γ for different external fields that are obtained by the routine described in the previous subsection. In order to suppress noise that is collected by the photodiode and the subsequent amplifier, a Savitzky–Golay filter with a window size of 501 and a polynomial order of 3 have been applied to smooth the data. The reference intensity of beam **B1** needed for the calculation of the gain factor is an average value of the first 5 s when the second beam is still blocked by the shutter. This value is employed to normalize the whole dataset to the uncoupled intensity and finally it allows to obtain γ. The two-beam coupling effect becomes clearly visible directly after the shutter is opened at $t = 5$ s and a rapid rise of the gain factor can be observed. Within the next 5 s γ reaches a maximum value until the shutter is closed at $t = 45$ s. The decay of the signal is even faster. For weak external fields ($E_{ext} < 30$ V μm^{-1}), the gain becomes < 1 indicating that parts of the light of beam **B1** might be diffracted or scattered. In case of the other compositions, the a comparably steep edge of the gain signal occurs only for the other TPD containing one, namely T-P. If PVK is the charge transporting agent, the buildup of the space-charge field and thus the refractive index grating is much slower and consequently the signal also rises slowly for almost for the full duration of 40 s. In contrast, the signal decay is as fast as for the TPD containing samples.

The data to calculate the gain coefficient are average values of the last 4 s of γ before the shutter is closed. Due to the chosen intensity of both beams to be 1 mW, the incident intensity ratio is $\beta_p = 1$. Based on γ, β, the internal angle of the gained beam $\theta = 22.2°$, and equation (6.17), the gain coefficients displayed in figure 6.14 are calculated. Obviously, the ranges of the applied external fields for the four sample types vary. The
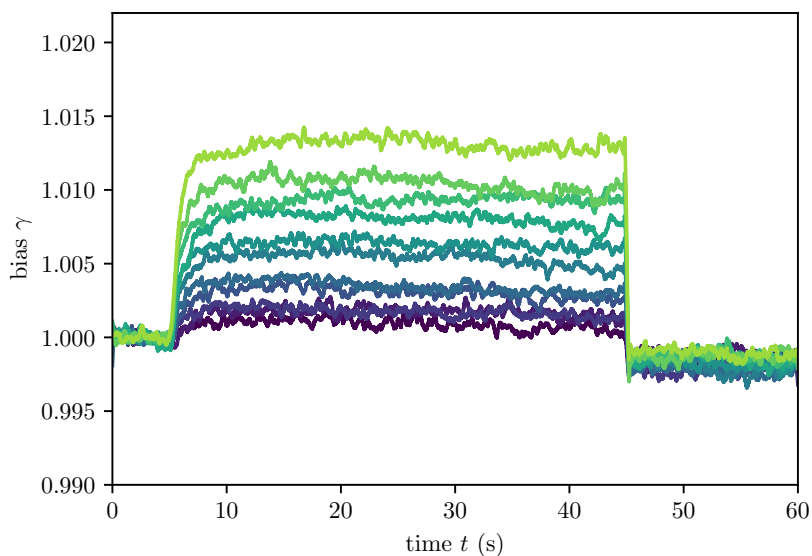
Figure 6.13: Time-dependent gain factor γ of the T-D sample for different applied external fields in the range of $10-40\,\mathrm{V\,\mu m^{-1}}$ with a step width of $2\,\mathrm{V\,\mu m^{-1}}$.
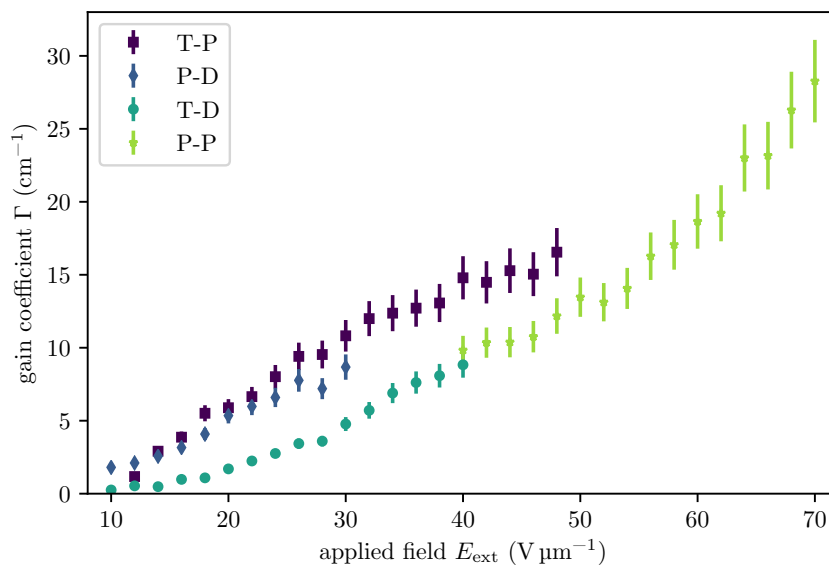
Figure 6.14: Gain coefficients of the different photorefractive sample. Different ranges of the applied external field originate from different short-circuit stabilities of the samples.

reasons for these differences are on one side the stability regarding short circuits and on the other side two-beam coupling performance at all. While T-P, P-D, and T-D samples provide gain already at rather low applied fields, it is not possible to observe the same for P-P samples. In turn, the TPD containing samples burned through for electric fields higher than $30\,\mathrm{V\,\mu m^{-1}}$. Exceptionally, few samples of a series "survived" higher fields and that is why figure 6.14 contains data for the T-D sample up to $40\,\mathrm{V\,\mu m^{-1}}$ and for the T-P sample up to $48\,\mathrm{V\,\mu m^{-1}}$. The low stability of most of them might be influenced by partial separation of PS and TPD and thus the occurrence of very high currents. Characterization of the P-P sample is conducted in the same electric field range ($40-70\,\mathrm{V\,\mu m^{-1}}$) as P-D samples were in the work by Ditte et al. [76].

Table 6.1: Gain coefficients taken from figure 6.14 at different electric field strengths. Additionally, the absorption coefficient of the different samples is provided.

E_{ext} ($\mathrm{V\,\mu m^{-1}}$)	10	30	48	max	
Sample	Γ (cm^{-1})				α (cm^{-1})
P-P	–	–	9.0 ± 1.0	26.6 ± 2.7 ($70\,\mathrm{V\,\mu m^{-1}}$)	21.52
P-D	1.80 ± 0.19	8.7 ± 0.9	–	8.9 ± 0.9 ($30\,\mathrm{V\,\mu m^{-1}}$)	16.49
T-P	–	10.8 ± 1.1	16.5 ± 1.7	16.5 ± 1.7 ($48\,\mathrm{V\,\mu m^{-1}}$)	21.32
T-D	0.25 ± 0.03	4.8 ± 0.5	–	8.8 ± 0.9 ($40\,\mathrm{V\,\mu m^{-1}}$)	18.33

In table 6.1 several values are taken from figure 6.14 and displayed for better comparison. In general, all gain coefficients are comparably low. Considering the absorption coefficients in the last column, it is obvious that no net gain is achieved except of the P-P sample for fields above $64\,\mathrm{V\,\mu m^{-1}}$. Comparing the Γ with similar samples from [76], the observations remain far beyond the expectations, especially because the prior determined photoconductivities indicated that charge generation and redistribution is more efficient in the TPD containing samples. In turn, the dark conductivity seems to be an explanation for the low PR performance. A low trap concentration enables charges to move easily across the material and thus enhances the dark- as well as the overall conductivity. Consequently, less charges redistributed during the two-beam coupling process are trapped. The larger amount is still mobile and does not contribute to a modulated charge distribution. Therefore, the charges cannot add to the formation of a space-charge field and induce a refractive index modulation.

6.3.3 History dependence

As already described in subsection 6.2.3, the synthesized compositions suffer from history dependence regarding their photo- and dark conductivity. To analyze the impact on the photorefractive performance, several two-beam coupling measurements have been

performed. Depending on the sample type, the applied external fields vary regarding their range. The resulting data of the T-D, P-D, and P-P samples are displayed in figure 6.15. Unfortunately, the T-P samples suffered from electric breakdown before they could be employed for multiple measurements. The data of the T-D sample in subfigure 6.15(a)
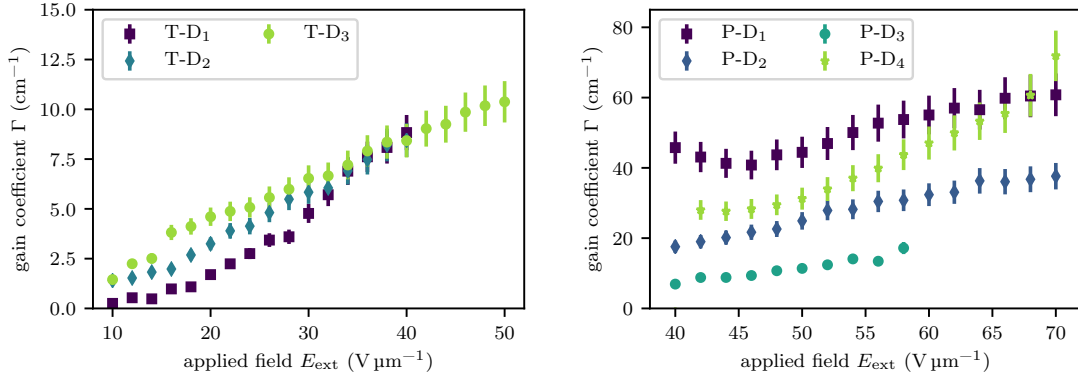
(a) 3 data sets of the T-D sample. Between the first 2 and the last one there is a pause of approximately 4 d.

(b) 4 data sets of the P-D sample. First three data sets are from the same day, the last one was taken one day later.
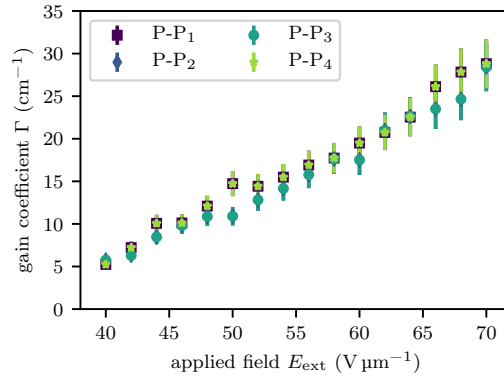
(c) 4 data sets of the P-P sample. First three data sets are from the same day, the last one was taken two days later.

Figure 6.15: Transient development of the two-beam coupling gain coefficient Γ for T-D, P-D, and P-P samples. The chronological sequence is color coded from dark to bright.

and of the P-P sample in 6.15(c) illustrate that the the gain coefficient Γ is almost stable for several measurements. In case of the T-D sample, Γ slightly varies at low applied external fields. These effects are attributed to the low poling voltages resulting in not perfectly aligned liquid crystal molecules.

Contrary behavior is observed for the P-D sample (cf. subfigure 6.15(b)) where no concrete tendency for increasing or decreasing gain with an increasing number of measurements can be observed. Relating this to the findings for the internal photocurrent efficiency in subsection 6.2.3, the behavior is completely different. While the conductivity decreases over time and subsequently the gain coefficient should do as well, no predictable behavior is found instead. Because the PR effect is based on the photoconductivity

and the electro-optic effect, both can be considered to be the origin of the varying gain coefficient. In case of the conductivity, molecular orientation of the charge generating and/or transporting moieties may change over time and thus not only a reduction of the conductivity occurs but also a temporarily enhancement that was not observed during the conductivity investigations. Considering the electro-optic effect, a lack of orientation of the liquid crystals can be neglected due to strong electric fields (here $40 - 70\,\mathrm{V\,\mu m^{-1}}$). The fields should reduce ionic influence on the orientation to very localized regions. Instead, starting crystallization has a larger impact and effectively reduces the electro-optic performance. A completely crystallized sample is heated to bring the sample back to a soft state. In turn, beginning crystallization is hard to observe and already has a detrimental influence on the characterization while the sample itself looks like to be in good, i.e., non-crystallized condition. Consequently, attention has to be paid to check the state of the composition and optionally heat them up to avoid any microcrystals within the mixture.

In order to clarify why the gain coefficient varies that much from sequence to sequence, the occurring currents and subsequently the conductivity should be recorded during the two-beam coupling experiment. This would enable to correlate the internal photocurrent efficiency and the dark conductivity to the achieved gain. This is not carried out so far, because it was not considered to be important when the experiments were planned.

7 Resume and outlook on the realized organic PR media

Finally, different PR compositions are compared regarding their absorption spectra, photoconductivity, and two-beam coupling gain coefficient. While the change of the sensitizer (from PCBM to diPBI) leads to possible broadband applications because of the broad absorption spectrum of diPBI, the mixture of TPD and PS as a replacement for PVK only leads to enhanced photoconductivity. The two-beam coupling efficiency of the TPD:PS is significantly lower than in case of PVK as CTA. This behavior is attributed to the higher dark conductivity of the TPD containing samples and thus to a reduced amount of trapping states essential for the photorefractive effect to occur. Consequently, in order to further enhance the PR performance of the TPD containing samples, the dark conductivity has to be significantly decreased and trap states have to be added. Thus, further additives can be introduced in the composition that have appropriate energy levels to act as traps for holes. Simultaneously, this additive should have only minor impact on the photoconductivity because a high photoconductivity is desired for high speed photorefractives. Additionally, the low electric fields and their influence on the chromophore orientation have to be considered. While an additive may be capable of making the composition more stable for high electric fields, a different electro-optic moiety more sensitive to electric fields in the range of $10 - 30\,\mathrm{V\,\mu m^{-1}}$ would be a great advance. The reason for this desired benefit is the demand for a very careful fabrication routine if strong electric fields have to be applied. In turn, some samples considered to be free from air bubbles, provide short circuits and consequently are destroyed.

All in all, a composition with a low dark conductivity, high internal photocurrent efficiency, a sufficient amount of trapping states, and which operates at electric fields that are as low as possible would be highly desirable. To aim this goal, especially, a suited transparent CTA has to be found since most highly conductive polymers are absorbing. The latter can be observed in the following part of the thesis where organic solar cells are considered.

Part III

Bulk-heterojunction solar cells

Organic solar cells have become an eligible add-on for the sunlight to electrical energy conversion. Especially if attributes such as light-weight and flexibility are considered, there is no silicon-based alternative so far. Flexibility in this context can be considered in multiple ways. On one hand, the absorption properties can be tuned over a broad wavelength range allowing for application in, e.g., energy-converting windows that only use the infrared (IR) and UV parts of the spectrum [17, 138, 139]. On the other hand, the flexibility can be also considered in terms of the pure mechanical properties that result from the possibility to employ thin foils as substrates resulting in cells that can be bend and consequently applied to non-planar surfaces. Possible use cases are surfaces of cars, buses or other mobile vehicles as well as facades of buildings or smartphones.

In addition, there are also solar cells that are organic-inorganics hybrids. Todays most prominent examples are dye-sensitized solar cells, in Germany typically called "Grätzel-Zelle" [140], and one of its derivatives, i.e., the so-called perovskite-based solar cells (PSC) [141]. The dye-sensitized solar cell is sometimes mixed up with the typical organic solar cell because its absorbing dye is organic, too. Also the term perovskite may lead to confusion because perovskites are inorganic crystals, namely calcium titanium oxide or also known as calcium titanate. In perovskite solar cells, the perovskites are actually compounds that possess a perovskite-like crystal structure. The most prominent ones are organometallic lead halides and especially methylammonium lead halides, whereas others, also purely inorganic perovskite materials are up-and-coming [142].

In order to compare recent recent solar cell efficiencies realized in different research labs, the National Renewable Energy Laboratory (NREL) publishes frequently a chart where different solar cell technologies are compared [5]. Figure 7.1 represents the state at the beginning of December 2016. While the most efficient solar cells ($\eta = 27.5 - 46.0\,\%$) are complex multijunction cells (purple), these are also very expensive to fabricate and thus seem to be not suitable for mass fabrication. The second group inf figure 7.1, displayed in blue, represents different types of silicon-based solar cells whose efficiencies vary between $21.2 - 27.6\,\%$. Today, these efficiencies almost reached by several thin-film cell technologies as well as these cell types are typically less expensive due to reduced material consumption and are therefore a suitable replacement for the silicon technology. Another group, displayed in orange, represents emerging solar cell technologies. Among these are OSCs, PSCs, and dye-sensitized solar cells. While the efficiency of the latter is almost stagnating for almost 20 years, all of the others provide dramatic enhancements over the last years. Especially PSCs seem potentially an alternative to other thin film technologies.

Organic solar cells reach efficiencies of $11.5\,\%$ and thus they are just half as efficient as PSCs. However, due to the several stability issues and the fact that PSCs are not completely organic, there is also need to study and improve organic solar cells. Especially due to their modular structure, OSCs possess a much broader adaptability than any other solar cell type and thus their only application limit is the need for high electrical output on a limited space. If space is not limited, OSCs can simply cover large areas and consequently convert large amounts of energy while keeping production costs low.
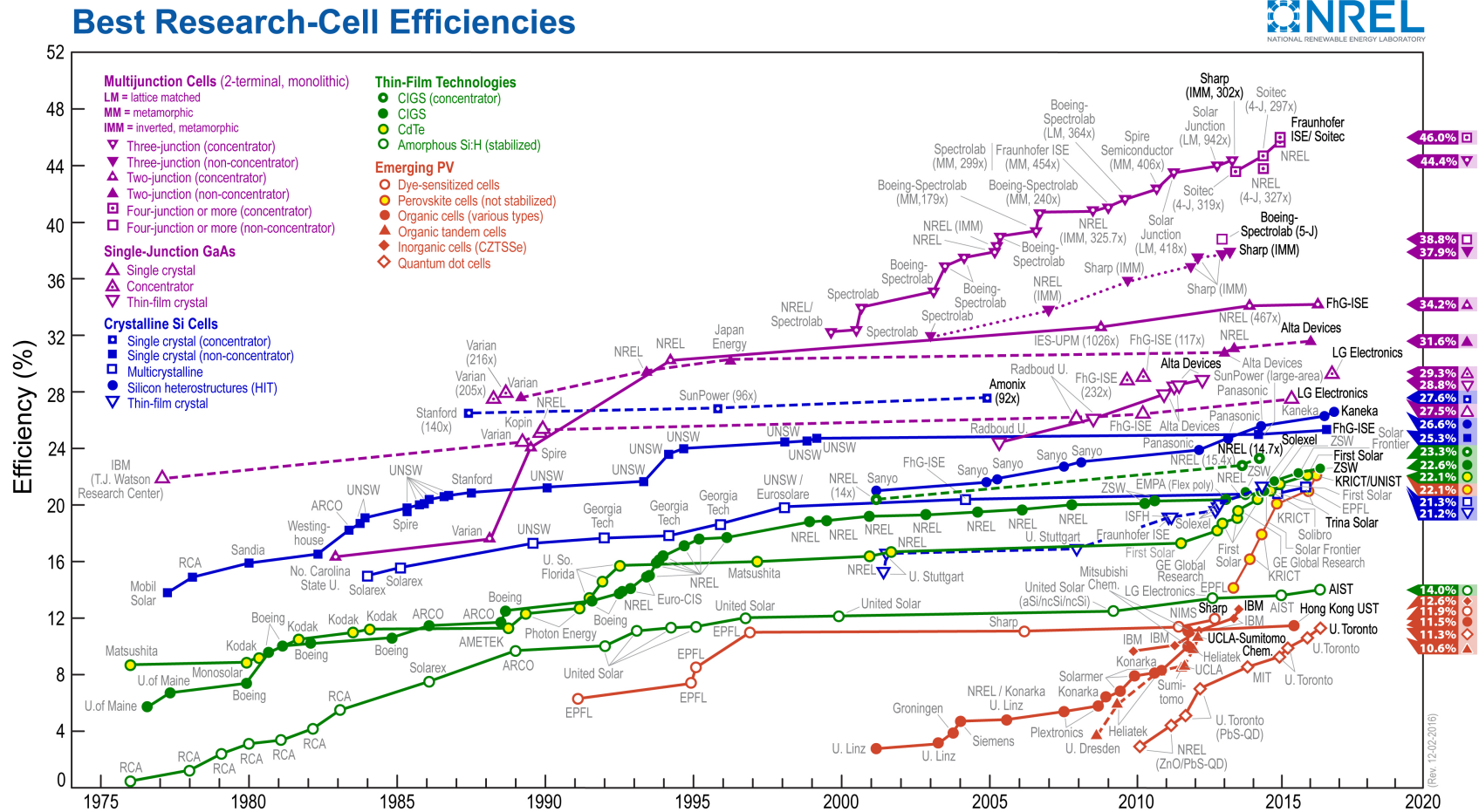
Figure 7.1: Best research-cell energy chart provided by NREL [5].

8 Concepts of organic solar cell design and fabrication

The main mechanisms of organic solar cells are explained in part I. Incident sunlight is absorbed by donor and/or acceptor components leading to the formation of an excited state within the molecule[1]. While the first organic solar cells realized consisted of only one molecular species [143] (no donor/acceptor approach), it provided very low performance due to the lacking driving force for charge separation. Consequently, cells that contain donors and acceptors were realized. If energetically matched to LUMO–LUMO distances of about $0.3\,\text{eV}$, this concept enables for high efficient exciton separation at the interface. Besides the energetic matching, also the spatial orientation of the molecules to each other plays a crucial role. The energy aspects can be considered before a solar cell is realized. In turn, orientational influences are typically observed during characterization. Consequently, a prediction technique for these influences is highly desirable as it would dramatically speed up solar cell evaluation and omit non-fitting material combinations. After the exciton is split at the donor/acceptor (D/A) interface, the separated charges are transported by donor and acceptor to the corresponding electrodes and finally extracted.

Based on the materials and the fabrication techniques employed, one of the solar cell concepts is chosen. Two of these concepts, the so-called bilayer heterojunction as well as the bulk heterojunction are introduced in the next sections. The names refer to the design of the active layer.

8.1 Bilayer heterojunction

The active layer in a bilayer heterojunction (also called planar heterojunction) is subdivided into two thin films consisting of donor or acceptor, respectively [144]. Consequently, the interface area between both materials is just the area between both films and thus, compared to other concepts, rather small. The beneficial aspect of this layout is the homogeneity of the layers themselves. Due to the fact that each layer consists only of one molecular species, hampering of charge transfer by trapping or recombination is extremely reduced. Thus, this approach provides good charge-transport combined with low charge separation rates due to the small interface area.

An example of a bilayer heterojunction is given in figure 8.1. The active layer, composed

Glass substrate
Transparent electrode
Hole transport layer
Donor & acceptor layers
Electron transport layer
Aluminum electrode
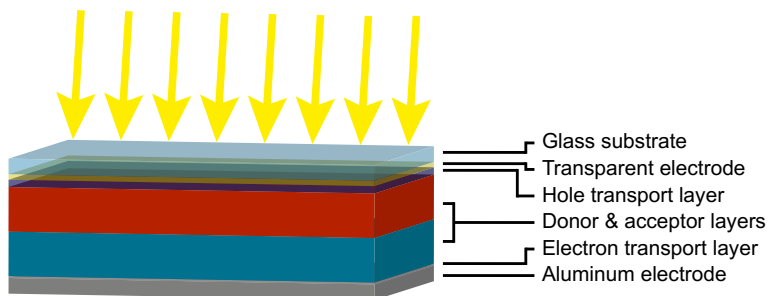
Figure 8.1: Schematic representation of a bilayer heterojunction (not true to scale).

of a donor and an acceptor sublayer, respectively, is located at the center of the scheme

---

1   Here, also polymers are treated as molecules.

and sandwiched between two electrode systems. The electrodes, depending on their function as anode or cathode, consist of one or more layers. The transparent front electrode is typically made of ITO and cast on a transparent substrate, i.e., glass or a plastic film. An additional hole transport layer, also acting as electron blocking layer, is composed of, e.g., poly(3,4-ethylenedioxythiophene) polystyrene sulfonate (PEDOT:PSS). The back electrode mainly consists of an aluminum (Al) film that may be supported by an additional thin film of alkali or alkaline earth metal-based materials adjusting the work function.

Technically, the generation of bilayer heterojunctions can be quite challenging. The complexity strongly depends on the materials that are employed as donor and acceptor as well as the manufacturing process that, in turn, is also affected by the materials. Small molecules are typically processed via evaporation techniques. In contrast, most polymeric materials often need solution processing [145, 146]. The latter can be rather critical as it demands incompatibility of solvents and materials. This becomes obvious, when the first sublayer of the active film has already been processed and the second should be applied. The solvent of the second component should not dissolve the first compound because this would damage the first layer. That is why bilayer cells are commonly realized by evaporation processes on the basis of small molecules for donor and acceptor [144].

8.2 Bulk heterojunction

Contrary to bilayer heterojuntion cells, bulk heterojunction (BHJ) solar cells (cf. figure 8.2) are typically manufactured from solutions and thus several possible fabrication techniques are proposed. Printing, spraying, roll-to-roll processing, and spin coating are just a variety of approaches currently applied [19–21, 147]. The common availability of these techniques makes themselves comparably cheap and easy to adapt for organic solar cell production. The substrates with electrode materials are coated by one of these techniques with the active layer ink. This ink consists of both, donor and acceptor material and is dissolved in a solvent or a solvent mixture compatible with both. During
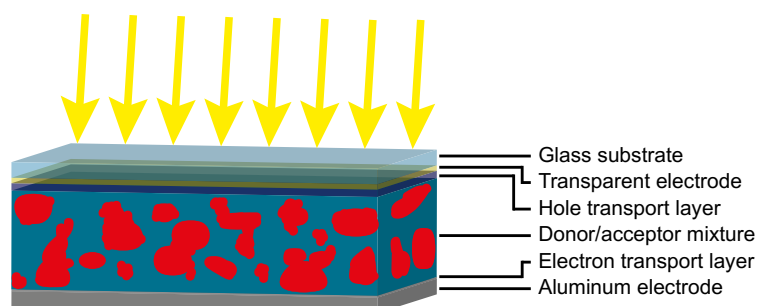
Figure 8.2: Schematic representation of a bulk heterojunction (not true to scale).

the drying process the components partially segregate and form small clusters as indicated in figure 8.2. These clusters are highly desirable because they compensate the strong homogenization that is caused by the mixing process. A homogeneous film provides the largest interface area between both materials but lacks charge transport paths to the electrodes. As a consequence, several processing steps that influence the active layer

morphology are carried out. Starting from annealing treatments of ink, substrate, and films, also solvent vapor as well as solvent additives within the ink are employed to steer cluster formation and size. The applied strategy strongly depends on the active layer components because some of them are sensitive to heat treatment and consequently a different approach has to be applied.

The basic idea behind all treatments is to keep the film temporarily soft. Having this in mind the influence of annealing is clear, while the impact of additives has to be enlightened. Compared to the "base" solvent that contains the donor and acceptor materials, additives possess higher boiling temperatures and thus are capable of keeping the film or parts of the film[1] soft to support cluster formation.

8.3 Fabrication of bulk heterojunction solar cells

In this thesis, all solar cells are based on the bulk heterojunction approach. The decision for this approach is directed by the materials: small molecules as acceptor materials and polymers as donors. Due to the feasibility on a laboratory scale, spin coating is the technique of choice for the preparation of thin films. It allows for reproducible results regarding thickness and smoothness of the film [148, 149].

The processing itself is based on the "standard" active layer composition consisting of PCBM and P3HT [79]. Various modifications regarding donor and acceptor as well as processing conditions are studied. A closer look to the analysis of several publications on this composition by Dang et al. [79] reveals a very inconsistent picture regarding the fabrication parameters. Almost every author describes the employed recipe more or less in detail. Most reports focus on the electrode-cleaning procedure, active layer ink synthesis, as well as general solar cell layout including back electrode materials. Not much information can be found on sheet resistance of the electrodes, spin coating parameters, and evaporation speed. While the spinning speed is provided very often, information about acceleration is typically missing completely.

The lack of crucial processing parameters makes it very difficult to reproduce results published previously. Some information might not have been considered to be of major importance and is left out consequently. However, every solar cell preparation setup is different. Starting with atmospheric conditions (ambient, glovebox and parameters therein) and ending with capabilities of the employed technical equipment such as spin coater or electrode evaporator. Crucial parameters have to be adapted to fit to specific needs of the whole setup. As an example, the reported concentrations of the active layer inks vary from $10-30\,\mathrm{mg\,mL^{-1}}$ with a direct impact on the resulting film thickness. As active layers are commonly in the $80-100\,\mathrm{nm}$ range and do not allow to be much thicker because of detrimental effects on the charge transporting capabilities, the spin coating parameters have to be adjusted to achieve films in the desired thickness range. Besides concentration and thus viscosity having a large impact on the spin coating behavior, ink and substrate temperature as well as boiling points of the employed solvents are crucial because of their influence on the drying rate of the applied materials and consequently

---

1   Additives may also influence only one component.

the film thickness and morphology.

Having these issues in mind, it becomes clear that organic solar cell research has to be performed with a "trial and error" approach because there are only few assumptions that can be made beforehand. Control of the film thickness itself is not difficult at all because tools such as UV/Vis spectroscopy, atomic force microscopy, or stylus profilometry are well established techniques that can be applied.

In contrast, active layer morphology has to be characterized via high resolution spectroscopy techniques such as AFM, STM, or electron microscopy (EM). Alternatively, theoretical modeling assists to predict possible molecular alignments in the film. However, experimental methods are typically capable to visualize the surface of the active layer while the structure within the bulk remains unclear. Finally,several sample parameters and recipes have to be evaluated if new components are utilized. As a starting point, parameters, inspired by a working composition, have to be chosen and subsequently adapted to new fabrication and material conditions. The resulting parameters for a P3HT:PCBM mixture are the following:

- P3HT: Plexcore® OS 2100, provided by *Sigma Aldrich*

- PCBM from *Solenne BV* with a purity $> 99.5\,\%$

- Material ratio: 1:1

- Solvent: Orthodichlorobenzene (ODCB)

- Mass concentration of both components $\rho = 30\,\mathrm{mg\,mL^{-1}}$

- PEDOT:PSS interlayer based on different batches of different type from *Sigma Aldrich*

- Aluminium back electrode

An additional work function adjustment via additional metal layers is omitted due to capabilities of the thermal evaporator. Processing parameters such as spinning speeds and durations are determined experimentally. Thermal treatments of the samples are performed at different stages of the preparation procedure and are provided with the specific information of each sample.

8.3.1 Spin coating

As already mentioned, the resulting films realized by spin coating depend on the spinning speed ν, the spinning duration t, and acceleration a, as well as on parameters of the solution such as the viscosity η, boiling point T_{bp} of the solvent, surface tension γ, wetting capabilities, etc. [150, 151].

The process is schematically illustrated in figure 8.3. The overall process can be divided into 4 steps. In step **1**, the covering of the substrate with the solution containing the the relevant compounds is depicted. Step **2** indicates the rotating sample and the spare material thrown away due to the centripetal force. The film thickness is reduced further by a material flow outwards due to the rotation and by the evaporating solvent as indicated in step **3**. Finally, the finished film is depicted in step **4**. Depending on the amount of materials that is poured onto the substrate in step **1**, step **2** may also have
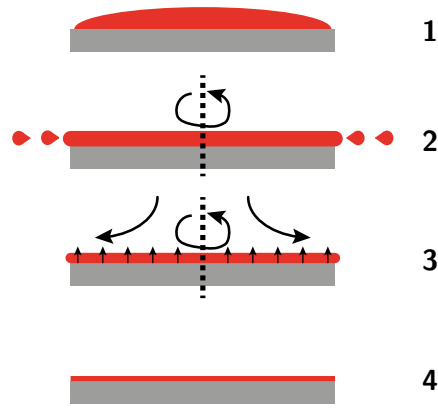
Figure 8.3: Schematic illustration of the spin coating process. Subprocess **1** indicates the covering of the substrate with the solution that contains the material to be deposited. In subprocess **2**, rotation is started and spare material is thrown away due to the centripetal force. Further rotation in subprocess **3** results in further thinning of the film by material flow and solvent evaporation. The final film is depicted in subprocess **4**.

the function to distribute material and to ensure that the whole substrate is covered. If the material does not cover the whole substrate, either too less solution has been applied or the surface properties of the substrate are not suited to the materials applied. An additional surface treatment of the substrate, e.g., by an UV ozone cleaner, can help to improve the coverage.

For the dispense process in step **1**, there are two possibilities. The first one is the so-called static dispense, where the sample is at rest, and the second is a combination of steps **1** and **2**, i.e., the substrate is already rotating when the material is applied.

Static dispense is preferably applied if sufficient amounts of material is available and the wetting capabilities are large enough to easily cover the substrate.

Dynamic dispense is advantageous if the wetting capabilities are considerably poor and and less material should be wasted. The drawback of this technique is the need for an exact positioning of the dispensing tip above the center of the substrate. Slight deviations result in an irregular coverage.

The spin coating device that is available for sample preparation only allows to adjust the speed in a range of $10 - 80 \, \text{s}^{-1}$ and no adjustment of the acceleration. As a consequence, rather viscous solutions or those with low boiling points have to be used for spin coating to achieve a layer of sufficient thickness.

8.3.2 UV/ozone cleaning

UV/ozone cleaning is a technique to modify the surface properties of materials, e.g., glass or ITO-coated glass substrates. A low-pressure mercury-vapor lamp within the ozone cleaner produces UV light at two different wavelengths – 254 nm and 185 nm. Light at 254 nm excites organic molecules that adhere to the surface of the substrate or

produces organic radicals. These can react with ozone molecules formed from molecular oxygen and oxygen radicals produced by the 185 nm light. The resulting compounds are volatile and can easily desorb from the surface. Additionally, also the OH radicals at the surface of the substrate have a crucial impact on subsequent processing steps such as spin coating. These radicals effect a hydrophilisation and consequently improve the wetting capabilities of water-based dispersions like PEDOT:PSS. Further details can be found in the report by Vig [152].

The available UV/Ozone ProCleaner™ by *BioForce Nanosciences* has a $5 \times 5 \, in^2$ sample stage and thus allows for parallel cleaning of up to 16 substrates with a size of $30 \times 30 \, mm^2$.

8.3.3 Thermal metal evaporation

There are several techniques to deposit thin films from vapors on top of substrates. They are roughly divided into physical vapor deposition (PVD) and chemical vapor deposition (CVD) processes. For metal deposition, typically PVD techniques are applied. Depending on the desired film properties, deposition speed, etc., a suitable technique is chosen. For the preparation of electrodes, sputter deposition and thermal evaporation are very common approaches. While the requirements regarding the vacuum quality are not so high in case of sputtering, thermal evaporation has a demand for high vacuum. Depending on the substrate and potentially already deposited layers, sputter deposition can lead to damage in the underlying materials because of the high kinetic energies of the metal atoms. This is the reason why thermal evaporation is the technique of choice for back electrode fabrication in organic solar cell research.

The thermal evaporation technique employed in this thesis is also known as resistive evaporation. Here, an evaporation source, i.e., a wire basket made of tungsten is exposed to a high current of several amperes and consequently heats up. Tungsten is chosen because of its high melting point and thus low tendency to evaporate and impurify the resulting metal film. The evaporation source is loaded with pieces of highly pure metal such as aluminium. These melt and finally evaporate due to the high temperature.

The whole operation has to be carried out in high vacuum, i.e., $p < 1 \times 10^{-3}$ mbar to ensure a mean free path length of the metal atoms which is large enough to avoid collisions with remaining gas atoms. Such collisions reduce the quality of the electrode film and additionally cause reactions if the collision partners are oxygen and aluminium for example. At the given pressure, the mean free path length is approximately $l_{\mathrm{mfp}} > 10 \, cm$ and consequently the probability for the metal atoms to reach the substrate without collisions is quite high.

The available device (Q150T ES by *Quorum Technologies*) is a combination of sputter coater and thermal evaporator. It is capable of coating one sample ($30 \times 30 \, mm^2$) at a time, employing deposition rates of up to several hundred nanometers per second. Sputter deposition occurs from the top of the chamber to the bottom. In turn, thermal evaporation can be performed from bottom to top or top to bottom. Both ways are tested and sometimes one technique is superior over the other but no systematics is discovered. For film-thickness control, the device is equipped with a quartz-based monitoring system providing information about the amount of deposited material.

8.3.4 ITO electrode preparation

In organic solar cells, at least one side of the cell has to be transparent and thus also a transparent electrode is needed. Due to this reason, ITO-coated glass substrates are used. The substrates of type CEC020S are provided by *Präzisions Glas & Optik GmbH, Iserlohn.* They consist of float glass with dimensions of $30.0 \times 30.0 \times 0.7\,\mathrm{mm}^3$ and a coating made of a $25\,\mathrm{nm}$ passivation layer SiO_2 and a $100\,\mathrm{nm}$ ITO layer resulting in a sheet resistance of $R_\square \leq 20\,\Omega/\square$. The function of the passivation layer is to hinder diffusion of alkali oxides from the glass into the organic layers.

Prior to organic solar cell fabrication, parts of the ITO have to be removed to avoid short circuits with the back electrode deposited later. An illustration of the desired substrate layout is provided in figure 8.4.
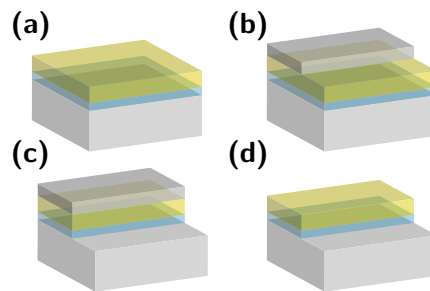
Figure 8.4: Schematic illustration of the ITO-structuring procedure. Subimage (a) shows the unstructured substrate with SiO_2 and ITO layers. In subimage (b), a mask of adhesive tape is attached. After the etching process in (c), SiO_2 and ITO are partially removed. Subimage (d) depicts the structured substrate without the mask. All thicknesses are not true to scale.

In order to partially remove the ITO and passivation layer from the glass substrate (figure 8.4(a)), a mask of adhesive tape with a width of $18\,\mathrm{mm}$ is attached to the surface as illustrated in figure 8.4(b). Subsequently, the masked samples are etched with diluted hydrochloric acid[1] for about $1-2$ hours until ITO as well as passivation are completely removed as illustrated in figure 8.4(c). Finally, the etched substrates are rinsed with demineralized water and subsequently the adhesive tape is removed, the substrate according to figure 8.4(d) is ready for further processing.

Due to the application of adhesive tape for masking, residual glue sticks to the ITO. These residues must be removed in subsequent steps. These procedures are extremely crucial for the following deposition of PEDOT:PSS. After the tape is pulled off, the substrates are washed again with demineralized water, then rinsed with isopropyl alcohol. If the substrates are determined to be used directly after the etching process, they are also stored in isopropyl alcohol. Prior to further use, the cleaning procedure is completed. It includes the following steps:

- Wiping with a sheet of lint-free paper that is rinsed with isopropyl alcohol to remove residual glue,

- Ultrasonication with demineralized water for 15 min,

---

1 Mixture of water and hydrochloric acid (37 %) in a volume ratio of 1:1.

- Ultrasonication with acetone for 15 min.

Due to the low boiling point of acetone, the substrates dry fast. Any other particles that still may stick to the surface are removed with lint-free paper rinsed with isopropyl alcohol once more. Finally, if all contaminations are removed, the substrates can be treated with the UV/ozone cleaner.

UV/ozone cleaning is performed for 20 min to remove residual organic contamination by the solvents and bring the ITO into an hydrophilic state. Further handling of the substrates is performed with the help of tweezers. Between all following processing steps, the substrates are stored in covered petri dishes to avoid contamination with moisture or ubiquitous dust particles to circumvent clean room atmosphere.

8.3.5 PEDOT:PSS layer deposition

Directly prior to PEDOT:PSS deposition, the dispersion has to be filtered through a $0.45\,\mu m$ Polyvinylidenfluorid (PVDF) syringe filter to remove aggregates that form in the container during storage. Then, a substrate is mounted to the spin coater and the spinning speed is adjusted to the terminal value of $n_{\mathrm{rev}} = (70 \pm 2)\,\mathrm{s}^{-1}$. The process itself is performed in the dynamic dispense mode with a coating duration of $t_{\mathrm{spc}} = (60 \pm 5)\,\mathrm{s}$. The dynamic dispense mode has been chosen because it provides the best results regarding PEDOT:PSS layer quality after several tests. Also by varying of the temperature of the dispersion between room temperature ($\approx 22\,°\mathrm{C}$) and $40 - 50\,°\mathrm{C}$, no significant influence of elevated temperatures were observed and thus room temperature was set to be standard.

After the deposition, PEDOT:PSS deposited on areas of the substrate without ITO is wiped away with a lens-cleaning tissue rinsed with demineralized water. Additionally, all films are inspected by the naked eye for inhomogeneities that are induced by unevenness of the ITO film or other impurities. Samples that provide inhomogeneities are sorted out. If the same substrate provides poor PEDOT:PSS layer quality for a second time, the substrate is discarded. Flawless samples are annealed on a hot plate for $t_{\mathrm{ann}} = 10\,\mathrm{min}$ at $100\,°\mathrm{C}$ to remove residual water from the film. Afterwards, the samples are stored in covered petri dishes.

8.3.6 Active layer deposition

As already mentioned, the active layer ink is a mixture of donor, acceptor and at least one solvent. Preparation and solving process take some time and the mixing process consequently has to be performed a few hours[1] prior to film deposition. Ideally, the preparation is started also prior to PEDOT:PSS deposition to avoid too long exposure of the film to ambient conditions.

For the sake of handling, two separate solutions for donor and acceptor are prepared, respectively. For each solution the specific amount of material is weighed and filled into a screw vial. The weighed amounts strongly depend on the amount of solution to be prepared and the aimed concentration. Typically, the amount is chosen not to be larger

---

1   The actual duration crucially depends on the employed materials and is kept as short as possible.

than the volume needed for the desired amount of cells. This procedure ensures that every solution is prepared freshly prior to cell fabrication and consequently aging of the solved materials is avoided. Additionally, also changes of the concentration due to partial evaporation of the solvent is prevented. Another advantage of the separate-solution approach is the possibility to prepare ink for the active layer of different ratios of donor and acceptor.

While the small molecule acceptor materials dissolve comparably fast in the solvents, the polymeric donors, especially P3HT need several hours to completely dissolve. The process can be speed up by heating the solution up to $\approx (50 \pm 10)\,°C$ and permanent stirring. After donor and acceptor are completely dissolved and no visible particles are left, the solutions are mixed at the aimed ratio. In a next step, the mixture has to be filtered to remove any aggregates that might still be in the solution. This step is performed with a $0.45\,\mu m$ Polytetrafluorethen (PTFE) syringe filter and finalizes the ink preparation.

The deposition on top of the PEDOT:PSS-coated substrates is performed in the static dispense mode at a spinning speed of $10-40\,s^{-1}$ depending on the ink properties. Detailed information is provided with the sample data. Static dispense is chosen because of the comparably high viscosity of the solution. Attention has to be paid to cover all areas of the sample to be coated with active layer material. After the deposition, all samples are inspected again with the naked eye to check for distortions in the layer. Due to the layout of the back electrodes dividing the sample into up to six subcells (cf. subsection 8.3.7), only disturbances in one of the subcells is accepted. In any other case, the substrates are cleaned and stored for possible later reuse.

After the spin casting, some samples are dried and annealed on a hot plate. This process has two effects. The first one is to remove residual solvent in the active layer, the second one assists the formation of aggregates of donor and acceptor material and finally boosts the solar cell performance. Whether this annealing step is performed crucially depends on the donor and acceptor materials because several of them are very sensitive to elevated temperatures and thus annealing must be omitted. Another detrimental effect can be the reaction with ambient air due to the lacking protective atmosphere. That is why, for some samples, the annealing step is performed after deposition of the back electrode.

In order to give an example for annealing temperatures and durations, the article by Dang et al. [79] should be read. They review lots of publications regarding P3HT:PCBM organic solar cells and the observed annealing duration are between $1-30\,min$ while the temperatures are in the range of $110-160\,°C$. Again, this points out that there is not only one recipe to fabricate organic solar cells but every setup demands its own recipe.

8.3.7 Application of the aluminium back electrode

The back electrode consisting of a single layer of aluminium is applied via thermal evaporation. An additional layer of calcium or lithium fluoride is omitted because the vacuum chamber has to be vented to change the material in the evaporation source. This exposure to ambient air has detrimental effects to the interlayer or the underlying organic layer. Additionally, the interlayer is too thin to protect the organic films against

air.

In order to get the possibility to generate several subcells on one substrate, a mask made of brass is attached to the sample before the aluminium film is evaporated. A schematic representation of the single steps during sample fabrication is provided in figure 8.5.
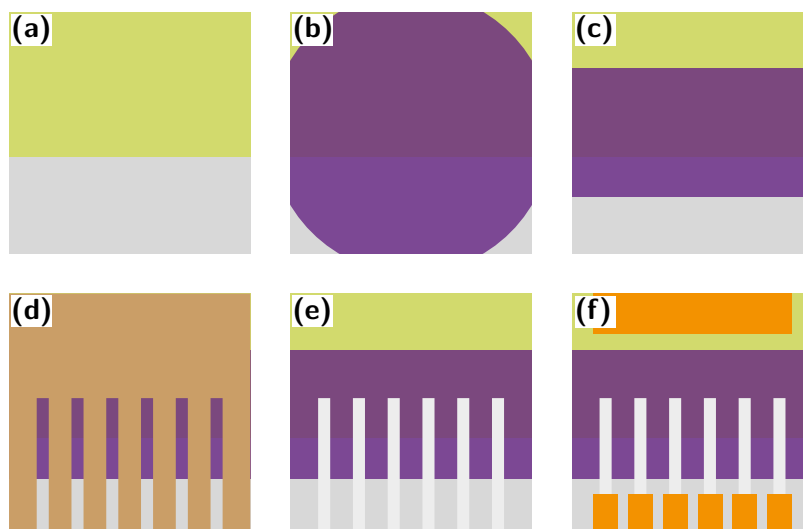
Figure 8.5: Schematic representation of the sample preparation process: substrate with prepared ITO electrode (subimage (a)), with additional organic layers (subimage (b)), with cleaned areas to avoid short circuits and for better electrode contact (subimage (c)), with mask before aluminium evaporation (subimage (d)), with aluminium contacts (subimage (e)), and finally with adhesive copper tape for better contact to measurement equipment (subimage (f)).

After the substrate is prepared as illustrated in figure 8.4, here depicted in figure 8.5(a), the organic layers are deposited (figure 8.5(b)). In the next step parts of the spin-coated layers are removed to avoid short circuits and assure good connectivity to the characterization setup (figure 8.5(c)). Subsequently (figure 8.5(d)), a brass-made mask is attached to the sample to guarantee subcell formation during the evaporation of the aluminium back electrode. Figure 8.5(e) depicts the result after the mask is removed and figure 8.5(f) illustrates the finalized sample where some adhesive copper tape is added to protect aluminium film as well as the ITO. Another advantage of the tape is an improved contact between measurement equipment and sample. After this last preparation step, the sample is characterized via the technique introduced in the following chapter 9.

9 Characterization of organic solar cells

The characterization of organic solar cells is performed via UV/Vis absorption spectrometry (cf. section 6.1) and determination of the diode characteristics [21]. Absorption spectra are important to determine the overlap of the cell's absorption with the solar spectrum and to detect additional absorption features that occur by formation of charge-transfer states within the the donor/acceptor system.

In principle, the simplest equivalent circuit of solar cells can be considered as a diode that is running parallel to a current source. In order to represent internal and external influences on the cell's performance, this circuit is expanded by the resistors R_S and R_{SH}. The series resistance R_S describing detrimental effects induced by connections, wires, etc., has to be as low as possible while the shunt resistance R_{SH} that reflects defects within the layer system and possible short circuits on a microscopic scale has to be as large as possible. The quantity j_{ph} denotes the photocurrent and j_d the current through the diode.
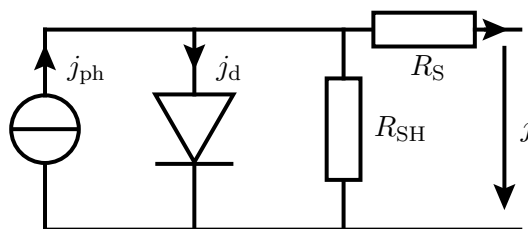
Figure 9.1: Equivalent circuit of a solar cell consisting of an ideal current source j_{ph}, diode j_d, series resistor R_S, and shunt resistor R_{SH}.

Translated into an equation, the current j is given by

$$j = j_{ph} - j_d - \frac{V_{SH}}{R_{SH}} = j_{ph} - j_{rlc}\left[\exp\left(\frac{V + R_S \cdot j}{nV_T}\right) - 1\right] - \frac{V + R_S \cdot j}{R_{SH}} \tag{9.1}$$

and the behavior – need for small R_S and large R_{SH} is represented properly [153]. Here, V denotes the cell voltage, V_T the temperature dependent voltage and n the emission coefficient of the diode that is typically in the range $1-2$. The quantity j_{rlc} describes the reverse leakage current of the diode that, as its name states, occurs if the diode is biased reversely.

Obviously, this equation has a recursive shape because j is self-dependent and consequently, numerical approaches like the Newton-Raphson technique are employed to solve it [153]. Because the characterization of R_S and large R_{SH} is not part of this work, the influence of both is only discussed qualitatively.

In a more advanced equivalent circuit [153, 154], a second diode that is set in parallel to the first one is included. This two-diode model is capable to represent a solar cell

even better by also including recombination losses. In contrast, for the introduction of the crucial parameters of the characterization, the simple model of diode and current source is usually employed. An example for a resulting characteristics is provided in figure 9.2. Despite the fact that the quantities at the current and voltage axes lie in a realistic range, the parameters to generate these curves were arbitrarily chosen and are not related to any real system and thus figure 9.2 has only illustrative purpose. The two
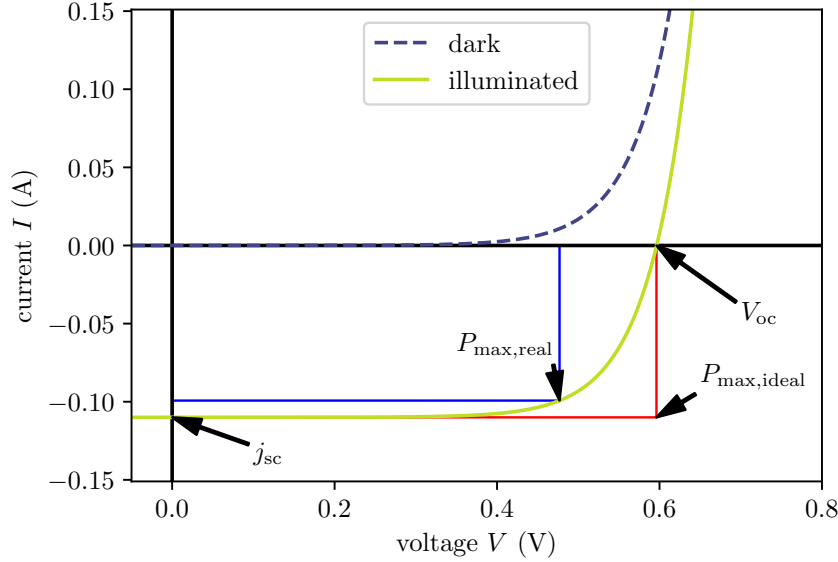
Figure 9.2: Diode characteristics of an illuminated and a non-illuminated solar cell. The arrows indicate crucial parameters including the open circuit voltage V_{oc}, the short circuit current j_{sc}, the maximum power point under real conditions $P_{max,real}$, and its counterpart, the unrealistic maximum power for a rectangular characteristic curve $P_{max,ideal}$. The two rectangles indicate the power that is converted if the cell is operated at $P_{max,real}$ or $P_{max,ideal}$, respectively.

exponential curves illustrate one solar cell that is exposed to light (solid) and one that is not (dashed). The curves that are taken without illumination provide information about the dark current, and thus they are taken for correction purposes of the photocurrent. In turn, the photocurrent curves possess the main information about the crucial parameters and are also taken for efficiency calculations.

Two crucial parameters of an organic solar cell are the short circuit current j_{sc} and the the open circuit voltage V_{oc}. The former describes the case of maximum current that is reached between both contacts of the cell if it is shorted. The latter can be determined directly at the contacts. A third parameter is the so-called maximum power point $P_{max,real}$ at which a solar cell is typically driven. At this point on the photocurrent curve, the product of voltage V_{mpp} and current j_{mpp} – the power– is maximized. Multiplying the two previously introduced parameters j_{sc} and V_{oc} yields $P_{max,ideal}$, the ideal maximum power of a perfectly rectangular characteristics. In turn, the ratio of $P_{max,real}$ and $P_{max,ideal}$ finally results in the so-called fill factor (FF)

$$FF = \frac{P_{max,real}}{P_{max,ideal}} = \frac{V_{mpp}\, j_{mpp}}{V_{oc}\, j_{sc}} \;, \tag{9.2}$$

i.e., a measure for the rectangularity of the characteristics. The FF is not a measure for the solar cell's total performance because it does only depend on intrinsic values of the cell itself. This means that a cell with low overall performance can have a quite high FF.

The power conversion efficiency (PCE) is the most common quantity of a solar cell that is applied for comparisons. It is defined as the ratio between converted power P_{conv} of the cell and of the incident light P_{light}:

$$\eta_{\text{PCE}} = \frac{P_{\text{conv}}}{P_{\text{light}}} \ . \tag{9.3}$$

Solar cell characterization demands several standard conditions to ensure reproducibility. These conditions include a defined sunlight intensity as well as ambient temperature. The intensity is defined to be $I_{\text{solar}} = 100 \, \text{mW} \, \text{cm}^{-2}$ and the standard temperature is $T = 25 \, °\text{C}$. Additionally to the defined temperature, also the spectrum employed for illumination must have a specific shape. For this purpose, the so-called "AM" standard spectra are introduced. AM is an abbreviation for the term "**air m**ass" that reflects the influence of the length sunlight traveling through earth's atmosphere. Extraterrestrial light at mean sun-to-earth distance is not influenced by air and thus has an air mass of zero or AM0. If light impinges perpendicular to the earth's surface, the air mass equals 1 at sea level, typically expressed as AM1. For solar cell characterization, a point on the northern hemisphere is assumed. At this point the light impinges with a zenith angle of 48.2° resulting in an air mass of 1.5 or AM1.5 and its specific spectrum. The AM1.5 spectrum itself is available in different variants. There is an AM1.5 D[1] spectrum only including light that comes directly from the source whereas the AM1.5 G[2] spectrum additionally includes diffusive reflected light.

A comparison of different solar spectra is provided in figure 9.3. The data based on the ASTM G-173-03 standard are obtained from the Renewable Resource Data Center of the NREL [155]. In addition to the spectra, the total intensity is calculated and provided within the figure. The spectra range from $280 - 4000 \, \text{nm}$ and their maximum is around $500 \, \text{nm}$. The shape of the spectra, especially of the extraterrestrial one, are very close to a black body. The AM1.5 versions exhibit a few dips caused by absorption and scattering in the atmosphere. Because the AM1.5 G spectrum includes also diffusive reflected light, the irradiation and the total intensity are higher than for the AM1.5 D spectrum and the intensity of the AM1.5 G spectrum coincides almost perfectly with the $100 \, \text{mW} \, \text{cm}^{-2} = 1000 \, \text{W} \, \text{m}^{-2}$ defined in the solar cell measurement standard. That is why this intensity is often referred to as 1 sun [155, 156].

In this thesis, the whole characterization is performed with the full AM1.5 G spectrum. In other works, spectra are modified regarding their width to better match the absorption spectrum of the solar cell. In turn, if the irradiance of these modified spectra is modified,

---

1 D is an abbreviation for "Direct + Circumsolar". Direct = Direct Normal Irradiance Nearly parallel (0.5 deg divergent cone) radiation on surface with surface normal tracking (pointing to) the sun, excluding scattered sky and reflected ground radiation. Circumsolar = Spectral irradiance within +/- 2.5 degree (5 degree diameter) field of view centered on the 0.5 deg diameter solar disk, but excluding the radiation from the disk [155].

2 G is an abbreviation for "Global Tilt". Global Tilt = spectral radiation from solar disk plus sky diffuse and diffuse reflected from ground on south facing surface tilted 37 deg from horizontal [155].
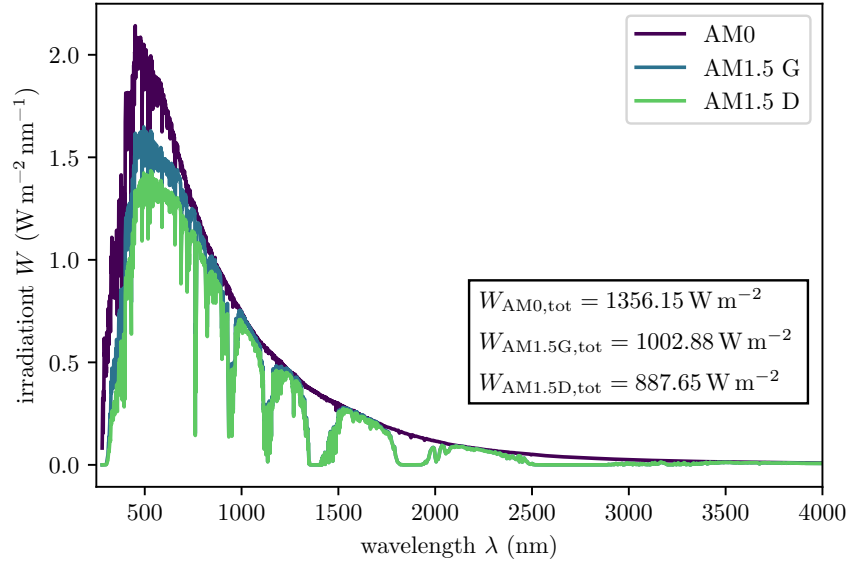
Figure 9.3: Comparison of AM0, AM1.5 G and AM1.5 D solar spectra. Their total intensity is determined by integration over wavelength and is provided in the box. Data based on the ASTM G-173-03 standard are obtained from NREL - National Renewable Energy Laboratory [155]

errors during the determination of the cell's efficiency cannot be avoided. Snaith [156] has reported on several crucial aspects that have to be considered during cell characterization. He names typical and common sources for overestimation of the cell's performance often made. Some of these are made intentionally to report on higher efficiencies but they are of course falsified during certification by an independent institution. Other errors are made accidentally due to the absence of better knowledge.

Besides the spectral composition of the light that is employed for characterization, also the intensity is of great importance. Thus, the intensity provided by the solar simulator, LS0106 by *L.O.T. Oriel*, is checked with a thermopile detector, type PM10, in combination with a suitable controller both from *Coherent Inc.* and adjusted if necessary. During characterization, a mask of black construction paper in combination with the fixed width of the aluminium electrodes defines the active area of the cell and therefore enables calculation of the desired current density from the measured current. Figure
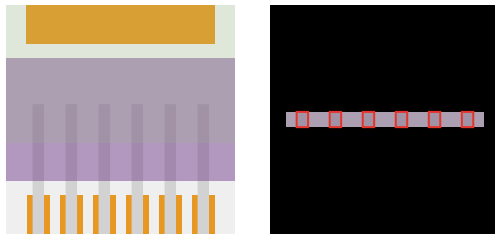
Figure 9.4: Application of a mask of black construction paper to define the active area of the subcell during characterization. Compared to figure 8.5 now the glass substrate is on the top side while all applied layers are on the back. The red rectangles (right part) are guides to the eye and do not exist on the real mask.

9.4 illustrates the solar cell presented in figure 8.5 in rotated manner. Now, the glass substrate is facing the front. On the right side of the image, the whole cell is covered by

the mask and the subcells with the defined area are indicated by the red rectangles. An additional mask to select every single cell is not necessary since detrimental effects could not be observed.

An illustration how the sample is mounted and positioned in front of the solar simulator is provided in figure 9.5. The left part contains a top view onto the setup whereas the right part shows the sample in its holder from the front. As already mentioned, dark as well as photocurrents are monitored. In order to enable the possibility to characterize both, a computer-driven shutter **Sh** is placed in front of the solar simulator **SoSim**. The aperture of the shutter is large enough to cover the whole output and thus illumination of the sample by scattered light is avoided. The sample itself is clamped on one side by
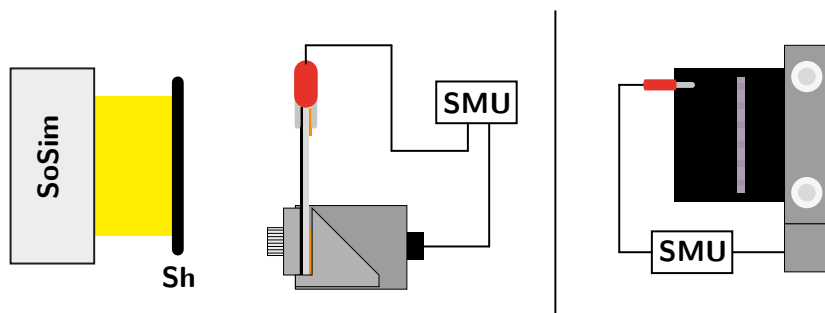
Figure 9.5: Schematic representation of the efficiency-characterization setup. The left part of the image contains a topview while the right part a front view of the sample in its holder. The term **SoSim** indicates the solar simulator and the collimated light it emits. The light is blocked by a computer-controlled shutter **Sh** to perform sequential measurements of photo- and dark current. The **SMU** drives a voltage through the sample and simultaneously monitors current and voltage.

a holder made of insulating plastic. The electrode connecting to the ITO electrode of the sample is integrated within this holder. The single electrodes on the other side of the sample are connected by an alligator clip. Via an adapter, the connections to the source measure unit (**SMU**) are realized in a 4-point probe method to avoid influences of the wiring. Characterization of the current-voltage characteristics of the subcells is carried out sequentially. As a consequence, the alligator clip has to be repositioned after each measurement to connect it to a different subcell.

The employed SMU type B2901A from *Agilent Technologies* (today known as *Keysight Technologies*) has a single channel input and can resolve drive currents up to $1\,\mathrm{pA}$ and voltages up to $1\,\mathrm{\mu V}$. The provided measurement resolution of current and voltage is $100\,\mathrm{fA}$ and $100\,\mathrm{nV}$, respectively. Additionally, the speed of a single take of a characteristic can be adjusted to the specific needs. In order to avoid heating of the sample due to the illumination, the data collection time hast to be as low as possible while the integration time is chosen to be sufficiently long to get reliable results. Consequently, the time is set to a number of power-lince-cycles (NPLC) rate of 0.01 corresponding to an integration time of $200\,\mathrm{\mu s}$. By typically choosing 1000 points per measurement, the overall time for the SMU to collect the data sums up to $0.2\,\mathrm{s}$. In addition, there is still additional overhead introduced by setting parameters and states of all devices leading to an overall data acquisition time of a few seconds. These capabilities enable the fast acquisition of highly resolved current-voltage characteristics and thus allow for a quick determination of the crucial cell parameters introduced before.

Practically, the maximum power point $P_{\text{max,real}}$ is determined by the largest area that is defined by the characteristics and the axes of current and voltage. With the known intensity (or surface power density) of the solar simulator ($I_{\text{solar}} = 100\,\text{mW}\,\text{cm}^{-2}$) and the defined illuminated area A_{cell}, the efficiency is calculated via

$$\eta_{\text{PCE}} = \frac{I_{\text{mpp}}}{I_{solar}} = \frac{V_{\text{mpp}}\,j_{\text{mpp}}}{P_{solar}} \ , \tag{9.4}$$

with $P_{\text{solar}} = I_{\text{solar}} \cdot A_{\text{cell}}$ and $I_{\text{mpp}} = V_{\text{mpp}} \cdot j_{\text{mpp}}/A_{\text{cell}}$. Due to the fact that j_{sc} and V_{oc} can be simply extracted from the data, the calculation of the FF by equation (9.2) is straightforward. Due to the quantity of I_{solar}, the product of $V_{\text{mpp}} \cdot j_{\text{mpp}}$ already provides the PCE in percent. Contrary to the characteristics in figure 9.2, the current density J is typically plotted against the voltage in order to get a representation that is independent from the actual size of the solar cell and allows for comparison with cells of different sizes.

9.1 Structure analysis of polymer chains of P3HT

A reference method for the investigation of the structure of the bulk heterojunction is theoretical modeling. Especially a combined multiscale approach of coarse grained molecular dynamics (MD) simulation and atomistic force field backmapping has turned out to be very successful. It provides deep insights into molecular arrangements and equilibration processes that are strongly temperature dependent [116] . The theoretical investigations are supported by UV/Vis spectroscopy and the resulting spectra are successfully linked to conformational changes of the characterized polymer P3HT.

The work described in this section is the result of a interdisciplinary collaboration between three different research groups of the fields physical chemistry, solid state theory, and applied physics. The author of this thesis contributed to the work resulting in a publication [116] by performing the experimental part that includes UV/Vis spectrometry of solutions of P3HT in CHCl$_3$ with different amounts of ethyl acetate (EtOAc) acting as a "bad solvent" added. Bad solvent in this context means P3HT is insoluble in EtOAc. As a consequence, adding amounts of EtOAc to a solution containing P3HT leads to aggregation and precipitation of the polymer. Hence, it is possible to record absorption spectra of P3HT in different states of order varying from completely disordered (solution) to partially ordered (aggregates). Details on the procedure are found in the following subsection.

9.1.1 Preparation of thin films and solution containing good and bad solvent

The commercially available P3HT (Plexcore OS 2100) whose molecular weight $M_{\text{n}} = (64.5 \pm 10.5)\,\text{kDa}$ is listed in table A.1 is dissolved in CHCl$_3$ at a concentration of $10\,\text{mg}\,\text{mL}^{-1}$. This solution is employed to produce thin films onto microscope slides by means of spin coating. The spinning speed is adjusted to $10\,\text{s}^{-1}$. During recording of the absorption spectra, an additional mask is placed in the beam path of the *Jasco* V-530 UV/Vis spectrometer to fix the illuminated area of the sample.

For the preparation of P3HT in good and bad solvent, another solution in CHCl$_3$ at a concentration of $10\,\mathrm{mg\,mL^{-1}}$ is prepared. In order to enhance the solubility of P3HT, the solution is annealed to approximately $(45 \pm 5)\,°\mathrm{C}$ for 5 min. After complete dissolution of the material indicated by a yellow to orange liquid with no visible particles left, the solution is diluted to $1\,\mathrm{mg\,mL^{-1}}$. On the basis of this concentration the solutions studied by absorption spectroscopy are synthesized by subsequently adding CHCl$_3$ and EtOAc at the desired ratio until the final concentration of $10\,\mathrm{mg\,mol^{-1}}$ is reached. Based on this approach, several concentrations have been realized. Table A.3 provides the corresponding data and table A.2 in the appendix contains parameters such as density ρ, molar mass M, and molar volume V_m of the employed solvents that are applied during the calculation of the solvent ratios.

9.1.2 Interpretation of the absorption spectra

The solutions are filled into quartz cuvettes whose dimensions allow a liquid thickness of 1 mm. The spectra obtained by absorption spectroscopy are displayed in figure 9.6. Here, lighter data line colors indicate a higher amount of EtOAc in the solution. In addition to
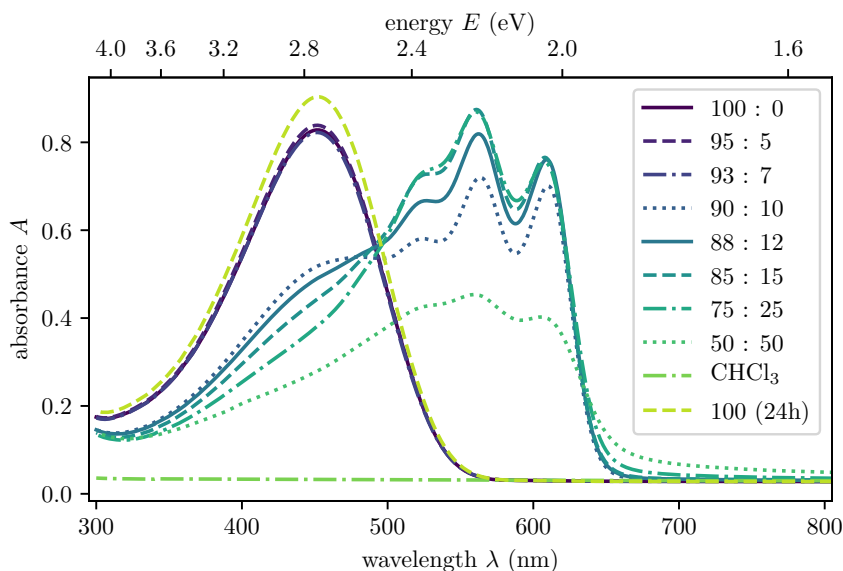
Figure 9.6: Absorption spectra of P3HT in different mixtures of chloroform and ethyl acetate. The dashed line indicates the spectrum after 24 hours whereas the dashed and dotted line represents a spectrum of CHCl$_3$.

the spectra of each solution, also a spectrum of pure CHCl$_3$ (dashed and dotted line) is recorded to illustrate the influence of one of the solvents. Further, a second measurement of P3HT in CHCl$_3$ (dashed line) is repeated after 24 hours in order to check if temporal aggregation occurs.

As the data clearly illustrate, there is no significant difference between the original spectrum and the one taken 24 hours later. The slightly enhanced absorption is attributed to a small concentration rise induced by evaporation of a part of the solvent. In contrast, the impact of EtOAc is clearly visible. While small amounts of the bad solvent have

no visible impact, there is a mercurial change of the spectrum when the amount rises above 7 mol %. Now a strong red shift of the spectrum occurs which becomes even more pronounced if the EtOAc amount is risen while the original absorption peak around 450 nm decays. These changes are not only visible by absorption spectroscopy but also by the naked eye. The color of dissolved P3HT is typically orange to yellow[1]. After the EtOAc is added, it is shifted to violet. At high bad solvent concentrations ($> 25\,\%$), the aggregation effect becomes even more pronounced. In this case, the aggregates themselves grow to an size that they are visible to the eye whereas parts of the liquid become transparent. Thus a dispersion with large aggregates of P3HT is formed. Due to the partially transparent liquid, the decay of the overall absorption in case of the 50:50 solvent ratio is explained.

An explanation for the behavior of the spectra is found if spectra of crystalline P3HT (cf. figure 9.7 (a)) are considered. Highly ordered, crystalline P3HT has its main absorption peak in the red region of the spectrum. Additionally, the spectrum of the film is very similar to the spectrum of the solution with a 50 : 50 ratio of good and bad solvent according to figure 9.6. By comparing with data of a thin film or dissolved P3HT,
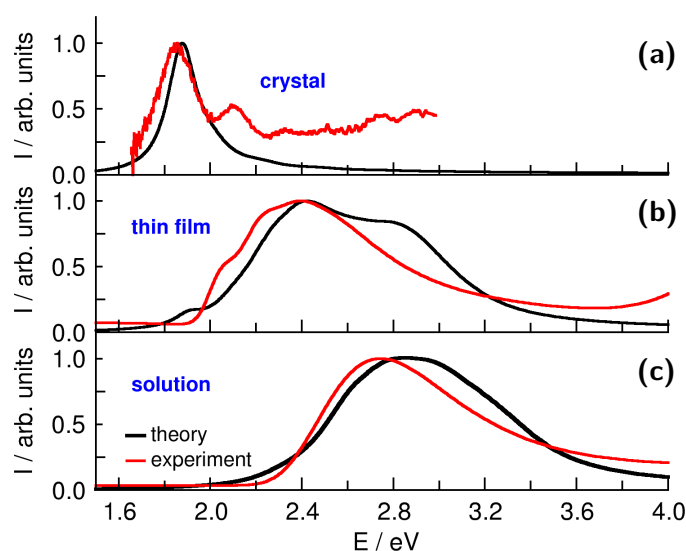
Figure 9.7: Experimental and simulated absorption spectra of a P3HT crystal (a), thin film (b), and dissolved in chloroform (100 %) (c). Experimental data of the crystal are taken by Rahimi et al. [157]. The calculated spectra are realized by the group of Nikos Doltsinis, University of Münster. The image is a reduced version of figure 5 from [116] - Published by the PCCP Owner Societies.

it can be concluded that the order of the molecules has an impact on the absorption properties of the molecules. A highly ordered crystal absorbs light with low energy while increasing disorder shifts the absorbed light to the blue regime of the spectrum. Here, the thin film can be seen as an intermediate state between ordered (crystal) and completely disordered structures (solution). Consequently, absorption spectroscopy represents an

---

1   Higher concentrations are orange or might be even reddish to brown if poorly dissolved, whereas low concentrations are yellow.

experimental technique to determine the order of P3HT. This is beneficial, because the structure has an impact on organic solar cell performance.

At this point, it is still unclear what the previously used term "disordered" means in this context. To understand the underlying changes of the molecular structure, numerical simulations of the polymer chain structure were carried out by the groups of Nikos Doltsinis, (atomistic simulations) and Andreas Heuer, (coarse grained simulations), both University of Münster. The combination of coarse grained and atomistic simulations revealed, that the dihedral angle of the thiophene rings (cf. **7** in figure 4.1) between neighboring monomers within one polymer chain plays an important role. This is due to the fact that torsion limits the conjugation or effective chain length that in turn determines the effective box length and thus the absorption wavelength. A reduced conjugation lengths implies that not all monomers contribute to the conjugated system. Instead, the polymer chain is divided into multiple parts that are conjugated. Contributions to the varied absorption by polymer bending and molecular packing have shown to be of less importance.

In detail, the simulations revealed that the dihedral angle between neighboring thiophene rings must be in the range of $\theta_{cut} = 70-80°$. Here, θ_{cut} denotes a crucial angle between neighboring rings. This torsion limits the length of the conjugated system also called the effective chain length. To determine the size of the angle, the HOMO depicted in figure 9.8 is compared to the other polymer chains in figure 9.8. These chains are colored regarding the effective chain lengths that form if a certain torsion angle is assumed. Consequently, the assumed angle has to be large enough to allow for the formation of a 7mer (size of the HOMO), i.e., seven monomers form the conjugated system. In turn, the torsion has to be small enough to inhibit longer conjugated systems. Consequently, there is a range that allows the 7mer corresponding to the HOMO to exist.
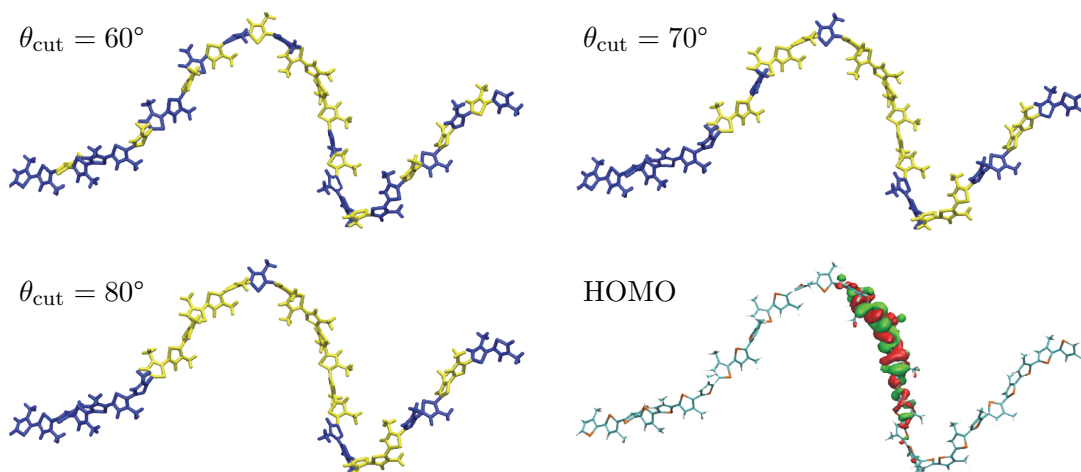
Figure 9.8: Illustration of the conjugated subchains of a 32mer P3HT. Different n-mers are indicated by alternating colors, i.e., yellow and blue. The subchains where $\theta_{cut} = 70°$ and $80°$ are set as crititcal angles contain a 7mer that corresponds to the HOMO, while the subchain in case of $\theta_{cut} = 60°$ is too short. This figure corresponds to figure 11 in [116] - Published by the PCCP Owner Societies. Only labels are slightly changed.

For $\theta_{\mathrm{cut}} = 60°$, the subchain is too short (only a 5mer). In turn, $\theta_{\mathrm{cut}} \geq 84°$ (not shown) would produce a subchain that is larger than the HOMO because the 7mer is merged with a neighboring dimer.

In order to check a more general subchain distribution, a group of 10 32mers is analyzed regarding the occurring subchain lengths in dependence on the critical angles 60°, 70° and 80°. A histogram displaying the results is provided in figure 9.9. The data clearly show that the behavior of the molecule in figure 9.8 is not an isolated case but the subchain distributions generally tend to larger conjugated subchains for larger critical angles. The amount of monomeric subunits in the 60° case is dominating in the percentage plot. For larger angles, the distribution becomes broader and broader. Additionally, this behavior is more pronounced in the solution case compared to thin films. This difference is obvious as a larger angle of acceptance for the conjugation length would allow for longer chains. This technique allows to model and verify the chain length of the real polymer system.

In the simulations it turned out that the polymer chains are bent and thus this is an additional difference to the linear shape that occurs in the crystal. Consequently, the end-to-end distance (from one terminal C-atom to the other terminal C-atom) is chosen as a measure for the degree of bending and therefore to find out the impact on the absorption properties. The analysis revealed that in average the chains are more bent in the thin film whereas the bending in solution is rather low and close to the planar configuration of the crystal. But, as seen earlier, the shift of the absorption in solution is much stronger compared to the thin film and in conclusion the bending has only a minor contribution to the absorption shift.

As a consequence, if absorption tuning of P3HT is considered, control over the torsion angles is needed. How to gain control over this functionality still needs to be recovered. So far, the techniques applied during film fabrication base on softening by heating or solvent vapor, or on reduced evaporation rates by applying solvents with high boiling points. Consequently, this is still a trial-and-error approach and might have or not the
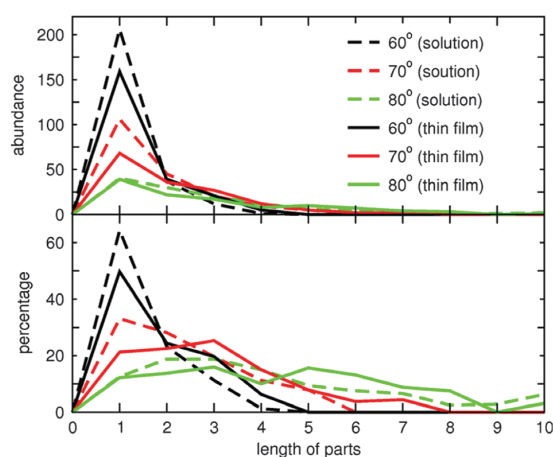
Figure 9.9: Histogram of conjugation length distribution dependent on different critical angles θ_{cut}. While the upper part illustrates the abundance, the lower one provides the percentage of occurring effective chain lengths. This figure corresponds to figure 10 in [116] - Published by the PCCP Owner Societies.

desired effect in every material composition. As the underlying effect is now known, more specialized approaches can be developed and more efforts have to be pushed in this direction because similar behavior may be also observed for the more recent donor polymers like PTB7 [158], PBDTTT-C-T [159], and others [160].

9.2 Absorption spectroscopy and numerical modeling of P3HT:diPBI solar cells

As already reported in the previous sections, thermal annealing is one method to modify the internal structure of an organic solar cell composition. Annealing temperatures are typically in the range of the boiling points of the employed solvents (or slightly below) to avoid too fast solvent evaporation. Too high temperatures lead to formation of solvent vapor bubbles in the film that are detrimental to the performance. Anyhow, even if the solvent is already completely removed, large amounts of heat in the film can cause chemical reactions of the components with each other or with other ambient compounds. Consequently, temperatures must be chosen carefully.

In order to study the conformational effects occurring in a heated film of a P3HT:diPBI (structures **7** and **18** in schemes 4.1 and 4.2, respectively) bulk heterojunction, a coarse grained molecular dynamics simulation is set up and carried out by the groups of Nikos Doltsinis and Andreas Heuer, both University of Münster. The scope of this analysis was to find a link between absorption spectroscopy and active layer morphology. The experimental part, i.e., absorption spectroscopy of strongly heated organic films is also a part of this thesis. The whole findings are published in a joint paper by Winands et al. [161].

The intention of this heating experiment is to find out if absorption spectroscopy can be also employed to predict molecular packaging within a bulk heterojunction of an organic solar cell. Coarse grained simulations of a model volume demand high temperatures (up to $900\,\mathrm{K}$) to observe molecular rearrangements in an adequate amount of simulation time. Calculated absorption spectra reveal that annealing followed by a rapid cool-down process leads to significantly different spectra and thus hints to freezing of a "hot" molecular state that does not occur in the room temperature regime. In turn, the simulations are carried out to examine the redistribution of molecules within the composition during annealing whose intention is the formation of aggregates to enhance charge transfer.

The experimental part includes sample preparation followed by annealing and absorption spectroscopy. The samples are prepared from P3HT (Plexcore OS 2100) and the triply-linked tetrachlorinated diperylene bisimide (12C-4CldiPBI) [162]. Both are dissolved at a concentration of $10\,\mathrm{mg\,mL^{-1}}$ in $CHCl_3$, stirred for $3\,\mathrm{h}$, subsequently heated to $(45 \pm 5)\,°\mathrm{C}$, and afterwards filtered through a $45\,\mathrm{\mu m}$ PTFE syringe filter. Thin films of P3HT, diPBI, and P3HT:diPBI at a $1:1$ ratio are prepared by means of spin coating onto microscope slides at a fixed spinning speed of $\nu = 10\,\mathrm{s^{-1}}$. In order to mimic the fast heating and cooling rates occurring during the simulation, the samples are put on a hot plate for $20\,\mathrm{s}$ at temperatures of $T_1 = (450 \pm 30)\,°\mathrm{C}$ or $T_2 = (250 \pm 30)\,°\mathrm{C}$. Subsequent to annealing, the samples are put on a solid block of copper for cooling down to room temperature. Absorption spectra of the films are taken via a *Jasco* V530 UV/Vis spectrometer with an additional mask in the beam path to seize the illuminated

area of each sample. In order to visualize the impact of the annealing, spectra are taken prior and post the heat treatment.

Changes of the coloring of the films during annealing can be directly observed by the naked eye. The first observation that can be made is a brightening combined with a wavelength shift after a few seconds of heating. The colors stay changed after the cooling procedure. The brightening may originate from partial evaporation of the material or other effects leading to a thinning of the film such as melting ($T_{\mathrm{m,P3HT}} = 485\,\mathrm{K} = 211.85\,°\mathrm{C}^1$) and thus diffluence of the film. The color change hints to structural changes in of the materials that may vary from orientational changes to chemical modifications via reactions with ambient molecules. To evaluate the behavior, the spectra are analyzed in more detail.

Figure 9.10 represents the resulting spectra of the different films. There are six datasets for each film type representing three samples of each type employed. Two samples of each type are annealed to $T_2 = (723 \pm 30)\,\mathrm{K}$. The last one is only annealed to $T_1 = (523 \pm 30)\,\mathrm{K}$. All spectra at room temperature (about $T_0 = 300\,\mathrm{K}$) are slightly different whereas P3HT provides the largest differences (cf. subfigure 9.10(a)).

The room-temperature spectra of samples P1 and P2 only differ regarding their intensity. In turn, the spectrum of P3 is additionally red shifted. This shift can be induced by a slightly different occurrence of torsional angles (see previous section). If the polymer chains in sample P3 are not as twisted as in the other two, longer conjugation lengths are formed and thus the absorption spectrum is closer to the crystalline one. The reason why this has happened remains unclear because all samples were treated equally.

Considering the annealed samples, a tendency of the spectra to become blue shifted combined with a loss of absorption intensity can be observed. While the 523 K spectrum is only slightly shifted and damped, the spectra taken of the samples heated to 723 K lose almost the whole characteristics of P3HT. Another effect is observed if the extremely heated spectra are compared to the spectra of the dissolved P3HT in figure 9.6. In this case, the spectra of the samples heated to $(723 \pm 30)\,\mathrm{K}$ seem to have even shorter conjugation lengths. In turn, the sample heated to T_1 seems to be in an intermediate state between the solution and film in figure 9.6. This effect may be partially caused by melting and thus shifting to a spectrum closer to the solution. The subsequent freezing in this state results in shorter conjugation lengths than in the typical film. The other already mentioned explanation is a reaction with ambient atoms or molecules. This can vary from oxidation of P3HT to the formation of other compounds that do not have much in common with P3HT at all because the hexyl chains as well as the thiophene units undergo modifications [163]. Consequently, attention has to be paid if P3HT is annealed. While moderate temperatures up to $200\,°\mathrm{C} = 473.15\,\mathrm{K}$ are not too harmful to the molecules, deterioration dramatically increases with higher temperatures as the spectra taken after the 523 K treatment indicate.

The spectra of the untreated diPBI films in subfigure 9.10(b) are only slightly different regarding their intensity. Small variations of the film thickness may be the reason for

---

1   The melting temperature (onset) was determined via differential scanning calorimetry by Stefan Ostendorp, Group of Prof. Gerhard Wilde, Institute of Materials Science, University of Münster.

(a) P3HT
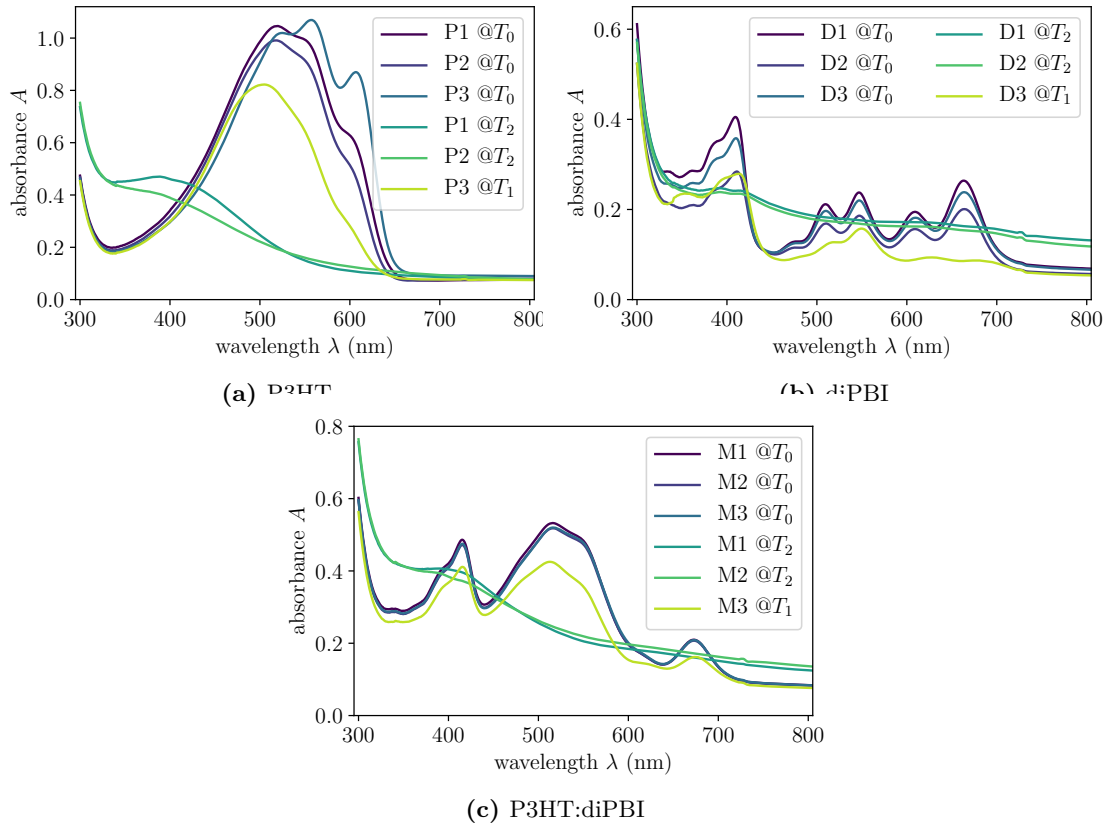
(b) diPBI

(c) P3HT:diPBI

Figure 9.10: Absortpion spectra of thin films of P3HT, diPBI, and P3HT:diPBI. Three samples of each type are characterized. The first two are heated up to $T_2 = (723 \pm 30)\,\mathrm{K}$ and the third one up to $T_1 = (523 \pm 30)\,\mathrm{K}$, respectively. Additional spectra at room temperature (about $T_0 = 300\,\mathrm{K}$) are also recorded.

this behavior. The changes induced by heating are also significant for this material. In the $523\,\mathrm{K}$ case, the overall amplitude decreases while the features in the orange-to-red region of the spectrum at $600-700\,\mathrm{nm}$ almost totally vanish. One reason for the decrease of the absorptivity may be partial ablation of molecules and thus thinning of the film. Additionally, tensions and twisting of the molecule changes the spectrum, as indicted by theoretical modeling in [161].

When heating up samples to $723\,\mathrm{K}$, the whole spectrum becomes rather flat and declines to larger wavelengths while the film starts to absorb stronger in regions where the magnitude was rather weak beforehand. This is especially remarkable in the range $430-480\,\mathrm{nm}$ and around $580\,\mathrm{nm}$. The origin of this extreme behavior also seems to originate from a decomposition of the molecules or formation of other compounds because the process is not reversible and the spectrum is neither similar to dissolved diPBI nor to other chlorinated perylene derivatives such as the monomer or higher oligomers. As a consequence, the assumed formation of a hot molecular state (that would be reversible) is not oberserved. Moreno-López et al. [164] reported that annealing of another perylene bisimide, N,N'-Bis(1-ethylpropyl)perylene-3,4,9,10-tetracarboxdiimide (EP-PTCDI), on a copper substrate led to the dissociation of the end groups that were attached to the imide position. Loss of the groups attached to the imide position does not significantly

change the absorption spectrum because this is mainly defined by the perylene core and the attached molecules in the bay position. Heat induced tensions and subsequent freezing within this state, as already mentioned for P3HT, also changes the spectrum as the theoretical modeling indicates but would still leave several remaining peaks within the spectrum instead of complete flattening.

The spectra of the P3HT:diPBI composition in subfigure 9.10(c) clearly show the superpositions of the single materials. This holds for all tested temperatures and consequently the spectrum at T_1 possess some remaining features of the original spectrum at T_0 even though slight blue shifts occurred. In the case of T_2 the peaks originating from diPBI are vanished while the maximum of P3HT is even more blue shifted and located at the position expected from subfigure 9.10(a).

The simulations results verify that the clusters consisting of different amounts of molecules rearrange over time when heated. Different heating temperatures lead to the formation of minor or larger voids in the simulation volume consisting of 1248 diPBI molecules and 416 P3HT 32mer chains. This molecules/32mer ratio of 3:1 was chosen to approximately mimic the experimentally employed ratio of 1:1 by weight.

The simulated temperatures, the samples are heated to, are $500\,\mathrm{K}$, $700\,\mathrm{K}$, and $900\,\mathrm{K}$. Slices ($2\,\mathrm{nm}$ thick, cf. [161]) through the simulation volume are employed to visualize the changes of aggregates during the annealing process and after cooling down. The first observation that is made prior to the annealing of the materials is the tendency to form aggregates with their own species. This aggregation is mirrored in a not homogeneously mixed composition. A second observation shows that the simulation volume thermally expands during the annealing process of $1\,\mathrm{\mu s}$. As expected, this effect is more pronounced when heating to higher temperatures. At temperatures of $700\,\mathrm{K}$ and $900\,\mathrm{K}$, voids can be monitored in the heated state while they are refilled after the cooling process.

A different behavior is be observed for the two material species. DiPBI forms π stacks at all temperatures whereas the P3HT 32mers tend to form large interconnected disordered domains. The latter decompose into smaller domains during the $900\,\mathrm{K}$ run. Consequently, this can be seen as an indication for a transition from order to disorder in the temperature range $700 – 900\,\mathrm{K}$. This transition points to a phase transition, e.g., from solid to liquid of the composition. As already mentioned, the melting temperature of P3HT is determined to be $T_{\mathrm{m,P3HT}} = 485\,\mathrm{K} = 211.85\,^{\circ}\mathrm{C}$, whereas $T_{\mathrm{m,diPBI}} = 537\,\mathrm{K} = 263.85\,^{\circ}\mathrm{C}$ [1]. Consequently, the solid-to-liquid phase transition already has occurred at temperatures below $700\,\mathrm{K}$. This assumption is additionally supported by analysis of PCBM compositions that melt at temperatures around $560\,\mathrm{K}$ and findings that the melting temperature of the composition is also within this regime [165].

Albeit the prediction of possible phase transitions does not match the experimental observations, changes of the morphology become clearly visible. This effect is expected to be more pronounced if it is possible to extend the simulation time to several seconds or even minutes. This allows to better mimic the experimentally observed changes of molecular aggregate formation and redistribution which typically occur on these

---

1   The melting temperature (onset) is determined via differential scanning calorimetry by Stefan Ostendorp, Group of Prof. Gerhard Wilde, Institute of Materials Science, University of Münster.

timescales [166]. Furthermore, switching to higher temperatures leads to different results and it also neglects molecular decomposition that is observed in air or nitrogen atmosphere at temperatures below 900 K. Thus the surrounding also has an impact on molecules' stability and cannot be neglected. Especially the formation of large domains is observed at "prolonged" annealing of P3HT:PCBM [166]. This is contrary to the finding that high temperatures lead to the break up of domains forming smaller ones. As already mentioned, higher temperatures do not seem to compensate for long-time effects occurring at lower temperatures. In turn, these simulations provide other important information about effects that arise if domains break up and consequently lead to a higher degree of homogeneity with smaller aggregates.

How the observed behavior can be transferred into practical applications and the detrimental decomposition effects can be avoided is still an open question. It would be a great breakthrough if a recipe could be found that would guarantee to form ideally-sized domains in a reproducible way. However, many boundary conditions come into play including the homogeneity of the initial composition, heating and cooling rates, temperatures or even multiple temperature steps, and boiling points of the involved solvents. Consequently, a multidimensional optimization problem is created and thus the "sweet spot" of OSC fabrication is hard to find. As a consequence, only smaller parts of the parameter space can be considered and therefore only more or less good approximations of the ideal processing conditions are found.

An additional difficulty of the optimization process is the fact that a detailed analysis of the morphology of the BHJ, especially if not only the interface to the electrodes are considered, is so far not possible by in-situ methods. Scanning techniques, such as STM, are capable to characterize the BHJ, but they cannot be applied during processing. Hence, the morphology can be different due to the different boundary conditions (missing top electrode, time scales, etc.).

Consequently, theoretical models are powerful tools to support experimentalists in finding an optimized recipe. Of course, the adaption of novel materials and other experimental parameters into the model is quite difficult. Especially as time scales in theory and experiment are completely different, trade-offs must be made and thus the findings must be interpreted and treated carefully. Finally, computation power and available memory of high-performance computer clusters continuously rise and so does the possibility to model experimental conditions more adequately.

10 Perylene derivative acceptors and applied donors

As already mentioned earlier, perylene derivatives are powerful acceptors that possess the ability to replace the commonly used PCBM in organic optoelectronics and thus in organic solar cells. In section 4.2, representatives of the perylene derivative family are already introduced. In order to further enhance the efficiency of organic solar cells, multiple functionalized perylene derivatives are developed and synthesized by the group of Prof. Zhaohui Wang, Institute of Chemistry, Chinese Academy of Sciences. These functionalized versions and their suitability as acceptors in organic solar cells are studied in the following sections.

10.1 Material properties

Perylene bisimides have several important fundamental properties that are already generally stated in the chapter describing organic materials. Functionalizations bring additional features that change the materials properties regarding solubility and their optical and electrical properties. The solubility properties are mainly controlled via groups in the imide position, e.g., dodecyl chains or other hydrocarbon groups. In turn, functional groups in the bay position are employed to tune the position of the energy levels.

10.1.1 PBI

The employed perylene derivative 12C-4Cl-PBI, similar to structure **15**, has two chlorine atoms in each bay position and dodecyl chains ($C_{12}H_{25}$) in the imide positions [167]. The whole structure is presented in scheme 10.1. In its solid state, it occurs as a flake
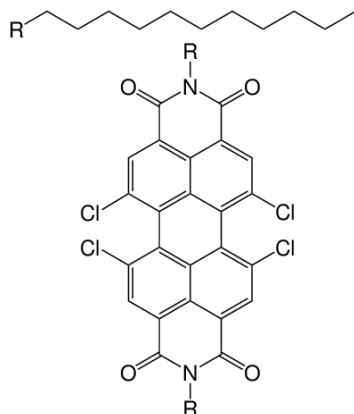
Scheme 10.1: Schematic representation of the 12C-4ClPBI molecule. One dodecyl chain, presented at the top of the scheme, is attached with its R position to each R position of the core molecule, respectively. Due to the chlorine atoms in the bay positions, the molecule is slightly twisted and not planar as illustrated.

material of orange color. As its derivatives, PBI possesses a strong electron affinity, that is enhanced compared to the variation without chlorine atoms [167]. Additionally, it provides outstanding absorption in the visible range of the spectrum, especially in the

green part (cf. figure 10.6). The positions of HOMO and LUMO levels (see figure 10.5) are very close to the ones of PCBM. Consequently, this proximity makes PBI to an ideal replacement if only energy levels are considered. Additionally, due to its almost planar structure, PBI tends to molecular π-stacking and thus enables for efficient charge transfer. Like in its derivative triply-linked diperylene bisimide (tdiPBI), the perylene backbone of PBI is slightly twisted because of the chlorine atoms [168]. The dodecyl chains in the imide position grant solubility in common solvents like $CHCl_3$, ODCB, chlorobenzene (CB), thiophene, and others. PBI is used without further purification.

10.1.2 Triply-linked diPBI

The tdiPBI that is employed to synthesize organic solar cells is the the same that is employed in the photorefractive composites and that is studied by the heating experiments in the previous chapter. Consequently, structure **18** in scheme 4.2 corresponds only to the core of 12C-4CldiPBI that has dodecyl chains ($C_{12}H_{25}$) in the imide positions and two chlorine atoms in each bay position [162]. A schematic representation of the employed structure is provided in scheme 10.2. In its solid state prior to solvation, the
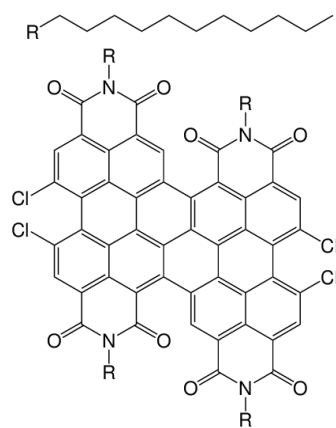
Scheme 10.2: Schematic representation of the triply-linked 12C-4CldiPBI molecule. One dodecyl chain, presented at the top of the scheme, is attached with its "R" position to each R position of the core molecule, respectively. Due to the chlorine atoms in the bay positions, the molecule is slightly twisted and not planar as illustrated.

material is a powder of purple color. In order to visualize the torsion of the tdiPBI molecule, a 3D representation via ChemBioDraw Ultra [169] is realized and displayed in figure 10.1. The visualization corresponds to the orientation of minimized energy. The energy of the dimer is minimized by the built-in function of the program. The influence of the neighboring oxygen and chlorine atoms on the structure becomes clearly visible. While the perylene backbone is typically perfectly flat, the chlorine and oxygen atoms induce bending of the whole molecule. The dodecyl groups in the imide position are not fixed regarding their orientation. Their position has to be considered as a snapshot because the connection to the backbone is still flexible. Due to its strong absorption and high electron affinity proven in photorefractive composites [74, 76, 77, 170, 171], tdiPBI seems to be an ideal candidate for solar cell applications. The almost planar structure allows for π-stacking[1] and thus for high-efficient charge transfer. The energy levels and the absorption spectrum are provided in figures 10.5 and 10.6, respectively. Due to its end chains, tdiPBI provides a good solubility in common non polar solvents

---

1 The stacking capabilities are verified by the theoretical modeling in section 9.2.
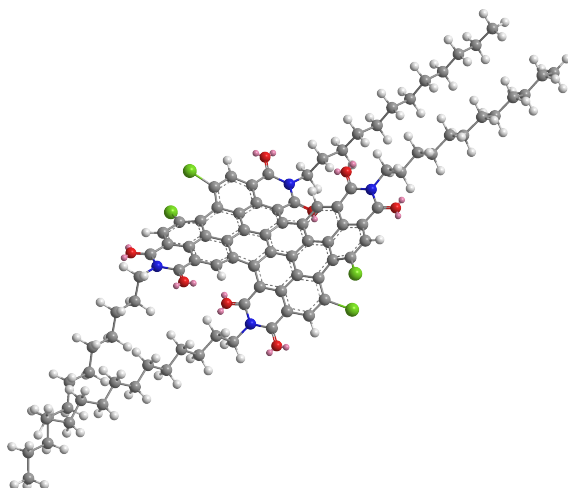
Figure 10.1: Three dimensional representation of the triply-linked 12C-4CldiPBI molecule. The coloring indicates different types of atoms. The coding is the following: carbon: gray; hydrogen: white; nitrogen: blue; chlorine: green; oxygen: red; the oxygens' lone pairs: pink. The visualization is performed with ChemBioDraw Ultra [169].

such as chloroform, dichlorobenzene, chlorobenzene, etc. As the energy levels indicate, the absorption spectrum of tdiPBI is slightly broader than the one of PCBM. Thus, tdiPBI additionally absorbs light in the red region of the spectrum. Considering the absolute value of the absorbance, tdiPBI significantly overcomes PCBM and therefore provides a better contribution to the solar cell's performance. In P3HT:PCBM solar cells the absorption is mainly provided by the polymer. Here, the perylene derivative could on the one hand extend the width of absorption spectrum and on the other hand increase the absorption magnitude. TdiPBI is used without further purification.

10.1.3 Singly-linked diPBI

The employed singly-linked diperylene bisimide (sdiPBI) depicted in scheme 10.3 is not functionalized in the bay position but has 6-undecyl groups in each of its imide positions for the sake of solubility. Consequently it is soluble in common non polar solvents such as chloroform, dichlorobenzene, chlorobenzene, etc. As for the other perylene derivatives, the energy levels and absorption spectra are illustrated in figures 10.5 and 10.6, respectively. Due to the single bond connecting both perylene units, repulsive forces lead to a twist between the monomers and consequently planar stacking of the molecules
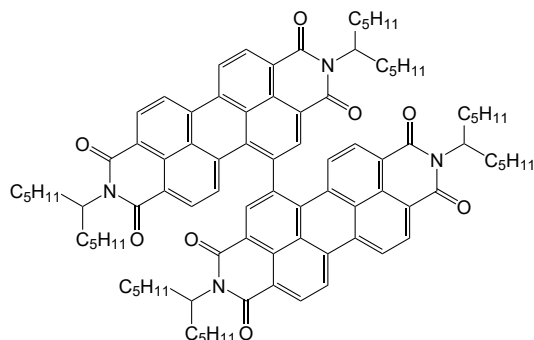
Scheme 10.3: Schematic representation of the singly-linked diPBI molecule with 6-undecyl groups at the imide positions. For the sake of readability, the structure is turned by some degrees with respect to the molecule in scheme 10.2.

is no longer possible. The prevented π-stacking might have negative effect on the charge transfer but in turn the almost perpendicular orientation results in an improved absorption of visible light [82] and thus the possibility to compensate for reduced charge

mobility. Figure 10.2 displays the 3D representation of the molecule. Similar to the case of its triply-linked relative, the molecule's energy is minimized via ChemBioDraw Ultra's built-in function. It is clearly visible that the perylene backbones of both units of the dimer are not completely flat and slightly bend whereas they are twisted against each other due to the repulsive forces of the oxygen atoms. The orientation of the undecyl groups has to be considered as a snapshot because they still possess some flexibility. The data of the energy levels and the absorption spectra are depicted in figures 10.5 and 10.6, respectively. SdiPBI is used without further purification.

10.1.4 PPDI

Scheme 10.4 depicts the imide-linked diperylene diimide (PPDI) molecule. Here, the bay positions contain no moieties for functionalization. In turn, the ending imide groups are equipped with 6-undecyl groups to enable solubility in common solvents like chloroform, chlorobenzene, dichlorobenzene, etc. Due to the positioning of the oxygen atoms, the single subunits are twisted by almost 90° to each other. Naturally, this angle is not fixed and can vary in a range allowed by the repulsive forces of the oxygen atoms. This
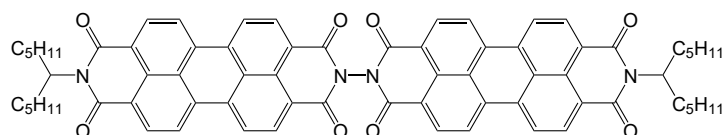
Scheme 10.4: Schematic representation of the imide-linked diPBI molecule with 6-undecyl groups at the imide positions at the ends. The molecule is also referred to as PPDI.

torsion is visualized in figure 10.3 by ChemBioDraw Ultra. The corresponding state is achieved after heating to 300 K via the built-in molecular dynamics simulation and subsequent energy minimization by the built-in function. The starting point seemed to be a metastable state displayed in figure 10.4. From this configuration, energy minimization alone did not lead to the subunit orientation depicted in figure 10.3 and thus demanded for the heating of the molecule to overcome the repulsive forces that keep the molecule in this state. In this metastable state, the perylene core units are aligned parallel and only slightly shifted to each other. Consequently the connecting bond is stretched and the whole molecule is tensed. The data of the energy levels and the absorption spectra are depicted in figures 10.5 and 10.6, respectively. PPDI is used without further purification.
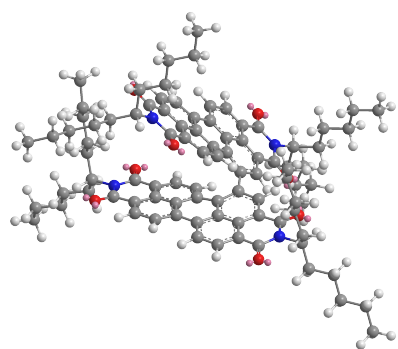
Figure 10.2: 3D representation of the singly-linked diPBI molecule. The color code is he following: carbon: gray; hydrogen: white; nitrogen: blue; oxygen: red.
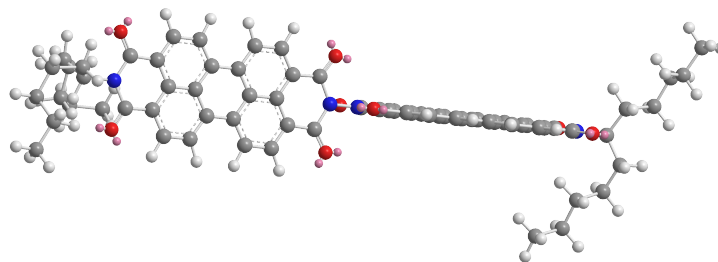
Figure 10.3: 3D representation of the imide-linked diPBI molecule. The color code is the following: carbon: gray; hydrogen: white; nitrogen: blue; oxygen: red; the oxygens' lone pairs: pink.
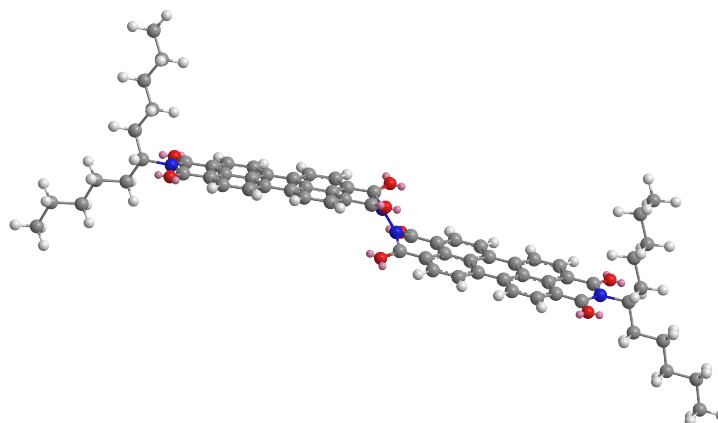
Figure 10.4: Untwisted, tensed 3D representation of PPDI[a]. This metastable state vanishes after molecular equilibration and turns into the configuration displayed in figure 10.3. The color code is the following: carbon: gray; hydrogen: white; nitrogen: blue; oxygen: red; the oxygens' lone pairs: pink.

---

a   Due to the fact that small temperature elevations are sufficient to transfer the molecule in the twisted state, it is assumed that this stretched parallel state has no importance in the real system because it does not occur.

10.1.5 PBDTTT-C-T

In addition to the applied P3HT also PBDTTT-C-T [172] is employed as a donor polymer. Similar to first one mentioned, it is also based on thiophene. Scheme 10.5 or alternatively structure **11** in scheme 4.1, depicts the molecule that is designed by following a copolymer strategy to foster the energy level tuning (cf. figure 10.5). The aim of this strategy is to generate absorption spectra also covering the red region of the spectrum (cf. figure 10.6). In turn, the donor character of the polymer is maintained by keeping the relative position of HOMO and LUMO slightly above the levels of typical acceptor molecules. In comparison to P3HT the difference of the energy levels is significantly reduced and thus the absorption is red-shifted. Additionally, the energy of the LUMO level is reduced resulting in a reduced amount of excess energy for an electron transferred from donor to acceptor.

PBDTTT-C-T is provided by the manufacturer *Solarmer Inc.* and used without any
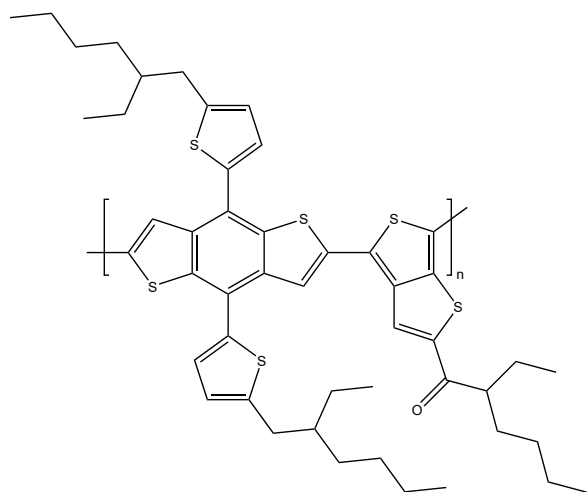
Scheme 10.5: Schematic representation of the PBDTTT-C-T molecule.

further purification. Data regarding molecular weight and the number of repeat units are listed in table A.1 in appendix A.2.

10.1.6 PEDOT:PSS

PEDOT:PSS (illustrated in scheme 10.6) is a hole conducting polymer mixture typically dispersed in water. One of the most prominent applications of this material is the coating of photographic films for antistatic purposes by *Agfa-Gevaert N.V.*. The latter is also the manufacturer of PEDOT:PSS. Depending on the application, PEDOT:PSS is available in different conductivity grades and with different pH and thus acidity. The latter is of importance for the interaction with other materials, e.g., etching of the ITO layer. High conductivity is crucial to avoid large sheet resistances and thus allows for fabrication of high performance OSCs or OLEDs. Additionally, the concentration of the polymer mixture within the dispersion varies and depending on the film processing technique an appropriate concentration has to be chosen.
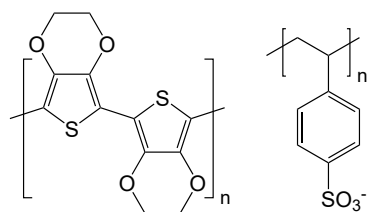
Scheme 10.6: Schematic representation of the two polymers comprised in PEDOT:PSS. The left one illustrates PEDOT while the right one is PSS.

In this thesis, different types of PEDOT:PSS are employed. The first one is a $3-4\%$ dispersion in H_2O (named PP1) already stored for few years in a closed container in a fridge. The age of the composition is important, because the PEDOT component tends to form aggregates which tend to trap holes at the PEDOT:PSS/P3HT interface and thus reduce the overall performance of the solar cells [173]. When organic solar cell research started in the frame of this thesis, the aging effects were unknown to the contributing researchers and thus the possibly denatured PEDOT:PSS was still used but, for the sake of usability, diluted with demineralized water. Later, as the overall performance remained lower than reported in the literature and with the awareness of

the acidic nature of PEDOT:PSS, a new batch of the pH-adjusted type Orgacon N-1005 (named PP2) is used. 18 months later, PP2 is replaced by Orgacon HIL-1005 (named PP3) because the former was also suspected to be aged. The type was changed, because the data provided by the distributor of Orgacon HIL-1005 promised a better performance in organic solar cells and the acidity of was no longer of importance and thus neglected because the cells are short-lived in general.

The findings by Namkoong et al. [173] that revealed the possibility to recover the performance of PEDOT:PSS were unknown when the experiments were carried out. Therefore, the testing of different types of PEDOT:PSS was not avoided. In addition, as reported by the authors, the polymer composition is very sensitive to the recovery process itself and thus this is another setscrew in organic solar cell research.

The multiplicity of PEDOT:PSS allows also for electrode fabrication without ITO or other metals. Especially if inverted solar cells are considered, a transparent PEDOT:PSS layer on top of the cell supports the ambitions for lightweight, purely organic, and flexible solar cells. Very recently, Y. Wang et al. [174] developed a transparent, stretchable, and conductive film on the basis of PEDOT:PSS that provides conductivities in the range $1 \times 10^1 - 1 \times 10^4\,\mathrm{S\,cm^{-1}}$ depending on the strain applied.

10.1.7 Energy levels and absorption spectra

The following two figures 10.5 and 10.6 illustrate the HOMO and LUMO levels of the applied materials as well as the absorption spectra in solution. The data of the energy levels are either taken from the manufacturers' or dealers' websites or from publications that are related to the materials, respectively. If values of an energy level differ between different references or an energy range is provided, the corresponding mean value is given in figure 10.5. The energy levels clearly indicate a tendency to smaller HOMO–LUMO
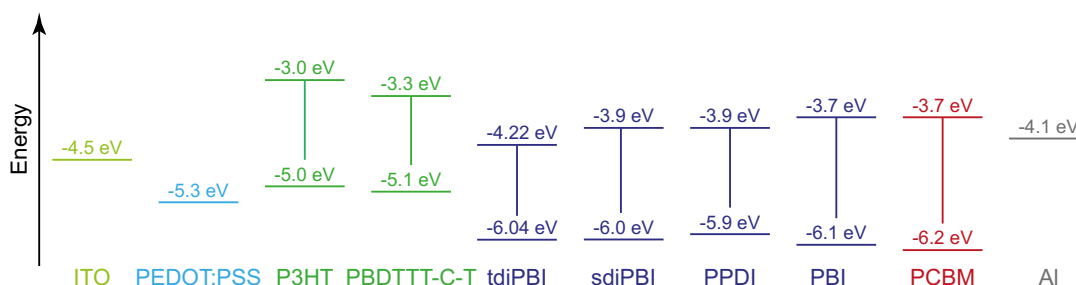
Figure 10.5: Energy levels of OSC materials employed in this work. From left to right: anode materials ITO [175, 176] and PEDOT:PSS [177, 178]; acceptors: tdiPBI [162], sdiPBI [159], PPDI [179, 180], PBI [118, 167], and PCBM [181]; donors: P3HT [182] and PBDTTT-C-T [172]; cathode: Al [183].

gaps allowing also absorption of light at longer wavelengths beyond the blue and green part of the spectrum. Highly ordered, crystalline P3HT absorbs in the red region of the spectrum. This is only valid for the real system typically consisting of P3HT and PCBM with sufficient high degree of order of the polymer. Considering figures 9.6 and 9.7, this seems to be the case for typical films of this composition within a BHJ. However, this effect has to be kept in mind because torsional-limited subchain lengths are assumed

to also occur in other polymers. Consequently, a large difference between spectra of solutions and thin films is expected. To determine the influence of torsion on polymers like PBDTTT-C-T, techniques applied to P3HT must be also applied find out how being tuned regarding their morphology.

Setting the energy levels of P3HT and PBDTTT-C-T in relation with their absorption spectra in solution as presented in figure 10.6, the difference of only 0.2 eV is not mirrored in the spectra. As expected, the spectrum of P3HT is obviously blue-shifted. In turn, PBDTTT-C-T is already absorbing at wavelengths that are below the HOMO–LUMO gap. This indicates, that the the polymer is highly ordered if dissolved and enables absorption below the "nominal bandgap" found in the references. The explanation sounds reasonable because highly ordered P3HT absorbs photons with less energy than the referenced energy gap suggests. Additionally, the referenced values of the HOMO–LUMO distances strongly depend on the way they were determined and thus the state and morphology of the materials. It is well known that there are several different gap energies for P3HT in the literature. The reason for these ranges as well as the absorption of photons with less than the gap energy lies in the existence of several vibrational states that are present. If absorption starts from such a level, the energy can be lower than the distance between HOMO and LUMO levels.
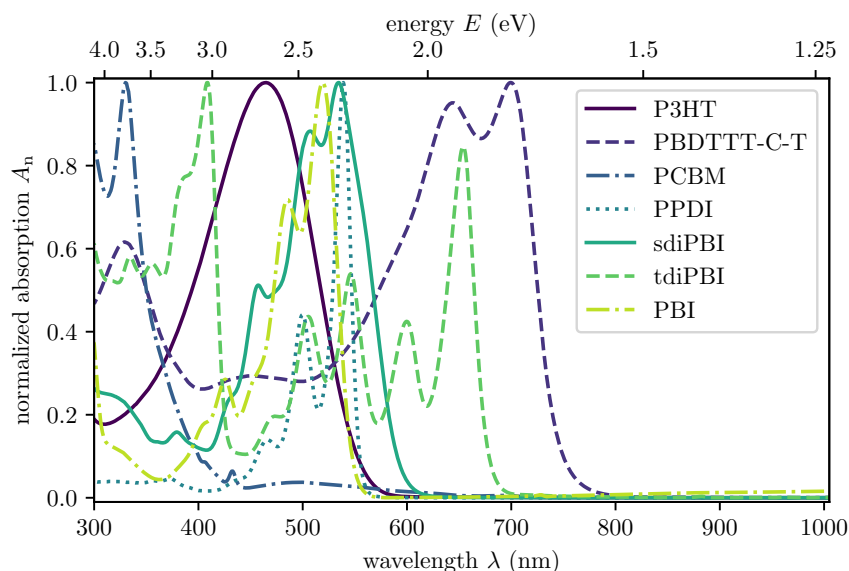
Figure 10.6: Normalized absorption A_n spectra of active layer components in solution.

In case of the acceptor materials, there is no large impact caused by the morphology because dimer materials fallback to an absorption spectrum similar to their monomeric building blocks. Considering the spectra PPDI and sdiPBI, this becomes particularly obvious. Regarding their location of the peak positions, both are quite similar to each other and to the spectrum of the PBI monomer. As already stated, the explanation can also be found in the twist and thus monomeric behavior. Additionally, the doubly-linked diperylene bisimide (ddiPBI) is twisted by about 90° and consequently provides absorption features similar to its monomeric counterpart (cf. figure 2 in [82]). Only the very rigid triply-linked diPBI is planar enough to provide additional absorption features

in the red region of the spectrum while keeping also the peaks of the monomer. As a further addition, tdiPBI provides extended absorption in the blue-to-UV part of the spectrum.

Compared to PCBM, all of the introduced perylene derivatives are superior if absorption of visible light is considered. The energy gap of PCBM indicates that absorption starting from $2.5\,eV$ ($\approx 500\,nm$) occurs. In this region, only a very broad peak with low intensity can be observed. The main contribution of PCBM's absorption arises in the deep blue-to-UV region of the spectrum.

Finally, if only the energy levels are considered, PCBM seems to be partially suited for application in organic solar cells. However, absorption spectroscopy reveals again that there are other materials, i.e., perylene derivatives, that seem to have the potential to replace the the common application of PCBM and its derivatives and relatives.

A drawback of the employed solar cell configuration can be the small difference of the perylenes' LUMO level and the work function of the aluminium electrode. Especially considering tdiPBI, the electron transfer from the active layer to the electrode is probably hampered and a different configuration of the back electrode is desirable. Due to the employed thermal evaporator, operated under ambient conditions, multilayer films consisting of different metals are hard to realize because the chamber has to be opened if the source material is changed. As a consequence, chemical reactions with oxygen, moisture, or other ambient influences would inevitably lead to rapid aging of the electrode material and as a result to low performance of the solar cells. The examinations in the following sections will enlighten the performance of organic solar cells in more detail.

10.2 Solar cell prototypes and and their performance

In order to characterize several organic solar cells based on different compositions and under different conditions, multiple cells are fabricated with the techniques described above. In order to have a reference composition, also PCBM:P3HT-based cells are synthesized. Additionally, different evaporation techniques are tested, i.e., evaporation is carried out from top to bottom or vice versa. Both techniques lead to working cells. However, it cannot be clearly distinguished whether one approach works better than the other one. Furthermore, also the age and the type of the employed PEDOT:PSS plays a crucial role.

10.2.1 Reference compostion: P3HT:PCBM

In order to develop a procedure for organic solar cell preparation for the available setup, the reference composition made of P3HT and PCBM based on a standard ratio of 1:1 is prepared. Basic information about the processing parameters as well as the resulting parameters are summarized in table 10.1.

Two examples for current densitiy-voltage (J-V) characteristics of working solar cells on the PCBM:P3HT-basis are provided in figure 10.7. The curves determined with and without illumination for samples SP3P1 and SP3P2 clearly provide the typical shape that is described in chapter 9. Deviating from the previously described sample layout,

Table 10.1: Specifications and processing parameters of working P3HT:PCBM samples. Sample SP3P6 is listed multiple times because the characterization is repeated for different ages of the sample (0 h, 25 h, 43 h and 79 h).

Sample	Ratio	Solvent	ρ (mg mL^{-1})	HTL	P3HT batch	$\nu_{\mathrm{SP,BHJ}}$ (s^{-1})	$t_{\mathrm{SP,BHJ}}$ (s)	$T_{\mathrm{an,BHJ}}$ (°C)	$t_{\mathrm{an,BHJ}}$ (min)	PCE (%)	FF (%)	V_{oc} (V)	J_{sc} (mA cm^{-2})
SP3P1	1:1	ODCB	30	PP1	1	20	120	140	10	2.50	52.3	0.49	9.71
SP3P2	1:1	ODCB	30	PP1	1	20	120	120	10	2.05	46.9	0.47	9.24
SP3P3	1:1	ODCB	30	PP3	1	20	120	130	8	0.25	23.4	0.48	2.17
SP3P4	1:1	ODCB	30	PP3	2	20	120	130	8	0.99	40.1	0.53	4.61
SP3P5	1:1	ODCB	30	PP2	2	20	120	130	8	0.02	11.3	0.51	0.41
SP3P6	1:1	ODCB	30	PP3	2	20	120	130	8	0.96	36.4	0.57	4.68
SP3P6	1:1	ODCB	30	PP3	2	20	120	130	8	0.19	23.0	0.56	1.47
SP3P6	1:1	ODCB	30	PP3	2	20	120	130	8	0.02	13.9	0.57	0.29
SP3P6	1:1	ODCB	30	PP3	2	20	120	130	8	6.3×10^{-5}	18.8	0.13	0.003

these are prepared as single cells per substrate and with relatively large electrodes that are similar to those of the photorefractive composites in part II. The reason for the different electrode layouts is the fabrication prior to the development of the electrode mask introduced earlier. Anyhow, the mask size used for sample illumination reduced
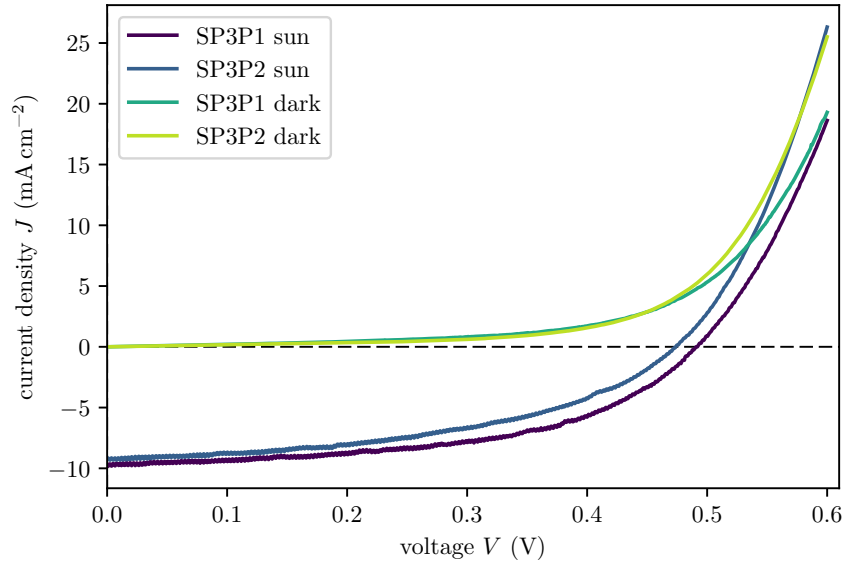
Figure 10.7: *J-V* characteristics of the BHJ organic solar cells SP3P1 and SP3P2, both based on a composition of PCBM:P3HT.

the active area to dimensions that are comparable to the layout introduced previously. Consequently, the dark currents are larger in these samples and they are more sensitive to defects in the active layer leading to short circuits. The determined parameters listed in table 10.1 are in the range of lower ones reported in the literature for this kind of composition. Most of the cells providing better performance are equipped with an additional electrode layer between BHJ and aluminium. Thus, these samples can be considered as comparably good reference cells for the employed setup.

In contrast, the characteristics displayed in figure 10.8 originate from samples that are prepared by the routine described previously and different batches of PEDOT:PSS and P3HT are employed to visualize the effect of aged components. Despite the fact that the crucial parameters are lower than the ones of samples SP3P1 und SP3P2, aged PEDOT:PSS seems to play a very crucial role in solar cell performance. However, as already mentioned, the age of PP1 is unknown and this batch provided good performance in SP3P1 and SP3P2, thus there seems to be also an impact on the specific type of PEDOT:PSS and its aging sensitivity. The effect of the fresh P3HT batch is of smaller importance compared to the fresh PEDOT:PSS as the data indicate. Nevertheless, the performance is four times lower compared to the sample comprising both materials from new batches. Additionally, the open-circuit voltages V_{oc} of these three samples are very similar. An effect avoiding the charge extraction can be assumed. One effect can be caused by the aggregated PEDOT:PSS reported by Namkoong et al. [173].

10.2.2 Stability considerations: Degradation of P3HT:PCBM cells

Another issue related to organic solar cells processed and stored under ambient conditions is degradation caused by moisture and oxygen. This degradation mainly influences the properties of the polymeric compounds as mentioned earlier and evaluated by Hintz et al. [22]. Figure 10.9 illustrates the change of the current-voltage characteristics at different
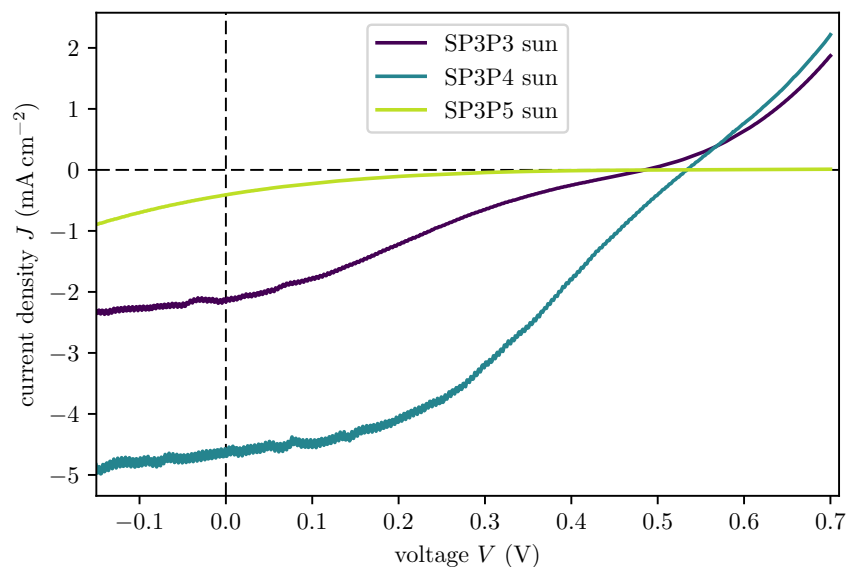
Figure 10.8: *J-V* characteristics of the BHJ organic solar cells SP3P3, SP3P4 and SP3P5, both based on a composition of PCBM:P3HT.

degrees of aging. Between the characterization steps, the sample is stored under ambient conditions and no special treatment is applied. Again, the processing parameters as well as the obtained performance measures are depicted in table 10.1. The open-circuit voltage remains almost constant around 0.55 V (except of the last measurement). In turn, the current density and thus the PCE dramatically decrease. The decrease of the
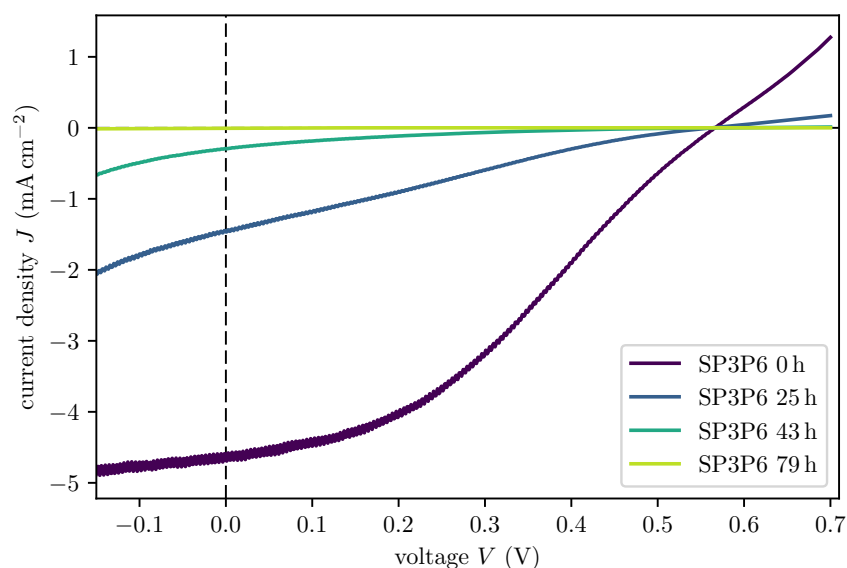
Figure 10.9: Aging effect of the *J-V* characteristics of the SP3P6 sample after several hours of storage in ambient conditions.

fill factor FF also indirectly monitors the efficiency drop because the current-voltage characteristics gets a more and more linear shape also indicating that not only less charges are produced but also shunt and series resistance have changed (cf. equation (9.1) and [154]). Due to the fact that the V_{oc} remains almost stable, the larger impact is induced by the series resistance and thus by the aluminium electrode. The latter is highly sensitive to oxidation and consequently to the formation of the insulating aluminium oxide Al_2O_3. These oxide layers typically reach a thickness of several nanometers which strongly depends on ambient conditions. Oxygen leads to a constant and comparably thin amorphous film of Al_2O_3 (about $1\,nm$). In addition, moisture leads to hydration and consequently to a thicker system comprised of hydrated and pure Al_2O_3 on top of the remaining aluminium [184]. Terminal oxide layer thicknesses are in the range of few tens of nanometers formed during timescales that reach from hours to years. Additionally, other substances like ozone, NO_2, SO_2 increase aluminium degradation [185]. Furthermore, degradation products from the active layer may also react with the aluminium.

A strong decrease of the shunt resistance necessarily leads to a drop of the open-circuit voltage and thus also to large currents above the voltage axis that are obviously not present in figure 10.9. Instead of this, the characteristics becomes flat and approaches to the voltage axis.

In order to determine the underlying effects, more detailed studies of the aged cells and the resulting cell condition are needed. Due to the fact that there are multiple effects that can occur simultaneously, a separated analysis of the single effects in a complete cell is the only way to find out what reduces the solar cells' performance. If only films of the single materials are characterized, the results can only provide hints to deterioration of the single materials but the interplay of all components is neglected. Additionally, PCE monitoring combined with fitted decay functions that include one or more parameters could hint to certain time constants. These time constants point to certain numbers of influences. Therefore, material analysis of the electrodes and active layer enables to develop control mechanisms over the aging effects.

The most common technique to inhibit degradation is encapsulation of the cells. For this purpose, typically a thin sheet of glass is glued to the coated side of the cell and thus avoiding influences of ambient influences when the cell is taken out of the typically employed protective atmosphere of nitrogen.

Throughout the characterization of all samples it turned out that none is stable at all and the PCE vanished after several hours. In order to provide a half-life for the samples without relating it to any specific effect within the cell the typical decay function

$$\eta_{PCE}(t) = \eta_{PCE,0} \exp\left(-\lambda_{dec}t\right) \tag{10.1}$$

for half-life determination via $t_{1/2} = \ln\left(2\right)/\lambda_{dec}$ is fitted to the PCE data of the different characteristics where t is the time, λ_{dec} the decay rate of the PCE, and $\eta_{PCE,0}$ the initial PCE of the cell.

For the characteristics in figure 10.9, the half-life is about $t_{1/2} = (10.2 \pm 0.2)\,h$. Other cells of the same substrate and thus the same processing conditions exhibited half-lifes in the range $t_{1/2} = 6-17\,h$. Since all cells provide efficiencies in the range $0.70-1.00\,\%$,

there is no clear tendency for more efficient cells to degrade faster. The quantities with a relation to each other are half-life and fill factor. This is concluded from the observation that cells with higher fill factors degrade faster. Additionally, this supports the assumption that oxidation of aluminium electrodes or effects within the active layer play a crucial role because series and shunt resistance seem to have changed.

10.2.3 Monomeric perylene bisimide as acceptor

Regarding to its molecular mass (cf. table A.1 in appendix A.2) and main peak position of the absorption spectrum (cf. figure 10.6, visible part), PBI is very similar to PCBM. In contrast, absorption in the visible part of the spectrum at comparable dye concentrations is much stronger in case of PBI and consequently is assumed to be the case in organic solar cells.

The employed processing parameters and the achieved performance data are listed in table 10.2. Sample SP3B1 is characterized with a mask of size $1.9 \times 6.5\,\mathrm{mm^2}$ applied, whereas the other samples are analyzed without a mask and thus the PCE cannot be determined. Figure 10.10 displays the current-voltage characteristics in the dark and

Table 10.2: Processing parameters and characterized quantities of P3HT:PBI samples. Here, $\nu_{\mathrm{SP,BHJ}}$ refers to the spin coating speed, $t_{\mathrm{SP,BHJ}}$ to the coating duration, $T_{\mathrm{an1,BHJ}}$ to the pre- and $T_{\mathrm{an2,BHJ}}$ to the postannealing temperature, whereas $t_{\mathrm{an1,BHJ}}$ and $t_{\mathrm{an2,BHJ}}$ denote the annealing durations.

Sample	SP3B1	SP3B2	SP3B3	SP3B4
Ratio	1:1	1:1	1:1	1:1
Solvent	$CHCl_3$	$CHCl_3$	$CHCl_3$	$CHCl_3$
ρ $(\mathrm{mg\,mL^{-1}})$	30	30	30	30
HTL	PP1	PP1	PP1	PP1
P3HT batch	1	1	1	1
$\nu_{\mathrm{SP,BHJ}}$ $(\mathrm{s^{-1}})$	20	20	20	20
$t_{\mathrm{SP,BHJ}}$ (s)	120	120	120	120
$T_{\mathrm{an1,BHJ}}$ (°C)	50	50	50	–
$t_{\mathrm{an1,BHJ}}$ (min)	10	10	10	–
$T_{\mathrm{an2,BHJ}}$ (°C)	–	–	50	–
$t_{\mathrm{an2,BHJ}}$ (min)	–	–	10	–
PCE (%)	1.4×10^{-5}	–	–	–
FF (%)	17.5	–	–	–
V_{oc} (V)	0.28	0.42	0.07	0.18
J_{sc} $(\mathrm{mA\,cm^{-2}})$	0.03	9 µA	1 µA	0.7 µA

in the illuminated case. It is clearly visible that the absolute value of the photocurrent density drops rapidly before becoming linear. Consequently the fill factor is very low (17 %) and so is the power conversion efficiency. Additionally, also the other crucial parameters V_{oc} and J_{sc} stay significantly below the values obtained for the P3HT:PCBM composition. Despite several processing parameters themselves including spin-coating speeds, durations, etc. are tested, it is impossible to achieve higher efficiencies based on this composition under the current processing conditions. The dependency on the
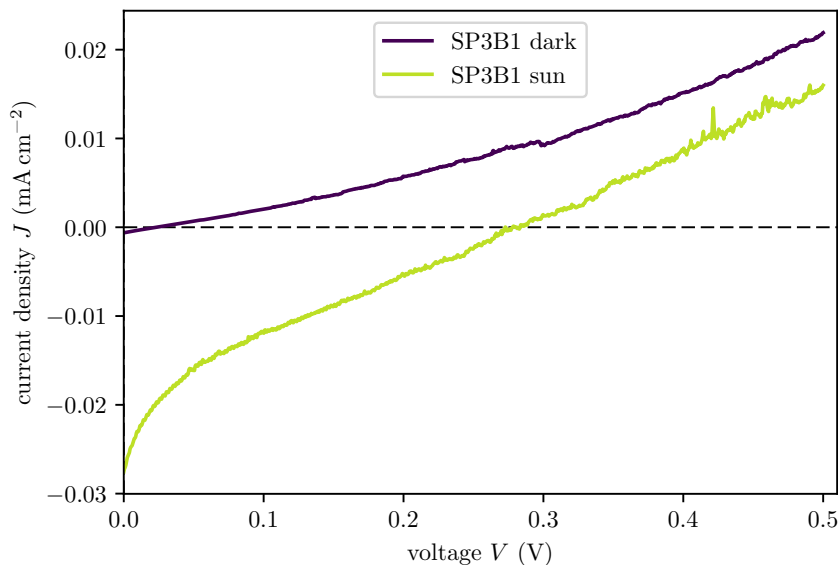
Figure 10.10: *J-V* characteristics of the P3HT:PBI sample SP3B1 with and without illumination.

annealing process and whether this step has to be carried out prior or post application of the aluminium electrode is tested and analyzed separately. Since the obtained currents are too low to be measured when a mask is applied, the mask is left out in this test and the resulting characteristics are provided in figure 10.11. Consequently, the current density cannot be calculated and this also holds for the PCE and FF. Despite the missing parameters that describe the cells' efficiencies, the figure provides clear evidence that the preannealing step is beneficial to the performance. In turn, missing annealing or an additional postannealing step are detrimental to the achieved currents and therefore the strategy that has been initially followed to produce sample SP3B1 is the best.

Anyhow, the performance of all characterized cells remains significantly below the reference system and thus PBI is not considered to be an appropriate alternative in combination with P3HT. The reasons why PBI-based cells perform so badly remains unclear but is expected to be grounded on morphological issues in the active layer. This is assumed because the proximity of PBI's energy levels to those of PCBM turn PBI into be a drop-in replacement for PCBM with the beneficial aspect of stronger light absorption in the green part of the spectrum and thus broader coverage. From an energy level perspective, there is no explanation for the behavior.

The morphological reason for the low performance is stacking of the PBI molecules and thus formation of large domains that break the charge separation capabilities. Additionally, the relative position of the PBI molecules to the P3HT chains is important. If the distance of both moieties is too large, charge separation is hindered. Other intrinsic effects can lead to geminate or bimolecular recombination and therefore reduce the current [186]. A further aspect includes the connection between PBI and the electrode materials. Positional misalignment can hamper charge extraction and consequently reduce the PCE. Studies of OFETs with a similar perylene bisimide having slightly
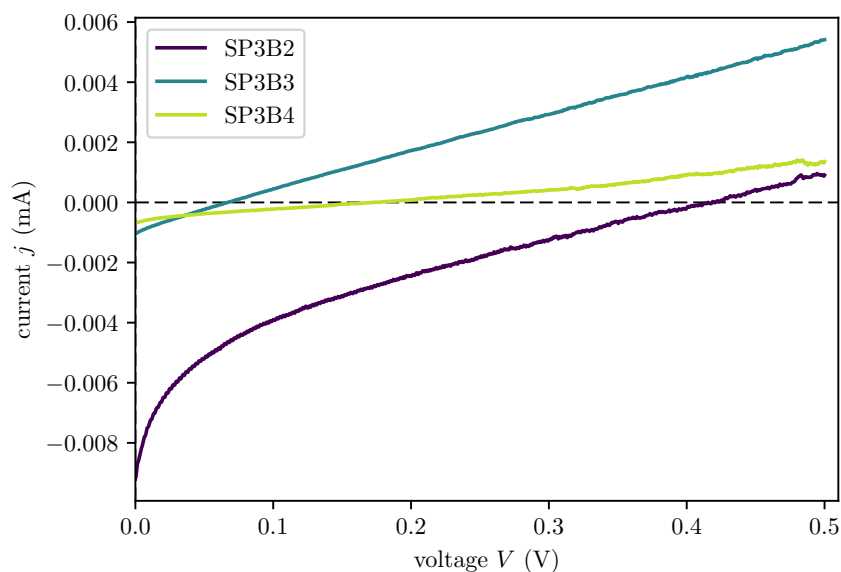
Figure 10.11: Current-voltage characteristics of three P3HT:PBI samples with different annealing treatments. Sample SP3B2 is only annealed prior to aluminium coating, while SP3B3 is heated prior and post electrode deposition. Sample SP3B4 is not annealed at all. Due to the low currents, characterization is carried out without mask and thus the current instead of the current density is given.

shorter chains in the imide positions (C_7H_{15}) showed that the performance was also lower than the performance of molecules where the imide chains are substituted by C_7F_{15} [187]. In that study, interaction with ambient conditions due to larger stacking distances is attributed to the lower conductivity and the observed aging. Additionally, the light sensitivity is lower in the non-flourinated molecule. In turn, suitable substituents can tune PBI's properties in a direction allowing for highly efficient solar cells.

10.2.4 Triply-linked diPBI as acceptor

As its monomeric sibling, also the triply-linked 12C-4CldiPBI is employed as an acceptor in organic solar cells and forms the active layer in combination with P3HT. The processing procedure is similar to the PBI containing samples except that only one preannealing step is carried out. Furthermore, both active-layer components are dissolved in different solvents since tdiPBI provides better solubility in $CHCl_3$ and the best performance of P3HT is achieved if it is dissolved in ODCB. Consequently, the active-layer ink contains a mixture of both solvents. Since tdiPBI is not completely insoluble in ODCB separation of both components is not expected during solvent evaporation. All processing parameters as well as the determined V_{oc} and short-circuit current j_{sc} are listed in table 10.3. Characterization of several P3HT:diPBI samples reveals that all of them provide low performance and that changes to various processing parameters do not result in significant enhancements. Like in the case of PBI with different annealing procedures, the obtained photocurrents are too low to perform characterization with an applied mask. Consequently, only V_{oc} and j_{sc} can be determined from the characteristics. Figure 10.12

Table 10.3: Processing parameters and characterized quantities of P3HT:tdiPBI samples.

Sample	SP3D1
Ratio	1:1
Solvent	ODCB (P3HT), CHCl$_3$ (tdiPBI)
ρ (mg mL^{-1})	30
HTL	PP1
P3HT batch	1
$\nu_{\text{SP,BHJ}}$ (s^{-1})	20
$t_{\text{SP,BHJ}}$ (s)	120
$T_{\text{an,BHJ}}$ (°C)	50
$t_{\text{an,BHJ}}$ (min)	10
V_{oc} (V)	0.03
j_{sc} (µA)	1.4

exemplarily illustrates the characteristics of the sample denoted in table 10.3. Obviously,
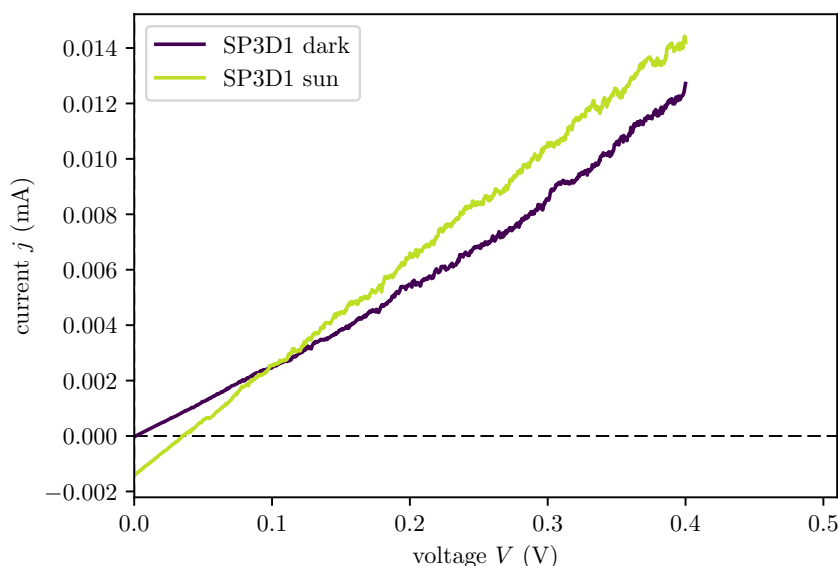
Figure 10.12: Current-voltage characteristics of the P3HT:diPBI sample SP3D1 with and without illumination.

dark- and photocurrent are both linear and thus a completely ohmic behavior of the sample is assumed. As mentioned previously, linear current-voltage curves are induced by low shunt and high series resistances. Thus, the cell's characteristics look like as if both electrodes are shorted. Additionally, the low current indicates that the series resistance is also large enough too keep the current in the µA range.

Considering the energy levels in figure 10.5, it can be noticed that LUMO of tdiPBI is lower than the work function of the aluminium electrode. Thus, charge extraction might be partially suppressed while some charges are extracted as the occurrence of photocurrent clearly indicates. Additionally, the aggregation of the tdiPBI molecules

studied in section 9.2 migth play a role. However, as the main focus was not set to charge transfer and exciton separation, the modeling does not reveal the impact on these processes. Another issue that has an impact on the charge transfer and extraction is charge recombination. Lacking exciton dissociation due to the Coulomb interaction is one explanation for this effect. Recombination of free charges on their way to the electrodes is another reason [186].

Other perylene bisimide derivative dimers presented in the following subsections provide better performance in organic solar cells. These effects are attributed to a reduced tendency for stacking due to the more twisted molecular structure and additionally to the better suited donor. In case of tdiPBI also other studies revealed the performance with an optimized donor and under ideal processing conditions did not lead to PCE above 1.36 % [82]. Consequently, the tdiPBI molecule does not seem to be very suited as acceptor in organic solar cells. A different functionalization can change the performance to a certain degree but unless the tendency for stacking is not hindered, major performance gains are not expected.

10.2.5 Imide-linked PPDI and PBDTTT-C-T

Another acceptor of the perylene family is the imide-linked PPDI that is combined with the donor polymer PBDTTT-C-T to form the active layer. Tests with P3HT reveal that this combination does not provide power conversion efficiencies above a self-defined threshold value of 0.0005 %. Consequently, this composition is not considered to be relevant. Due to its twisted character, PPDI avoids stacking and thus crystallization of the acceptor material and therefore overcomes the limitations of tdiPBI and PBI [179, 188]. The reference recipe employed by Ye et al. [180] based on chlorobenzene (CB) as solvent for both components and a material ratio of 1:1 at a concentration of $15\,\mathrm{mg\,mL^{-1}}$ provides also the best results in this thesis. In contrast, the composition that employs dichlorobenzene (DCB) suffers from low performance.

Table 10.4 displays the processing parameters and obtained performance data of several PBDTTT-C-T:PPDI BHJ organic solar cells. Sample SPBPP3 provides a characteristics of the typical diode-like shape, whereas this is not the case for SPBPP1 and SPBPP2. The reason for the poor performance of SPBPP1 and SPBPP2 is considered to originate from aging effects of the active layer materials as well as the aluminium electrode. Further, the determined parameters are far below the data found in the literature. The processing conditions under ambient air and without any interlayers between the active materials and aluminium have impact on the overall performance. Consequently, the attribution of the change characteristics to aging seems reasonable. Especially the aluminium films have proven to be sensitive to processing temperature, evaporation speed and condition of the tungsten coil.

Table 10.4: Processing parameters and characterized quantities of PBDTTT-C-T:PPDI samples. All samples are prepared with a donor:acceptor ratio of 1:1 at a concentration of $\rho = 15\,\mathrm{mg\,mL^{-1}}$, while the hole transport layer is always made with PP3. Except of SPBPP7 that corresponds to all six subcells, the sample names represent only one subcell on a substrate. The performance data of SPBPP7 are the averages of all subcell with their standard deviation. Here, $\nu_{\mathrm{SP,BHJ}}$ refers to the spin coating speed, $t_{\mathrm{SP,BHJ}}$ to the coating duration, $T_{\mathrm{an1,BHJ}}$ to the pre- and $T_{\mathrm{an2,BHJ}}$ to the postannealing temperature, whereas $t_{\mathrm{an1,BHJ}}$ and $t_{\mathrm{an2,BHJ}}$ denote the annealing durations.

Sample	Solvent	$\nu_{\mathrm{SP,BHJ}}$ (s^{-1})	$t_{\mathrm{SP,BHJ}}$ (s)	$T_{\mathrm{an1,BHJ}}$ (°C)	$t_{\mathrm{an1,BHJ}}$ (min)	$T_{\mathrm{an2,BHJ}}$ (°C)	$t_{\mathrm{an2,BHJ}}$ (min)	PCE (%)	FF (%)	V_{oc} (V)	J_{sc} (mA cm^{-2})
SPBPP1	CB	25	120	–	–	–	–	0.15	27.1	0.48	1.17
SPBPP2	CB	25	120	–	–	–	–	0.14	15.3	0.48	1.82
SPBPP3	CB	25	120	–	–	–	–	0.31	36.8	0.40	2.10
SPBPP4	ODCB	25	120	–	–	–	–	0.085	38.9	0.41	0.48
SPBPP5	ODCB	25	120	130	8	–	–	6.5×10^{-4}	16.2	0.51	0.008
SPBPP6	ODCB	25	120	–	–	130	8	1.7×10^{-4}	17.8	0.32	0.003
SPBPP7	CB	20	120	–	–	–	–	0.17 ± 0.02	25.80 ± 0.04	0.53 ± 0.08	1.24 ± 0.10

As the evaporation speed and aluminium temperature are dependent on the current driven through the tungsten coil, exact reproducibility of the electrode is not guaranteed. The reason is the current that has to be adjusted manually depending on the actual evaporation rate. Additionally, the maximum evaporation time is limited to 4 min by the evaporator. Thus, the evaporation speed has to be comparatively high ($> 25\,\mathrm{nm\,min^{-1}}$) to achieve the desired thickness of 100 nm. As a consequence, the electrode may not be of sufficient quality due to the rapid film growth and additionally the active layer is exposed to unregulated annealing during the evaporation process and thus the material may degrade during electrode deposition.
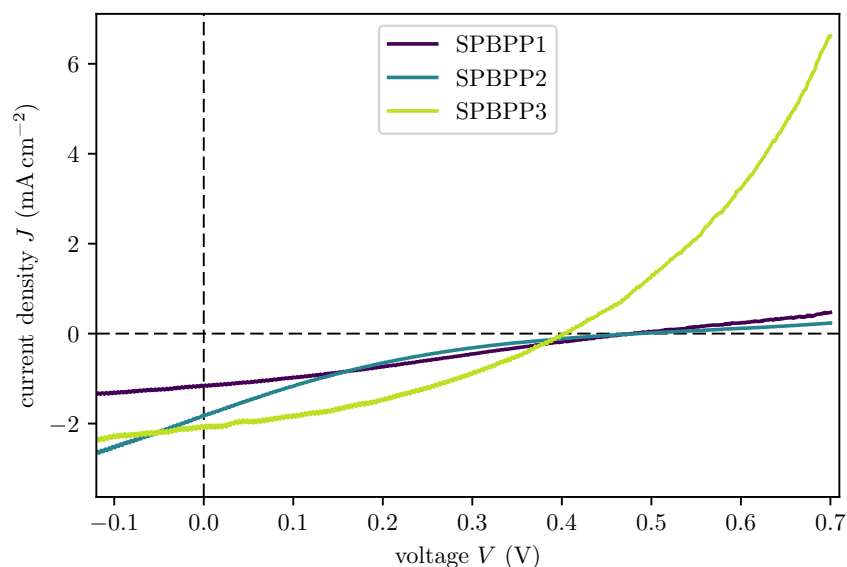
Figure 10.13: *J-V* characteristics of the PBDTTT-C-T:PPDI samples SPBPP1 – SPBPP3 under illumination.

The temperature-sensitivity is supported by figure 10.14 because SPBPP5 is pre- and SPBPP6 is postannealed (cf. table 10.4) and both samples almost behave like insulators. Thus, the heating during electrode deposition may have an impact on the cell's performance but this impact is lower than systematic heating in an annealing step. As already mentioned, the current of the evaporator has to be regulated manually and is dependent on the condition of the tungsten coil. Liquid aluminium tends to wet the tungsten coil and thus the resistance of the coil changes during operation demanding for adjustments of the current. Overregulation can lead to higher deposition rates and thus overheating of the samples. As this does not occur every time an electrode is evaporated, not all samples are overheated and thus provide normal operation. Anyhow, it cannot be excluded that these samples are aggrieved to a lower degree.

In order to characterize the influence of storage under ambient conditions on the performance of a PBDTTT-C-T:PPDI cell, repeated recording of current-voltage characteristics of all subcells of sample SPBPP7 is performed. The averaged data of all subcells of SPBPP7 with their corresponding standard deviation of PCE, V_{oc}, J_{sc}, and FF are listed in table 10.4.
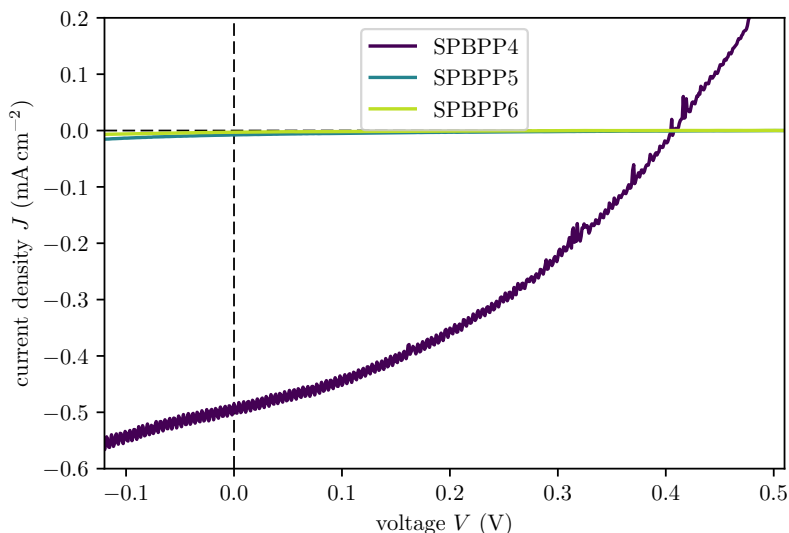
Figure 10.14: *J-V* characteristics of the PBDTTT-C-T:PPDI samples SPBPP4 – SPBPP6 fabricated with ODCB under illumination.

In contrast to the other samples listed in the table, this sample is produced with a reduced spin-coating speed. The outcome of the test series is that the concentration of $\rho = 15\,\mathrm{mg\,mL^{-1}}$ is the only one that resulted in significant performances with $\eta_{\mathrm{PCE}} > 0.005\,\%$. Also the sample with a spin-coating speed of $\nu_{\mathrm{SP,BHJ}} = 25\,\mathrm{s^{-1}}$ is not providing satisfying data and performing much worse compared to the samples before. Thus, there is a large sample-to-sample variation of the performance despite of obeying the same processing routine and consequently parameter constellations that might not seem to function may work if the procedure is repeated. As a consequence, it is hard to determine a clear direction for pushing to the right film thickness because neither concentration variations nor changes of the spin-coating parameters provided hints for performance improvements. Additionally, the results of higher efficiencies are spread over the parameter space. The reason for this behavior remains unclear but improvements can get lost in degradation effects, e.g., the already mentioned difficulties during aluminium electrode deposition or aging effects caused by the ambient conditions. Consequently, a great step towards a higher reproducibility is the change of the processing conditions to an inert atmosphere and lower evaporation rates.

The development of the PCE during the degradation measurements are depicted in figure 10.15. Subfigures 10.15(a) and 10.15(d) clearly indicate that the degradation of the PCE coincides with a reduced short-circuit current density. Considering in addition the half-lifes of both quantities in table 10.5, it can be observed that they are similar. In turn, fill factor and open circuit voltage have rather long half-lifes or are almost constant which is in coincidence with the graphs 10.15(b) and 10.15(c). Thus, the decrease of the PCEs is attributed to reduced charge generation and extraction while only minor contributions originate from the reduced open circuit voltages. The FF initially slightly decays. Subsequently, it is more or less constant or even tends to increase. The decay at the beginning is attributed to the changes of open-circuit voltage and short-circuit current density. Furthermore, the origin of the increase probably stems from error

(a) Evolution of the power-conversion efficiency of the subcells of sample SPBPP7.

(b) Evolution of the fill factor of the subcells of sample SPBPP7.

(c) Evolution of the open-circuit voltage of the subcells of sample SPBPP7.

(d) Evolution of the short-circuit current density of the subcells of sample SPBPP7.
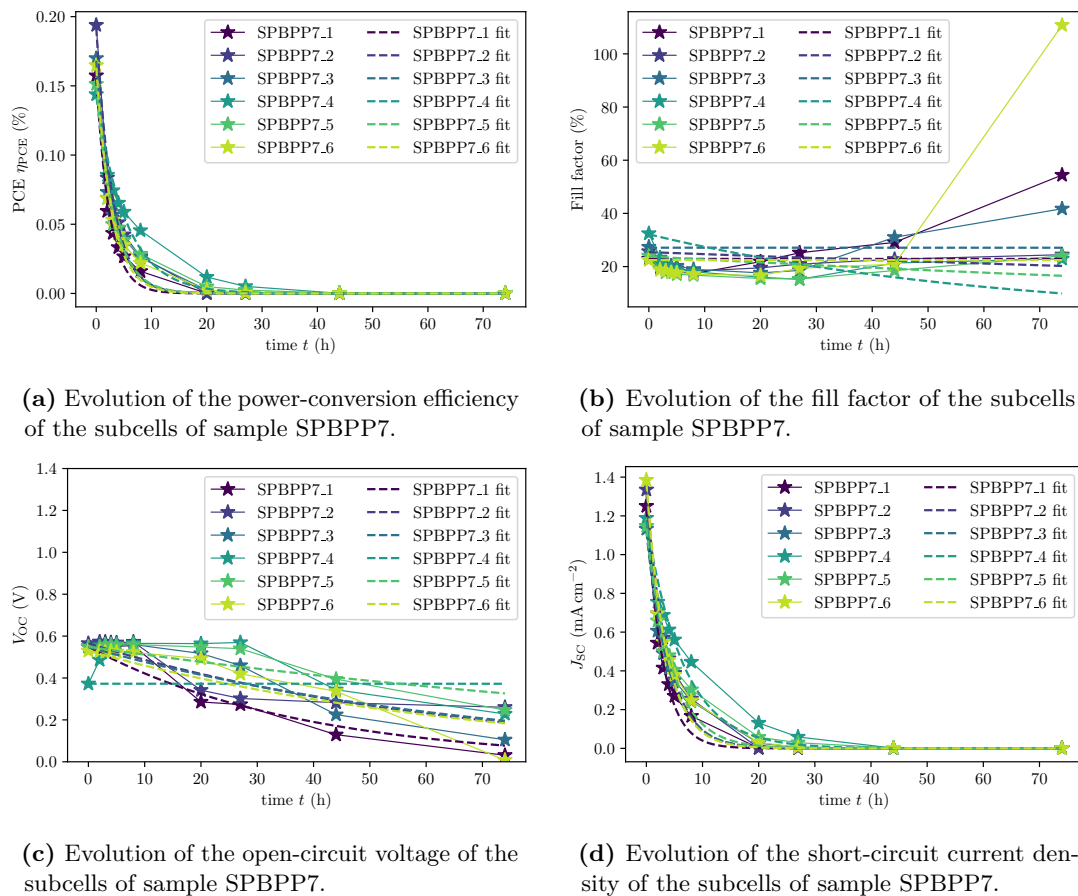
Figure 10.15: Time-dependent degradation of PCE, FF, V_{oc}, and J_{sc}.

Table 10.5: Half-lifes of crucial parameters of PBDTTT-C-T:PPDI cells. Due to the strong variation of the data from each other and because of the quality of the fits, the deviation of the single values is considered to be at least 20 %.

Sample	$t_{1/2,\mathrm{PCE}}$ (h)	$t_{1/2,\mathrm{FF}}$ (h)	$t_{1/2,\mathrm{V_{oc}}}$ (h)	$t_{1/2,\mathrm{J_{sc}}}$ (h)	$t_{1/2,\mathrm{j_{dark,0.8\,V}}}$ (h)
SPBPP7_1	1.69	–	26.12	2.02	1.20
SPBPP7_2	2.02	224.80	46.45	2.63	1.27
SPBPP7_3	2.07	–	49.90	2.77	1.26
SPBPP7_4	3.73	43.56	–	4.57	0.64
SPBPP7_5	2.23	140.91	98.75	3.14	1.24
SPBPP7_6	1.96	–	48.29	2.47	1.45

propagation of the determination of the underlying quantities that is caused by noise in the characteristics.

In order to determine the underlying effect of the performance decrease and whether it is attributed to charge generation or transport, absorption spectroscopy of the cells is carried out. Figure 10.16 depicts the spectra taken at the beginning of the characterization and after 74 h. The part of the spectrum that originates from the PPDI (cf. figure 10.6) remains almost unchanged . In contrast, the contribution of PBDTTT-C-T is dramatically reduced indicating that the material has significantly altered its properties. As already discussed in the case of P3HT, chemical reactions with moisture and air can be the reason for the degradation of the polymers. Additionally, decomposition that is induced by ambient conditions and under the influence of illumination can lead to structural changes that of course also change the physical properties. In order to determine that not only the absorption of the solar cell decreases, the dark currents are analyzed. In case of the dark current there is no fix point such as the maximum power point, short circuit-current density, or open-circuit voltage. Instead, an applied external voltage of 0.8 V is chosen as a reference. The decay of the dark current at this voltage is displayed in figure 10.17 and the corresponding half-lifes are listed in table 10.5.

As both, the plotted data and the fitted half-lifes indicate, the dark current decays much faster than the PCE and J_{sc}. Exceptionally, the subcell with the largest half-life of the short-circuit current density possesses the shortest half-life of the dark current. Nevertheless, this subcell provides a significantly higher initial dark current. The reason for this artifact is unclear but might be due to accumulated charges which are reorganized during the first characterization. Ionic contributions that elevate initial dark currents are expected to be almost similar over the whole sample and not only present for one subcell. Additionally, all other subcells provide very close data that are not spread over a larger milliampere scale.
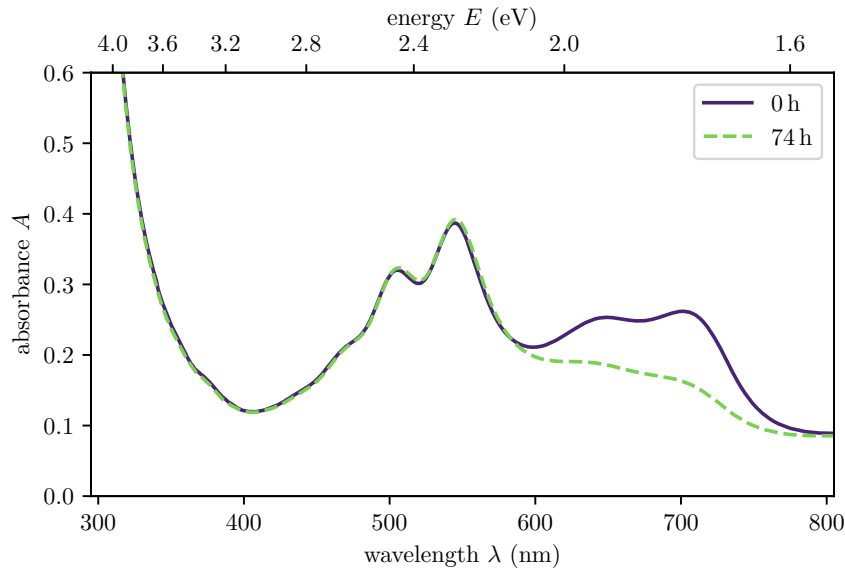
Figure 10.16: Degradation of the absorption of sample SPBPP7.
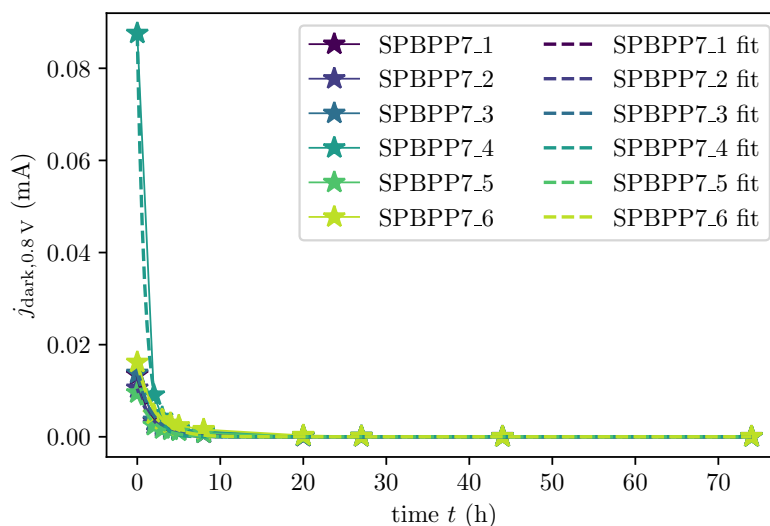
Figure 10.17: Degradation of the dark current at an applied external voltage of $0.8\,\mathrm{V}$ of sample SPBPP7. For ages larger than $10\,\mathrm{h}$, the currents only slightly vary and have reached the noise level of the measurements.

The decay of the dark currents also indicates that there is degradation of the active layer materials since the cells loose conductivity and the characteristics become more and more flat and get closer to the voltage axis. As the part of the absorption spectrum that is contributed by PPDI decreases, the performance reduction is totally attributed to PBDTTT-C-T while PPDI seems to be stable under ambient conditions for the time range the sample is characterized. Furthermore the short half-lifes indicate that the samples probably have lost a certain amount of efficiency during the cell processing because the material is almost permanently exposed to ambient influences. The only exception is the evaporation of the aluminium electrode. But, as already discussed for other solar cell types, the high evaporation rates may have an additional detrimental impact on the cells. Consequently, PBDTTT-C-T-based cells are not suited to be processed or characterized under ambient conditions without application of any protective atmosphere or encapsulation during characterization. Thus, as typically applied in organic solar cell processing, a protecting atmosphere is highly desired to determine the maximum efficiency of solar cell prototypes and to perform further studies that include photobleaching or the application of different light-trapping structures on the same cell. The latter is of importance to determine the absolute efficiency enhancement since there still might be smaller variations of the solar cells' efficiencies even under ideal processing conditions.

Additionally, from a processing perspective, materials that are stable under ambient conditions are highly desirable as they do not demand for costly processing equipment and may let the vision of home-processable cells become true. But not only these stable materials are needed. In addition, they also have to be soluble in more common and environmentally friendly solvents like ethanol, isopropyl alcohol, or even water[1].

---

1   Of course they should not dissolve when applied outside.

In the following subsection, another perylene bisimide derivative is introduced as an acceptor material. Due to the fact that PBDTTT-C-T is the donor material and the processing conditions are unchanged, the same issues as in the current case regarding stability, etc., will be present.

10.2.6 Singly-linked diPBI as acceptor and PBDTTT-C-T as donor materials

The already introduced singly-linked perylene bisimide derivative (cf. subsection 10.1.3) is employed as acceptor in organic solar cells and combined with PBDTTT-C-T as donor material. As already performed by Ye et al. [189], the cells are prepared with the solvent additives 1-chloronaphthalene (CN) and 1,8-diiodooctane (DIO), each taking $1.5\,\mathrm{vol}\%$ of the total solvent. Based on the proposed recipe, several samples are realized but the reported efficiencies are not achieved. As an example, see sample SPBSD1 in table 10.6 and figure 10.18. Also variations of the concentration, spin-coating parameters, donor-acceptor ratio, abdication of the additives, and annealing do not lead to significant improvements as the exemplary provided data of samples SPBSD2 and SPBSD3 indicate.

As for the PBDTTT-C-T:PPDI samples, the characteristics in figure 10.18 indicate several detrimental effects in the samples. SPBSD1 provides moderate J_{sc} and shape of the characteristics but has a significantly reduced open-circuit voltage compared to the other examples. SPBSD2 exhibits a quite good V_{oc} but the curve is deformed leading to a low fill factor and additionally the short-circuit current is very low. Sample SPBSD3 provides the highest measured PCE of this sample type but the short-circuit current does not achieve the value of SPBSD1. Furthermore, the current rises too fast avoiding a more rectangular shape of the characteristics and thus significantly reducing the fill factor and efficiency. Anyhow, the enhanced V_{oc} compensates the reduced short-circuit current and thus is the origin of the enhanced efficiency. The low open-circuit voltage in the sample

Table 10.6: Processing parameters and characterized quantities of PBDTTT-C-T:sdiPBI samples. Here, $\nu_{\mathrm{SP,BHJ}}$ refers to the spin coating speed, $t_{\mathrm{SP,BHJ}}$ to the coating duration, $T_{\mathrm{an,BHJ}}$ to the preannealing temperature, whereas $t_{\mathrm{an,BHJ}}$ denotes the annealing duration.

Sample	SPBSD1	SPBSD2	SPBSD3
Ratio (PBDTTT-C-T:sdiPBI)	1:1	1:1	1:0.5
Solvent	CB:CN:DIO	CB	CB:CN:DIO
ρ $(\mathrm{mg\,mL^{-1}})$	15	25	20
HTL	PP3	PP3	PP3
$\nu_{\mathrm{SP,BHJ}}$ $(\mathrm{s^{-1}})$	25	20	20
$t_{\mathrm{SP,BHJ}}$ (s)	120	120	120
$T_{\mathrm{an,BHJ}}$ (°C)	130	–	–
$t_{\mathrm{an,BHJ}}$ (min)	8	–	–
PCE (%)	0.178	0.037	0.207
FF (%)	33.9	14.1	29.2
V_{oc} (V)	0.27	0.57	0.46
J_{sc} $(\mathrm{mA\,cm^{-2}})$	1.94	0.47	1.53

is probably caused by a too low shunt resistance that in turn is the result of a low film thickness that is observable by the naked eye easily identifying low absorbance. Also
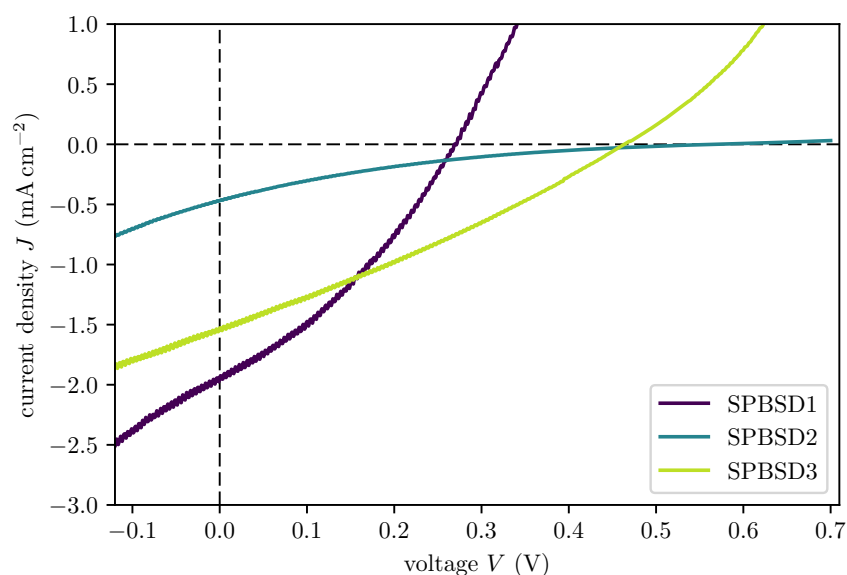
Figure 10.18: *J-V* characteristics of the PBDTTT-C-T:sdiPBI samples SPBSD1 to SPBSD3.

the low photocurrents may result from low film thicknesses since the active-layer inks containing the additives dry very slowly and thus are very sensitive to the spin-coating parameters. The low solvent evaporation rates are especially attributed to CN because of its high boiling point (cf. table A.2 in appendix A.3). Exactly this behavior has led to the approach to avoid the additives to create larger film thicknesses but as SPBSD2 indicates, achieved data are worse compared to the samples containing additives. As a consequence, the only possibility to increase the film thickness is the application of higher concentrations and lower spin-coating speeds. This ansatz generally results in a slightly enhanced efficiency as exemplary demonstrated by sample SPBSD3. Here, the ratio of PBDTTT-C-T:sdiPBI is varied between 0.5:1 and 1:0.5 but the determined performance data do not hint to an optimized composition. Samples SPBSD1 and SPBSD3 provide similar PCE despite the totally different composition of the active layer. This behavior holds as well for other tested ratios. Consequently there is either a very broad acceptance region for different ratios or the variation between the tested ratios is too large and a composition with an optimized PBDTTT-C-T:sdiPBI is not found. Another reason is the already discussed sample-to-sample variation. It avoids systematic analysis of this kind of dependency to some extend because it demands for a large amount of fabricated cells of the same type to possibly find the most efficient configuration. However, even large numbers of prepared samples do not guarantee to identify the ideal composition. This is due to the ambient processing conditions which degrade the samples' performance.

The general stability of the PBDTTT-C-T:sdiPBI samples seemed to be very short compared to the case of PPDI as acceptor. A detailed degradation analysis is omitted due to the fact that the processing conditions cannot be changed and thus it is not expected that the application of sdiPBI would lead to significantly longer half-lifes.

10.3 Differences between theoretical open-circuit voltage and obtained data

The short-circuit current j_{sc} or the short-circuit current density J_{sc} strongly depend on the incident amount of light and the subsequent processes of absorption, exciton formation, exciton separation, charge transfer and charge extraction. The open-circuit voltage theoretically depends on other quantities. A first guess leads to the assumption that it is mainly influenced by the work function of the electrode materials. This is not true as studies by C. J. Brabec et al. [190] reveal. In contrast, the V_{oc} is mainly steered by the energetic difference of the acceptor's LUMO and the donor's HOMO level $\Delta E_{A,D} = |E_{D,HOMO}| - |E_{A,LUMO}|$ and thus regarding to Scharber et al. [61] the dependency

$$V_{oc} \leq \frac{1}{e} \left(|E_{D,HOMO}| - |E_{A,LUMO}| \right) - 0.3\,\text{V} \tag{10.2}$$

holds. Here, e denotes the elementary charge and the $0.3\,\text{V}$ is a correction with empirical origin. Consequently, an upper limit of the open-circuit voltage can be directly estimated from the molecules comprised in the active layer. The empirical correction results from the dark current-voltage curve of the cell, i.e., the diode that is determined by the ideality factor and the reverse dark current. An additional contribution originates from the fact that the photocurrent in BHJ cells is mainly field-driven [61].

If the estimates of the V_{oc} are compared to determined data of the realized cells (cf. table 10.7), it can be observed that the estimates are dramatically larger.

Table 10.7: Estimated and maxima of the determined open-circuit voltages V_{oc}.

Composition	Est. V_{oc} (V)	Max. det. V_{oc} (V)
P3HT:PCBM	1.0	0.57
P3HT:PBI	1.0	0.42
P3HT:tdiPBI	0.48	0.03
PBDTTT-C-T:PPDI	0.9	0.51
PBDTTT-C-T:sdiPBI	0.9	0.57

These discrepancies are attributed on the one hand to loss mechanisms like internal recombination [191] and on the other hand to too low film thicknesses as in the case of the PBDTTT-C-T:sdiPBI cell SPBSD1. Vandewal et al. [191] have created a theoretical model to describe the dependencies of V_{oc} on different conditions and among other things they also name explicitly the processing conditions like stoichiometry alterations and annealing. These processing conditions would lead to spectral shifts of the charge-transfer bands and thus alter the V_{oc}. As a consequence, processing has to be optimized not only with respect to obtain larger photocurrents but also for an enhanced open-circuit voltage because it does not only depend on the energy levels of the contributing molecules in their original, uninfluenced shape but strongly from the morphology of the active layer.

11 Resume on organic solar cell processing under ambient conditions

Several different compositions of organic bulk heterojunction (BHJ) solar cells were characterized in this part of the thesis. They are all processed on ITO-coatad glass substrates equipped with an additional hole-transporting and electron-blocking layer of PEDOT:PSS. Although the type of the PEDOT:PSS is changed throughout different sample generations, the type does not seem to have large impact on the samples' performance. In contrast, the age of the PEDOT:PSS batch seems to be of larger importance because the material tends to form aggregates. Additionally, different treatments of the PEDOT:PSS are carried out. These are in detail dilution in deionized water, ethanol, or isopropyl alcohol of PP1. This step is necessary because the concentration is considerably high. Without dilution, rather rough and thick films with visible islands form. The dilution leads to improved film quality and consequently to a higher cell performance. Employing the other PEDOT:PSS batches, the dilution step is not necessary and the material is applied purely. Dilution is tested with these batches as well but the cells do not provide any significant performance enhancement. As a consequence, different types of PEDOT:PSS must be tested regarding their processability and influence on the solar cell performance[1].

Age-dependent behavior of the performance is observed in the case of P3HT. An older batch provides slightly lower performance. The reason is not only attributed to the age itself but rather also to chemical degradation of the material in the storage container. This degradation is due to the exchange with ambient air during the production of a new donor solution. Compared to the film processing, the amount of time when the container is opened and the amount of air that is exchanged is rather low. Therefore, the degradation speed is much lower during solution fabrication. This behavior is similar to the case of PBDTTT-C-T although the degradation in the container of this material might be even faster than P3HT.

The sensitivity of the perylene derivatives to ambient conditions is much less compared to the donor materials. They provide at least similar absorption spectra in thin films in the time range of observation. Especially diPBI has proven its stability when employed in photorefractive composites [74, 76]. Thus, the perylene derivatives are considered to be employed in organic solar cells or other optoelectronics devices without need of further encapsulation. In general the aging of the donor is much faster. If there is degradation of the perylene derivatives, it cannot be completely excluded but is of minor importance until more stable donors are developed.

In general, PBI and its derivatives performed worse compared to PCBM. This behavior is attributed to the application of donor materials that are not optimized for this kind of

---

1 This fact is also supported by private communication with Long Ye during a stay in his lab in September 2014. Long Ye is an expert in the field of organic solar cell fabrication in the group of Prof. Jianhui Hou, Institute of Chemistry, Chinese Academy of Sciences, Beijing, P.R. China.

acceptors, i.e., perylene derivatives. Until PBIs have come back into the scientists minds as possible replacement for PCBM, most of the employed donors are optimized to be combined with the prominent fullerene derivative. PBDTTT-C-T is more suited to work with perylene derivatives. This is a result of the strong efforts in the development of novel donors that are even better suited. Especially the concept of copolymerization is very promising because PBDTTT-C-T and other members of its family already provide an outstanding performance in organic solar cells [159, 160, 180]. Under optimized processing conditions combined with appropriate donors, the tested perylene derivatives are capable of providing PCEs that can keep up with PCBM or even overcome its performance. The only exception is tdiPBI. Even under ideal conditions it is not able to provide efficiencies larger than 1.36 % [82].

In summary, the tested materials are not able to provide their full potential compared to literature data. These lacks of efficiency are attributed to the processing conditions because ambient air and moisture has a detrimental effect on the donor materials and the aluminium electrodes. The acceptors are considered to be stable materials. Consequently, there is a demand for processing under optimized processing conditions, i.e., working with gloveboxes with a clean nitrogen atmosphere. Clean rooms with cleaned and dry air are not sufficient as oxygen is still detrimental to the cell. These ideal processing conditions exclude several influences that have a negative effect on the cells. Additionally, compositions that leave the prototype stadium and will head for production still demand for encapsulation to avoid any contact to the ambient atmosphere.

An alternative approach is the development of more stable materials that do not deteriorate due to ambient conditions. This must include active layer materials as well as electrodes. The advantage of totally ambient stable materials is their ease of processability. This is even more important if electrode materials are no longer metals but also organic compounds that can be applied without any need of vacuum-dependent evaporation processes. With the availability of such materials, organic solar cells will be easily manufactured, in a best case scenario even at home via printing, etc. For this last vision to become true, materials also must be more environmentally friendly. This holds for the materials in the cells as well as for solvents used during processing. Despite the fact that material consumption in organic solar cells is very low, all components must be recyclable. Of course, there is already research done pushing materials into the direction of easy and environmentally friendly processing but a breakthrough is a long time coming.

Recent findings regarding highly efficient PSCs are very promising but the employed perovskites typically contain lead and thus have to be considered as critical [141]. This cell type is in general a special type of the well-known dye-sensitized solar cell or Grätzel cell, i.e., it is a hybrid of organic and inorganic materials. Typically, an inorganic perovskite material is combined with an organic dye, e.g., $N^2,N^2,N^{2'},N^{2'},N^7,N^7,N^{7'},N^{7'}$-octakis(4-methoxyphenyl)-9,9'-spirobi[fluorene]-2,2',7,7'-tetraamine (Spiro-MeOTAD) [192]. The most common perovskite types are organometal halide perovskites, in more detail methylammonium lead halides. Here, the halide can vary but iodine is very common [141, 192–197].

Lately, other dyes are employed as alternatives to Spiro-MeOTAD. Examples of these substances are PCBM and N,N0-dimethyl-3,4,9,10-tetracarboxylic perylene diimide

(PTCDI), a member of the perylene diimide family [198]. Consequently, also other members of this family may be suited for application in perovskite solar cells albeit PTCDI, PCBM, and Spiro-MeOTAD are so far rather employed as an electron conduction material than as an absorber. Absorption is mainly governed by the perovskite but of course can be extended to other wavelengths by appropriately absorbing materials. Although there is much research on improving the long-term stability of perovskite solar cells, they are not the Holy Grail in solar cell research, yet [199–201].

This part of the thesis focused on the internal design of organic solar cells, cell fabrication, and efficiency optimization via parameter variation and material changes. The next part considers the development and simulation of patterned polymer films that might be used as light-trapping structures on top of solar cells. Alternatively, stamps for active-layer patterning can be prepared or patterned films are employed as structured substrates for arbitrary applications.

Part IV

Photopatterning of azopolymers and light-propagation simulations

As mentioned in the introductory part, azopolymers are employed for the fabrication of surface relief grating (SRG). In detail, the so-called cis-trans isomerization of azopolymers is exploited for the fabrication of structured polymer films. These films are in the first instance made of the azopolymers themselves but can be transferred in a second step into another material like the well-known PDMS. Upon irradiation with a light pattern the employed azopolymers tend to form SRGs whose trenches correspond to the regions of high light intensity while the protrusions are located in areas of low (or zero) intensity. The achieved height modulation is analyzed via phase-contrast microscopy, AFM, and stylus profilometry. Additionally, the transfer into PDMS is successfully carried out.

There are many possible utilizations of these structured films. Besides applications where templates with a height modulation on the nano- to micrometer scale are desired, the developed films are considered to act as light harvesting films on top of solar cells. Due to their multiplicity, the application is not limited to organic solar cells but can be also applied to any other type of solar cells. Detailed information about the processing procedure, the experimental setup, pattern transfer, and light propagation simulation is provided in the following chapters. Further, to analyze the light propagation of plane waves that impinge on a structured PDMS sheet and subsequently travel through glass, an FDTD simulation is set up. This simulation allows to compare different patterns regarding their light redistribution capabilities.

12 Azo compounds and cis-trans isomerization

The underlying effect of the patterning process of azopolymers is the cis-trans isomerization of molecules that contain an azo coupling. These couplings typically result from a chemical reaction between a diazonium compound[1] and another aromatic compound [202]. A very common family of dyes is the group of azobenzenes where two benzene rings are connected via an azo coupling [203]. The benzene rings in turn can have additional side groups.

Figure 12.1 schematically illustrates the cis-trans isomerization process of a single azobenzene molecule. Starting with the molecule either in its cis- (right) or trans state (left), it is excited by energy intake, e.g., absorption of a photon. In the excited state, the electron can relax to the energy minimum of this state. From this position, relaxation to the trans- or cis state is probable. As a result, the isomerization state switches or not. In the displayed case, the excitation energies are slightly different. This is not necessarily the case for all azo compounds. For example, the switching process of the material employed in this work occurs at a single wavelength in both directions. Additionally, absorption spectroscopy does not reveal different maxima for cis- and trans
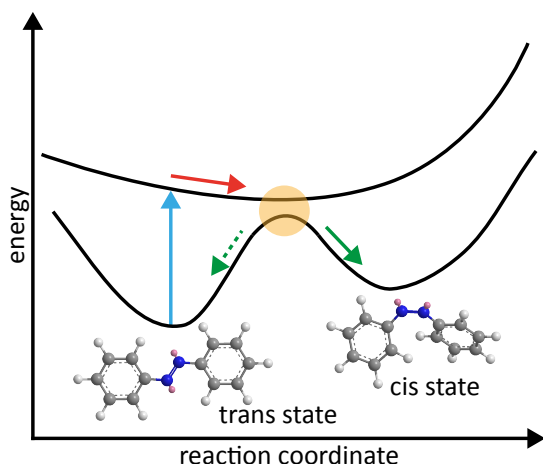
Figure 12.1: Schematic representation of the cis-trans-isomerization mechanism. An azobenzene molecule absorbs a photon and thus is excited from its cis- or trans state to a an energetically higher state. The minimum of this higher state is slightly shifted regarding the reaction coordinate (indicated by the circle) of the molecule and as a consequence it can relax either into the cis (right) or trans state (left).

states. Instead, a broad absorption maximum is obtained and thus, the energies are close enough to result in overlapping peaks. Another explanation is the presence of only one state during absorption spectroscopy. Anyhow, permanent illumination does not lead to fixing in one state and thermal relaxation from one state to the other is considered to be slow. As a consequence, reversible switching via optical excitation occurs. Finally, the exact position of the energetic states is of minor importance in this thesis.

In scheme 12.1 the azo dyes Disperse Orange 3 (structure **21**) and Disperse Red 1 (structure **22**) are illustrated. As the name indicates, the appearance of the dyes

---

1   The structure of a diazonium compound is the following: $R-N_2^+X^-$ where R is an organic group and X can be either inorganic or organic.
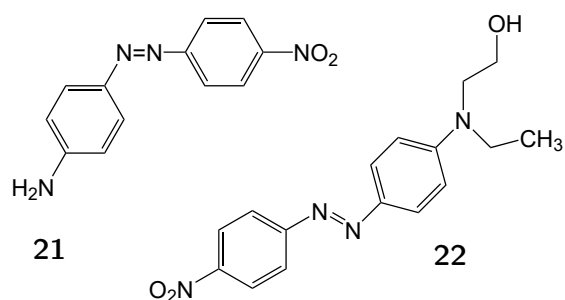
Scheme 12.1: Chemical structures of the azo dyes Disperse Orange 3: **21**, and Disperse Red 1: **22**.

is orange and red, respectively, and so are the emission spectra considered to be. In turn, absorption spectra are located in the blue to UV region of the spectrum. The azo materials, i.e., polymers based on these dyes employed in this thesis are depicted in scheme 12.2. These two compounds, namely poly(Disperse Orange 3 methacryl-amide) (PDO3MAA) (structure **23**) and poly(Disperse Red 1 methacrylate) (PDR1MA) (structure **24**) are the polymerized versions of the single dye molecules depicted in scheme 12.1. The polymer backbone in this case is methacrylate that is also the backbone of acrylic glass (poly(methyl methacrylate), PMMA) with the only difference that the methyl group is replaced by the corresponding azo dyes [204]. PDO3MAA and PDR1MA
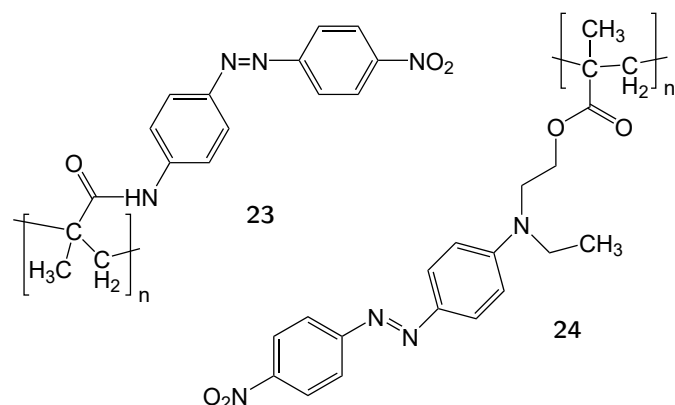
Scheme 12.2: Chemical structures of the azopolymers PDO3MAA: **23** and PDR1MA: **24**.

are provided by *Sigma-Aldrich* and used without further purification. Both compounds are soluble in common solvents such as chloroform, cyclohexanone, tetrahydrofuran, and more. Independent of the employed solvent, solutions possess a very low viscosity also in case of high concentration such as $10\,\mathrm{wt}\%$ (in cyclohexanone). As a consequence, the film thickness achieved during spin-coating deposition is only as low as approximately $200\,\mathrm{nm}$. Thicker films are achieved by drop casting, i.e., trickling dissolved azopolymer onto a prepared substrate without any further processing. The resulting films are much thicker. However, they are convex, lack smoothness, and consequently provide good surface reliefs on a considerably small area ($< 0.5 \times 0.5\,\mathrm{mm}^2$).

The absorption spectra of PDO3MAA and PDR1MA are depicted in figure 12.2. They are obtained from a solution of the polymers dissolved in $\mathrm{CHCl_3}$ with a concentration of $\rho \approx 9.1 \times 10^{-2}\,\mathrm{mg\,mL^{-1}}$. The absolute value of the absorbance of PDO3MAA at the peak position might be underestimated because of the solubility in chloroform. Not all of the polymer (PDO3MAA) is dissolved, and thus the concentration is only an approximate. Anyhow, both spectra provide a qualitative impression of the range of the light sensitivity. At wavelengths below $350\,\mathrm{nm}$ the glass of the cuvettes containing the
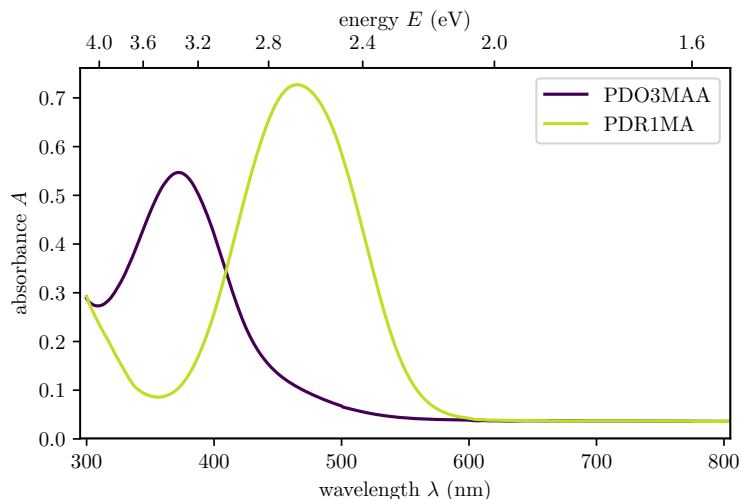
Figure 12.2: Absorption spectra of employed azopolymers PDO3MAA and PDR1MA in CHCl$_3$ with a concentration of $\rho \approx 9.1 \times 10^{-2}\,\mathrm{mg\,mL^{-1}}$.

solutions start to absorb and thus add an additional contribution.

The spectra of the polymers clearly indicate the different absorption regions of the dye molecules. The blue-shift of the spectrum of PDO3MAA (peak at 372 nm) with respect to the spectrum of PDR1MA (peak at 465 nm) is about 90 nm. Consequently, PDR1MA is better suited to be structured by light of the visible part of the spectrum whereas PDO3MAA only weakly absorbs visible light. Therefore, PDO3MAA demands a light source emitting in the blue-to-UV regime of the spectrum. In turn, PDO3MAA enables operation in devices where most of the visible light is not supposed to be absorbed by the patterned azopolymers, i.e., in solar cells. Due to the fact that the patterns are transferred into PDMS, and PDO3MAA demands for high light intensities, PDR1MA is employed for most of the structuring within this thesis.

13 Photomigration and surface relief gratings

The formation of surface-relief gratings is strongly connected to the isomerization process described in the previous chapter. In this chapter, the process that finally leads to the grating formation is elucidated. On one side, there is a phenomenological view on the effect. This view describes the patterning on the base of observations. On the other side, there are several theoretical models which try to explain the underlying effects that lead to the observations made.

If the light-induced switching process between the two isomeric states, also called photoswitching, is repeated multiple times, a mass transfer occurs. This transport mechanism is also called photomigration and leads to the formation of surface reliefs that correspond to the shape of the incident light intensity distribution [205–208]. In regions with high intensity, the material amount, i.e., the film thickness is reduced whereas it increases in regions of low light intensity. The mass transfer mechanism is also referred to photofluidization since the material's viscosity is assumed to be reduced resulting in a plastic deformation of the original film [209, 210]. If material that has been exposed to an inhomogeneous intensity distribution is illuminated with incoherent homogeneous light, prior induced height modulations are erased. This process can also be achieved via heating above the glass transition temperature T_{g} of the azopolymer. The reversibility of the structuring process enables the possibility to write and erase several structures on the same sample in the same place. Another application that is typically related to azopolymers is holographic data storage [211] due to the write and erase capabilities.

The underlying mechanism of the photofluidization is still not completely understood and described. There are several models that try to explain the mass migration effect but all of them have minor drawbacks because they are lacking to include all boundary conditions that are necessary for this effect to occur. One of the most prominent conditions that is neglected in a couple of models is the dependency on the light polarization due to the fact that molecules only absorb photons that are polarized parallel to their long axis. Consequently this is a critical aspect to be considered also in the experimental realization as linear polarized light would only excite molecules with the appropriate orientation. Additionally, light polarization also influences the direction in which the excited molecules migrate since movement is typically along the polarization axis [209, 212–214]. This is of importance for two-dimensional material structuring because this demands for polarization contributions in more than one direction and thus, circular polarization is an ideal candidate. Another issue of multiple models is their over- or underestimation of crucial quantities like forces that are assumed to be responsible for the mass transfer. In the following section, a brief introduction of several of the common models is provided and their drawbacks with respect to accuracy are mentioned while personal considerations are added.

13.1 Proposed mechanisms of light-induced mass transfer

The already mentioned light-induced mass-transfer process is described by several models that are more or less adequate but still do not totally include all aspects at once. In order to get an idea of these models, brief summaries of the models are introduced and rated based on the comparison of S. Lee et al. [215].

13.1.1 Model 1: Optical-field gradient force model

This model describes the mass-transfer mechanism as induced by an electrical field gradient that is caused by the incident light pattern [216]. The model considers the direction of the movement to the polarization of the incident light field. The drawback is the model-inherent underestimation to predict force densities correctly [215].

13.1.2 Model 2: Mean-field model

The mean-field model by Pedersen et al. [217] assumes that there are attractive forces between aligned azopolymer molecules. The drawback of this model is that it is only applicable on liquid crystalline azopolymers and does not work for other azo-based materials [215].

13.1.3 Model 3: Pressure gradient force model

The pressure gradient force model by Barrett et al. [205] assumes that forces originating from the isomerization process lead to the formation of the reliefs. The different isomeric states need different amounts of space and thus lead to tension and pressure gradients in the volume. This model is only applicable to intensity interference patterns whereas the effect of polarization patterns that maintain an unstructured intensity distribution is neglected [215]. Additionally, the model also neglects the possibility to reconfigure isolated structures of azo material via single beam illumination [215].

13.1.4 Model 4: Asymmetric diffusion model

The asymmetric diffusion model by Lefin et al. [218, 219] assumes an inchworm-like motion of the azo-molecules and is capable to describe the movement along the polarization direction of the incident light field. Unfortunately, it cannot describe the hole burning, i.e., aggregation of molecules with dipole moment perpendicular to the direction of polarization or the movement of large molecules [215].

13.1.5 Model 5: Photoinduced molecular diffusion model

A more recent multiscale model by Juan et al. [220] describes the azopolymer patterning as photoinduced molecular diffusion (PIMD). It is very precise in predicting photofluidic motions of azo-materials that include near- and far-field photofluidization [215]. A specialty of this model is its description of the interaction between the azo-material's

dipole with the incident light field. In turn, the drawbacks are the optimization for azo materials that are close to their T_g. Again the movement of large molecules such as oligomers or polymers is not described [215]. The latter is of special importance for considering the polymers employed of this work. The explanation of a single molecules' movement does not need to hold for dyes that are attached to a polymeric backbone. This backbone can keep the azo-part in its place because it is to rigid to follow the movement. This becomes very crucial if all of the other dye units are not excited.

13.1.6 Model 6: Thermal models

Thermal models assume that the fluidization is thermally induced. One of these models was proposed by Yager et al. [221]. They observe that the temperature elevation that occurs at typical experimental conditions ($50\,\mathrm{mW\,cm^{-2}}$) after a few microseconds is on the order of $1 \times 10^{-3}\,\mathrm{K}$ and reaches a few Kelvin ($\approx 10\,\mathrm{K}$) after several minutes of irradiation. Consequently, thermally induced fluidization can be excluded since the temperature of the material stays far below the glass transition temperature.

Another study by Böckmann et al. [222] revealed that temperature elevation combined with photoisomerization can lead to experimentally observed photofluidization that is also dependent on the incident light's polarization. Heating without photoswitching does not lead to molecular migration. The drawback is the very large temperature elevation and a very short simulation interval that is not consistent with typical experimental conditions as the study by Yager et al. [221] reveals. If it is possible to adjust simulation time and temperature to values that are closer to experimental properties, atomistic simulations can provide deep insights into the light-induced dynamics of azopolymers.

13.2 Conclusion of the proposed models

None of the introduced models is capable to describe all aspects of surface-relief grating generation that are experimentally observed and reported so far. Whereas one or another model seems to be more appropriate in one aspect, it crucially neglects another. Consequently, the models need to be expanded or corrected if possible, or they may be dead ends that do not describe the molecular behavior in any case. The models that assume temperatures close to the glass transition can be totally adequate in the particular case but low-temperature migration could origin from a different mechanism or the model just needs an extension that also covers the $T \ll T_g$ case.

In summary, at least the following aspects (with no claim to be complete) have to be considered in a single model:

- Photoswitching is necessary for the structuring process. Temperature elevation can be employed to erase written structures.

- The temperature does not have to be close to T_g.

- Photomigration occurs parallel to the polarization direction of the incident light.

- Intensity gradients are not necessary. Polarization modulation also leads to the formation of surface reliefs.

- The impact of molecule size or polymer backbone is not completely clear. The backbone might provide flexibility to allow slight movements. As a consequence a more detailed analysis on larger system has to be carried out.

- The impact of the photon flux and the resulting amount of molecules that is switched at once is rather low. Typically, the flux at experimentally realized intensities is not large enough to excite all of the dyes attached to a polymer chain at once. Thus, there might be a pulling mechanism (if the occurring forces are large enough) that moves the whole polymer chain in one direction if one (or more) attached dye units are excited.

14 Fabrication of surface relief gratings

SRGs are realized by illumination of thin azopolymer films with intense structured light of an appropriate wavelength. As a starting point, interference patterns of two intersecting laser beams are employed. This type is chosen to perform very basic structuring and learn the fundamental properties of the process. In a second step, a more advanced setup containing a spatial light modulator (SLM) as light-patterning element is applied. This technique allows for creation of arbitrary patterns that vary from very basic stripe gratings to complexly shaped surface landscapes or even completely random patterns.

14.1 Two-beam interference setup
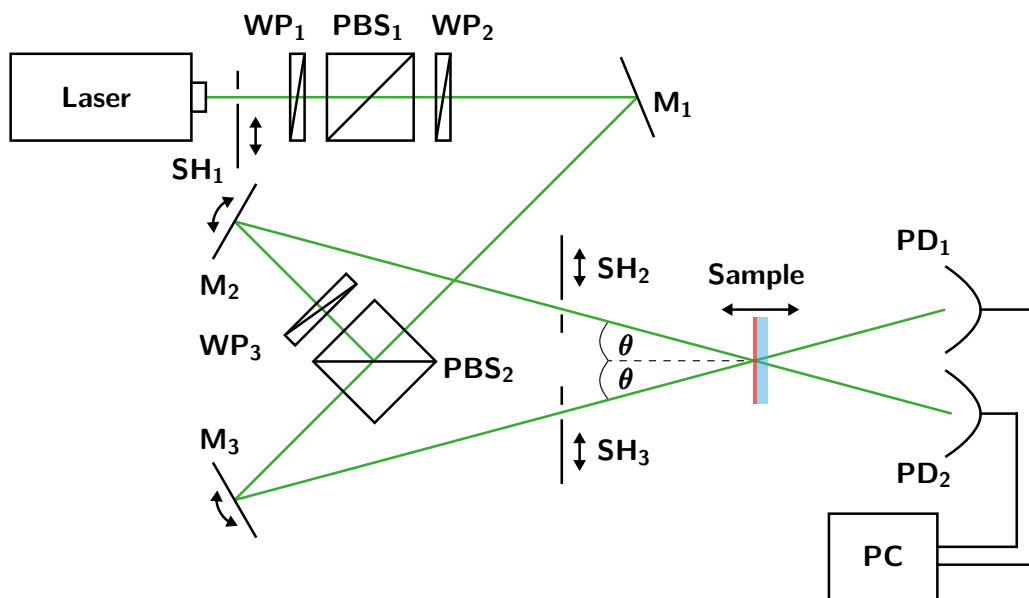
Figure 14.1: Schematic representation of the azopolymer structuring setup that is based on the interference of two beams. Here, **SH_x** denote shutters blocking the beams if necessary, **PD_x** are photodiodes that detect the transmitted intensity. The **WP_x** are half-wave plates to adjust the light's polarization and **PBS_x** are polarizing beam splitters for intensity and ratio control. Mirrors **M_2** and **M_3** are rotatable and the **Sample** is shifted to adjust the grating spacing of the interference pattern. The second beam generated by **PBS_1** is not shown.

The basic setup is illustrated in figure 14.1. The overall light intensity is adjusted by **WP_1** and **PBS_1**, whereas **WP_2** adjusts the splitting ratio and thus the intensity ratio of the two beams that illuminate the **Sample**. **WP_3** rotates polarization again to achieve parallel polarization of both beams. The shutters **SH_x** are applied to block either one of the beams or the whole illumination at all. Light transmitted through the semitransparent sample is recorded via the photodiodes **PD_x** connected to a computer

PC. Adjustment of the angle of incident and consequently the grating spacing of the interference pattern is achieved via rotating the mirrors M_2 and M_3, whereas the sample position is corrected via shifting to the new position of the beam intersection. The grating period Λ is calculated analog to the period in the case of the PR composites via a slightly modified version of equation 6.8. Due to the symmetric incidence of the beam, the simplified equation

$$\Lambda = \frac{\lambda}{2n \sin \theta} \tag{14.1}$$

only demands for the angle θ that is determined by one of the incident beams and the normal of the sample. Further, n is the sample's refractive index and λ is the wavelength of the incident light.

14.2 Phase-only spatial light modulator-based setup

The phase-only SLM (PSLM)-based setup is depicted in figure 14.2. The beam of a laser, here an optically-pumped semiconductor laser operating at a wavelength of $\lambda = 488\,\text{nm}$, is adjusted regarding power and polarization via half-wave plates HWP_x combined with a polarizing beam splitter **PBS**. Subsequently, the beam is expanded and spatial-frequency filtered by a microscope objective MO_1, a pin hole **PH**, and a lens L_1. The computer-controlled **PSLM** converts the plane-wave illumination into a structured light field. A more detailed explanation of light-field modulation is provided in subsection 14.2.1. As already mentioned, azopolymers are sensitive to the polarization of the incident light. To enable the possibility of high-quality 2D structuring, the polarization is switched to circular by a quarter-wave plate **QWP** and thus all molecules regardless of their orientation are excited. Imaging and demagnification ($\approx 10\,\text{x}$) is realized by lenses L_2 and L_3. The iris **I** filters all incoming light except the first diffraction order that contains the undisturbed structural information.

The pattern inspection system (PINS), indicated by the dashed line, is mounted on a table (**z-shift**) that allows movement along the beam propagation direction and thus repositioning of the sample to the image plane. In a subsequent step, the **Sample** is shifted into the image plane via another z-shift (not shown) and is adjustable along the lateral direction to allow for automated sequential writing of multiple patterns next to each other. The PINS consists of a microscope objective MO_2, beam splitter **BS**, a lens L_4, and the cameras Cam_1 analyzing the image at the sample surface and Cam_2 recording the Fourier transform of the image.

14.2.1 Light patterning via phase-only spatial light modulation

The employed PSLM, model LETO from *HOLOEYE Photonics AG*, consists of a reflective liquid crystal on silicon (LCoS) display with a spatial resolution of 1920×1080 pixels[1] and a pixel pitch of $6.4\,\mu\text{m}$. It can induce a relative phase shift of at least 2π in

---

1 During the experiments only a central part of the PSLM of 1080×1080 pixels is employed due to symmetry reasons of some pattern types.
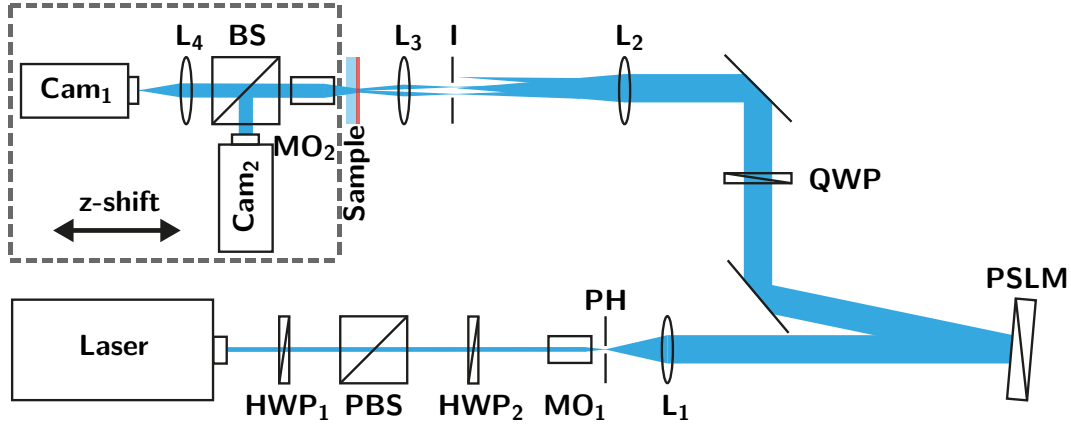
Figure 14.2: Schematic representation of the azopolymer structuring setup that is based on a computer-controlled **PSLM**. The power of a beam of a **Laser** is adjusted via half-wave plates **HWP$_x$** and a polarizing beam-splitter. A subsequent expansion system consisting of a microscope objective **MO$_1$**, pinhole **PH**, and lens **L$_1$** enables plane-wave illumination of the PSLM. The quarter-wave plate **QWP** generates circularly polarized light. The lenses **L$_2$** and **L$_3$** image the structured light field demagnified on the **Sample**. An iris **I** filters undesired diffraction orders. The pattern inspection system consisting of a microscope objective **MO$_2$**, beam splitter **BS**, lens **MO$_4$** and the cameras **Cam$_x$** is mounted on a **z-shift** that enables repositioning of the pattern inspection system (indicated by the dashed line) into the image plane. The cameras allow to monitor light pattern and its Fourier transform. The x-y-shift of the sample is not shown.

the visible part of the spectrum. The phase resolution is 8 bit and thus the phase can be subdivided into 256 steps addressable by a computer. In order to optimize the phase response to the employed wavelength of 488 nm, the SLM is calibrated to exactly shift the phase by 2π within the 256 steps and thus to obtain the ideal phase resolution.

Considering phase modulation only, this calibration is be sufficient. Since the amplitude of the light field is additionally modulated, a more complex approach described by Davis et al. [223] is applied. In this procedure, a blazed grating is employed to diffract the desired intensity distribution into the first diffraction order while the zeroth order carries the residual light that is later blocked by an iris. Of course, there are also higher diffraction orders and their complements, but they are also blocked and not imaged to the sample surface. In order to obtain the desired modulation that is generated in real-space, the blazed grating itself is modulated and contains phase and amplitude information. The resulting phase information in its 8 bit representation to be displayed on the PSLM can be calculated via

$$\Phi_{\mathrm{SLM}} = S_{\max} \; A_{\mathrm{cor}} \; \left((BG + \Phi_{\mathrm{pat}} + C_\Phi - C_{\mathrm{Amp}}) \bmod 1 \right) \;. \tag{14.2}$$

Here, $S_{\max}$ is the number of phase resolution steps, i.e., 256, A_{cor} is the corrected amplitude (or intensity) of the pattern, BG corresponds to the phase information of the blazed grating, Φ_{pat} is the phase distribution of the pattern. Furthermore, C_Φ is a phase correction term that considers deviations from a perfectly flat PSLM and influences from non-perfect alignment of other optical components. Finally C_{Amp} is a correction of the

phase that results from the employed amplitude modulation technique. Except S_{max} and C_{Amp}, all quantities are in the range $[0,1[$. C_{Amp} is in the interval $[0,0.5[$. In a last operation prior to sendig to the SLM, Φ_{SLM} has to be converted to integer values.

The need for the corrected amplitude A_{cor} and C_{Amp} is described by Davis et al. [223] and results from the intensity progress in the first diffraction order for normalized values of the phase. The progress is represented by a $1 - \mathrm{sinc}\,(u)$-function where u lies in the interval $[0,1[$. To linearize the diffraction intensity, the expression containing the sinc-function has to be inverted. As there is no analytical solution and only discrete values are desired, a look-up table containing the inverted data of the sinc-function is calculated and employed for correction of the amplitude A to obtain A_{cor}. The phase correction term is calculated via

$$C_{\mathrm{Amp}} = \left(\frac{\pi A_{\mathrm{cor}}}{2\pi} \right) \bmod 1 \; . \tag{14.3}$$

The impact of the phase correction term C_{Φ} on the quality of the resulting structured light field is considerably low[1]. In turn, the amplitude correction term and the correction of the amplitude itself lead to significant enhancements of the signal-to-noise ratio and thus this step is very crucial. This step can be even more optimized[2] if the diffraction curve of the PSLM is measured and an adequate approximation that can be inverted is found. The quality achieved after the previously mentioned calibration steps is considerably sufficient. Therefore, further optimizations that only have minor contributions is omitted.

14.3 Azopolymer film preparation

In order to prepare thin azopolymer films on glass substrates, the material powder is dissolved in a solvent. Typical candidates are $CHCl_3$, cyclohexanone, or tetrahydrofuran (THF). The concentration of the azopolymer is set to $3\,\mathrm{wt}\%$. In case of $CHCl_3$, a lower concentration of $2\,\mathrm{wt}\%$ has to be realized because the solubility in this solvent is observed to be significantly lower and thus is a limiting factor.

Thin films are fabricated by means of spin coating of the prepared solution on glass substrates. The substrates are slices of microscope slides cleaned with dishwater, isopropyl alcohol, and acetone. Spin coating in static-dispense mode is carried out at different speeds ranging from $10-30\,\mathrm{s}^{-1}$, whereas $10\,\mathrm{s}^{-1}$ is the minimum speed that can be realized by the available device. In addition, some samples are also realized via drop casting. Here, the solution is dropped onto the substrate. The solvent evaporates without any further treatment. Consequently, in case of the latter procedure, the realized film thicknesses vary. The drop cast films are rather thick but rough and convex compared to the spin coated ones that are thinner and flat. The former are thus better suited to generate larger height modulation with the cost of a smaller useful area due to the curvature. In turn, the latter can be patterned almost over the whole area but the resulting patterns are limited regarding their height.

---

1   The influence strongly depends on the quality of the PSLM and the adjustment of other components. Consequently, the impact of C_{Φ} is higher if the modulator is not as flat as the employed one.

2   In case the diffraction curve of the SLM does not exactly correspond to a $1 - \mathrm{sinc}\,(u)$ function.

The absolute film thickness is measured via atomic force microscopy. Substrate-to-film steps are created by a partial lift-off of the film via adhesive tape or alternatively by a blade. The obtained height information vary more than $50\,\mathrm{nm}$. An inspection of the prepared steps reveals that the edges do not have perfect contact to the substrate. Consequently, thicknesses of PDO3MAA films characterized via AFM are considered to be unreliable.

Anyhow, the main aspect is the realization of complex patterns in azopolymers in general, the impact of a limited film thickness is only considered to be a limit for the maximum modulation height that can be achieved. Consequently, the main focus is set on the realization of the patterns themselves whereas maximizing the modulation depth is considered to be an issue of initial film thickness, illumination duration and intensity.

In case of the PDR1MA films, a different approach to characterize the dimension of the film height is chosen. Samples made from a standard recipe, i.e., $3\,\mathrm{wt\%}$ PDR1MA in cyclohexanone, coated at $15\,\mathrm{s}^{-1}$ are characterized with a stylus profilometer by staff members of the group of Dr. Frank Berkemeier, Institute of Materials Science, University of Münster. The observed film thicknesses are about $(170 \pm 10)\,\mathrm{nm}$. With further optimization regarding employed solvents, concentrations, and azopolymers themselves, higher film thicknesses should be easily realizable. Especially the polymer itself seems to have an impact, since sources report on thicknesses up to several hundred nm [224, 225]. The drawback is, that these are achieved with compounds that are not commercially available and thus demand a separate step for synthesis. Consequently the employed polymers are chosen to avoid additional processing.

In general, the patterning procedure can be also adapted to other materials and is not limited to PDO3MAA and PDR1MA. Therefore, the modulation limit that is generated by small film thicknesses can be overcome.

15 Realized patterns via two-beam interference

Two-beam interference of two coherently superposed plane waves generates an intensity pattern comprised of equally-spaced dark and bright stripes whose grating period can be calculated via equation 14.1. Due to the monitoring capabilities of the employed setup, it is observed that the signals of the power of the transmitted light are not stable but oscillate temporarily. The oscillation is not an instability of the incident light intensity but is a coupling phenomenon that is related to two-beam coupling in photorefractive materials (cf. part II). It can be directly observed that the portion of light that vanishes in one of the beams is transferred to the other and vice versa. Summed up, the overall power remains almost stable. A slight decay of the detected power of the two transmitted beams is attributed to diffraction into higher orders that are not logged. Due to the nature of the inscribed gratings, they are considered as thin, and thus, Raman-Nath diffraction is observed [226]. For a better understanding, the following paragraph provides an example for the differentiation of different diffraction regimes.

Taking the typically applied criterion for thin and thick gratings to distinguish between the Raman-Nath and the Bragg regime

$$Q = \frac{2\pi\lambda L}{\Lambda^2 n} \tag{15.1}$$

with λ as wavelength of incident light, grating thickness L, grating spacing Λ, and average refractive index n into account, also higher diffraction orders are expected [227]. For typical parameters in this experiment of $\lambda = 500\,\text{nm}$, $L = 100\,\text{nm}$, $\Lambda = 1.5\,\mu\text{m}$, and $n = 1.57$ the quality factor $Q \approx 0.095$ hints to the Raman-Nath regime. If the modulation depth, i.e., the grating thickness is enhanced further while the grating period is reduced, the transition regime is reached. However, regarding to [136], Q as a criterion is not necessarily sufficient to distinguish between Bragg and Raman-Nath diffraction. They introduce another factor called ρ that is similar to Q but additionally is dependent on the refractive index modulation. As this parameter is not known for the employed material, Q is considered as sufficient. Additionally, the type of diffraction can be directly observed in the experiment.

Figure 15.1 illustrates the power signal of the two transmitted beams and the sum of both. The sample is based on PDO3MAA in THF that is spin coated on glass. The angle of incidence of each beam with respect to the sample normal is set to $\theta = 9.3°$ resulting in a grating spacing of $\Lambda = (1.64 \pm 0.07)\,\mu\text{m}$. the operating wavelength of the laser is $\lambda = 532\,\text{nm}$, the power of each beam is adjusted to approximately $30\,\text{mW}$ to generate an interference pattern of maximum contrast, and p-polarization is chosen. Due to the low absorption of PDO3MAA at this wavelength (cf. figure 12.2), most of the incident light is transmitted as can be observed in the figure at the beginning of the measurement. Additionally, the pattern formation is considerably slow. The signals are almost stable during the first $1000\,\text{s}$. This behavior changes when the power of beam 1 increases while the one of beam 2 drops. The further temporal evolution displays an
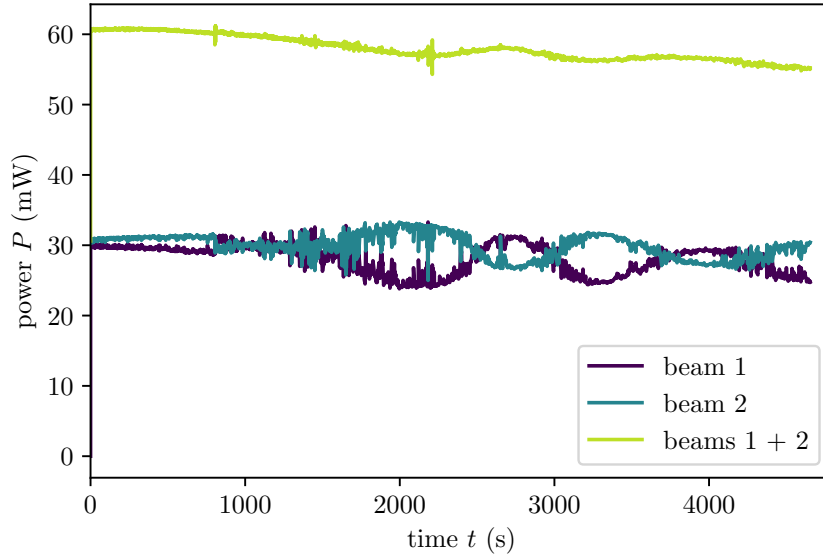
Figure 15.1: Recorded power of the transmitted beams and the sum of both. The sample is based on PDO3MAA in THF. The grating spacing is adjusted to $\Lambda = (1.64 \pm 0.07)\,\mu m$.

oscillation of both signals while the overall power remains almost constant. Thus, the phase shift of the signal amplitudes is almost perfectly π. The oscillation frequency is about $(0.8 \pm 0.1)\,mHz$. It has to be noted that the data concerning the oscillation process are only valid for this single writing process. If the same procedure is repeated, either on the same sample or on a different one, the oscillation behavior changes regarding its starting point, frequency, and amplitude. Consequently, there is no characteristic behavior of the structuring process with the employed boundary conditions regarding material and experimental parameters.

There are multiple explanations to be considered. The first one considers an effect by the film morphology. The dye parts of the molecules are differently ordered or they are even completely random. This has a crucial impact on the photofluidization behavior and thus on the grating formation. Anyhow, this effect only explains that the buildup of the grating can vary between different inscription processes but not the observed oscillations.

An explanation considering the refractive index grating formed due to photoswitching in the bulk of the film can help to understand the oscillating signals [205]. This index grating does not necessarily have to completely coincide regarding its lateral position with the surface-relief grating that is, of course, a phase grating, i.e., a modulation of the optical path length. At different stages of the inscription process, the different gratings have a varying impact on diffraction and thus especially the oscillation behavior might originate from the superposition of both gratings that changes over time.

In general, no oscillations are expected at all because two-beam coupling requires a $\pi/2$-phase shift of the refractive index grating with respect to the light pattern (cf. part II). If there is a phase grating only, light is expected to be diffracted statically while the power of each beam is conserved. In this case, the phase shift between phase grating

and interference pattern is π. This shift coincides with the observation that material moves from regions of high intensity to those of low intensity.

In contrast, the oscillations hint to a refractive index grating changing its relative phase with respect to the light pattern and thus, leads to beam coupling. The phase shift of the refractive index grating in common photorefractive media depends on redistribution of excited charge carriers. In the applied azopolymers, the underlying mechanism is different. Here, charges are excited as well but the material is not considered to be conductive. Thus charges are not transported through the medium. Consequently no space-charge field is build up. Conductivity is neglected because of the lacking conjugation of the polymer backbone. The only way charges can be transferred is hopping from one dye molecule to another. Even this is unlikely to occur as there is no interface where exciton separation occurs. As a consequence, the excited charge carriers are still bound.

Finally, the only mechanism that leads to a refractive index modulation is the isomerization process inducing density changes and thus, changes of the refractive index. In summary, the origin of the varying phase shift remains unclear. A purely thermal effect that causes drifting of the interference pattern is not considered as the origin of the oscillation due to the different behaviors during separate writing processes without changing the ambient conditions.

The slight drop of the overall transmitted power is explained by diffraction into higher orders, as already mentioned. As this diffraction strongly depends on the condition of the inscribed grating, changes during the writing process also lead to variations of the detected overall power.

15.1 Maximization of height modulation

The structured polymer films are transferred into PDMS to act as light harvesting structures on solar cells. For this purpose, a large height modulation is desirable to diffract the incident light into higher orders to elongate the optical path in the absorbing material. In this context, the height modulation is of particular interest because it has an impact on the "amount" of light that is diffracted [228].

In order to determine a measure for maximum height modulation during the inscription process, multiple approaches are considered. The first one involves the observation of the power of the transmitted beams. As the previously described coupling and the oscillation occurs in every sample, the difference of the transmitted power of both beams after the first buildup of the grating is considered as a parameter for the modulation strength. Of course the measured signal is strongly influenced by the refractive index pattern but in-situ characterization that bases on diffraction will always be influenced by the refractive index pattern. Another possibility requires blocking one of the writing beam and an analysis of the transmitted and diffracted signals. In a more advanced version, the signals generated by a second laser probing the sample are recorded. This laser ideally emits light of a wavelength[1] not absorbed by the azopolymer and thus it

---

1   For the employed materials, the wavelength of the probe beam must be in the red part of the spectrum.

cannot change the grating itself. Monitoring of the signal to assure maximum diffraction helps to stop the inscription process in a state where the surface relief is not distorted by a drifted interference pattern. Such a pattern can overwrite the existing pattern and thus, reduce the modulation height.

In this thesis, the first approach is employed as it is simple to realize and does not need further components in the experiment. For the characterization after the inscription process, an atomic force microscope (AFM) is applied to uncover the absolute height modulation.

In section 14.3, where sample preparation is described, it is also noted that strong height modulation demands large film thicknesses. Consequently, a drop casted film based on PDO3MAA in cyclohexanone is fabricated on a glass substrate. In comparison with other solvents, cyclohexanone provides the smoothest films when this technique is applied. Anyhow, the film is still convex and not suited for large area structuring. Since the intersecting beams are only covering an area of approximately $20\,\mathrm{mm}^2$ and the scanned area by the employed AFM is only $20 \times 20\,\mu\mathrm{m}^2$, the curvature is neglected in this proof-of-principle demonstration.
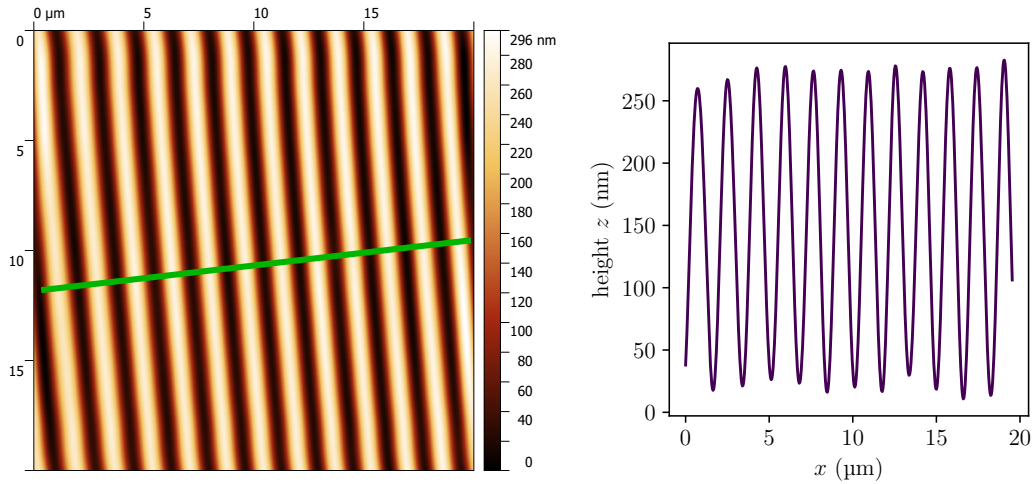
(a) AFM scan of a patterned sample. The green line indicates the position of the height profile displayed in 15.2(b).

(b) Height profile of the scan in 15.2(a) that is located at the position of the green line.

Figure 15.2: AFM-scan and extracted height profile of a drop casted film of PDO3MAA where cyclohexanone is used as solvent. The lateral spacing of the stripes is determined via FFT and results in $\Lambda = 1.67\,\mu\mathrm{m}$. Data evaluation is carried out via WSxM [229, 230] and Gwyddion [231].

As in the previous case, the experimental parameters are set to $\Lambda = 1.64\,\mu\mathrm{m}$ for the grating spacing and $P \approx 30\,\mathrm{mW}$ for each of the writing beams. Of course, the transmitted power is much lower due to the larger film thickness and thus the power at the output side drops to about $9\,\mathrm{mW}$. The inscription time is set to $1000\,\mathrm{s}$ and an AFM scan of the resulting pattern is displayed in figure 15.2. The image in 15.2(a) and the profile in 15.2(b) that is taken at the position of the green line in (a) clearly show a sinusoidal SRG with a height modulation $> 250\,\mathrm{nm}$. An Fast Fourier Transform (FFT) analysis (not shown) of (a) additionally reveals that the grating spacing ($\Lambda_{\mathrm{FFT}} = 1.67\,\mu\mathrm{m}$) almost perfectly coincides with the spacing of the interference pattern ($\Lambda_{\mathrm{IP}} = 1.65\,\mu\mathrm{m}$). The

outcome of this measurement is that also large modulation heights can be achieved easily with thick films. The drawback of thick films is the considerably high absorption and thus here is a strong need to transfer the pattern into a transparent material. One aspect having a large impact on the successful inscription process of this deep modulation is the employed solvent cyclohexanone. If films are prepared on the basis of PDO3MAA and $CHCl_3$ or THF, the inscribed patterns do not reach such high quality and modulation. Thus, for all subsequent experiments cyclohexanone is the solvent of choice. This holds also for spin coated films that are obviously thinner but will act as the standard template for 2D structures that are realized with the SLM-based technique.

16 Realization of complex 2D patterns – between disorder and order

In this, chapter the fabrication of 2D patterns with the PSLM-based approach that is introduced in section 14.2 is reported. Due to the lower light intensity available in the sample plane, the polymer is switched to PDR1MA. Due to the higher sensitivity of PDR1MA in the visible range and a different laser operating at 488 nm, enhanced light-matter interaction and thus higher patterning speed is achieved.

The boundary conditions for the writing procedure regarding azopolymer, solvent, and film fabrication are determined in the previous section. The crucial part in this section is the generation of complex patterns. On the one hand, these have to be generated by a computer and send to the PSLM. On the other hand the light field has to be imaged onto the azopolymer film. In case of so-called nondiffracting beams, i.e., light fields that do not change their lateral intensity profile along a certain propagation distance, imaging is also possible within this nondiffracting regime [232]. In turn, if other arbitrarily shaped patterns are generated, the sample has to be exactly positioned in the image plane. In order to achieve an exact sample placement, the camera system is moved to record the image plane. If this is realized, the sample can be shifted to the image plane of the light field.

In order to understand the basic principles of nondiffracting beams, their generation, and their properties, a short introduction is provided in the next section.

16.1 Nondiffracting beams: a short introduction

As mentioned previously, nondiffracting beams do not change their lateral intensity profile over a certain propagation length. To describe the generation and their features, considerations in real space and in Fourier space, i.e., frequency space are carried out. Typically, the most general illustration is made in the latter. A beam is considered to be nondiffracting if its intensity distribution in frequency space is positioned on a ring of equal spatial frequency [233]. In turn, the intensity-distribution function on this ring can be completely arbitrary. Figure 16.1 illustrates the Fourier space representation of the intensity distribution that leads to nondiffracting beams. The left part depicts plane waves that possess the same inclination and thus the same spatial frequency with respect to the direction of propagation K_z. Consequently, they form a cone around this z-direction. The subimages on the right side represent a cut through the depicted cone and a top view of the cone, i.e., a circle. Especially the latter depicts that all wavevectors possess the same absolute value of the transverse component k_t. In addition, the former illustrates the composition of the wavevector k by the transverse component k_t and longitudinal component k_z.

In real space, the superposition of the plane wave with the described properties leads to the formation of an interference pattern whose shape strongly depends on the number of plane waves and their mutual phase. The so-called nondiffracting length, i.e., the
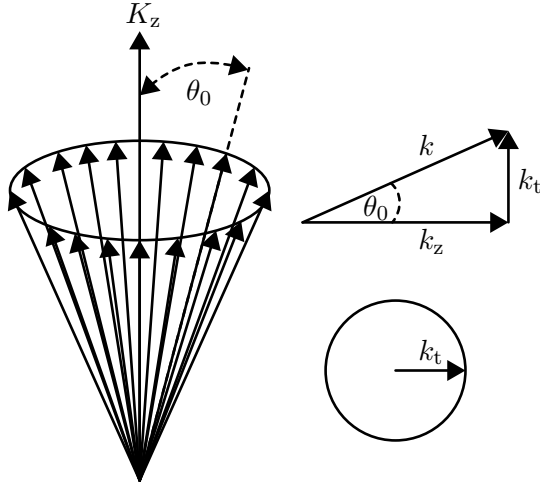
Figure 16.1: Schematic representation of the wavevector orientation in a nondiffracting light field. Here, K_z indicates the propagation direction, θ_0 is the inclination angle of the incident plane waves with wavevector k with respect to K_z, while k_t and k_z are the transverse and z-components of the wavevector k, respectively. Adapted from [234].

longitudinal length that the light field can propagate without changing its transverse profile also depends strongly on the length of the transverse component. Small transverse components result in a long nondiffracting length and a large structural parameter (lattice constant in case of periodic patterns) of the resulting light field. This relation is reversed for large transverse components.

Under real experimental conditions, perfectly nondiffracting beams cannot be realized as this demands for infinite energy on an infinitely thin ring. Thus, all realized beams are pseudo-nondiffracting beams but the term "pseudo" is typically omitted [233]. In addition, the so-called self-healing feature is attributed to nondiffracting beams. This effect enables the beams to recreate itself behind a nontransparent obstacle that blocks parts of the beam [233]. However, if a typical experimental realization of a nondiffracting beam is considered, i.e., the superposition of plane waves that form an interference pattern, the nondiffracting beam exists within the volume that is formed by the intersecting beams. An obstacle (not too large) that is placed within this volume will create a shadow partially destroying the nondiffracting beam. Anyhow, as long as the obstacle is not completely blocking the light of one of the plane waves, there will still be interference of all contributing plane waves behind the obstacle. Therefore, there is not active effect to be considered as healing and thus the term self-healing is misleading.

The important aspects of nondiffracting beams in the context of this work are that their lateral intensity profile is constant over a certain propagation length. This length depends on the transverse length of the wavevectors. The nondiffracting characteristic reduces the need for a high sample positioning accuracy during the pattern inscription process. Additionally, the generation instruction, i.e., plane waves located on a circle and consequently forming a nondiffracting beam allows for a broad variety of different beam types [96]. The number of plane waves and if they are distributed discretely or continuously only has impact on the shape but not on the character. Thus, any function modulating the intensity distribution on the circle can be employed to generate different shapes of nondiffracting beams. However, of course the superposition has to be coherent to assure interference.

The inscription of the simplest nondiffracting beam – an interference pattern of two

coherent beams – is already discussed in chapter 15. Two more representatives of the nondiffracting family, Bessel and Penrose patterns, and their inscription process are introduced in the following sections.

16.2 Bessel patterns – circular symmetry

In this section, the so-called Bessel pattern whose intensity profile corresponds to the square of the absolute value of the rotated zero-order Bessel function of the first kind [232] is introduced (cf. figure 16.2). In frequency space, the spectrum of the Bessel pattern resembles a ring of equal intensity, i.e., all possible wavevectors of a specific radial component are contributing to the formation of the Bessel pattern [232].

The general idea behind the inscription of Bessel pattern is its circular symmetry. Typical structures applied on solar cells possess a certain angle selectivity because of they are based on highly regular square patterns. A way to overcome this selectivity is switching to circular patterns.

The intensity profile of a Bessel pattern has a very high peak at its center (cf. subfigure 16.2(a)) and the intensity of the side lobes decreases with increasing radius. This kind of structure in its original shape is not very suited for the inscription into azopolymers. The central peak leads to the formation of a hole at the center, whereas the side lobes are hardly pronounced. As a solution, only the underlying phase information (cf. subfigure 16.2(b)) of the real space is employed for the inscription process[1]. This phase pattern has a binary nature with alternating high level and low level rings that are perfectly concentric. Consequently, the amplitude term A_{cor} is considered to be constant while the phase term Φ_{pat} carries the information to be send to the PSLM (cf. equation (14.2)). In addition, the normalized spatial frequency data is provided in subfigure 16.2(c). Here, the perfect ring structure of the Fourier components becomes evident. The slight nonzero components within the circle result from the FFT. The ring spacing of 250 µm in figure 16.2 is chosen arbitrarily.

In the experiment, the spacing can be reduced down to 35 µm. Further reduction leads to superposition with another diffraction order of the SLM, and thus to increased crosstalk in the image plane. However, the demagnification enables to pattern azopolymer films with a spacing of about 3.5 µm. Further reduction is possible if the demagnification factor is increased or an SLM with a higher resolution and smaller pixel pitch is employed. The latter would enable better separation of the diffraction orders while maintaining the patterning size.

Subfigure 16.2(d) finally displays a phase contrast image of a successfully inscribed the Bessel pattern (ring spacing of 3.5 µm) into a PDR1MA film. The whole inscription process takes 120 min at an intensity of 189 mW cm^{-2}. Of course, due to the nature of this characterization technique, it visualizes both, refractive index pattern and SRG. An analysis of the surface structure with a stylus profilometer (Dektak$^{®}$ XT, *Bruker*) reveals good coincidence with the spacing of the light pattern and also a height modulation of $l = (50 \pm 5)$ nm. The image also illustrates that the application of circularly polarized

---

1   The impact of the missing amplitude modulation on the nondiffracting property is neglected here.

(b) Phase information.

(c) Normalized spectral components.   **(d)** Pattern in PDR1MA.
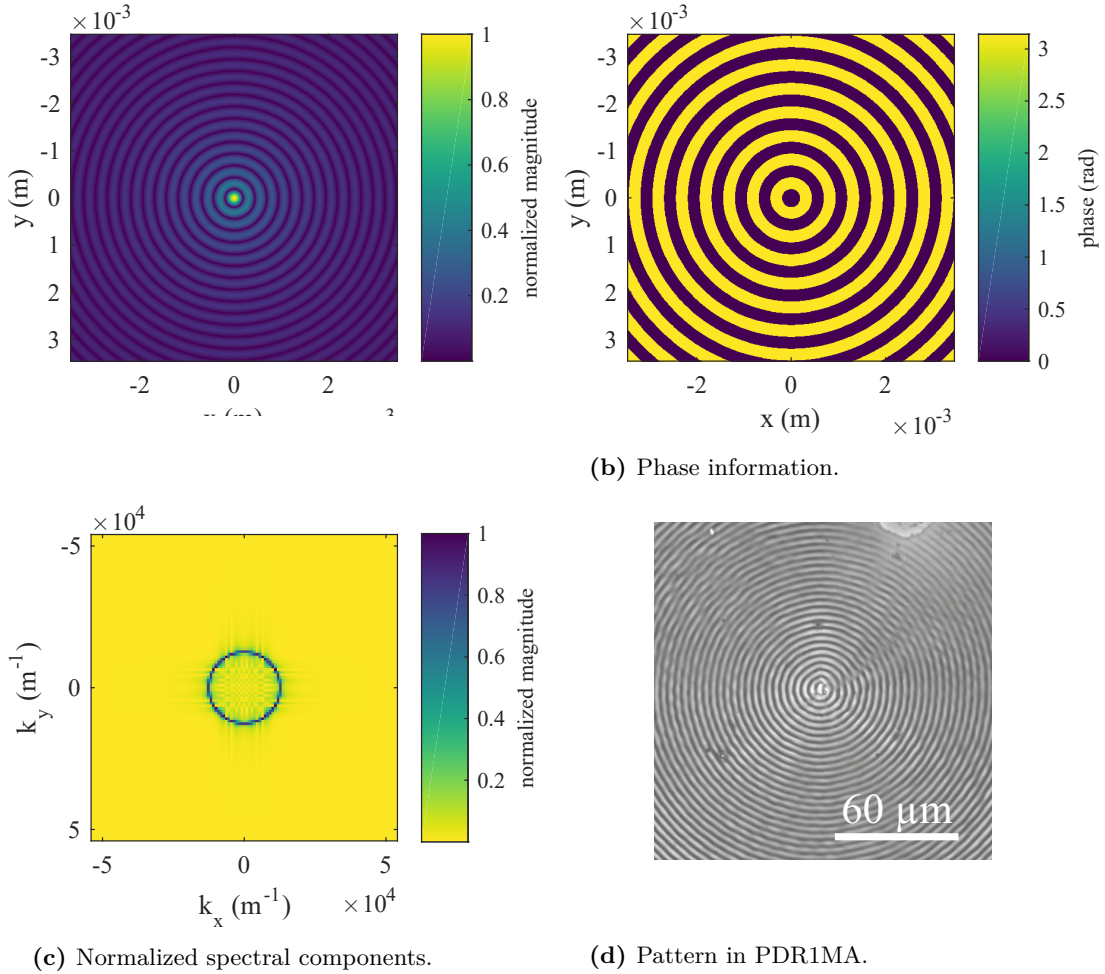
Figure 16.2: Normalized absolute data of the field information of a Bessel pattern with a ring spacing of $250\,\mu\text{m}$ corresponding to a ring diameter in frequency space of $K = 2.51 \times 10^4\,\text{m}^{-1}$ (a). Subfigure (b) contains the corresponding phase information while (c) contains the spectral composition where the magnitudes are also normalized. A phase contrast image of a realized pattern in PDR1MA is provided in (d). The ring spacing is $3.5\,\mu\text{m}$ which corresponds to $K = 1.80 \times 10^6\,\text{m}^{-1}$. Subfigures (a)-(c) contain calculated data while the data subfigure (d) result from a measurement.

light allows for 2D structuring. If linear polarization is applied, the ring pattern is very weak or not even present at all along one direction [209]. Regarding its shape, the pattern provides similarity to a Fresnel axicon [235]. The Fresnel type axicon is, like Fresnel lenses, reduced regarding its volume and consequently space requirements. This is achieved by structuring of the surface. The Fresnel axicon reported by Golub [235] also consists of a ring structure but all these rings have slants on their top. The pattern illustrated in subfigure 16.2(d) is expected to be flat top in general, but the edges are not infinitely steep due to the cut-off of higher harmonics of the signal. Consequently the shape of the side lobes is sinusoidal.

16.3 Penrose patterns – quasiperiodic and nondiffracting

The second representative of the nondiffracting-beam family, the so-called Penrose pattern, is generated by superposition of five plane waves that are equally spaced on the previously described ring. Superpositions of two, three, four, or six plane waves lead to patterns with transverse periodicity. This is not the case for the Penrose pattern or patterns created by superposition of more than six plane waves [96]. These structures only possess rotational symmetry of $2\pi/n$ where n is the number of plane waves. Furthermore, these more complex gratings are called quasiperiodic [96]. The Penrose pattern type is considered to be superior to conventional patterns regarding its light redistribution capabilities in solar cells. Because of the lacking symmetry and thus a reduced number of escape possibilities, optical path lengths are longer than in highly periodic patterns. As a consequence, light becomes more concentrated in the active material.

Figure 16.3 depicts field distributions in the spatial domain, frequency domain, and phase distribution in the spatial domain of a Penrose pattern with structure size of $250\,\mu\text{m}$, i.e., a ring diameter in frequency space of $K = 2.51 \times 10^4\,\text{m}^{-1}$. In subfigure 16.3(a), the lacking translational symmetry is clearly visible. Also in the phase pattern (subfigure 16.3(b)) this is evident whereas this structure is no longer binary but has a continuous phase in a couple of regions. Finally, subfigure 16.3(c) demonstrates that the pattern is spatially composed of five plane waves arranged on a pentagon and equally spaced from the center. Thus, the corners are on a ring indicating that the light field is nondiffracting. For the inscription process, either only the phase pattern or the phase pattern in combination with the field pattern can be employed. The main aspect between both variations is small differences regarding the intensity distribution of the light field. Consequently, both are capable to form a Penrose pattern that is quasiperiodic and has similar light redistribution properties.

Figure 16.4 depicts phase contrast and bright field images of a pattern inscribed in PDR1MA. The writing process takes $120\,\text{min}$ and is carried out with an intensity in the sample plane of $189\,\text{mW}\,\text{cm}^{-2}$. Phase contrast (subfigure 16.4(a)) and bright field image (subfigure 16.4(b)) clearly depict the successful inscription process. The phase-contrast image provides information on the refractive index and height modulation. Additionally, the bright field image visualizes the absorption modulation of the film. This modulation originates on the one hand from the thickness variations of the film and is thus an additional proof of the existence of an SRG. On the other hand, the dye parts of the polymer chains may lose their absorption because they are either destroyed [213] or excited to triplet states and thus relaxation is slow due to the spin-forbidden transition [236].

Again, this film is analyzed via stylus profilometry and also a height modulation of $l = (50 \pm 5)\,\text{nm}$ is obtained. Due to the nature of the Penrose pattern, the structure parameter cannot be directly characterized by simply measuring from one repeat unit to another. The reason is the lacking periodicity. Thus, the only way is the analysis of the components in the frequency domain that can be obtained by the FFT of the phase contrast or bright field images. As expected, the structure parameter does not vary from the quantity of the incident light pattern.
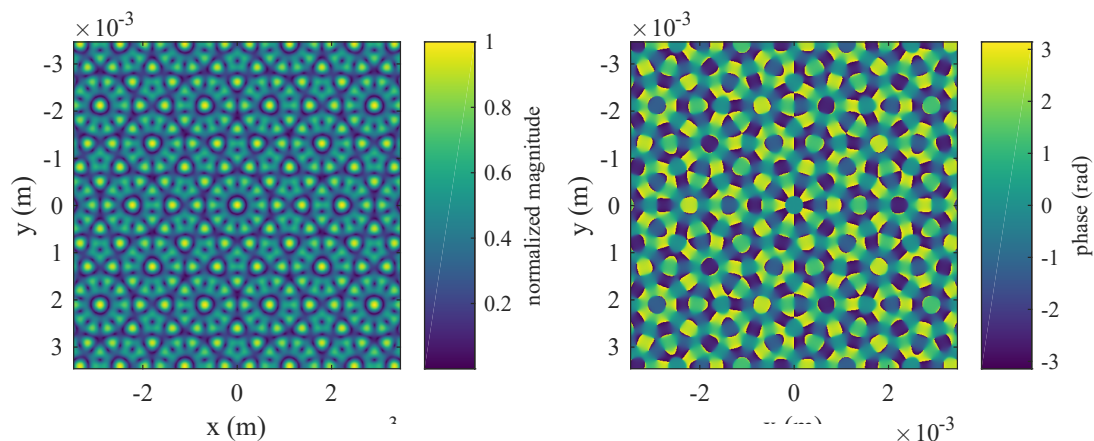
(a) Normalized absolut
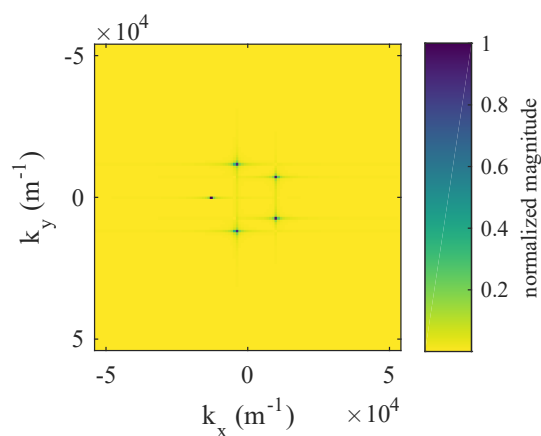
(c) Normalized spectral components.

Figure 16.3: Normalized absolute data of the field information of a Penrose pattern with a structure parameter of $250\,\mu m$ corresponding to a ring diameter in frequency space of $K = 2.51 \times 10^4\,m^{-1}$ (a). Subfigure (b) contains the corresponding phase information while (c) contains the spectral composition where the magnitudes are also normalized.
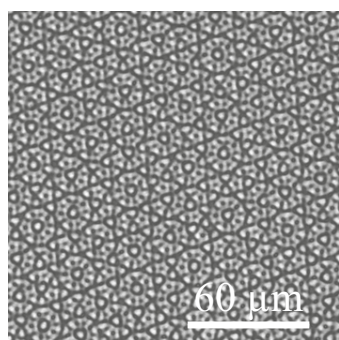
(a) Phase contrast image.
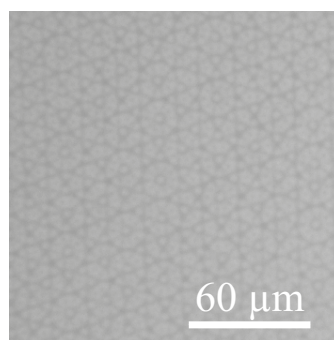
(b) Bright field image.

Figure 16.4: Phase contrast (a) and bright field image (b) of a Penrose pattern with a structure parameter of $3.5\,\mu m$ corresponding to a ring diameter in frequency space of $K = 1.80 \times 10^6\,m^{-1}$.

16.4 Cobblestone pattern – continuous frequency spectrum

Another approach to enhance the spatial redistribution of light is the expansion of the components in the frequency domain and thus allow for a spectrally broad redistribution. To achieve this goal, completely new pattern types are developed or existing patterns are modified. A simple strategy is to randomize one of the parameters of a given pattern. For example, this can be amplitude, spacing, or even both. In the actual case, the amplitude of a square or checkerboard pattern is randomized. Due to the similarity to pavings in cities, it is called "cobblestone" pattern. For the generation, a different technique for the calculation of the field distribution is developed. The nondiffracting beams are generated via superposition of plane waves. In contrast, the fundamental approach in cobblestone pattern development is the convolution of a Gaussian beam profile with a pattern containing the height information[1]. The latter is generated via setting single pixels of a zero-valued 2D array[2] to the desired relative height value.

Actually, each 18th pixel in each row of the array is set to a random value in the interval $[-1,1]$. Negative values are set in an alternating fashion with positive ones to additionally modify the phase of the pattern and consequently enhance the quality. The spacing of $18\,px$[3] combined with a pixel pitch of $6.4\,\mu m$ of the PSLM leads to an effective spacing of $115.2\,\mu m$ at the modulator and thus $11.52\,\mu m$ in the sample plane. Another crucial parameter is the size of the Gaussian beam that is employed in the convolution since it determines the width of the troughs and also the overall light intensity employed for illumination of the sample. For this inscription process the full width at half maximum (FWHM) of the beam is set to $8.9\,\mu m$ in the sample plane and thus $89\,\mu m$ at the modulator surface.

Subfigures 16.5 (a)-(c) depict field distribution, phase, and spectral components of a cobblestone pattern with an adapted spot spacing of $250\,\mu m$. The spectrum in subfigure (c) illustrates the broadening of the sharp frequency peaks of the underlying square pattern due to the randomization of the amplitudes. The FWHM of the Gaussian beams is proportionally scaled to maintain the relations to the previously described dimensions. Subfigure 16.5(d) finally provides a phase contrast image of an inscribed pattern in PDR1MA. The inscription process is carried out for $180\,min$ at an intensity of $90\,W\,cm^{-2}$. Due to the nature of the pattern, the maximum writing intensity decreases to this value and consequently the elongated inscription time is adapted. Height analysis via stylus profilometry reveals a maximum height difference in the scanned area of $\Delta l = 25\,nm$. Here, of course only a maximum value can be provided because all other heights between zero and this maximum should also occur on the patterned area. In general, a randomized height pattern has lower (maximum) height modulations than a pattern with equal intensity spots. This is due to the migration process, since ridges are formed via contributions of multiple high intensity spots. Consequently, if a high intensity spot is neighbored by a low intensity spot, the former will still create the same

---

1   For the sake of computational speed, the convolution theorem is applied and thus the spectra of both patterns are multiplied.
2   The dimensions of the array are typically suited to the resolution of the modulator or rather the region of the modulator to be used.
3   Here, px is employed as abbreviation for pixel.
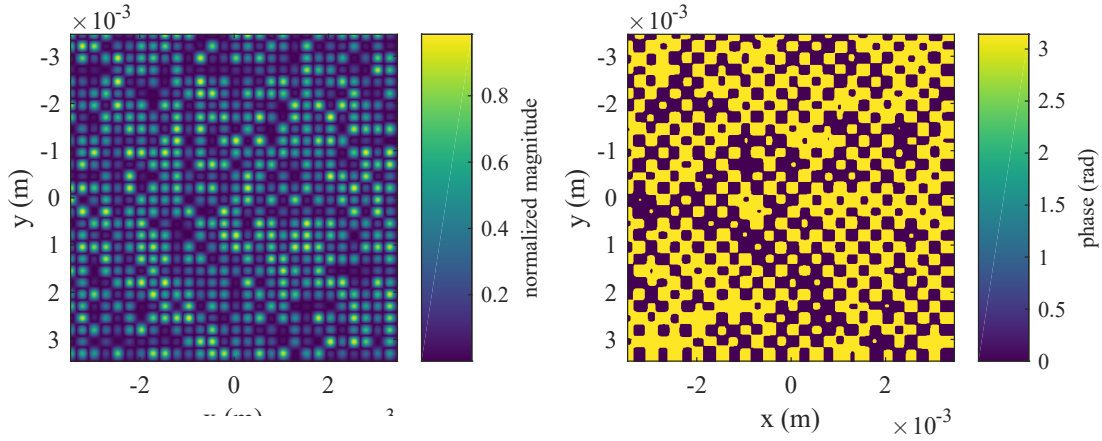
(b) Phase information.
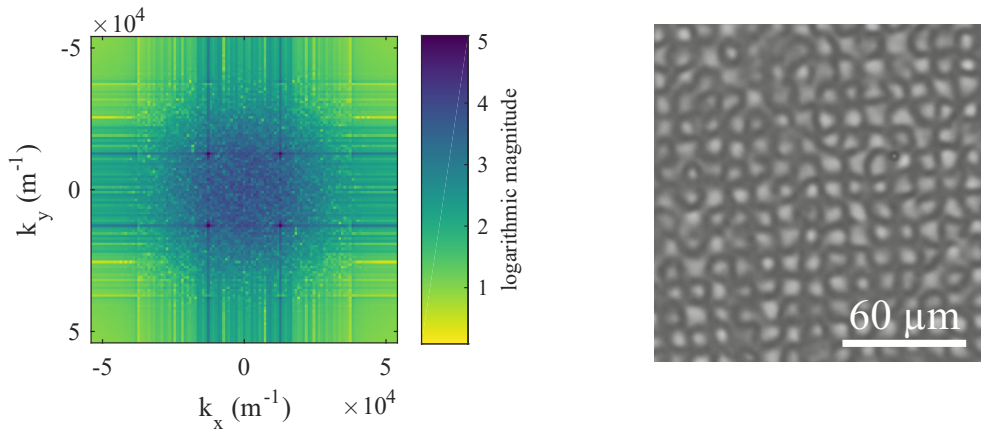
(c) Normalized spectral components.

(d) Pattern in PDR1MA.

Figure 16.5: Normalized absolute data of the field information of a cobblestone pattern with a spot spacing of $250\,\mu m$ (a). Subfigure (b) contains the corresponding phase information while (c) contains the spectral composition where the magnitudes are also normalized. In (d), a phase contrast image of a realized pattern with a different spacing in PDR1MA is provided.

trough but the material that forms the ridge is less due to the reduced contribution of the low intensity spot.

One issue clearly observable in subfigure 16.5(a) is the irregular distribution of the random heights. There are small aggregations of high intensity spots and those of low intensity. Additionally, there are larger ones consisting of spots exhibiting almost half of the maximum intensity. Of course, the present distribution is still random[1] but other distributions may spread the different values better over the surface and thus provide a random pattern whereas the height information is spread more homogeneously.

---

1 The randomness crucially depends on the quality of MATLAB's standard generator for uniformly spread random numbers.

16.5 Vogel spiral patterns – mimicking nature

Vogel spiral patterns look like the head of a sunflower and they are named after the mathematician Helmut Vogel who provided an adequate construction rule [95, 237]. The structure itself is completely aperiodic and the spatial components provide a broad distribution. The construction of the pattern regarding to Vogel is realized via setting the n-th spot in a polar coordinate system according to

$$r_n(\rho,\phi) = \left(c \cdot \sqrt{n}, n \cdot \theta\right) , \tag{16.1}$$

where ρ is the radial position of the current spot, ϕ is the angle, c is a scaling factor, and $\theta \approx 137.5°$ is the golden angle. In order to set all spots within a unit circle, $c = 1/\sqrt{n_{\text{tot}}}$ whereas n_{tot} is the total number of spots to be set. Following the construction rule, pixels at the respective position in a zero-valued 2D array are set to one and subsequently convolved with a profile of a Gaussian beam, i.e., the same routine as in case of the cobblestone pattern.

Subfigure 16.6(a) depicts a Vogel spiral pattern with a spot spacing of 250 µm that is created following the routine described above. Although there is no clear systematic order that defines the spot spacing, the uniform distribution of spots over a certain area allows to create a pattern on a spacing parameter. The parameter Δd is given by the relation

$$\Delta d = \sqrt{\frac{A_{\text{PSLM}}}{n_{\text{Spot}}}} , \tag{16.2}$$

whereas A_{PSLM} is the employed area of the PSLM and n_{Spot} is the number of spots to be placed on this area. The only variation with respect to the original generation recipe is the modification of the phase that is depicted in subfigure 16.6(b). During construction, each point obtains an additional phase contribution that corresponds to its angle on the spiral. As a consequence, the whole spiral is a vortex pattern where the center of the vortex corresponds to the center of the spiral. The reason for adding the momentum was originally a slight enhancement of the contrast and a suppression of boundary effects. Later, the convolution technique is modified by calculating on larger arrays. Consequently dramatic improvements regarding bright-to-dark contrast and edge-effect suppression are achieved.

The frequency spectrum depicted in subfigure 16.6(c) provides several components that contribute to the pattern formation. While there is a large constant component at the center, also a very concise ring is prominent [238]. The ring diameter is approximately twice as large as the the diameter of $K = 2.51 \times 10^4 \, \text{m}^{-1}$ which corresponds to the spacing of $\Delta d = 250$ µm. The former partially originates from a slight amplitude offset observable in the spiral pattern (subfigure 16.6(a)) and is caused by by the superposition of the tails of the Gaussian beams. The latter hints to the spiral nature of the pattern indicating that the patten is close to radial symmetry. But this symmetry is not evident because of the irregular nature of the golden angle that does not allow to achieve the same pattern via rotation of an angle $\theta \neq 360°$. The phase-contrast image in subfigure 16.6(d) proofs the successful inscription of an SRG into PDR1MA. The inscription process is
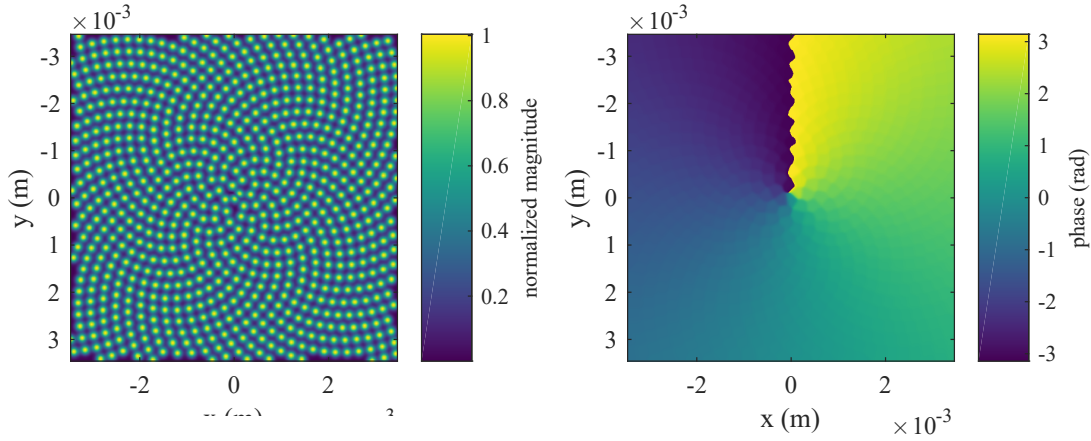
(b) Phase information.
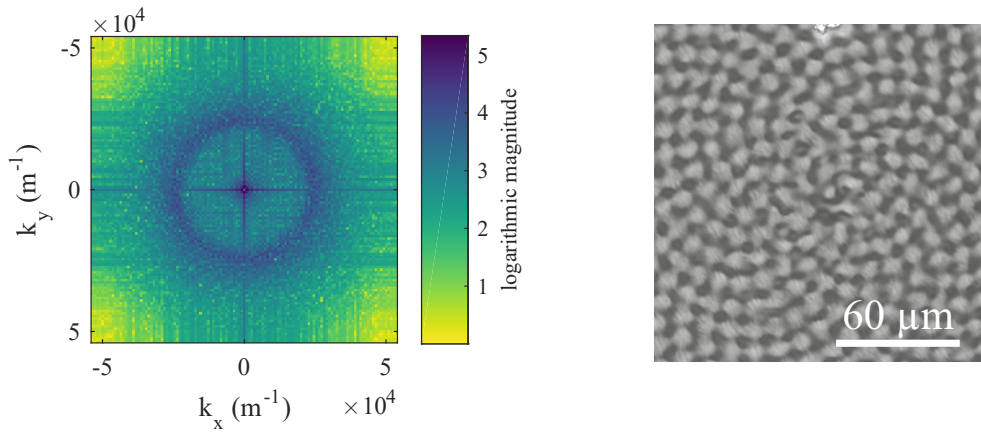
(c) Normalized spectral components.

(d) Pattern in PDR1MA.

Figure 16.6: Normalized absolute data of the field information of a Vogel spiral pattern with a spot spacing of $250\,\mu m$ (a). Subfigure (b) contains the corresponding phase information while (c) contains the spectral composition where the magnitudes are also normalized. A phase contrast image of a realized pattern with a different spacing in PDR1MA is provided in (d).

carried out with an intensity of $189\,\text{mW}\,\text{cm}^{-2}$ for $120\,\text{min}$. The the spot spacing in the sample plane is set to $\Delta d_{\text{insc}} = 11.4\,\mu m$ combined with a FWHM of the Gaussian beams of $7.1\,\mu m$. Profilometry reveals a height modulation of $\Delta l = (30 \pm 10)\,\text{nm}$ and a spacing of $(11 \pm 2)\,\mu m$ perfectly matching the value set during the writing process.

Subfigure 16.7(a) depicts the top view of a height profile of nine Vogel spiral patterns in PDR1MA that is written sequentially via spatial multiplexing with the help of the x-y-shift of the experimental setup. This technique enables to structure also larger areas of polymer. The drawback of this approach is time consumption since there is no speed-up effect and each pattern takes its specific duration. Subfigure 16.7(b) represents a 3D visualization of a part of the scan on the left side. The bright spots that are also very high result from small particles that stick on the polymer film and thus the height scale does not match to the modulation achieved by the writing process. Additionally, the connections between the single patterns form small ridges because of the sequential

(a) Top view of nine sequentially written Vogel spiral patterns.

(b) 3D representation of a subset of the profile in subfigure 16.7(a). The red square approximately indicates the origin of the data.
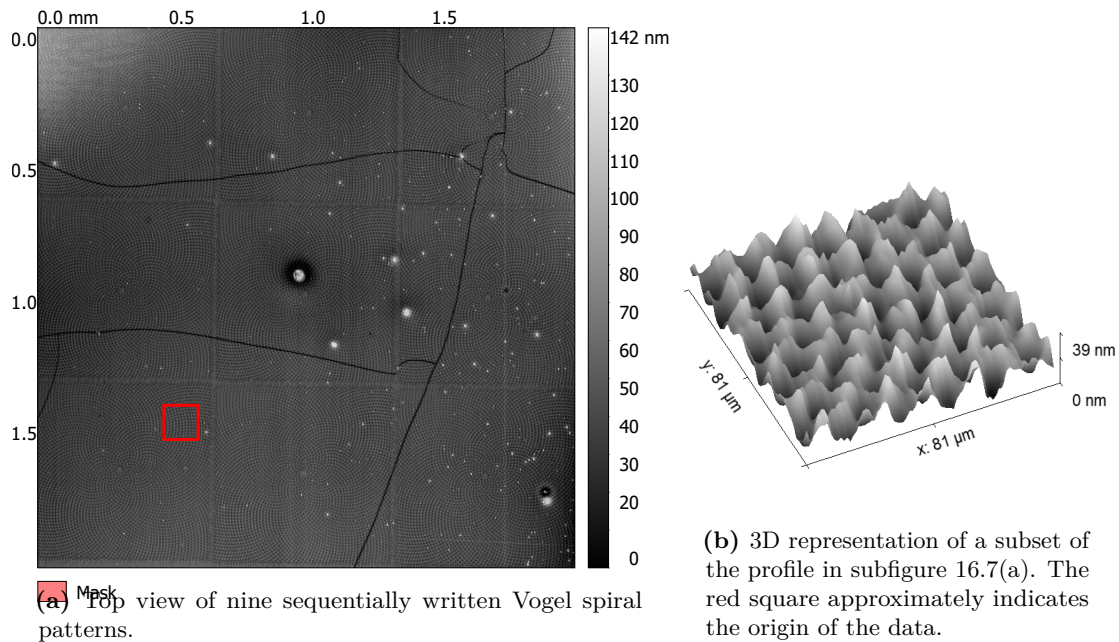
Figure 16.7: Height profiles of Vogel spiral patterns. Data is obtained via stylus profilometry by staff members of the group of Dr. Frank Berkemeier, Institute of Materials Physics, WWU Münster.

writing technique. This effect can be reduced if the patterns are not written completely in one step. Instead, a switching process between the single patterns allows a more parallelized structure formation process. Thus, a reduction or even avoidance of edge effects is expected. As a consequence of this approach, a highly precise x-y-shift is necessary to guarantee exact repositioning and therefore tolerances have to be on the nm scale. This is of special importance if the structure is further reduced by demagnification and even more sequential steps are needed to modulate areas on a mm^2-scale.

The 3D representation on the right part of figure 16.7 illustrates that the ridges between the deep spots do not have the same height but vary to a certain amount. Additionally, they are very similar to peaks of mountains. Partially, this effect is attributed to the stylus of the profilometer and not caused by the writing process. Consequently, the exact geometry of the hills and also its maximum height is not known but may be resolved by a more sensitive technique. In turn, the valleys possess an almost Gaussian shape (not shown).

An alternative to stylus profilometry is AFM. This is typically the technique of choice for height characterization. However, the limited lateral transverse path makes it difficult to resolve multiple features of the pattern in one scan and thus to evaluate the height information and feature shape. In turn, if the structure size is decreased, AFM can become the approach of choice for analysis.

Another technique to proof the existence of an SRG is the structure transfer into another material. Considering the structures to be employed on top of solar cells, pattern transfer into a transparent material is needed. Thus, the transparent polymer PDMS is chosen. The transfer process and proof of its success is provided in the following chapter.

17 Molding of SRGs into PDMS

In order to proof the existence of SRGs and to fabricate light redistributing films for solar cells or patterned substrates for arbitrary applications, the structures are casted in a mold. The chosen material to take up the surface reliefs is PDMS, i.e., Sylgard® 184 from *Dow Corning*. Prior to processing, PDMS has to be prepared. When delivered it consists of two components, i.e., the base and a curing agent. The ratios of both components vary between 10:1 and 5:1 depending on the desired stiffness. Here, the typical ratio of 10:1 is chosen to preserve enough elasticity to avoid damage of the film during the lift-off process. Figure 17.1 illustrates the employed technique to fabricate patterned PDMS. The first part depicts the structured illumination of an azopolymer
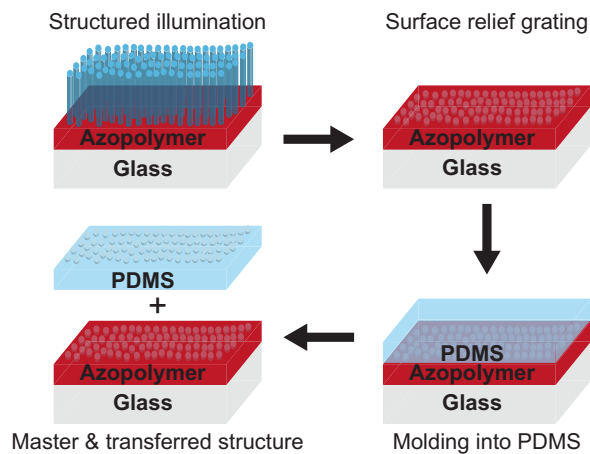
Figure 17.1: Schematic illustration of the PDMS patterning process. After the azopolymer is structured, PDMS is poured on the film. Finally, the PDMS is patterned, whereas the azopolymer also keeps its structure.

film on glass substrate, i.e, the previously described patterning process. Subsequently, PDMS is poured onto the film. In general, this can be achieved by spin coating of PDMS onto the azopolymer and consequently very low film thicknesses are achieved. For the sake of manageability of the final films, a larger thickness (approx. 1 mm) is chosen. This is achieved by wrapping of adhesive tape around the edges of the glass substrate so that a pan is formed by tape and substrate. This pan acts as a container for the PDMS and avoids drain of the material during the subsequent baking process. The latter is employed to speed-up the cross-linking process that is strongly temperature dependent. Thus, the substrate covered with PDMS is put in an oven and heated up to 60 °C for 60 min. After cooling down to avoid damage to the azopolymer film, the elastic PDMS film can be lift off and finally characterized. In turn, the azopolymer film can again act as a master as far as the pattern is still in good condition.

Figure 17.2 demonstrates the successful transfer of all tested structure types into PDMS. While Bessel, cobblestone, and Vogel spiral patterns can be directly recognized,
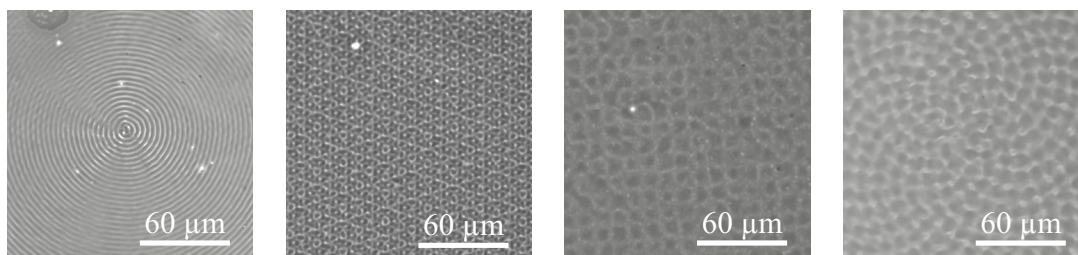
Figure 17.2: Phase contrast images of Bessel, Penrose, cobblestone, and Vogel spiral patterns that are transferred into PDMS (f.l.t.r).

this is more difficult for the Penrose pattern. The observed features seem to be different to the pronounced circular structures of the light field. This effect is explained by the fact the pattern in PDMS is the inverse of the structure in the azopolymer. As a consequence, the colors in the image are reversed with respect to the usual use, and thus it is more difficult to recognize the pattern. Here, the brighter areas are typically dark and vice versa. Additionally, the refractive index contrast is much weaker since the PDMS pattern only contains the height pattern and not the refractive index pattern that is present in the bulk of the azopolymer. The described effects are also present in case of the other patterns. However, they are easier to recognize due to their shape.

All in all, the generation of complex 2D patterns in azopolymer film and their transfer into PDMS is proven. The employed setup allows for creation of arbitrary structures and thus enables to follow a rapid-prototyping strategy. Limits so far are the comparably low height modulation resulting mainly from a low azopolymer-film thickness and the lower limit of the lateral spacing or feature size. In order to further reduce the latter, stronger demagnification and a lower pixel size of the PSLM are needed. Ideally, a higher resolution is also beneficial as it allows for patterning of larger areas.

Due to the lacking stability of the solar cells, the effect on the PCE could not be tested. That is why a simulations of the light propagation through a stack made of a thin patterned PDMS film on top of a glass substrate is simulated. Detailed information regarding the employed model and technique as well as the obtained results are provided in the next chapter.

18 Modeling of light propagation through patterned surfaces

In order to analyze the influence of a structured PDMS layer on the light redistribution, FDTD simulations of plane waves propagating through a stack of a PDMS film and a glass substrate are performed. There are multiple other techniques (rigorous coupled-wave analysis (RCWA) [239], finite element method (FEM) [240], etc.) to carry out light propagation simulations. However, FDTD is chosen because it is neither limited to small angles of incident nor to periodic structures. Thus, FDTD is suited to simulated different positions of the sun throughout the day or year. FEM is even more powerful, but due to its higher complexity it is not as easy to start as FDTD. Additionally, there was no known open source implementation of FEM available when the simulations were carried out. Consequently, the openEMS package [241] developed by Thorsten Liebig, University of Duisburg-Essen, is employed. The software is permanently developed further, bug reporting to the developer is easy, and bugs are fixed rapidly. Additionally, the modeling process process can be completely carried out in MATLAB. Thus it is possible to employ exactly the same structures used for optical induction in azopolymers. Another great advantage of this package is that it works with SI units and consequently the adaption of real dimensions becomes much easier.

Bessel, Penrose, cobblestone, and Vogel spiral patterns are compared regarding their light redistribution capabilities. The aim of the simulation is to find grating parameters that allow to diffract as much light as possible into transverse directions. Simultaneously homogeneous illumination of the solar cell has to be maintained and thus light concentration has to be avoided. Hence, the lateral field distributions and the tilt of the light field vectors are analyzed and compared.

18.1 FDTD technique

The FDTD method is a technique to solve time-dependent differential equations whereas the most prominent use case is the solution of Maxwell's equations. The technique was first proposed by the Chinese American mathematician Yee [242] in 1966. Employing the general approach, several problems involving electromagnetics can be solvend via this method. The basic idea is to subdivide the simulation volume into many small so-called Yee cells forming a Yee grid, and calculate the solution of Maxwell's equations for all of the faces of the simulation unit. A scheme of such a Yee grid is provided in figure 18.1. Here the different fields are indicated by different colors, i.e., the electric field E in red and the magnetic field H in green. Both fields are shifted by half a cell length with respect to each other. As a consequence, the components of the magnetic field are located as centered face normals on the subcell of the electric field whereas the components of the latter are located at the edges. The relation is reversed if the subcell of the magnetic field is considered. The basic technique of FDTD is to solve the
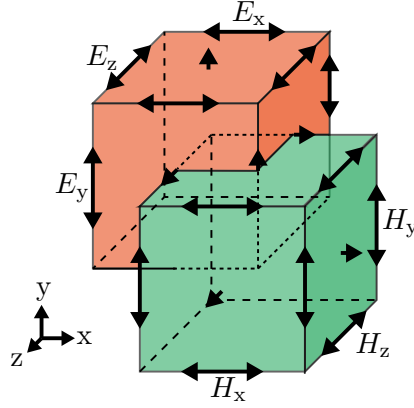
Figure 18.1: Schematic representation of a Yee grid that consists of two Yee subcells. Inspired by the scheme of the Yee cell drawn by the Wikipedia user FDominec[a] and the original publication by Yee [242].

---

macroscopic Maxwell's equations [243, 244]

$$\vec{\nabla} \cdot \vec{D} = \rho + \vec{\nabla} \cdot \vec{P} \ , \tag{18.1}$$

$$\vec{\nabla} \cdot \vec{B} = 0 \ , \tag{18.2}$$

$$\vec{\nabla} \times \vec{E} = -\frac{\partial \vec{B}}{\partial t} \ , \text{ and} \tag{18.3}$$

$$\vec{\nabla} \times \vec{H} = \vec{j}_{\text{free}} + \frac{\partial \vec{D}}{\partial t} \tag{18.4}$$

alternately for electric and magnetic field since both depend on each other and on their respective previous value. In these fundamental equations, $\vec{E}$ denotes the electric field, $\vec{B}$ the magnetic field, $\vec{D} \equiv \varepsilon_0 \vec{E} + \vec{P}$ is the electric displacement field, $\vec{H} \equiv 1/\mu_0 \vec{B} - \vec{M}$ corresponds to the magnetic field strength, and $\vec{j}_{\text{free}}$ is the current. Additionally $\vec{P}$ is the induced polarization, $\vec{M}$ the magnetization of the material, ε_0 the permittivity in vacuum, and μ_0 the permeability in vacuum.

18.2 Simulation parameters and the PDMS-glass model

In order to simulate light propagation through material, the whole model has to be created. The materials have to be defined by their permittivity ε and permeability μ. Here, instead of the permittivity, the refractive index n is employed via $\varepsilon = n^2$. In turn, the magnetic permeability is considered to be $\mu = 1$. Since simulation of an infinite grid is impossible, appropriate boundary conditions have to be defined due to limited computational resources. Further, the available memory of the computer directly influences the size of the whole simulation volume. Simulation speed is influenced by

the volume, and the speed of memory and processor of the computer. As a compromise, the volume is set to $24 \times 24 \times 80 \, \mu m^3$ since this size allows computation on conventional desktop computers in a reasonable amount of time (several hours to days). Another crucial parameter is the grating parameter of the Yee grid that has to be chosen to be small enough, i.e., smaller than the wavelength of the impinging plane wave. Consequently, the lattice resolution is set to 160 nm in the transverse direction and 50 nm in propagation direction. Along the latter, the volume consists of two materials, a structured PDMS layer (50 μm thickness, refractive index $n_{PDMS} = 1.41$) and 30 μm of glass (refractive index $n_{glass} = 1.50$). The latter partially represents the substrate of a solar cell. Due to the limited computational resources, it is impossible to set up a model based on dimensions close to the actual device. Figure 18.2 depicts the described material stack and its dimensions. As an example structure, the bottom of the PDMS film has a
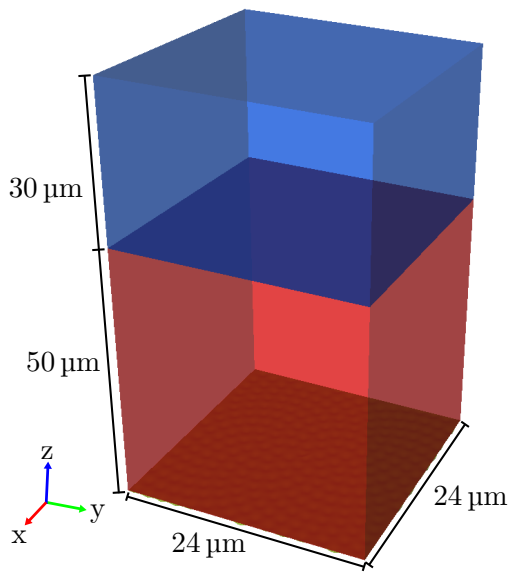
Figure 18.2: Schematic representation of the cuboid simulation volume. The red part indicates the structured PDMS film. Exemplarily, a Vogel pattern is used. The blue part on top depicts the glass layer. Incident waves travel along the z-direction from bottom to top.

Vogel spiral pattern. Throughout all simulations, the overall thickness of the stack is kept constant whereas the modulation height of the pattern is varied. The plane wave illumination starts 0.5 wavelengths in front of the pattern. In order to avoid reflections at the output side, 8 perfectly matched layers (PMLs) are attached to the material. The number of the PMLs is chosen to be a good compromise between computational cost and accuracy. Additionally, the faces in x- and y-direction are configured as perfect magnetic conductors and perfect electric conductors, respectively. Hence, the material stack forms a waveguide for the light because its linear polarization is chosen to be along the x-direction. The wavelength of the illuminating plane waves is set to $\lambda = 500 \, nm$ due to the proximity to the peak position of the solar spectrum. The amplitude is set to $E_{ex} = 0.5 \, V \, m^{-1}$. The simulation itself is carried out for 5000 time steps, each is $1.561 \times 10^{-4} \, ps$ long and thus yielding the overall simulation time of 0.758 ps.

18.3 Visualization of redistributed light

In order to visualize the light propagation through the volume, cross sections ($24 \times 24 \, \mu m^2$) normal to the z-direction of the stack are taken. The position of these cross sections is

79.50 μm far above the origin of the plane wave illumination. The data of the obtained field magnitudes (proportional to the square root of the light intensity) are averaged over 2200 time steps. As a starting point, light redistribution of the patterns experimentally realized (cf. chapter 16) are simulated and depicted in figure 18.3. The scalebar on the right side is fixed for this and the following figures. This allows an easier comparison of the different types and parameters. The disadvantage of this procedure is the low contrast, especially in subfigures 18.3(c) and 18.3(d). The maxima of the magnitudes are listed in table A.4 in the appendix.

(a) Bessel:
$\Delta d = 3.5\,\mu m$,
$\Delta l = 50\,nm$.

(b) Penrose:
$\Delta d = 3.5\,\mu m$,
$\Delta l = 50\,nm$.

(c) Cobblestone:
$\Delta d = 11.5\,\mu m$,
$\Delta l = 25\,nm$.

(d) Vogel spiral:
$\Delta d = 11\,\mu m$,
$\Delta l = 25\,nm$.
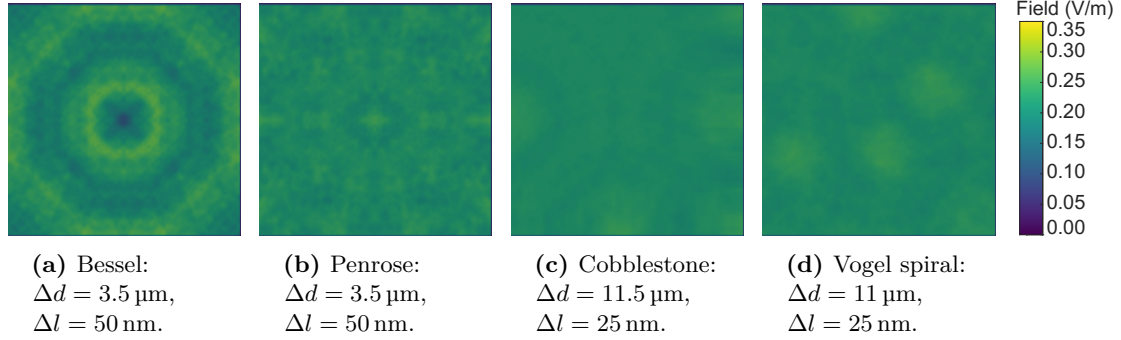
Figure 18.3: Redistributed field magnitudes for the experimentally realized patterns with their corresponding structure size Δd and modulation height Δl.

Due to their different structure sizes Δd and modulation heights Δl, no conclusion can be made regarding the superiority of one of the pattern types in general. First of all it is of importance that the patterns influence the light at all. This is the case for all patters but is most prominent for the Bessel pattern in subfigure 18.3(a) and the Penrose pattern in subfigure 18.3(b). In contrast, the cobblestone pattern in subfigure 18.3(c) and the Vogel spiral in subfigure 18.3(d) perform much less. This behavior is clearly attributed to the lower modulation height of the cobblestone and Vogel patterns. But also between the two former are differences. The Bessel pattern provides a much larger magnitude contrast, which is not so pronounced for the Penrose pattern. This is explained by the nature of the structure since its character is not binary and thus the magnitude differences are less in diverse regions of the pattern. Especially the flower-like structure in the center (cf. subfigure 16.3(a)) has one maximum at the center while the others have a significantly lower amplitude and thus the modulation height in this regions is also lower. A similar case can be observed for the cobblestone pattern. The random height distribution not necessarily generates spots that are close to the maximum amplitude. This especially holds for the small sample size of only five remarkable spots in this case. The Vogel spiral pattern provides moderate modulation but due to the low number of spots, large regions are only poorly modulated. Comparing the Vogel pattern with the Penrose pattern, the maximum amplitudes are very close ($0.249\,\mathrm{V\,m^{-1}}$ and $0.252\,\mathrm{V\,m^{-1}}$, respectively).

In order to analyze the impact of the amplitude, cobblestone and Vogel spiral patterns are simulated again with a height modulation of $\Delta l = 50\,nm$. The spacing parameter is kept for each pattern. The resulting cross sections are depicted in subfigure 18.4(c) and 18.4(d). Here, the magnitude modulation by the cobblestone pattern is significantly increased. In contrast, the magnitude distribution caused by the Vogel spiral pattern

(a) Bessel:
$\Delta d = 3.5\,\mu\text{m}$,
$\Delta l = 50\,\text{nm}$.

(b) Penrose:
$\Delta d = 3.5\,\mu\text{m}$,
$\Delta l = 50\,\text{nm}$.

(c) Cobblestone:
$\Delta d = 11.5\,\mu\text{m}$,
$\Delta l = 50\,\text{nm}$.

(d) Vogel spiral:
$\Delta d = 11\,\mu\text{m}$,
$\Delta l = 50\,\text{nm}$.

(e) Bessel:
$\Delta d = 3.5\,\mu\text{m}$,
$\Delta l = 250\,\text{nm}$.

(f) Penrose:
$\Delta d = 3.5\,\mu\text{m}$,
$\Delta l = 250\,\text{nm}$.

(g) Cobblestone:
$\Delta d = 11.5\,\mu\text{m}$,
$\Delta l = 250\,\text{nm}$.

(h) Vogel spiral:
$\Delta d = 11\,\mu\text{m}$,
$\Delta l = 250\,\text{nm}$.
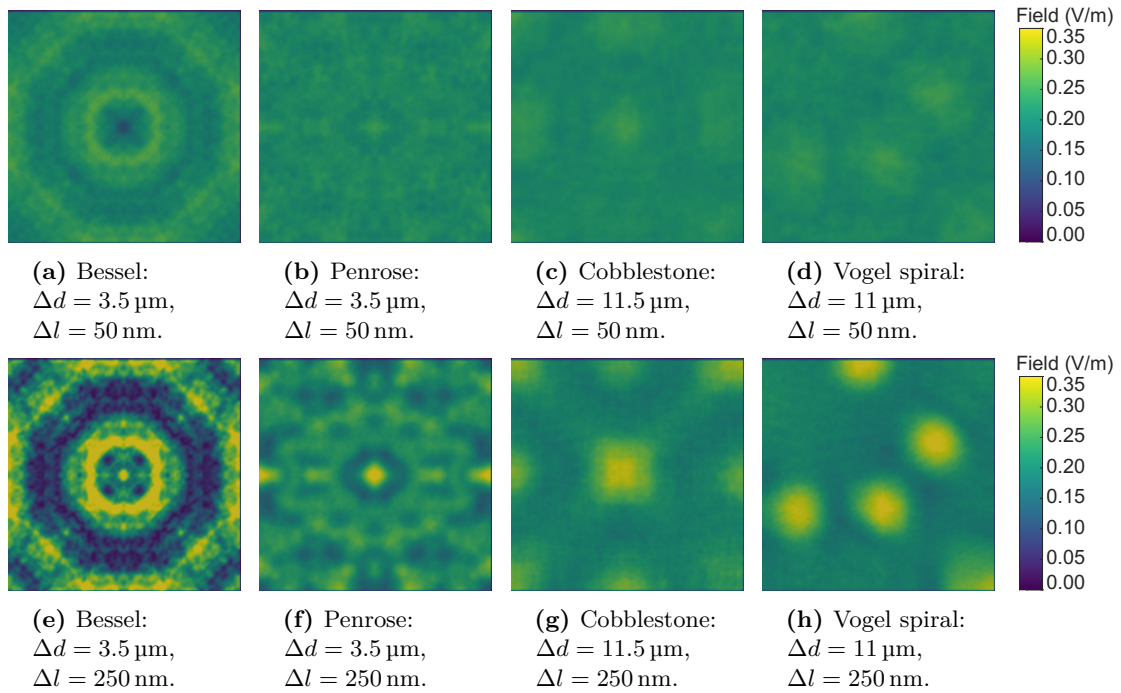
Figure 18.4: Redistributed field magnitudes for the experimentally realized patterns with their corresponding structure size Δd and modulation height Δl.

has changed only slightly. Consequently, the height modulation is significantly raised to 250 nm. This value is chosen, because patterns with this modulation height are achieved via two-beam interference (cf. chapter 15). This is also considered to be realizable via the PSLM method if an appropriate film thickness is prepared. The corresponding cross sections through the simulation volume are displayed in subfigures 18.4(e) to 18.4(h). It has to be mentioned that high intensities are cut-off to maintain the same scalebar for all cross sections (cf. table A.4).

Subfigure 18.4(e) impressively demonstrates the effect of an increased modulation height as the magnitude on the smaller ring is drastically raised. This also holds for the other patterns but the effect is not as pronounced as in case of the Bessel pattern. It is also remarkable that the Bessel pattern tends to focus the light on rings. Additionally, there are also rings which almost lost their field magnitude. This supports the assumption that the pattern acts similar to a Fresnel axicon, because the resulting profile is close to a Bessel beam. In turn the Penrose pattern has gained an intense peak at the center whereas the rest of the pattern has got high-contrast but the lateral redistribution remains still rather low.

The spots of cobblestone and Vogel spiral patterns also gain intensity. However, the light is not redistributed homogeneously. As a consequence, in another simulation, the spacing parameter Δd is varied and set to $\Delta d = 1.5\,\mu\text{m}$ while the height modulation of $\Delta l = 250\,\text{nm}$ is maintained. The value of $\Delta d = 1.5\,\mu\text{m}$ is chosen because it can be experimentally realized with modifications of the demagnification part of the setup. Cross sections of this simulation runs are provided in figure 18.5. Here, especially the Bessel pattern in subfigure 18.5(a) has a dramatically overexposed spot at the center and

(a) Bessel:
$\Delta d = 1.5\,\mu m$,
$\Delta l = 250\,nm$.

(b) Penrose:
$\Delta d = 1.5\,\mu m$,
$\Delta l = 250\,nm$.

(c) Cobblestone:
$\Delta d = 1.5\,\mu m$,
$\Delta l = 250\,nm$.

(d) Vogel spiral:
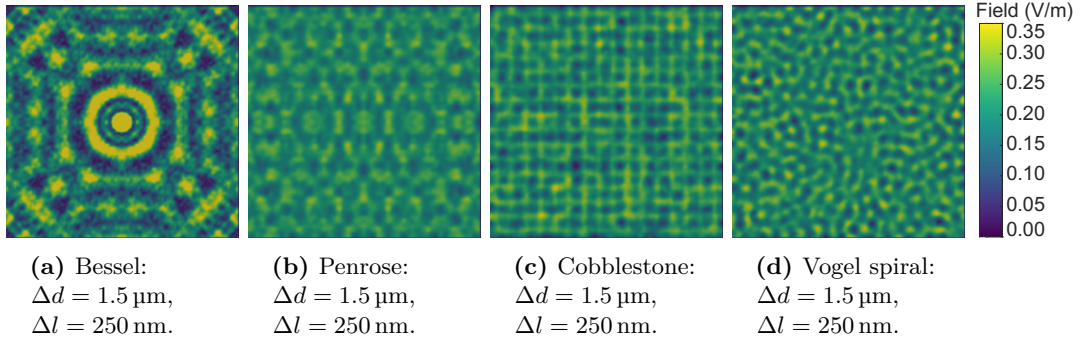$\Delta d = 1.5\,\mu m$,
$\Delta l = 250\,nm$.

Figure 18.5: Redistributed field magnitudes for the experimentally realized patterns with their corresponding structure size Δd and modulation height Δl.

also the inner ring is overexposed. In contrast, the residual parts either have a moderate magnitude or almost none. Again, this axicon-like behavior makes the Bessel pattern better suited for applications where high light intensities are desired, e.g., concentrator solar cells. In turn, the distribution of the other patterns has become more fine grained and distributed all over the cross section.

The Penrose pattern in subfigure 18.5(b) still provides certain regularity, i.e., several structural repetitions in a lateral direction. In turn, the rotational symmetry is lost. The latter may be due to reflections from the sides that are caused by the waveguide configuration. This effect is also present in case of the other patterns and can be best observed for the Bessel pattern where the reflections lead to the transfer from most of the rings to dotted stripes that are parallel to the edges of the cross section.

In case of the cobblestone pattern (subfigure 18.5(c)), the described effect does not occur due to the rectangular nature of the pattern. However, as the parameters that are the base of this pattern are comparable to the others, the magnitude pattern is also a superposition of the original pattern with reflection from the sides. Anyhow, the pattern still looks more or less similar to an inverted cobblestone pattern. In contrast, the Vogel pattern in 18.5(d) does not have much in common with a spiral as it is randomized. Here, the reflections at the waveguide edges play a larger role and thus the superposition leads to the formation of the randomized pattern.

In order to characterize the redistribution capabilities of the patterns, the cross sections as images are not sufficient because they make an absolute comparison between the patterns difficult. As a measure to differentiate the redistribution potential the sum of the absolute value of the z-components of the electric field polarization are taken. This is possible since the simulation is based on vectorial quantities and thus allows to determine how large the z-component induced by the SRG is. In table 18.1, the data of the E_z components of the cross sections of figure 18.3 (column **1**), subfigures 18.4(e) to 18.4(h) (column **2**), and figure 18.5 (column **3**) are listed. The data in the table partially reflects what is already known from the cross sections. The Bessel patterns provide the strongest redistribution. However, considering the cross sections, the patterns are only suited if strong localization of the intensity is desired. Consequently, the Bessel pattern is neglected in the following comparisons. The Penrose pattern in turn provides moderate redistribution properties over the employed parameter space. It is superior

Table 18.1: Absolute values of the sum of the E_z-components for the different patterns. Here column **1** corresponds to the patterns in figure 18.3, column **2** to the patterns in subfigures 18.4(e) to 18.4(h), and column **3** to patterns in figure 18.5.

Type	**1** E_z (a.u.)	**2** E_z (a.u.)	**3** E_z (a.u.)
Bessel	41.92	197.82	303.93
Penrose	32.83	78.13	153.99
Cobblestone	11.25	38.86	173.32
Vogel spiral	14.84	38.68	223.83

over cobblestone and Vogel spiral pattern in columns **1** and **2**. This relation is reversed in column **3**. Of course, the superiority of the first two cases is attributed to the stronger modulation and the smaller feature size of the Penrose pattern. Both modifications have a significant influence on the change of the E_z component as the comparison of the data of the Penrose pattern indicates. Comparing only cobblestone pattern and Vogel spiral, only slight differences are observed. Both patterns base on almost the same spacing parameter and the same modulation height. Consequently, they are equally suited regarding the parameters in the first two columns.

In column **3**, the Vogel spiral pattern provides the largest E_z value[1]. The lower value of the cobblestone pattern might be caused by an unfavorable height distribution. Thus, an average over several different cobblestone patterns is beneficial to determine the impact of different distributions over the pattern. Because of the large amount of computation time for the simulation of multiple cobblestone patterns, this step is omitted. Finally, this analysis reveals that both, lateral spacing and height modulation, play a crucial role for maximizing light redistribution. Whereas the spacing is limited by the employed devices, the thickness of the azopolymer film is one limiting factor of the achievable height modulation. Both parameters $\Delta d = 1.5\,\mu\text{m}$ (in the sample plane) and $\Delta l = 250\,\text{nm}$ are experimentally realizable after changes of the setup and film thickness. Therefore, they are considered as a reasonable choice of parameters.

Another quantity of importance is the wavelength or wavelength range the SRG is optimized for. This optimization has to occur regarding the wavelength range that is only weakly absorbed because the strongly absorbed wavelengths are already vanished after a single pass through the film. Consequently, the path for weakly absorbed light has to be increased and diffraction is a first step to increase the optical path length. If this simple elongation is not large enough, also the reflection at the bottom electrode has to be considered leading to another passage through the absorbing film. If even two-time passing does not lead to total absorption of the incident light, tailored light trapping has to be taken into account. This is achieved by simultaneous patterning of top and bottom electrode layers to maximize the number of reflections before light is coupled out of the cell. These more complex structures need also simulations of the propagation behavior within the active layer and the influence of the reflections since ideally patterns are adjusted to provide constructive interference of the wavelength of interest in the

---

1   As mentioned earlier, the Bessel pattern is not considered in this comparison.

absorbing film. To perform this kind of simulation, deeper insights regarding refractive index distributions and absorption behavior within the film are needed. This is far beyond the scope of this work and thus is not carried out.

As the introduced cobblestone pattern does not perform as well as the Vogel spiral pattern, there are multiple approaches for improvement. A first one is so-called tailored disorder that can be the strategy of choice [245, 246]. Here, the fundamental properties of the SRG are slightly changed until the desired performance is achieved. Additionally, other patterns act as a base for a height modulated pattern, e.g., hexagonal patterns or other nondiffracting beams composed of more than six plane waves. Further, also Vogel spiral patterns can be modulated regarding their peak height distribution.

Another approach slightly randomizes the lateral spacing of a pattern while the modulation is kept fix or is also randomized. Further, the FWHM of the Gaussian beam employed in the convolution step can be varied resulting in different feature diameters. Technically, the randomized height modulation is the easiest to implement as the height information is encoded in the array that is later convolved with the Gaussian beam. Lateral randomization can be realized in a similar way by shifting the location to an arbitrary direction. Here, care has to be taken to not create holes and larger hills but maintain an almost equal spacing that is only slightly varied. The difficulty with this approach is also the scaling of the magnitudes since contributions of neighboring spots sum up and thus overexposed regions are created. In turn, the magnitude in other regions is dramatically scaled down. Consequently, different approaches to distribute the spots over the area are needed. An appropriate technique would distribute the spots equally over the available space. A good example, although not random, is the Vogel spiral that inherently provides an equal distribution of the spots over the whole area.

Even more difficult is the variation of the FWHM while the modulation height is maintained. In order to create a pattern composed of features of different size, single Gaussian beams have to be added to the pattern as such kind of intensity distribution cannot be created via the simple convolution approach. A certain number of neighboring pixels set to the desired level lead to broader features than single pixels that are convolved with a Gaussian beam. But if this realization is chosen, there is again the mentioned scaling problem. Single peaks are not only broadened but they also gain higher relative peak intensities as it is the case for the laterally randomized pattern. As a consequence, a technique allowing individual scaling of the single spots is needed to overcome undesired superelevation of effective spot sizes.

19 Resume on SRG generation and light propagation

At the beginning of this part, the general patterning process is tested via inscription of a simple 1D sinusoidal pattern. It is revealed that the terminal modulation height depends on the inscription duration and intensity but also on the initial film thickness. After determination of the appropriate solvent and other processing parameters, an PSLM-based approach is employed to write more complex structures into the azopolymer films. The written structures vary from the highly symmetric Bessel pattern to the aperiodic Vogel spiral pattern. Thus, they cover parts of the so far unexplored[1] intermediate regime between periodic and completely random patterns. All types are successfully inscribed into azopolymer films and subsequently transferred into PDMS. Analysis via phase contrast microscopy and stylus profilometry reveals the successful transfer into PDMS and the absolute modulation height in the azopolymer films, respectively.

To determine the light propagation through a stack of PDMS and glass, an FDTD simulation is set up and the influence of the different patterns on light redistribution is analyzed. As a zero-order approximation, plane-wave illumination with green light linearly polarized is used in the employed model. This light source shines on a stack made of a patterned PDMS film on top of a glass substrate. Propagation through the realized patterns and additionally through those with changed parameters is simulated. Cross sections through the simulation volume at the end of the propagation length illustrate how effective the single patterns work. The Bessel-type pattern is identified to strongly localize light at the center and in the first ring around the center. Thus it is a candidate for concentrator solar cells. In turn Penrose, cobblestone, and Vogel spiral patterns redistribute the light over the whole area and only produce small overexposed spots. An analysis of the field components additionally demonstrates that cobblestone and Vogel spiral patterns provide similar redistribution capabilities. The effectivity of the cobblestone pattern strongly depends on the actual height distribution of the spots. Due to the limited number of spots over the base of the simulation volume, it is difficult to determine the maximum change of the E_z component that is possible. The drawback of the Penrose pattern is its partially regular redistribution that still provides a kind of periodicity and thus tends to stronger localization after longer propagation lengths.

---

1   The regime is unexplored if light harvesting in solar cells is considered

20 Outcome and outlook

Part I of this thesis is a general part that explains what organic materials are, how they are excited, and energy and charges are transferred. The goal of this part is to provide fundamental information that is needed to understand the following parts. The three main topics are treated and reported in the parts II to IV. The parts describe the experimental characterization and interpretation of the light-matter interaction with different organic materials. Additionally, the last part contains theoretical modeling of light propagation and light-matter interaction.

In part II, the refractive index of the photorefractive composites is modified by the incident light field. Consequently, the light field itself has an influence on the transmitted intensity distribution via the refractive index change. The photorefractive composites allow to control light with light. Part III focuses on the application of perylene bisimides derivatives as acceptors in organic bulk-heterojunction solar cells. Consequently, in this part light is absorbed by organic materials and converted into electric energy. The last part IV describes patterned materials. In turn, the patterns themselves influence light propagation. This influence is either generated by the patterned azopolymer itself or by an patterned PDMS film whose structure is molded from a SRG of an azopolymer.

The first two experimental parts clearly illustrate the difficulties that exist in the development and optimization of organic optoelectronic compositions consisting of two or even more substances. In both parts, components, on their own superior to the respective prior used material, are employed. However, contrary to the assumption that the overall performance of the resulting composition is enhanced, the efficiencies stagnate or even decrease. Due to the fact that the reasons of this behavior is different for both types of compositions, they are considered separately.

Summary of part II

In case of the photorefractive composites, the enhanced photoconductivity does not lead to an enhanced photorefractive response because of the increased dark conductivity combined with a reduced number of trapping states that are essential for a refractive index modulation. So as the photorefractive effect in organic composites is a process of multiple steps, it is not enough to only enhance charge-carrier generation. Trapping has to be existent in an appropriate extent. Additionally the strength of the electric field necessary for the poling of the chromophores has to be considered. Consequently, it is difficult to deduce the photorefractive performance of a composition from the energy levels of the CTA and the sensitizer. As a result, compositions comprising the more effective CTA mixture of PS and TPD have a significantly lower gain coefficient while the PVK comprising samples provide a higher gain despite their lower dark conductivity.

Summary of part III

In organic bulk-heterojunction solar cells, the consideration of only the energy levels of the active layer components has turned out to be insufficient. The crucial part in this compositions is the morphology and the clustering of both materials within the active layer. If the intermolecular distance of the materials is too large, the probability for charge separation dramatically decreases and so does the cells performance. A point even more crucial in context of this thesis is the processing conditions. The PCBM and the perylene-based acceptor materials provide good stability in ambient air. This is not the case for the donor polymers. Consequently, the performance of the cells decreases dramatically. Therefore, it is very difficult to compare different cells quantitatively or even to carry out long-term illumination for stability tests.

Furthermore, in collaboration with groups from theory, absorption spectroscopy based analysis of effective chain lengths of P3HT chains is carried out. Multiscale modeling enables to determine a critical angle that limits the effective chain length of a P3HT chain. Thus, it explains the different absorption in crystalline, amorphous (film), and dissolved P3HT.

In the frame of this collaboration, the bulk-heterojunction of P3HT and tdiPBI is analyzed. Here, especially thermal annealing is experimentally carried out and simulated. Due to the limited simulation time, temperatures are set extremely higher than typically applied in solar cell fabrication. However, the modeling reveals morphology changes and cluster formation of both materials. If the simulated temperatures are realized experimentally, dramatic changes of the material can be observed with the spectrometer and with the naked eye. These changes are not only attributed to materials reorganization but also to deterioration that is induced by the high temperatures combined with oxygen. In an inert atmosphere, effects are different but it is assumed that at least partial evaporation or separation of ligands occurs.

Summary of part IV

In the the last part (IV) the fabrication of surface-relief gratings in azopolymers and the light propagation through a stack of structured PDMS and glass is discussed. First, the general structuring process is tested by two-beam illumination and thus sinusoidal SRGs are generated. Later, a more advanced setup based on a PSLM and capable to create arbitrary patterns in 2D is employed. Different patterns, namely Bessel, Penrose, cobblestone, and Vogel spiral patterns are realized. In order to employ them as light redistributing patterns on top of solar cells, they are successfully transferred into PDMS. Lateral spacing parameters of the different patterns vary between $3.5-11.5\,\mu m$. The height modulation is up to $50\,nm$. In case of the sinusoidal pattern, even more than $200\,nm$ are achieved. The lower modulation in the complex pattern case is mainly caused by the film thickness. Consequently, thicker films led to higher modulations in case of the 2D patterns.

In order to determine the light redistribution capabilities of the different grating types, an FDTD simulation is set up. Linearly polarized plane-wave illumination propagates through a stack of a patterned PDMS film on a glass substrate. On the other side

of the system, cross sections are taken to evaluate the redistribution. The outcome of the analysis of these cross sections is that Bessel pattern tend to focus the light, i.e., similar to a Fresnel axicon. In turn, the other pattern types redistribute the light quite well. If the modulation is enhanced while the feature spacing is decreased, the focusing of the Bessel pattern and the redistribution by the other patterns become even more pronounced. Consequently, the Bessel pattern extremely focuses the light. As a consequence, it becomes a candidate for concentrator solar cells. In contrast, the other structures more or less homogeneously add some tilt to the electric field vectors. Therefore, they are in principle suited for application on conventional (organic and inorganic) solar cells. Of course, due to the different dimensions and thicknesses of the layers, spacing parameter as well as modulation height have to be adapted to fit to the specific needs of the desired application.

Perspectives of part II

There is a diverse future perspective for all of the introduced organic devices. So far, most photorefractive polymer composites demand high electric fields, are not long-term stable, and have rather low switching frequencies. If these drawbacks are overcome, there would be a real chance for photorefractive polymer composites to be enabled in mass market applications like optical switches or even 3D displays as presented by Blanche et al. [4] in 2010. As stated earlier, the limitations originate from different components. Thus, a better tuning of all parts has to be found to achieve the desired of properties. This optimization have to consider switching speed of the electro-optic moieties but also efficient charge transfer combined with enough trapping to generate the refractive index change [247]. Finally, this results in large gain coefficients. So, either further dopants have to be added to already existing compositions or materials providing the needed properties have to be tailored.

Perspectives of part III

A few years ago, organic solar cell have got a great competitor – perovskite solar cells. This new type can be considered as a fork of the well-known dye-sensitized solar cell and thus as a hybrid system that is partially inorganic and organic. Currently, PSCs achieve efficiencies that are much higher than those of typical organic solar cells (cf. figure 7.1). Additionally, this solar cell type can be easily manufactured on large scales, is lightweight, and is partially tunable regarding the absorption wavelength if an appropriate dye is employed or the perovskite is modified. As a consequence, the organic solar cell is outdated to some extent because there is an alternative providing almost the same properties and advantages but is even more powerful. However, the perovskite cell has also stability issues and it contains lead. Thus, the perovskite cell is far away from being environmentally friendly. This also holds for the organic solar cell. In case of the latter, there are larger prospects for finding materials that can be processed with harmless solvents [248] and that are themselves bio-degradable or at least fully recyclable [249]. Such an approach is a large step towards really "green" energy conversion. In turn, development of a more efficient donor and acceptor combination that is still not

environmentally friendly may be a dead end in research. The reason for this assumption is the enormous advance of perovskite cells that still seems to have the potential to grow.

Perspectives of part IV

Template fabrication via azopolymer patterning has to be considered as a powerful tool for rapid prototyping of complex patterns for testing purposes or small-series fabrication. The drawback is the small area that can be structured in one step if small feature spacings are needed. Thus, either sequential writing is necessary or costly high-resolution SLMs have to be employed. Contrary, if there is no need of large area processing, feature sizes can still be significantly reduced via optical demagnification, and thus the diffraction limit is the lower limit for the feature size. Consequently, the introduced approach enables soft-matter patterning on a lateral scale down to the submicrometer range while the height modulation can achieve more than 200 nm.

So far, the applied FDTD simulation of light propagation is limited to normal incidence. In order to simulate inclined incidence with angles larger than a few degrees, reflection from the surface becomes more important and so also reflections from the sides of the simulation volume have to be considered. At this point, boundary conditions have to be determined more carefully. This is because the angle between the light and the walls is no longer parallel or normal. Thus, simulations may lead to some side effects. A way to overcome this is the implementation of more advanced boundary conditions, i.e., periodic ones, and an enhancement of the simulation volume. The latter should be expanded in all directions. If the lateral dimensions are expanded, the influence of the pattern becomes more visible while a longer propagation in the z-direction would result in data that are closer to the real redistribution. So far, the glass is much thinner than in any solar cell while the PDMS film would be thicker in a more realistic scenario. The cost of a larger simulation volume is the need for more computational resources. Especially if the simulation grid is chosen to be even more fine grained to obtain more appropriate results, the memory consumption grows rapidly and thus computation on a high-performance computer cluster should be considered. In addition, high-performance computing would allow to vary the parameters of the patterns in finer steps because calculations would be much faster. Consequently, more data would produce a more detailed picture of light redistribution and would help to find an optimized pattern geometry.

Bibliography

[1] H. Letheby: "XXIX.–On the Production of a Blue Substance by the Electrolysis of Sulphate of Aniline", J. Chem. Soc. **15**, 161 (1862) (cit. on p. 1).

[2] C. K. Chiang, C. R. Fincher, Y. W. Park, A. J. Heeger, H. Shirakawa, E. J. Louis, S. C. Gau, and A. G. MacDiarmid: "Electrical Conductivity in Doped Polyacetylene", Phys. Rev. Lett. **39**, 1098 (1977) (cit. on pp. 1, 11).

[3] A. G. MacDiarmid: "'Synthetic Metals': A Novel Role for Organic Polymers (Nobel Lecture)", Angew. Chem. Int. Ed. **40**, 2581 (2001) (cit. on p. 1).

[4] P.-A. Blanche et al.: "Holographic three-dimensional telepresence using large-area photorefractive polymer", Nature **468**, 80 (2010) (cit. on pp. 2, 183, 223).

[5] NREL - National Renewable Energy Laboratory: *Best Research-Cell Efficiencies*, [Online; accessed 20-December-2016], (2016) `http://www.nrel.gov/pv/assets/images/efficiency_chart.jpg` (cit. on pp. 2, 73, 74).

[6] K. Harasaka, A. Okamoto, M. Bunsen, and M. Yamamoto: "Photorefractive Connection Module with Organic Photorefractive Polymer PATPD", CLEO/Pacific Rim 2005 (IEEE), p. 1390 (cit. on p. 2).

[7] J. Thomas, C. W. Christenson, P.-A. Blanche, M. Yamamoto, R. A. Norwood, and N. Peyghambarian: "Photoconducting Polymers for Photorefractive 3D Display Applications", Chem. Mater. **23**, 416 (2011) (cit. on p. 2).

[8] J. Scott, L. Pautmeier, and L. Schein: "Mean mobilities of charge-carriers in disordered media", Phys. Rev. B **46**, 8603 (1992) (cit. on p. 2).

[9] S. Silence, C. Walsh, J. Scott, T. Matray, R. Twieg, F. Hache, G. Bjorklund, and W. Moerner: "Subsecond grating growth in a photorefractive polymer", Opt. Lett. **17**, 1107 (1992) (cit. on p. 2).

[10] S. Silence, C. Walsh, J. Scott, and W. Moerner: "C-60 sensitization of a photorefractive polymer", Appl. Phys. Lett. **61**, 2967 (1992) (cit. on p. 2).

[11] W. E. Moerner and S. M. Silence: "Polymeric photorefractive materials", Chem. Rev. **94**, 127 (1994) (cit. on pp. 2, 29, 41, 62).

[12] D. Wright, M. Diaz-Garcia, J. Casperson, M. DeClue, W. Moerner, and R. Twieg: "High-speed photorefractive polymer composites", Appl. Phys. Lett. **73**, 1490 (1998) (cit. on p. 2).

[13] M. Diaz-Garcia, D. Wright, J. Casperson, B. Smith, E. Glazer, W. Moerner, L. Sukhomlinova, and R. Twieg: "Photorefractive properties of poly(N-vinyl carbazole)-based composites for high-speed applications", Chem. Mater. **11**, 1784 (1999) (cit. on p. 2).

[14] O. Ostroverkhova and W. Moerner: "Organic photorefractives: Mechanisms, materials, and applications", Chem. Rev. **104**, 3267 (2004) (cit. on pp. 2, 21, 29, 32, 41, 61–63).

[15] B. Lynn, P.-A. Blanche, and N. Peyghambarian: "Photorefractive polymers for holography", J. Polym. Sci., Part B: Polym. Phys. **52**, 193 (2013) (cit. on pp. 2, 29, 41).

[16] J. Zhang and K. D. Singer: "Homogeneous photorefractive polymer/nematogen composite", Appl. Phys. Lett. **72**, 2948 (1998) (cit. on pp. 2, 40, 43).

[17] R. R. Lunt and V. Bulovic: "Transparent, near-infrared organic photovoltaic solar cells for window and energy-scavenging applications", Appl. Phys. Lett. **98**, 61 (2011) (cit. on pp. 3, 73).

[18] Y. Zhao, G. A. Meek, B. G. Levine, and R. R. Lunt: "Near-Infrared Harvesting Transparent Luminescent Solar Concentrators", Adv. Opt. Mater. **2**, 606 (2014) (cit. on p. 3).

[19] C. J. Brabec, S. Gowrisanker, J. J. M. Halls, D. Laird, S. Jia, and S. P. Williams: "Polymer-fullerene bulk-heterojunction solar cells", Adv. Mater. **22**, 3839 (2010) (cit. on pp. 3, 76).

[20] C. Brabec, U. Scherf, and V. Dyakonov, eds.: *Organic Photovoltaics* (Wiley-Blackwell, Apr. 2014) (cit. on pp. 3, 76).

[21] W. Tress: *Organic Solar Cells* (Springer International Publishing, 2014) (cit. on pp. 3, 9–12, 15–20, 22, 76, 85).

[22] H. Hintz, H.-J. Egelhaaf, L. Lüer, J. Hauch, H. Peisert, and T. Chassé: "Photodegradation of P3HT-A Systematic Study of Environmental Factors", Chem. Mater. **23**, 145 (2011) (cit. on pp. 3, 111).

[23] C. Rockstuhl, S. Fahr, K. Bittkau, T. Beckers, R. Carius, F.-J. Haug, T. Söderström, C. Ballif, and F. Lederer: "Comparison and optimization of randomly textured surfaces in thin-film solar cells", Opt. Express **18**, A335 (2010) (cit. on p. 3).

[24] S. Albrecht, S. Schäfer, I. Lange, S. Yilmaz, I. Dumsch, S. Allard, U. Scherf, A. Hertwig, and D. Neher: "Light management in PCPDTBT: PC$_{70}$BM solar cells: A comparison of standard and inverted device structures", Org. Electron. **13**, 615 (2012) (cit. on p. 3).

[25] F. Pratesi, M. Burresi, F. Riboli, K. Vynck, and D. S. Wiersma: "Disordered photonic structures for light harvesting in solar cells", Opt. Express **21**, A460 (2013) (cit. on p. 3).

[26] S. Wiesendanger, M. Zilk, T. Pertsch, C. Rockstuhl, and F. Lederer: "Combining randomly textured surfaces and photonic crystals for the photon management in thin film microcrystalline silicon solar cells", Opt. Express **21**, A450 (2013) (cit. on p. 3).

[27] Z. Yu, A. Raman, and S. Fan: "Nanophotonic light-trapping theory for solar cells", Appl. Phys. A **105**, 329 (2011) (cit. on p. 3).

[28] U. Rau, U. W. Paetzold, and T. Kirchartz: "Thermodynamics of light management in photovoltaic devices", Phys. Rev. B **90**, 035211 (2014) (cit. on p. 3).

[29] M. Jošt, S. Albrecht, L. Kegelmann, C. M. Wolff, F. Lang, B. Lipovšek, J. Krč, L. Korte, D. Neher, B. Rech, et al.: "Efficient Light Management by Textured Nanoimprinted Layers for Perovskite Solar Cells", ACS Photonics **4**, 1232 (2017) (cit. on p. 3).

[30] B. Lipovšek, A. Čampa, F. Guo, C. J. Brabec, K. Forberich, J. Krč, and M. Topič: "Detailed optical modelling and light-management of thin-film organic solar cells with consideration of small-area effects", Opt. Express **25**, A176 (2017) (cit. on p. 3).

[31] S.-I. Na, S.-S. Kim, J. Jo, S.-H. Oh, J. Kim, and D.-Y. Kim: "Efficient Polymer Solar Cells with Surface Relief Gratings Fabricated by Simple Soft Lithography", Adv. Funct. Mater. **18**, 3956 (2008) (cit. on pp. 3, 4).

[32] P. Kowalczewski, M. Liscidini, and L. C. Andreani: "Light trapping in thin-film solar cells with randomly rough and hybrid textures", Opt. Express **21**, A808 (2013) (cit. on p. 4).

[33] C. Cho, H. Kim, S. Jeong, S.-W. Baek, J.-W. Seo, D. Han, K. Kim, Y. Park, S. Yoo, and J.-Y. Lee: "Random and V-groove texturing for efficient light trapping in organic photovoltaic cells", Sol. Energ. Mat. Sol. Cells **115**, 36 (2013) (cit. on p. 4).

[34] S.-I. Na, S.-S. Kim, S.-S. Kwon, J. Jo, J. Kim, T. Lee, and D.-Y. Kim: "Surface relief gratings on poly(3-hexylthiophene) and fullerene blends for efficient organic solar cells", Appl. Phys. Lett. **91**, 173509 (2007) (cit. on p. 4).

[35] Wikipedia: *Organic chemistry — Wikipedia, The Free Encyclopedia*, [Online; accessed 12-April-2016], `https://en.wikipedia.org/wiki/Organic_chemistry` (cit. on p. 7).

[36] Wikipedia: *Stockholm Convention on Persistent Organic Pollutants — Wikipedia, The Free Encyclopedia*, [Online; accessed 09-June-2017], `https://en.wikipedia.org/wiki/Stockholm_Convention_on_Persistent_Organic_Pollutants` (cit. on p. 7).

[37] H. Haken and H. C. Wolf: *Molekülphysik und Quantenchemie* (Springer-Verlag, 2006) (cit. on pp. 9, 10).

[38] L. Pauling: "The Application of the Quantum Mechanics to the Structure of the Hydrogen Molecule and Hydrogen Molecule-Ion and to Related Problems.", Chem. Rev. **5**, 173 (1928) (cit. on p. 9).

[39] J. E. Lennard-Jones: "The electronic structure of some diatomic molecules", Trans. Faraday Soc. **25**, 668 (1929) (cit. on p. 9).

[40] W. Kutzelnigg: "Friedrich Hund and Chemistry", Angew. Chem. Int. Ed. **35**, 572 (1996) (cit. on p. 9).

[41] H. Haken and H. C. Wolf: *Atom- und Quantenphysik* (Springer Berlin Heidelberg, 2004) (cit. on pp. 9, 11).

[42] N. C. Handy and D. J. Tozer: "Excitation energies of benzene from kohn–sham theory", J. Comput. Chem. **20**, 106 (1999) (cit. on p. 10).

[43] H. Kuhn: "A Quantum-Mechanical Theory of Light Absorption of Organic Dyes and Similar Compounds", J. Chem. Phys. **17**, 1198 (1949) (cit. on pp. 10, 11).

[44] H. Shirakawa, E. J. Louis, A. G. MacDiarmid, C. K. Chiang, and A. J. Heeger: "Synthesis of electrically conducting organic polymers: halogen derivatives of polyacetylene, $(CH)_x$", J. Chem. Soc., Chem. Commun., 578 (1977) (cit. on p. 11).

[45] A. J. Heeger: "Nobel Lecture: Semiconducting and metallic polymers: The fourth generation of polymeric materials", Rev. Mod. Phys. **73**, 681 (2001) (cit. on p. 11).

[46] W. Pauli: "Über den Zusammenhang des Abschlusses der Elektronengruppen im Atom mit der Komplexstruktur der Spektren", ZS f. Phys. **31**, 765 (1925) (cit. on p. 11).

[47] N. Bohr: "Atomic Structure", Nature **107**, 104 (1921) (cit. on p. 11).

[48] F. Hund: "Zur Deutung der Molekelspektren. I", ZS f. Phys. **40**, 742 (1926) (cit. on p. 11).

[49] F. Hund: "Zur Deutung der Molekelspektren. II", ZS f. Phys. **42**, 93 (1927) (cit. on p. 11).

[50] M. Fink, R.-D. Heuer, H. Kleinpoppen, K.-P. Lieb, N. Risch, and P. Schmüser: *Bestandteile der Materie. Atome, Moleküle, Atomkerne, Elementarteilchen*, edited by W. Raith, 2nd ed. (Walter de Gruyter, Berlin, Boston, 2008) (cit. on p. 12).

[51] M. Kasha: "Characterization of electronic transitions in complex molecules", Discuss. Faraday Soc. **9**, 14 (1950) (cit. on p. 13).

[52] B. Valeur: *Molecular Fluorescence* (Wiley-Blackwell, 2001) (cit. on pp. 13, 17, 18).

[53] A. Rao, P. C. Y. Chow, S. Gélinas, C. W. Schlenker, C.-Z. Li, H.-L. Yip, A. K.-Y. Jen, D. S. Ginger, and R. H. Friend: "The role of spin in the kinetic control of recombination in organic photovoltaics", Nature **500**, 435 (2013) (cit. on p. 13).

[54] W. Chang, D. N. Congreve, E. Hontz, M. E. Bahlke, D. P. McMahon, S. Reineke, T. C. Wu, V. Bulović, T. V. Voorhis, and M. A. Baldo: "Spin-dependent charge transfer state design rules in organic photovoltaics", Nat. Commun. **6**, 6415 (2015) (cit. on p. 13).

[55] J. Nelson: "Organic photovoltaic films", Curr. Opin. Solid State Mater. Sci. **6**, 87 (2002) (cit. on p. 15).

[56] M. Nič, J. Jirát, B. Košata, A. Jenkins, and A. McNaught, eds.: *IUPAC Compendium of Chemical Terminology* (International Union of Pure and Applied Chemistry (IUPAC), June 2009) (cit. on pp. 15, 17, 18).

[57] J. Michl and E. Thulstrup: "Why is azulene blue and anthracene white? a simple mo picture", Tetrahedron **32**, 205 (1976) (cit. on p. 15).

[58] M. Schwoerer and H. C. Wolf, eds.: *Organic Molecular Solids* (Wiley-Blackwell, Dec. 2006) (cit. on p. 16).

[59] T. Förster: "Zwischenmolekulare Energiewanderung und Fluoreszenz", Ann. Phys. **437**, 55 (1948) (cit. on p. 17).

[60] D. L. Dexter: "A Theory of Sensitized Luminescence in Solids", J. Chem. Phys. **21**, 836 (1953) (cit. on p. 18).

[61] M. C. Scharber, D. Mühlbacher, M. Koppe, P. Denk, C. Waldauf, A. J. Heeger, and C. J. Brabec: "Design Rules for Donors in Bulk-Heterojunction Solar Cells – Towards 10 % Energy-Conversion Efficiency", Adv. Mater. **18**, 789 (2006) (cit. on pp. 19, 127).

[62] R. A. Marcus: "On the Theory of Oxidation-Reduction Reactions Involving Electron Transfer. I", J. Chem. Phys. **24**, 966 (1956) (cit. on p. 19).

[63] A. Miller and E. Abrahams: "Impurity Conduction at Low Concentrations", Phys. Rev. **120**, 745 (1960) (cit. on p. 19).

[64] H. Bässler: "Localized states and electronic transport in single component organic solids with diagonal disorder", phys. stat. sol. (b) **107**, 9 (1981) (cit. on p. 19).

[65] H. Bässler: "Charge Transport in Disordered Organic Photoconductors a Monte Carlo Simulation Study", phys. stat. sol. (b) **175**, 15 (1993) (cit. on pp. 19, 21).

[66] G. Schönherr, H. Bässler, and M. Silver: "Dispersive hopping transport via sites having a Gaussian distribution of energies", Philos. Mag. B **44**, 47 (1981) (cit. on p. 19).

[67] I. I. Fishchuk, A. Kadashchuk, H. Bässler, and S. Nešpůrek: "Nondispersive polaron transport in disordered organic solids", Phys. Rev. B **67**, 224303 (2003) (cit. on p. 19).

[68] H. Bässler and A. Köhler: "Charge Transport in Organic Semiconductors", *Unimolecular and Supramolecular Electronics I*, Vol. 312, edited by R. M. Metzger, Topics in Current Chemistry (Springer Berlin / Heidelberg, 2012) (cit. on p. 21).

[69] J. Frenkel: "On Pre-Breakdown Phenomena in Insulators and Electronic Semi-Conductors", Phys. Rev. **54**, 647 (1938) (cit. on p. 22).

[70] S. Sze: *Physics of Semiconductor Devices*, 2nd (John Wiley and Sons (WIE), 1981) (cit. on p. 22).

[71] Y. Sun, L. Tan, S. Jiang, H. Qian, Z. Wang, D. Yan, C. Di, Y. Wang, W. Wu, G. Yu, S. Yan, C. Wang, W. Hu, Y. Liu, and D. Zhu: "High-Performance Transistor Based on Individual Single-Crystalline Micrometer Wire of Perylo[1,12-b,c,d]thiophene", J. Am. Chem. Soc. **129**, 1882 (2007) (cit. on p. 23).

[72] T. Schiros, S. Mannsfeld, C.-y. Chiu, K. G. Yager, J. Ciston, A. A. Gorodetsky, M. Palma, Z. Bullard, T. Kramer, D. Delongchamp, D. Fischer, I. Kymissis, M. F. Toney, and C. Nuckolls: "Reticulated Organic Photovoltaics", Adv. Funct. Mater. **22**, 1167 (2012) (cit. on p. 23).

[73] G. B. Jung, M. Yoshida, T. Mutai, R. Fujimura, S. Ashihara, T. Shimura, K. Araki, and K. Kuroda: "High-speed TPD-based Photorefractive Polymer Composites", Sen'i Gakkaishi **60**, 193 (2004) (cit. on p. 23).

[74] **T. Schemme**, E. Travkin, K. Ditte, W. Jiang, Z. Wang, and C. Denz: "TPD doped polystyrene as charge transporter in DiPBI sensitized photorefractive composites", Opt. Mater. Express **2**, 856 (2012) (cit. on pp. 23, 26, 44, 102, 129).

[75] J.-L. Maldonado, M. Bishop, C. Fuentes-Hernandez, P. Caron, B. Domercq, Y.-D. Zhang, S. Barlow, S. Thayumanavan, M. Malagoli, J.-L. Brédas, S. R. Marder, and B. Kippelen: "Effect of Substitution on the Hole Mobility of Bis(diarylamino)biphenyl Derivatives Doped in Poly(Styrene)", Chem. Mater. **15**, 994 (2003) (cit. on p. 23).

[76] K. Ditte, W. Jiang, **T. Schemme**, C. Denz, and Z. Wang: "Innovative Sensitizer DiPBI Outperforms PCBM", Adv. Mater. **24**, 2104 (2012) (cit. on pp. 23, 26, 44, 47, 65, 102, 129).

[77] K. Ditte, W. Jiang, **T. Schemme**, J. Liu, Z. Wang, and C. Denz: "Photorefractive Composite", PCT/EP2011/065876 WO/2013/037404 (2013) (cit. on pp. 23, 44, 102).

[78] M. Geoghegan and G. Hadziioannou: *Polymer Electronics (Oxford Master Series in Condensed Matter Physics)* (Oxford University Press, 2013) (cit. on p. 23).

[79] M. T. Dang, L. Hirsch, and G. Wantz: "P3HT:PCBM, Best Seller in Polymer Photovoltaic Research", Adv. Mater. **23**, 3597 (2011) (cit. on pp. 24, 77, 83).

[80] Y. He, H.-Y. Chen, J. Hou, and Y. Li: "Indene-C_{60} Bisadduct: A New Acceptor for High-Performance Polymer Solar Cells", J. Am. Chem. Soc. **132**, 1377 (2010) (cit. on p. 25).

[81] F. Fernandez-Lazaro, N. Zink-Lorre, and A. Sastre-Santos: "Perylenediimides as non-fullerene acceptors in bulk-heterojunction solar cells (bhjscs)", J. Mater. Chem. A **4**, 9336 (2016) (cit. on p. 25).

[82] W. Jiang, L. Ye, X. Li, C. Xiao, F. Tan, W. Zhao, J. Hou, and Z. Wang: "Bay-linked perylene bisimides as promising non-fullerene acceptors for organic solar cells", Chem. Commun. **50**, 1024 (2014) (cit. on pp. 26, 103, 108, 118, 130).

[83] D. Meng, D. Sun, C. Zhong, T. Liu, B. Fan, L. Huo, Y. Li, W. Jiang, H. Choi, T. Kim, J. Y. Kim, Y. Sun, Z. Wang, and A. J. Heeger: "High-Performance Solution-Processed Non-Fullerene Organic Solar Cells Based on Selenophene-Containing Perylene Bisimide Acceptor", J. Am. Chem. Soc. **138**, 375 (2016) (cit. on p. 26).

[84] O. N. Witt: "Zur Kenntniss des Baues und der Bildung färbender Kohlenstoffverbindungen", Ber. Dtsch. Chem. Ges. **9**, 522 (1876) (cit. on p. 26).

[85] M. V. Orna: *The Chemical History of Color* (Springer Berlin Heidelberg, 2012) (cit. on p. 26).

[86] A. Ashkin, G. D. Boyd, J. M. Dziedzic, R. G. Smith, A. A. Ballman, J. J. Levinstein, and K. Nassau: "Optically-Induced Refractive Index Inhomogeneities in $LiNbO_3$ and $LiTaO_3$", Appl. Phys. Lett. **9**, 72 (1966) (cit. on pp. 29, 31).

[87] P. Yeh: *Introduction to photorefractive nonlinear optics* (John Wiley & Sons Inc., Apr. 11, 1993) (cit. on p. 29).

[88] P. Günter and J.-P. Huignard: *Photorefractive Materials and Their Applications 1: Basic Effects*, edited by P. Günter and J.-P. Huignard (Springer New York, Apr. 9, 2006) (cit. on p. 29).

[89] P. Günter and J.-P. Huignard: *Photorefractive Materials and Their Applications 2: Materials*, edited by P. Günter and J.-P. Huignard (Springer New York, Nov. 13, 2007) (cit. on p. 29).

[90] P. Günter and J.-P. Huignard: *Photorefractive Materials and Their Applications 3: Applications*, edited by P. Günter and J.-P. Huignard (Springer New York, Aug. 30, 2007) (cit. on p. 29).

[91] K. Buse: "Light-induced charge transport processes in photorefractive crystals I: Models and experimental methods", Appl. Phys. B: Lasers Opt. **64**, 273 (1997) (cit. on p. 29).

[92] K. Buse: "Light-induced charge transport processes in photorefractive crystals II: Materials", Appl. Phys. B: Lasers Opt. **64**, 391 (1997) (cit. on p. 29).

[93] P. Rose, B. Terhalle, J. Imbrock, and C. Denz: "Optically induced photonic superlattices by holographic multiplexing", J. Phys. D: Appl. Phys. **41**, 224004 (2008) (cit. on p. 29).

[94] P. Rose, M. Boguslawski, and C. Denz: "Nonlinear lattice structures based on families of complex nondiffracting beams", New J. Phys. **14**, 033018 (2012) (cit. on p. 29).

[95] F. Diebel, P. Rose, M. Boguslawski, and C. Denz: "Optical induction scheme for assembling nondiffracting aperiodic Vogel spirals", Appl. Phys. Lett. **104**, 191101 (2014) (cit. on pp. 29, 165).

[96] M. Boguslawski, P. Rose, and C. Denz: "Increasing the structural variety of discrete nondiffracting wave fields", Phys. Rev. A **84**, 013832 (2011) (cit. on pp. 29, 158, 161).

[97] M. Boguslawski, N. M. Lučić, F. Diebel, D. V. Timotijević, C. Denz, and D. M. J. Savić: "Light localization in optically induced deterministic aperiodic Fibonacci lattices", Optica **3**, 711 (2016) (cit. on p. 29).

[98] W. Moerner, A. Grunnet-Jepsen, and C. Thompson: "Photorefractive Polymers", Annu. Rev. Mater. Sci. **27**, 585 (1997) (cit. on pp. 29, 40, 59, 62).

[99] S. Köber, M. Salvador, and K. Meerholz: "Organic Photorefractive Materials and Applications", Adv. Mater. **23**, 4725 (2011) (cit. on p. 29).

[100] B. Kippelen and N. Peyghambarian: "Photorefractive Polymers and their Applications", *Polymers for Photonics Applications II*, Advances in Polymer Science (Springer Science + Business Media, 2003) (cit. on pp. 33, 34, 36, 37, 41).

[101] B. E. A. Saleh and M. C. Teich: *Fundamentals of Photonics*, 2nd ed. (John Wiley & Sons, Inc., Aug. 2007) (cit. on pp. 34, 35, 61).

[102] K.-S. Lee, ed.: *Polymers for Photonics Applications II* (Springer Berlin Heidelberg, 2003) (cit. on pp. 37, 39, 62, 63).

[103] W. E. Moerner, S. M. Silence, F. Hache, and G. C. Bjorklund: "Orientationally enhanced photorefractive effect in polymers", J. Opt. Soc. Am. B **11**, 320 (1994) (cit. on pp. 38, 40).

[104] O. Ostroverkhova and K. Singer: "Space-charge dynamics in photorefractive polymers", J. Appl. Phys. **92**, 1727 (2002) (cit. on p. 40).

[105] G. Gray, K. Harrison, and J. Nash: "New family of nematic liquid crystals for displays", Electron. Lett. **9**, 130 (1973) (cit. on pp. 40, 41).

[106] P. J. Collings and M. Hird: *Introduction to liquid crystals: chemistry and physics (liquid crystals book series)* (CRC Press, 1997) (cit. on p. 40).

[107] D. A. Dunmur and A. E. Tomes: "Molecular properties of pentyl-cyano mesogens having different core structures", Mol. Cryst. Liq. Cryst. **97**, 241 (1983) (cit. on pp. 41, 42).

[108] D. Demus and T. Inukai: "Calculation of molecular, dielectric and optical properties of 4'-n-pentyl-4-cyano-biphenyl (5CB)", Liq. Cryst. **26**, 1257 (1999) (cit. on p. 41).

[109] S. J. Clark, G. J. Ackland, and J. Crain: "Ab initio molecular polarisabilities of liquid crystals: Application to DOBAMBC and 5CB", EPL **44**, 578 (1998) (cit. on pp. 41, 42).

[110] J. D. Cox and F. J. G. de Abajoatlab: "Electrically tunable nonlinear plasmonics in graphene nanoislands", Nat. Commun. **5**, 5725 (2014) (cit. on pp. 41, 213).

[111] MATLAB, version 9.0.0.341360 (R2016a), The Mathworks, Inc., (2016) `https://www.mathworks.com` (cit. on p. 41).

[112] S.-P. Ju, S.-C. Huang, K.-H. Lin, H.-Y. Chen, and T.-K. Shen: "Prediction of optical and dielectric properties of 4-Cyano-4-pentylbiphenyl liquid crystals by molecular dynamics simulation, coarse-grained dynamics simulation, and density functional theory calculation", J. Phys. Chem. C **120**, 14277 (2016) (cit. on p. 41).

[113] S. M. Risser, J. Wolfgang, and K. F. Ferris: "N-state interpretations of the first and second hyperpolarizabilities of cyanobiphenyl-based liquid crystal molecules", Molecular Crystals and Liquid Crystals Science and Technology. Section A. Molecular Crystals and Liquid Crystals **309**, 133 (1998) (cit. on p. 42).

[114] E. Mecher: "Erhöhung der Sensitivität photorefraktiver holographischer Speichermedien auf Basis von amorphen organischen Materialien", PhD thesis (Fakultät für Chemie und Pharmazie, LMU München, 2001) (cit. on p. 42).

[115] S.-S. Sun and N. S. Sariciftci: *Organic photovoltaics: mechanisms, materials, and devices*, Optical Science and Engineering (CRC Press, 2005), 629 pp. (cit. on p. 47).

[116] M. Böckmann, **T. Schemme**, D. H. de Jong, C. Denz, A. Heuer, and N. L. Doltsinis: "Structure of P3HT crystals, thin films, and solutions by UV/Vis spectral analysis", Phys. Chem. Chem. Phys. **17**, 28616 (2015) (cit. on pp. 47, 90, 92–94).

[117] D. F. Swinehart: "The beer-lambert law", J. Chem. Educ. **39**, 333 (1962) (cit. on p. 47).

[118] H. Qian, F. Negri, C. Wang, and Z. Wang: "Fully Conjugated Tri(perylene bisimides): An Approach to the Construction of n-Type Graphene Nanoribbons", J. Am. Chem. Soc. **130**, 17970 (2008) (cit. on pp. 49, 107).

[119] E. J. Meijer, D. M. de Leeuw, S. Setayesh, E. van Veenendaal, B. H. Huisman, P. W. M. Blom, J. C. Hummelen, U. Scherf, and T. M. Klapwijk: "Solution-processed ambipolar organic field-effect transistors and inverters", Nat. Mater. **2**, 678 (2003) (cit. on p. 49).

[120] J. Morgado, L. Alcácer, M. Esteves, N. Pires, and B. Gigante: "New stylbene-based arylamines with dehydroabietic acid methyl ester moieties for organic light-emitting diodes", Thin Solid Films **515**, 7697 (2007) (cit. on p. 49).

[121] M. Klessinger and J. Michl: *Excited states and photo-chemistry of organic molecules* (John Wiley & Sons Inc., 1995), 537 pp. (cit. on p. 49).

[122] D. V. Steenwinckel, E. Hendrickx, and A. Persoons: "Dynamics and steady-state properties of photorefractive poly(N-vinylcarbazole)-based composites sensitized with (2,4,7-trinitro-9-fluorenylidene)malononitrile in a 0–3 wt % range", J. Chem. Phys. **114**, 9557 (2001) (cit. on p. 50).

[123] M. de Podesta: *Understanding the properties of matter* (CRC Press, 2002) (cit. on p. 50).

[124] D. Meschede: *Gerthsen physik*, Vol. 22 (Springer, 2004) (cit. on p. 51).

[125] T. K. Däubler, R. Bittner, K. Meerholz, V. Cimrová, and D. Neher: "Charge carrier photogeneration, trapping, and space-charge field formation in PVK-based photorefractive materials", Phys. Rev. B **61**, 13515 (2000) (cit. on p. 52).

[126] C. Deibel and V. Dyakonov: "Polymer-fullerene bulk heterojunction solar cells", Rep. Prog. Phys. **73**, 096401 (2010) (cit. on p. 53).

[127] O. Ostroverkhova, M. He, R. J. Twieg, and W. E. Moerner: "Role of temperature in controlling performance of photorefractive organic glasses", ChemPhysChem **4**, 732 (2003) (cit. on p. 55).

[128] K. Balakrishnan, A. Datar, T. Naddo, J. Huang, R. Oitker, M. Yen, J. Zhao, and L. Zang: "Effect of side-chain substituents on self-assembly of perylene diimide molecules: morphology control", J. Am. Chem. Soc. **128**, 7390 (2006) (cit. on p. 58).

[129] F. Carreño, J. Martínez-Antón, and E. Bernabeu: "Use of spectrogoniometric-ellipsometric techniques for the determination of optical properties of films of trinitrofluorenone and poly-n-vinylcarbazole", Thin Solid Films **263**, 206 (1995) (cit. on p. 59).

[130] T. Scharf: *Polarized light in liquid crystals and polymers* (John Wiley & Sons Inc., 2006) (cit. on p. 59).

[131] P. Melpignano, S. Sinesi, G. Rotaris, M. Antonipieri, F. Cicoira, M. Loi, M. Muccini, R. Zamboni, M. Gale, and S. Westenhöfer: "Optical coupling of flexible microstructured organic light sources for automotive applications", Synth. Met. **139**, 913 (2003) (cit. on p. 59).

[132] N. Sultanova, S. Kasarova, and I. Nikolov: "Dispersion properties of optical polymers", Acta Phys. Pol. A **116**, 585 (2009) (cit. on p. 59).

[133] M. N. Polyanskiy: *Refractive index database*, [Online; accessed 02-November-2016], `http://refractiveindex.info` (cit. on p. 59).

[134] A. Grunnet-Jepsen, C. Thompson, R. Twieg, and W. Moerner: "Amplified scattering in a high-gain photorefractive polymer", J. Opt. Soc. Am. B **15**, 901 (1998) (cit. on p. 60).

[135] H. Kogelnik: "Coupled wave theory for thick hologram gratings", Bell System Technical Journal **48**, 2909 (1969) (cit. on p. 61).

[136] M. Moharam, T. Gaylord, and R. Magnusson: "Criteria for raman-nath regime diffraction by phase gratings", Opt. Commun. **32**, 19 (1980) (cit. on pp. 61, 151).

[137] P. Yeh: "Two-wave mixing in nonlinear media", IEEE J. Quantum. Electron. **25**, 484 (1989) (cit. on pp. 61, 62).

[138] H. Imahori, T. Umeyama, and S. Ito: "Large pi-Aromatic Molecules as Potential Sensitizers for Highly Efficient Dye-Sensitized Solar Cells", Acc. Chem. Res. **42**, 1809 (2009) (cit. on p. 73).

[139] B. Cocilovo, A. Hashimura, D. J. Tweet, T. Voutsas, and R. A. Norwood: "Highly transparent light-harvesting window film", Appl. Opt. **54**, 8990 (2015) (cit. on p. 73).

[140] B. O'Regan and M. Grätzel: "A low-cost, high-efficiency solar cell based on dye-sensitized colloidal tio2 films", Nature **353**, 737 (1991) (cit. on p. 73).

[141] A. Kojima, K. Teshima, Y. Shirai, and T. Miyasaka: "Organometal Halide Perovskites as Visible-Light Sensitizers for Photovoltaic Cells", J. Am. Chem. Soc. **131**, 6050 (2009) (cit. on pp. 73, 130).

[142] J. Liang, C. Wang, Y. Wang, Z. Xu, Z. Lu, Y. Ma, H. Zhu, Y. Hu, C. Xiao, X. Yi, et al.: "All-Inorganic Perovskite Solar Cells", J. Am. Chem. Soc. **138**, 15829 (2016) (cit. on p. 73).

[143] G. Chamberlain: "Organic solar cells: a review", Solar cells **8**, 47 (1983) (cit. on p. 75).

[144] P. Kumar and S. Chand: "Recent progress and future aspects of organic solar cells", Prog. Photovolt: Res. Appl. **20**, 377 (2012) (cit. on pp. 75, 76).

[145] A. Tada, Y. Geng, Q. Wei, K. Hashimoto, and K. Tajima: "Tailoring organic heterojunction interfaces in bilayer polymer photovoltaic devices", Nat. Mater. **10**, 450 (2011) (cit. on p. 76).

[146] D. C. Borrelli, M. C. Barr, V. Bulović, and K. K. Gleason: "Bilayer heterojunction polymer solar cells using unsubstituted polythiophene via oxidative chemical vapor deposition", Sol. Energ. Mat. Sol. Cells **99**, 190 (2012) (cit. on p. 76).

[147] W. Tress: "Device Physics of Organic Solar Cells", PhD thesis (Technische Universität Dresden, 2011) (cit. on p. 76).

[148] L. Scriven: "Physics and applications of dip coating and spin coating", Mrs proceedings, Vol. 121 (Cambridge Univ Press, 1988), p. 717 (cit. on p. 77).

[149] M. Tyona: "A theoritical study on spin coating technique", Adv. Mater. Res. **2**, 195 (2013) (cit. on p. 77).

[150] University of Louisville - Micro/Nanao Technology Center: *Spin coating theory*, [Online; accessed 09-January-2017], (2013) `https://louisville.edu/micronano/files/documents/standard-operating-procedures/SpinCoatingInfo.pdf` (cit. on p. 78).

[151] Ossila: *Spin Coating: A Guide to Theory and Techniques*, [Online; accessed 09-January-2017], (2016) `https://www.ossila.com/pages/spin-coating` (cit. on p. 78).

[152] J. R. Vig: "Ultraviolet-Ozone Cleaning of Semiconductor Surfaces", Research and Development Technical Report (1992) (cit. on p. 80).

[153] V. Tamrakar, S. Gupta, and Y. Sawle: "Single-Diode and Two-Diode PV Cell Modeling Using Matlab For Studying Characteristics Of Solar Cell Under Varying Conditions", ECIJ **4**, 67 (2015) (cit. on p. 85).

[154] N. Hossain, S. Das, and T. L. Alford: "Equivalent circuit modification for organic solar cells", Circuits and Systems **6**, 153 (2015) (cit. on pp. 85, 113).

[155] NREL - National Renewable Energy Laboratory: *Reference Solar Spectral Irradiance: ASTM G-173*, [Online; accessed 20-January-2017], (2017) `http://rredc.nrel.gov/solar/spectra/am1.5/astmg173/astmg173.html` (cit. on pp. 87, 88).

[156] H. J. Snaith: "The perils of solar cell efficiency measurements", Nat Photon **6**, 337 (2012) (cit. on pp. 87, 88).

[157] K. Rahimi, I. Botiz, J. O. Agumba, S. Motamen, N. Stingelin, and G. Reiter: "Light absorption of poly (3-hexylthiophene) single crystals", RSC Adv. **4**, 11121 (2014) (cit. on p. 92).

[158] A. Martinez-Otero, X. Elias, R. Betancur, and J. Martorell: "High-Performance Polymer Solar Cells Using an Optically Enhanced Architecture", Adv. Opt. Mater. **1**, 37 (2013) (cit. on p. 95).

[159] L. Ye, W. Jiang, W. Zhao, S. Zhang, D. Qian, Z. Wang, and J. Hou: "Selecting a Donor Polymer for Realizing Favorable Morphology in Efficient Non-fullerene Acceptor-based Solar Cells", Small **10**, 4658 (2014) (cit. on pp. 95, 107, 130).

[160] L. Ye, W. Jiang, W. Zhao, S. Zhang, Y. Cui, Z. Wang, and J. Hou: "Toward efficient non-fullerene polymer solar cells: Selection of donor polymers", Org. Electron. **17**, 295 (2015) (cit. on pp. 95, 130).

[161] T. Winands, M. Bockmann, **T. Schemme**, P.-M. T. Ly, D. H. de Jong, Z. Wang, C. Denz, A. Heuer, and N. L. Doltsinis: "P3HT:DiPBI bulk heterojunction solar cells: morphology and electronic structure probed by multiscale simulation and UV/vis spectroscopy", Phys. Chem. Chem. Phys. **18**, 6217 (2016) (cit. on pp. 95, 97, 98).

[162] A. Lv, S. R. Puniredd, J. Zhang, Z. Li, H. Zhu, W. Jiang, H. Dong, Y. He, L. Jiang, Y. Li, W. Pisula, Q. Meng, W. Hu, and Z. Wang: "High Mobility, Air Stable, Organic Single Crystal Transistors of an n-Type Diperylene Bisimide", Adv. Mater. **24**, 2626 (2012) (cit. on pp. 95, 102, 107).

[163] M. Manceau, A. Rivaton, J.-L. Gardette, S. Guillerez, and N. Lemaître: "The mechanism of photo- and thermooxidation of poly(3-hexylthiophene) (P3HT) reconsidered", Polym. Degrad. Stab. **94**, 898 (2009) (cit. on p. 96).

[164] J. C. Moreno-López, O. Grizzi, and E. A. Sánchez: "Thermal Stability of N,N'-Bis(1-ethylpropyl)perylene-3,4,9,10-tetracarboxdiimide Films on Cu(100)", J. Phys. Chem.C **120**, 19630 (2016) (cit. on p. 97).

[165] A. Rodrigues, M. C. R. Castro, A. S. Farinha, M. Oliveira, J. P. Tomé, A. V. Machado, M. M. M. Raposo, L. Hilliou, and G. Bernardo: "Thermal stability of P3HT and P3HT:PCBM blends in the molten state", Polym. Test. **32**, 1192 (2013) (cit. on p. 98).

[166] F. Liu, D. Chen, C. Wang, K. Luo, W. Gu, A. L. Briseno, J. W. P. Hsu, and T. P. Russell: "Molecular Weight Dependence of the Morphology in P3HT:PCBM Solar Cells", ACS Appl. Mater. Interfaces **6**, 19876 (2014) (cit. on p. 99).

[167] Z. Chen, M. G. Debije, T. Debaerdemaeker, P. Osswald, and F. Wurthner: "Tetrachloro-substituted Perylene Bisimide Dyes as Promising n-Type Organic Semiconductors: Studies on Structural, Electrochemical and Charge Transport Properties", Chem. Eur. J. of Chem. Phys. **5**, 137 (2004) (cit. on pp. 101, 107).

[168] R. Schmidt, J. H. Oh, Y.-S. Sun, M. Deppisch, A.-M. Krause, K. Radacki, H. Braunschweig, M. Könemann, P. Erk, Z. Bao, and F. Würthner: "High-Performance Air-Stable n-Channel Organic Thin Film Transistors Based on Halogenated Perylene Bisimide Semiconductors", J. Am. Chem. Soc. **131**, 6215 (2009) (cit. on p. 102).

[169] ChemBioDraw Ultra, version 14.0.0.117, PerkinElmer Informatics, (2014) `https://www.cambridgesoft.com/` (cit. on pp. 102, 103, 214).

[170] **T. Schemme**, K. Ditte, E. Travkin, W. Jiang, Z. Wang, and C. Denz: "Perylene bisimide derivatives as innovative sensitizers for photorefractive composites", Proc. SPIE **8435**, 843526 (2012) (cit. on p. 102).

[171] **T. Schemme**, K. Ditte, and C. Denz: "Effektive Lichtverstärker", Laborpraxis **36**, 20 (2012) (cit. on p. 102).

[172] L. Huo, S. Zhang, X. Guo, F. Xu, Y. Li, and J. Hou: "Replacing alkoxy groups with alkylthienyl groups: a feasible approach to improve the properties of photovoltaic polymers", Angew. Chem. Int. Ed. **50**, 9697 (2011) (cit. on pp. 105, 107).

[173] G. Namkoong, E. M. Younes, T. M. Abdel-Fattah, E. El-Maghraby, A. H. Elsayed, and A. A. Elazm: "Aging process of PEDOT:PSS dispersion and robust recovery of aged PEDOT:PSS as a hole transport layer for organic solar cells", Org. Electron. **25**, 237 (2015) (cit. on pp. 106, 107, 111).

[174] Y. Wang et al.: "A highly stretchable, transparent, and conductive polymer", Sci. Adv. **3**, e1602076 (2017) (cit. on p. 107).

[175] R. Schlaf, H. Murata, and Z. Kafafi: "Work function measurements on indium tin oxide films", J. Electron Spectrosc. Relat. Phenom. **120**, 149 (2001) (cit. on p. 107).

[176] Y. Park, V. Choong, Y. Gao, B. R. Hsieh, and C. W. Tang: "Work function of indium tin oxide transparent conductor measured by photoelectron spectroscopy", Appl. Phys. Lett. **68**, 2699 (1996) (cit. on p. 107).

[177] Sigma Aldrich: *Poly(3,4-ethylenedioxythiophene)-poly(styrenesulfonate)*, [Online; accessed 13-March-2017], (2017) `http://www.sigmaaldrich.com/catalog/product/aldrich/768642` (cit. on p. 107).

[178] A. Nardes, M. Kemerink, M. de Kok, E. Vinken, K. Maturova, and R. Janssen: "Conductivity, work function, and environmental stability of PEDOT:PSS thin films treated with sorbitol", Org. Electron. **9**, 727 (2008) (cit. on p. 107).

[179] R. Shivanna, S. Shoaee, S. Dimitrov, S. K. Kandappa, S. Rajaram, J. R. Durrant, and K. S. Narayan: "Charge generation and transport in efficient organic bulk heterojunction solar cells with a perylene acceptor", Energy Environ. Sci. **7**, 435 (2014) (cit. on pp. 107, 118).

[180] L. Ye, K. Sun, W. Jiang, S. Zhang, W. Zhao, H. Yao, Z. Wang, and J. Hou: "Enhanced Efficiency in Fullerene-Free Polymer Solar Cell by Incorporating Fine-designed Donor and Acceptor Materials", ACS Appl. Mater. Interfaces **7**, 9274 (2015) (cit. on pp. 107, 118, 130).

[181] Sigma Aldrich: *[6,6]-phenyl c61 butyric acid methyl ester*, [Online; accessed 13-March-2017], (2017) `http://www.sigmaaldrich.com/catalog/product/aldrich/684449` (cit. on p. 107).

[182] Sigma Aldrich: *Poly(3-hexylthiophene-2,5-diyl)*, [Online; accessed 13-March-2017], (2017) `http://www.sigmaaldrich.com/catalog/product/aldrich/698997` (cit. on p. 107).

[183] Chemical Rubber Company, ed.: *CRC Handbook of Chemistry and Physics* (Chapman & Hall, Boca Raton, Fla, 2008) (cit. on p. 107).

[184] M. S. Hunter and P. Fowle: "Natural and Thermally Formed Oxide Films on Aluminum", J. Electrochem. Soc. **103**, 482 (1956) (cit. on p. 113).

[185] S. Oesch and M. Faller: "Environmental effects on materials: The effect of the air pollutants SO2, NO2, NO and O3 on the corrosion of copper, zinc and aluminium. A short literature survey and results of laboratory exposures", Corros. Sci. **39**, 1505 (1997) (cit. on p. 113).

[186] J. D. Servaites, M. A. Ratner, and T. J. Marks: "Organic solar cells: A new look at traditional models", Energy Environ. Sci **4**, 4410 (2011) (cit. on pp. 115, 118).

[187] C. Liu, C. Xiao, Y. Li, W. Hu, Z. Li, and Z. Wang: "High performance, air stable n-type single crystal transistors based on core-tetrachlorinated perylene diimides", Chem. Commun. **50**, 12462 (2014) (cit. on p. 116).

[188] S. Rajaram, R. Shivanna, S. K. Kandappa, and K. S. Narayan: "Nonplanar perylene diimides as potential alternatives to fullerenes in organic solar cells", J. Phys. Chem. Lett. **3**, 2405 (2012) (cit. on p. 118).

[189] L. Ye, S. Zhang, W. Zhao, H. Yao, and J. Hou: "Highly Efficient 2D-Conjugated Benzodithiophene-Based Photovoltaic Polymer with Linear Alkylthio Side Chain", Chem. Mater. **26**, 3603 (2014) (cit. on p. 125).

[190] C. J. Brabec, A. Cravino, D. Meissner, N. S. Sariciftci, T. Fromherz, M. T. Rispens, L. Sanchez, and J. C. Hummelen: "Origin of the Open Circuit Voltage of Plastic Solar Cells", Adv. Funct. Mater. **11**, 374 (2001) (cit. on p. 127).

[191] K. Vandewal, K. Tvingstedt, A. Gadisa, O. Inganäs, and J. V. Manca: "On the origin of the open-circuit voltage of polymer – fullerene solar cells", Nat. Mater. **8**, 904 (2009) (cit. on p. 127).

[192] Y. Wang, S. Bai, L. Cheng, N. Wang, J. Wang, F. Gao, and W. Huang: "High-Efficiency Flexible Solar Cells Based on Organometal Halide Perovskites", Adv. Mater. **28**, 4532 (2015) (cit. on p. 130).

[193] S. Collavini, S. F. Völker, and J. L. Delgado: "Understanding the outstanding power conversion efficiency of perovskite-based solar cells", Angew. Chem. Int. Ed. **54**, 9757 (2015) (cit. on p. 130).

[194] K. Wang, C. Liu, C. Yi, L. Chen, J. Zhu, R. A. Weiss, and X. Gong: "Efficient Perovskite Hybrid Solar Cells via Ionomer Interfacial Engineering", Adv. Funct. Mater. **25**, 6875 (2015) (cit. on p. 130).

[195] B. Yang, O. Dyck, J. Poplawsky, J. Keum, S. Das, A. Puretzky, T. Aytug, P. C. Joshi, C. M. Rouleau, G. Duscher, D. B. Geohegan, and K. Xiao: "Controllable Growth of Perovskite Films by Room-Temperature Air Exposure for Efficient Planar Heterojunction Photovoltaic Cells", Angew. Chem. Int. Ed. **54**, 14862 (2015) (cit. on p. 130).

[196] C. C. Stoumpos and M. G. Kanatzidis: "Halide Perovskites: Poor Man's High-Performance Semiconductors", Adv. Mater. **28**, 5778 (2016) (cit. on p. 130).

[197] C.-H. Chiang and C.-G. Wu: "Bulk heterojunction perovskite-PCBM solar cells with high fill factor", Nat Photon **10**, 196 (2016) (cit. on p. 130).

[198] M. Kaltenbrunner, G. Adam, E. D. Głowacki, M. Drack, R. Schwödiauer, L. Leonat, D. H. Apaydin, H. Groiss, M. C. Scharber, M. S. White, N. S. Sariciftci, and S. Bauer: "Flexible high power-per-weight perovskite solar cells with chromium oxide–metal contacts for improved stability in air", Nat. Mater. **14**, 1032 (2015) (cit. on p. 131).

[199] T. A. Berhe, W.-N. Su, C.-H. Chen, C.-J. Pan, J.-H. Cheng, H.-M. Chen, M.-C. Tsai, L.-Y. Chen, A. A. Dubale, and B.-J. Hwang: "Organometal halide perovskite solar cells: degradation and stability", Energy Environ. Sci. **9**, 323 (2016) (cit. on p. 131).

[200] F. Bella, G. Griffini, J.-P. Correa-Baena, G. Saracco, M. Gratzel, A. Hagfeldt, S. Turri, and C. Gerbaldi: "Improving efficiency and stability of perovskite solar cells with photocurable fluoropolymers", Science **354**, 203 (2016) (cit. on p. 131).

[201] M. Saliba, T. Matsui, K. Domanski, J.-Y. Seo, A. Ummadisingu, S. M. Zakeeruddin, J.-P. Correa-Baena, W. R. Tress, A. Abate, A. Hagfeldt, and M. Gratzel: "Incorporation of rubidium cations into perovskite solar cells improves photovoltaic performance", Science **354**, 206 (2016) (cit. on p. 131).

[202] M. B. Smith and J. March: *March's Advanced Organic Chemistry: Reactions, Mechanisms, and Structure* (Wiley John + Sons, 2013) (cit. on p. 137).

[203] M. Böckmann, C. Peter, L. D. Site, N. L. Doltsinis, K. Kremer, and D. Marx: "Atomistic Force Field for Azobenzene Compounds Adapted for QM/MM Simulations with Applications to Liquids and Liquid Crystals", J. Chem. Theory Comput. **3**, 1789 (2007) (cit. on p. 137).

[204] C. A. Harper and E. M. Petrie: *Plastics Materials and Processes: A Concise Encyclopedia* (John Wiley & Sons, 2003) (cit. on p. 138).

[205] C. J. Barrett, A. L. Natansohn, and P. L. Rochon: "Mechanism of Optically Inscribed High-Efficiency Diffraction Gratings in Azo Polymer Films", J. Phys. Chem. **100**, 8836 (1996) (cit. on pp. 141, 142, 152).

[206] C. J. Barrett, P. L. Rochon, and A. L. Natansohn: "Model of laser-driven mass transport in thin films of dye-functionalized polymers", J. Chem. Phys. **109**, 1505 (1998) (cit. on p. 141).

[207] A. Natansohn and P. Rochon: "Photoinduced Motions in Azo-Containing Polymers", Chem. Rev. **102**, 4139 (2002) (cit. on p. 141).

[208] C. Cojocariu and P. Rochon: "Light-induced motions in azobenzene-containing polymers", Pure Appl. Chem. **76**, 1479 (2004) (cit. on p. 141).

[209] P. Karageorgiev, D. Neher, B. Schulz, B. Stiller, U. Pietsch, M. Giersig, and L. Brehmer: "From anisotropic photo-fluidity towards nanomanipulation in the optical near-field", Nat. Mater. **4**, 699 (2005) (cit. on pp. 141, 160).

[210] P. Gruner, M. Arlt, and T. Fuhrmann-Lieker: "Surface Wrinkling Induced by Photofluidization of Low Molecular Azo Glasses", ChemPhysChem **14**, 424 (2012) (cit. on p. 141).

[211] N. K. Viswanathan, D. Yu Kim, S. Bian, J. Williams, W. Liu, L. Li, L. Samuelson, J. Kumar, and S. K. Tripathy: "Surface relief structures on azo polymer films", J. Mater. Chem. **9**, 1941 (1999) (cit. on p. 141).

[212] J. Zhou, J. Shen, J. Yang, Y. Ke, K. Wang, and Q. Zhang: "Fabrication of a pure polarization grating in a cross-linked azopolymer by polarization-modulated holography", Opt. Lett. **31**, 1370 (2006) (cit. on p. 141).

[213] A. Ambrosio, A. Camposeo, A. Carella, F. Borbone, D. Pisignano, A. Roviello, and P. Maddalena: "Realization of submicrometer structures by a confocal system on azopolymer films containing photoluminescent chromophores", J. Appl. Phys. **107**, 083110 (2010) (cit. on pp. 141, 161).

[214] A. Priimagi and A. Shevchenko: "Azopolymer-based micro- and nanopatterning for photonic applications", J. Polym. Sci., Part B: Polym. Phys. **52**, 163 (2014) (cit. on p. 141).

[215] S. Lee, H. S. Kang, and J.-K. Park: "Directional Photofluidization Lithography: Micro/Nanostructural Evolution by Photofluidic Motions of Azobenzene Materials", Adv. Mater. **24**, 2069–2103 (2012) (cit. on pp. 142, 143).

[216] J. Kumar, L. Li, X. L. Jiang, D.-Y. Kim, T. S. Lee, and S. Tripathy: "Gradient force: the mechanism for surface relief grating formation in azobenzene functionalized polymers", Appl. Phys. Lett. **72**, 2096 (1998) (cit. on p. 142).

[217] T. G. Pedersen, P. M. Johansen, N. C. R. Holme, P. S. Ramanujam, and S. Hvilsted: "Mean-field theory of photoinduced formation of surface reliefs in side-chain azobenzene polymers", Phys. Rev. Lett. **80**, 89 (1998) (cit. on p. 142).

[218] P. Lefin, C. Fiorini, and J.-M. Nunzi: "Anisotropy of the photo-induced translation diffusion of azobenzene dyes in polymer matrices", Pure Appl. Opt. **7**, 71 (1998) (cit. on p. 142).

[219] P. Lefin, C. Fiorini, and J.-M. Nunzi: "Anisotropy of the photoinduced translation diffusion of azo-dyes", Opt. Mater. **9**, 323 (1998) (cit. on p. 142).

[220] M. L. Juan, J. Plain, R. Bachelot, P. Royer, S. K. Gray, and G. P. Wiederrecht: "Multiscale Model for Photoinduced Molecular Motion in Azo Polymers", ACS Nano **3**, 1573 (2009) (cit. on p. 142).

[221] K. G. Yager and C. J. Barrett: "Temperature modeling of laser-irradiated azopolymer thin films", J. Chem. Phys. **120**, 1089 (2004) (cit. on p. 143).

[222] M. Böckmann and N. L. Doltsinis: "Towards understanding photomigration: insights from atomistic simulations of azopolymer films explicitly including light-induced isomerization dynamics", J. Chem. Phys. **145**, 154701 (2016) (cit. on p. 143).

[223] J. A. Davis, D. M. Cottrell, J. Campos, M. J. Yzuel, and I. Moreno: "Encoding amplitude information onto phase-only filters", Appl. Opt. **38**, 5004 (1999) (cit. on pp. 147, 148).

[224] C. Cocoyer, L. Rocha, C. Fiorini-Debuisschert, L. Sicot, D. Vaufrey, C. Sentein, B. Geffroy, and P. Raimond: "Implementation of a submicrometer patterning technique in azopolymer films towards optimization of photovoltaic solar cells efficiency", Thin Solid Films **511-512**, 517 (2006) (cit. on p. 149).

[225] C.-K. Lee, C.-W. Pao, and C.-W. Chu: "Multiscale molecular simulations of the nanoscale morphologies of P3HT:PCBM blends for bulk heterojunction organic photovoltaic cells", Energy Environ. Sci. **4**, 4124 (2011) (cit. on p. 149).

[226] M. G. Moharam and L. Young: "Criterion for Bragg and Raman-Nath diffraction regimes", Appl. Opt. **17**, 1757 (1978) (cit. on p. 151).

[227] W. Klein and B. Cook: "Unified Approach to Ultrasonic Light Diffraction", IEEE Trans. Sonics Ultrason. **14**, 123 (1967) (cit. on p. 151).

[228] X. Jing and Y. Jin: "Transmittance analysis of diffraction phase grating", Appl. Opt. **50**, C11 (2011) (cit. on p. 153).

[229] *WSxM*, WSxM solutions, `http://www.wsxmsolutions.com` (cit. on p. 154).

[230] I. Horcas, R. Fernández, J. M. Gómez-Rodríguez, J. Colchero, J. Gómez-Herrero, and A. M. Baro: "WSXM: A software for scanning probe microscopy and a tool for nanotechnology", Rev. Sci. Instrum. **78**, 013705 (2007) (cit. on p. 154).

[231] *Gwyddion*, Department of Nanometrology, Czech Metrology Institute., `http://gwyddion.net` (cit. on p. 154).

[232] J. Durnin: "Exact solutions for nondiffracting beams. I. The scalar theory", J. Opt. Soc. Am. A **4**, 651 (1987) (cit. on pp. 157, 159).

[233] Z. Bouchal: "Nondiffracting optical beams: physical properties, experiments, and applications", Czech. J. Phys. **53**, 537 (2003) (cit. on pp. 157, 158).

[234] C. López-Mariscal and J. C. Gutiérrez-Vega: "The generation of nondiffracting beams using inexpensive computer-generated holograms", Am. J. Phys **75**, 36 (2007) (cit. on p. 158).

[235] I. Golub: "Fresnel axicon", Opt. Lett. **31**, 1890 (2006) (cit. on p. 160).

[236] L. Song, C. Varma, J. Verhoeven, and H. Tanke: "Influence of the triplet excited state on the photobleaching kinetics of fluorescein in microscopy", Biophys. J. **70**, 2959 (1996) (cit. on p. 161).

[237] H. Vogel: "A better way to construct the sunflower head", Math. Biosci. **44**, 179 (1979) (cit. on p. 165).

[238] J. Trevino, S. F. Liew, H. Noh, H. Cao, and L. D. Negro: "Geometrical structure, multifractal spectra and localized optical modes of aperiodic Vogel spirals", Opt. Express **20**, 3015 (2012) (cit. on p. 165).

[239] M. Moharam and T. Gaylord: "Rigorous coupled-wave analysis of planar-grating diffraction", J. Opt. Soc. Am. **71**, 811 (1981) (cit. on p. 171).

[240] G. Demésy, F. Zolla, A. Nicolet, M. Commandré, and C. Fossati: "The finite element method as applied to the diffraction by an anisotropic grating", Opt. Express **15**, 18089 (2007) (cit. on p. 171).

[241] T. Liebig: *openEMS - Open Electromagnetic Field Solver*, General and Theoretical Electrical Engineering (ATE), University of Duisburg-Essen, `http://openEMS.de` (cit. on p. 171).

[242] K. Yee: "Numerical solution of initial boundary value problems involving maxwell's equations in isotropic media", IEEE T. Antenn. Propag. **14**, 302 (1966) (cit. on pp. 171, 172).

[243] W. Nolting: *Grundkurs Theoretische Physik 3: Elektrodynamik (Springer-Lehrbuch) (German Edition)* (Springer, 2001) (cit. on p. 172).

[244] A. Wachter and H. Hoeber: *Repetitorium Theoretische Physik* (Springer-Verlag GmbH, Sept. 15, 2004) (cit. on p. 172).

[245] M. Piraud, A. Aspect, and L. Sanchez-Palencia: "Anderson localization of matter waves in tailored disordered potentials", Phys. Rev. A **85** (2012) (cit. on p. 178).

[246] *SPP 1839: Tailored Disorder - A science- and engineering-based approach to materials design for advanced photonic applications*, Deutsche Forschungsgemeinschaft, `http://gepris.dfg.de/gepris/projekt/255652081` (cit. on p. 178).

[247] P.-A. Blanche, ed.: *Photorefractive organic materials and applications* (Springer International Publishing, 2016) (cit. on pp. 183, 223).

[248] J. Zhao, Y. Li, G. Yang, K. Jiang, H. Lin, H. Ade, W. Ma, and H. Yan: "Efficient organic solar cells processed from hydrocarbon solvents", Nature Energy **1**, 15027 (2016) (cit. on pp. 183, 224).

[249] M. Irimia-Vladu: "'Green' electronics: biodegradable and biocompatible materials and devices for sustainable future", Chem. Soc. Rev. **43**, 588 (2014) (cit. on pp. 183, 224).

[250] Wikipedia: *Molar mass distribution — Wikipedia, The Free Encyclopedia*, [Online; accessed 27-September-2016], `https://en.wikipedia.org/wiki/Molar_mass_distribution` (cit. on p. 214).

Acronyms

Notation	Description
1D	one-dimensional 4, 179
2D	two-dimensional 4, 146, 155, 157, 160, 163, 165, 170, 182, 223
3D	three-dimensional 2, 102, 104, 105, 166, 167, 183, 223
5CB	4'-Pentyl-4-biphenylcarbonitrile 40–45, 59, 214
AFM	atomic force microscope 154
AFM	atomic force microscopy 58, 78, 135, 149, 154, 167
Al	aluminum 76, 107
BaTiO$_3$	barium titanate 29
BHJ	bulk heterojunction 76, 99, 107, 111, 112, 118, 127, 129, *see also in Glossary:* bulk heterojunction
C$_{60}$	(C$_{60}$-I$_h$)[5,6]fullerene 40, 43, 214
CB	chlorobenzene 102, 119, 125, 214
CB	conduction band 31
CHCl$_3$	chloroform 43–45, 90, 91, 95, 102, 114, 116, 117, 138, 139, 148, 155, 214, 215
CN	1-chloronaphthalene 125, 126, 214
CTA	charge-transporting agent 32, 40, 43–45, 48, 49, 69, 181, *see also in Glossary:* charge-transporting agent
CVD	chemical vapor deposition 80
D/A	donor/acceptor 75
ddiPBI	doubly-linked diperylene bisimide 108
DIO	1,8-diiodooctane 125, 214
diPBI	diperylene bisimide 25, 29, 40, 44, 48, 53, 58, 69, 95–98, 104, 105, 108, 116, 129
DMNPAA	2,5-dimethyl-4-(p-nitrophenylazo)anisole 42

Notation	Description
DOS	density of states 20, 21
DR	disperse red 42
EA	electron affinity 15
EM	electron microscopy 78
EO	electro-optic 31, 35
EP-PTCDI	N,N'-Bis(1-ethylpropyl)perylene-3,4,9,10-tetracarboxdiimide 97
esu	electro static unit 41, 213
EtOAc	ethyl acetate 90–92, 214, 215
FDTD	finite-difference time-domain 4, 135, 171, 179, 182, 184, 223, 224
FEM	finite element method 171
FF	fill factor 86, 87, 90, 110, 113–115, 119–122, 125
FFT	Fast Fourier Transform 154, 159, 161
FRET	Förster resonant energy transfer 17, 18
FWHM	full width at half maximum 163, 166, 178
GDM	Gaussian disorder model 19, 20, 22
HOMO	highest occupied molecular orbital 10, 11, 15–17, 19, 32, 47, 48, 53, 58, 93, 94, 102, 105, 107, 108, 127
ICBA	1',1",4',4"-tetrahydro-di[1,4]methanonaphthaleno[5,6]fullerene-C_{60} 25
IP	ionization potential 15
IR	infrared 73
ITO	indium tin oxide 42, 43, 55, 76, 79, 81, 82, 84, 89, 106, 107, 129
IUPAC	International Union of Pure and Applied Chemistry 23
LC	liquid crystal 43
LCoS	liquid crystal on silicon 146
$LiNbO_3$	lithium niobate 29, 35
LUMO	lowest unoccupied molecular orbital 10, 11, 15–17, 19, 32, 47, 48, 75, 102, 105, 107–109, 117, 127

Notation	Description
MD	molecular dynamics 90
MEH-PPV	poly[2-methoxy-5-(2-ethylhexyloxy)-1,4-phenylenevinylene] 24
NPLC	number of power-lince-cycles 89, *see also in Glossary:* number of power-lince-cycles
NREL	National Renewable Energy Laboratory 73, 74, 87
ODCB	orthodichlorobenzene 78, 102, 116, 117, 119, 121, 214
OFET	organic field effect transistor 23, 26, 115
OLED	organic light emitting diode 11, 13, 23, 106
OLET	organic light emitting transistor 23
OSC	organic solar cell 3, 13, 23, 73, 99, 106, 107
P3HT	poly(3-hexylthiophene-2,5-diyl) 23, 24, 77, 78, 83, 90–99, 103, 105–112, 114–118, 123, 127, 129, 182, 214, 215, 222
PA	polyacetylene 1, 11
PANI	polyaniline 1
PBDTTT-C-T	poly[(2,6-Bis(trimethyltin)-4,8-bis(5-(2-ethylhexyl)thiophen-2-yl)-benzo[1,2-b:4,5-b']dithiophene)] 24, 95, 105–108, 118–127, 129, 130, 214
PBI	perylene bisimide 25, 26, 29, 101, 102, 107, 108, 114–116, 118, 127, 129, 130, 214
Pc	phthalocyanine 23
$PC_{60}BM$	phenyl-C_{61}-butyric acid methyl ester 211
$PC_{70}BM$	phenyl-C_{71}-butyric acid methyl ester 211
PCBM	phenyl-C_{61}-butyric acid methyl ester 25, 40, 43, 44, 48, 49, 58, 69, 77, 78, 83, 98, 99, 101–103, 107, 109–112, 114, 115, 127, 129–131, 182, 212, 214, 222, *see also in Glossary:* PCBM
PCDTBT	poly[N-9'-heptadecanyl-2,7-carbazole-alt-5,5-(4',7'-di-2-thienyl-2',1',3'-benzothiadiazole)] 24
PCE	power conversion efficiency 87, 90, 110, 112–115, 118–123, 125, 126, 130, 170
PDI	perylene diimide 25

Notation	Description
PDMS	poly(dimethylsiloxane) 4, 135, 139, 153, 167, 169–171, 173, 179, 181, 182, 184, 221–223, 225
PDO3MAA	poly(Disperse Orange 3 methacrylamide) 138, 139, 149, 151, 152, 154, 155
PDR1MA	poly(Disperse Red 1 methacrylate) 138, 139, 149, 157, 159–161, 163–166
PEDOT:PSS	poly(3,4-ethylenedioxythiophene) polystyrene sulfonate 76, 78, 80–83, 106, 107, 109, 111, 129, 212
PET	polyethylene terephthalate 1
PINS	pattern inspection system 146
PML	perfectly matched layer 173, *see also in Glossary:* perfectly matched layer
PMMA	poly(methyl methacrylate) 1
PPDI	imide-linked diperylene diimide 104, 105, 107, 108, 118–127, 214
PPV	poly(p-phenylene vinylene) 24
PR	photorefractive 29, 31, 32, 36, 38, 40–43, 47–50, 55, 59, 63, 65, 66, 69, 146, 211, 212
PS	polystyrene 23, 44, 55, 58, 65, 69, 181, 214, 222
PSC	perovskite-based solar cells 73, 130, 183, 224
PSLM	phase-only SLM 146–148, 157, 159, 163, 165, 170, 175, 179, 182
PTB7	poly[(4,8-bis-(2-ethylhexyloxy)-benzo(1,2-b:4,5-b')dithiophene)-2,6-diyl-alt-(4-(2-ethylhexyl)-3-fluorothieno[3,4-b]thiophene-)-2-carboxylate-2-6-diyl)] 24, 95
PTCDI	N,N0-dimethyl-3,4,9,10-tetracarboxylic perylene diimide 130, 131
PTFE	Polytetrafluorethen 83, 95
PVD	physical vapor deposition 80
PVDF	Polyvinylidenfluorid 82
PVK	poly(9-vinylcarbazole) 23, 24, 40, 43, 44, 53, 55, 56, 58, 59, 63, 69, 181, 214, 222
RCWA	rigorous coupled-wave analysis 171

Notation	Description
SBN	strontium barium niobate, $Sr_xBa_{1-x}Nb_2O_6$ for $0.32 \leq x \leq 0.82$ 29, 35
SCF	space-charge field 38, 39, 62
sdiPBI	singly-linked diperylene bisimide 103, 104, 107, 108, 125–127, 214
SiO_2	silicon dioxide 42, 43
SLM	spatial light modulator 145–148, 155, 159, 184, 206
SMU	source measure unit 89
Spiro-MeOTAD	$N^2,N^2,N^{2'},N^{2'},N^7,N^7,N^{7'},N^{7'}$-octakis(4-methoxyphenyl)-9,9'-spiro-bi[fluorene]-2,2',7,7'-tetraamine 130, 131
SRG	surface relief grating 135, 145, 154, 159, 161, 165, 167, 169, 176–178, 181, 182
STM	scanning tunneling microscopy 58, 78, 99
tdiPBI	triply-linked diperylene bisimide 102, 103, 107, 109, 116–118, 127, 130, 182, 214, 222
THF	tetrahydrofuran 148, 151, 152, 155
TPD	N,N'-Bis(3-methylphenyl)-N,N'-diphenylbenzidine 23, 24, 40, 44, 53, 55, 56, 58, 59, 63, 65, 69, 181, 214, 222
UV	ultraviolet 3, 73, 79, 82, 109, 138
VB	valence band 31

List of Symbols

Notation	Description
j	current through the sample 51, 85, 86, 90
J_{sc}	short circuit current density 110, 114, 119, 120, 122, 123, 125, 127
J	current density 90, 109, 111, 112, 115, 120, 121, 126
I	light intensity or surface power density 87
j_{sc}	short circuit current 86, 90, 116, 117, 127
M_{w}	weight average molecular weight 214
M	molecular weight 43, 214
M_{n}	number average molecular weight 90, 214
T_{g}	glass transition temperature 38, 41, 62, 141, 143, *see also in Glossary:* glass transition temperature
T_{NC}	nematic clearing point 41, *see also in Glossary:* nematic clearing point
V	voltage 109, 111, 112, 115, 120, 121, 126
V_{oc}	open circuit voltage 86, 90, 110, 111, 113, 114, 116, 117, 119, 120, 122, 125, 127

Glossary

active layer

> The active layer of a bulk heterojunction of an organic solar cell typically consists of a donor and an acceptor compound, absorbs the incident photons, and separates the resulting excitons into free charges. 95

bulk heterojunction

> Mixture of at least two materials, typically one donor and one acceptor, whose interface is maximized and spread all over the bulk. 76, 95, 129, 203, 211

charge-transporting agent

> Hole conducting component within a PR material. Typically transparent in the visible region. 32, 203

chromophore

> Component within an PR composite that provides the electro-optic functionality and thus is also responsible for the refractive index change. 36, 37, 41

glass transition temperature

> The temperature at which a polymer or other amorphous compound goes from a brittle glassy state over to a viscous, rubber-like state. 209

nematic clearing point

> The nematic clearing point is also called nematic-isotropic transition temperature. Above this temperature, the liquid crystal features vanish and an isotropic liquid remains. The transition is typically reversible. 41, 209

number of power-lince-cycles

> Number of power-line-cycles ($0.2\,\text{s}$ for the frequency of $50\,\text{Hz}$ in european contries) employed as integration time for a single value. 89, 205

PCBM

> The term PCBM is used as a synonym for phenyl-C_{61}-butyric acid methyl ester ($PC_{60}BM$). If a different fullerene is employed as basis, like in phenyl-C_{71}-butyric acid methyl ester ($PC_{70}BM$), it is stated separately 25, 205

perfectly matched layer

> A strongly absorbing layer that is attached to a material in order to avoid reflections from the edges. 173, 206

PP1

PEDOT:PSS type one. A $3-4\%$ dispersion in H_2O, see also subsection 10.1.6. 106, 110, 111, 114, 117, 129

PP2

PEDOT:PSS type two. Orgacon N-1005, see also subsection 10.1.6. 107, 110

PP3

PEDOT:PSS type three. Orgacon HIL-1005, see also subsection 10.1.6. 107, 110, 119, 125

sensitizer

Component within a PR composite that is sensitive to light of an appropriate wavelength and thus enables absorption and charge generation. Dyes are typically employed as sensitizers. PCBM is most common. 29, 40, 43, 44

A Additional information and parameters

A.1 Conversion factors of the polarizability

These factors are employed for conversion of the polarizability between electro static units (esu in $[\mathrm{m}^3]$), atomic units (a.u.), and SI units (in $[\mathrm{C}^2\,\mathrm{m}^2\,\mathrm{J}^{-1}]$). Factors A.2 and A.1 have been taken from Cox et al. [110] and reformulated to common physical constants and factor A.3 has been derived from the others. Contrary to Cox et al., the conversion factors do not have the unit the polarizability would have in the final unit system but instead are considered to be multiplied with the unit of the original system in the this way: $\alpha_{\mathrm{fin.}} = c_{\mathrm{orig.,fin.}} \cdot \alpha_{\mathrm{orig.}}$. Therefore, the resulting conversion factors $c_{\mathrm{orig.,fin.}}$ are the following:

$$c_{\mathrm{esu,SI}} = 4\pi\varepsilon_0 = 1.113 \times 10^{-10}\,\mathrm{C}^2\,\mathrm{J}^{-1}\,\mathrm{m}^{-1} \tag{A.1}$$

$$c_{\mathrm{esu,a.u.}} = \frac{\pi^3 m_{\mathrm{e}}^3 e^6}{\varepsilon_0^3 h^6} = 6.748 \times 10^{30}\,\mathrm{m}^{-3} \tag{A.2}$$

$$c_{\mathrm{a.u.,SI}} = \frac{4\varepsilon_0^4 h^6}{\pi^2 m_{\mathrm{e}}^3 e^6} = 1.649 \times 10^{-41}\,\mathrm{C}^2\,\mathrm{m}^2\,\mathrm{J}^{-1}\ . \tag{A.3}$$

Within these factors, ε_0 denotes the electric constant, h the Planck constant, m_{e} the electron mass, and e the elementary charge.

Assuming the unit of the first hyperpolarizability in esu is given in $[\mathrm{m}^5/\mathrm{statC}]$, the conversion factors for β are A.4, A.5, and A.6 are:

$$d_{\mathrm{esu,SI}} = 10 \cdot 4^2 \pi^2 \varepsilon_0^2 c = 3.711 \times 10^{-11}\,\mathrm{C}^3\,\mathrm{J}^{-2}\,\mathrm{m}^{-2}\,\mathrm{statC} \tag{A.4}$$

$$d_{\mathrm{esu,a.u.}} = \frac{10\pi^5 m_{\mathrm{e}}^5 e^{11}}{\varepsilon_0^5 h^{10}} = 1.158 \times 10^{42}\,\mathrm{m}^{-5}\mathrm{statC} \tag{A.5}$$

$$d_{\mathrm{a.u.,SI}} = \frac{4^2 \varepsilon_0^7 h^{10}}{\pi^3 m_{\mathrm{e}}^5 e^{11}} = 3.206 \times 10^{-53}\,\mathrm{C}^3\,\mathrm{m}^3\,\mathrm{J}^{-2}\ . \tag{A.6}$$

The constant c is the speed of light in vacuum. The application scheme is the same as for the polarizability.

A.2 Molecular weights of employed compounds

Table A.1 provides some data regarding molecular weights (M) that have been applied during various calculations. Data of single molecules as well as monomeric units of polymers are determined with the program ChemBioDraw Ultra 14.0 [169]. In case of polymers, either the values the manufacturer printed on the packaging or from the manufacturers' or dealers' website are used. These are either the number average molecular weight (M_n) or weight average molecular weight (M_w) [250]. If a distribution is given, the mean value is calculated and provided in the table. Additionally, the number of repeat units in polymers based on the (averaged) M_n and M_w data is given.

Table A.1: M, M_n, and M_w as well as the approximate number of monomer units in polymers of employed compounds. Because M_w and M_n typically vary over a certain range, this holds for the repetiton lengths as well.

Component	M (u = g mol^{-1})	M_w or M_n (u)	monomers
5CB	249.36	-	1
C$_{60}$	720.66	-	1
PBI	864.77	-	1
tdiPBI	1585.72	-	1
sdiPBI	1395.88	-	1
PPDI	1084.29	-	1
PCBM	910.90	-	1
P3HT ($\overline{M}_n$)	166.28	64 500	388
PBDTTT-C-T	841.34	20 000	24
PS (M_w)	104.15	200 000	1920
PVK ($\overline{M}_n$)	193.25	37 500	194
TPD	516.69	-	1

A.3 Solvent data

Table A.2 contains some data of different solvents applied in this thesis.

Table A.2: Density ρ, molar mass M, molar volume V_m, and boiling point T_b of some of the employed solvents.

Solvent	ρ (g mL^{-1})	M (g mol^{-1})	V_m (mL mol^{-1})	T_b (°C)
EtOAc	0.89	88.11	98.56	77.00
CHCl$_3$	1.48	119.38	80.66	61.00
CB	1.11	112.56	101.41	132.00
ODCB	1.31	147.00	112.56	179.00
CN	1.19	162.62	136.66	259.00
DIO	1.84	366.02	198.92	168.00

A.4 Good and bad solvent data

Table A.3 contains the data of the compositions applied in the experiment with P3HT in good and bad solvent.

Table A.3: Composition of the solutions employed for characterization of P3HT aggregation via absorption spectroscopy.

EtOAc (mol %)	solvent volume (mL)	EtOAc (mL)	CHCl$_3$ (mL)
0.00%	0.707	0.000	0.707
5.00%	0.716	0.049	0.666
7.00%	0.719	0.069	0.650
10.00%	0.725	0.099	0.626
12.00%	0.728	0.118	0.610
15.00%	0.733	0.148	0.586
25.00%	0.751	0.246	0.505
50.00%	0.796	0.493	0.303

A.5 Maximum amplitudes obtained from simulated cross sections

Table A.4: Maxima of the magnitudes of the cross sections. Here, column **1** corresponds to the patterns in figure 18.3, column **2** to the patterns in subfigures 18.4(e) to 18.4(h), and column **3** to patterns in figure 18.5.

Type	**1** E (V m^{-1})	**2** E (V m^{-1})	**3** E (V m^{-1})
Bessel	0.274	0.446	1.137
Penrose	0.252	0.386	0.326
Cobblestone	0.250	0.344	0.362
Vogel spiral	0.249	0.372	0.402

Publications

Scientific publications and patents

1. K. Ditte, W. Jiang, **T. Schemme**, C. Denz, and Z. Wang: "Innovative Sensitizer DiPBI Outperforms PCBM", Adv. Mater. **24**, 2104 (2012).

2. **T. Schemme**, K. Ditte, and C. Denz: "Effektive Lichtverstärker", Laborpraxis **36**, 20 (2012).

3. **T. Schemme**, K. Ditte, E. Travkin, W. Jiang, Z. Wang, and C. Denz: "Perylene bisimide derivatives as innovative sensitizers for photorefractive composites", Proc. SPIE **8435**, 843526 (2012).

4. **T. Schemme**, E. Travkin, K. Ditte, W. Jiang, Z. Wang, and C. Denz: "TPD doped polystyrene as charge transporter in DiPBI sensitized photorefractive composites", Opt. Mater. Express **2**, 856 (2012).

5. K. Ditte, W. Jiang, **T. Schemme**, J. Liu, Z. Wang, and C. Denz: "Photorefractive Composite", PCT/EP2011/065876 WO/2013/037404 (2013).

6. M. Böckmann, **T. Schemme**, D. H. de Jong, C. Denz, A. Heuer, and N. L. Doltsinis: "Structure of P3HT crystals, thin films, and solutions by UV/Vis spectral analysis", Phys. Chem. Chem. Phys. **17**, 28616 (2015).

7. T. Winands, M. Bockmann, **T. Schemme**, P.-M. T. Ly, D. H. de Jong, Z. Wang, C. Denz, A. Heuer, and N. L. Doltsinis: "P3HT:DiPBI bulk heterojunction solar cells: morphology and electronic structure probed by multiscale simulation and UV/vis spectroscopy", Phys. Chem. Chem. Phys. **18**, 6217 (2016).

Contributions to international conferences

1. **T. Schemme**, K. Ditte, W. Jiang, Z. Wang, and C. Denz: "DiPBI as an Innovative Sensitizer for Photorefractive Composites", Photorefractive Materials, Effects, and Devices - PR 11 (2011).

2. **T. Schemme**, K. Ditte, E. Travkin, W. Jiang, Z. Wang, and C. Denz: "Perylene bisimide derivatives as innovative sensitizers for photorefractive composites", SPIE Photonics Europe (2012).

3. **T. Schemme**, M. Boguslawski, and C. Denz: "Fabrication of tailored surface relief gratings for solar cell applications", CLEO/Europe-EQEC 2015 (2015).

4. **T. Schemme**, M. Boguslawski, and C. Denz: "Surface relief gratings for light management in solar cells", SPIE Photonics Europe (2016).

Contributions to annual meetings and PhD workshops of the Collaborative Research Center TRR 61

Despite the fact the name is not listed in all contributions, the author of this thesis provided input to all of them.

1. **T. Schemme**, K. Ditte, W. Jiang, Z. Wang, and C. Denz: "Perylene Bisimide Derivatives as Innovative Sensitizers for Photorefractive Composites", TRR 61 PhD Student Workshop (2011).

2. C. Denz, N. Doltsinis, and Z. Wang: "High performance organic solar cells with tailored light trapping structures", Evaluation of the applications for the second funding period of the Collaborative Research Center TRR 61 (2012).

3. M. Böckmann, C. Denz, N. Doltsinis, T. Kohne, W. Jiang, J. M. Miranda Muñoz, **T. Schemme**, and Z. Wang: "High performance organic solar cells with tailored light trapping structures", TRR 61 Annual Symposium (2013).

4. **T. Schemme**, J. M. Miranda Muñoz, and C. Denz: "Enhancement of Optical Transmission of Thin Electrode Layers by Azopolymer Coatings", TRR 61 PhD Student Workshop (2013).

5. M. Böckmann, C. Denz, N. Doltsinis, W. Jiang, **T. Schemme**, K. Sun, and Z. Wang: "High performance organic solar cells with tailored light trapping structures", TRR 61 Annual Symposium (2014).

6. **T. Schemme** and C. Denz: "Generation of tailored surface relief gratings for solar cell applications", TRR 61 PhD Student Workshop (2014).

7. C. Denz, N. Doltsinis, and Z. Wang: "High performance organic solar cells with tailored light trapping structures", TRR 61 Annual Symposium (2015).

8. **T. Schemme**, M. Boguslawski, and C. Denz: "Tailored surface relief gratings for solar cell applications", TRR 61 PhD Student Workshop (2015).

9. C. Denz, N. Doltsinis, Y. Li, and X. Zhu: "Multidimensional photoresponsive-molecular architectures for high performance solar cells", Evaluation of the applications for the third funding period of the Collaborative Research Center TRR 61 (2016).

Contributions to project proposals

1. "High performance organic solar cells with tailored light trapping structures", Proposal in the frame of the first continuation of the DFG Collaborative Research Center (CRC) TRR 61.

2. "IMPACT - Hybrid Organic-Inorganic Materials: Preparation, Advanced Characterization, Emerging Applications and Technologies", Erasmus Mundus Joint Doctorate Proposal to the EU in the frame of the seventh EU Framework Programme (FP7).

3. "Multidimensional photoresponsive molecular architectures for high performance solar cells", Proposal in the frame of the second continuation of the DFG CRC

TRR 61.

4. "Multidimensional photoresponsive molecular architectures for high performance solar cells", Proposal to DFG.

Deutschsprachige Zusammenfassung

Der erste Teil dieser Arbeit ist allgemein gehalten und erklärt was organische Materialien sind, wie sie angeregt werden und wie Energie und Ladungsträger transportiert werden. Dieser Teil stellt somit grundlegende Informationen für der Verständnis der folgenden Teile zur Verfügung. In den Teilen II bis IV werden die drei Hauptthemen dieser Dissertation behandelt. Diese Teile beschreiben die experimentelle Charakterisierung der Licht-Materie-Wechselwirkung unterschiedlicher organischer Materialien sowie die Interpretation der gewonnenen Resultate. Darüber hinaus wird im letzten Teil der Arbeit die Lichtpropagation und Licht-Materie-Wechselwirkung theoretisch modelliert.

In Teil II wird die Brechungsindexmodifikation eines photorefraktiven Komposits durch ein Lichtfeld beschrieben. Im Gegenzug bedeutet dies, dass das Lichtfeld durch die Brechungsindexänderung des Materials einen Einfluss auf die transmittierte Intensitätsverteilung hat. Photorefraktive Polymerkomposite erlauben somit die Steuerung von Licht mit Licht. Teil III behandelt den Einsatz von Perylenbisimidderivaten in organischen Solarzellen mit Bulkheteroübergang. Das bedeutet, das Licht durch organische Materialien absorbiert und in elektrische Energie konvertiert wird. Der letzte Teil (IV) beschreibt die strukturierte Materialien, die wiederum die Lichtpropagation beeinflussen. Dieser Einfluss entsteht entweder durch das strukturierte Azopolymer selbst oder durch einen PDMS-Film, der vom Azopolymer abgeformt worden ist.

Die ersten beiden experimentellen Teile verdeutlichen die Schwierigkeiten, die bei der Entwicklung und Optimierung organischer, optoelektronischer Komposite, die aus zwei oder sogar mehr Komponenten bestehen, auftreten können. In beiden Teilen werden Materialien, die jeweils dem vorher eingesetzten Material überlegen sind, eingesetzt. Entgegen der Annahme, dass die daraus resultierenden Komposite eine verbesserte Leistungsfähigkeiten zeigen sollten, stagnieren die ermittelten Effizienzen oder nehmen sogar ab. Aufgrund der Tatsache, dass die Ursachen dieses Verhalten für beide Komposittypen unterschiedlich sind, werden diese separate behandelt.

Zusammenfassung von Teil II

Im Fall der photorefraktiven Komposite führte die verbesserte Photoleitfähigkeit nicht zu einer verbesserten photorefraktiven Antwort. Der Grund liegt in der verstärkten Dunkelleitfähigkeit in Kombination mit einer reduzierten Anzahl von Fallenzuständen, die essentiell für die Brechungsindexmodulation sind. Da der photorefraktive Effekt in organischen Kompositen ein mehrstufiger Prozess ist, reicht eine Steigerung der Ladungsträgererzeugung nicht aus. Das Fangen von Ladungsträgern muss auch zu einem gewissen Ausmaß gewährleistet sein. Darüber hinaus muss auch die Stärke des angelegten elektrischen Feldes für die Polung der Chromophormoleküle beachtet werden. Aus diesen Gründen ist es schwierig die photorefraktive Leistungsfähigkeit eines Komposits nur aus den Energieniveaus des Ladungstransporters und Sensibilisators

abzuleiten. Im Ergebnis hat sich herausgestellt, dass Komposite, die den effektiveren Ladungstransporter, eine Gemisch aus PS und TPD, enthalten, einen wesentlich geringen photorefraktiven Verstärkungskoeffizienten aufweisen. Im Gegenzug is die Verstärkung bei Proben die PVK enthalten aufgrund der geringeren Dunkelleitfähigkeit geringer.

Zusammenfassung von Teil III

Für den organischen Solarzellen mit Bulkheteroübergang hat sich ebenfalls herausgestellt, dass eine Betrachtung der Energieniveaus nicht ausreichend ist. Die Morphologe und das Verklumpen dieser Materialkompositionen in der aktiven Schicht spielen auch eine enorm wichtige Rolle. Falls der Molekülabstand der Materialien zu groß wird, sinkt die Wahrscheinlichkeit für die Ladungstrennung drastisch und somit auch der Effizienz der Zelle. Ein noch wichtigerer Punkt betrifft die Herstellungsbedingungen der Zelle. PCBM und perylenbasierte Akzeptormaterialien besitzen eine gute Stabilität an Luft. Dies gilt nicht für die verwendeten Donatorpolymere. Daher sinkt die Effizienz der Zellen an Luft stark. Aus diesem Grunde ist es sehr schwierig verschiedene Zellen quantitativ zu vergleichen oder Langzeitmessungen für Stabilitätstests durchzuführen.

Weiter wird in einer Zusammenarbeit mit Gruppen aus der Theorie wird die effektive Kettenlänge von P3HT mittels Absorptionsspektroskopie untersucht. Multiskalenmodellierung erlaubt es einen Grenzwinkel zu bestimmen, der die effektive Kettenlänge begrenzt. Die Kombination aus Spektroskopie und Simulation erlaubt es somit die unterschiedlichen Spektren von kristallinem, amorphem (innerhalb von dünnen Filmen) und gelösten P3HT zu erklären.

Im Rahmen dieser Zusammenarbeit wird auch der Bulkheteroübergang von P3HT und tdiPBI analysiert. Hierbei wird im besonderen thermisches Erwärmen dieser Mischung experimentell durchgeführt und simuliert. Aufgrund der beschränkten Zeit innerhalb der Simulation werden die Temperaturen sehr viel höher gewählt also während der Solarzellenherstellung üblich. Trotzdem zeigt die Modellierung Klumpenbildung und Morphologieänderungen im Materialgemisch. Werden die simulierten Temperaturen auch im Experiment angewandt, werden starke Materialveränderungen sowohl mit dem bloßen Auge als auch mit dem Spektrometer wahrgenommen. Die Veränderungen werden nicht nur die Materialreorganisation zugeschrieben, sondern sind auch auf Materialschädigungen zurückzuführen. Diese werden durch die hohen Temperaturen kombiniert mit dem Sauerstoff in der Umgebung erzeugt. In einer inerten Atmosphäre hingegen werden andere Effekte erwartet. Dennoch wird angenommen, dass es dort auch zu einem partiellen Verdampfen von Material kommt und ebenso Abtrennung von Liganden auftritt.

Zusammenfassung zu Teil IV

Im letzte Teil (IV) wird die Erzeugung von Oberflächenreliefs in Azopolymeren und die Lichtpropagation durch einen Stapel aus strukturiertem PDMS und Glas diskutiert. Zunächst wird der grundlegende Strukturierungsprozess mittels Zweistrahlinterferenz getestet und sinusförmige Oberflächenrefliefs erzeugt. Danach wird ein komplexeres Setup, das auf einem Lichtmodulator basiert, verwendet. Dieses Setup erlaubt es beliebige

Muster in 2D zu erzeugen. Unterschiedliche Strukturen, nämlich Bessel-, Penrose-, Cobblestone- und Vogelspiralstrukturen werden realisiert. Um diese Strukturen für die Lichtumverteilung auf Solarzellen einsetzen zu können, werden sie erfolgreich in PDMS übertragen. Die lateralen Abstandsparameter der Strukturen variieren liegen dabei im Bereich 3,5 – 11,5 μm. Die Höhenmodulation erreicht bis zu 50 nm. Im Falle des sinusförmigen Reliefs werden sogar mehr als 200 nm erreicht. Die geringere Modulation bei de komplexen Strukturen ist im wesentlichen der geringen Filmdicke geschuldet. Somit führen auch im Fall der komplexen 2D Muster größere Filmdicken zu höheren Modulationsgraden.

Um die Lichtumverteilungsfähigkeiten der unterschiedlichen Strukturen zu charakterisieren wird eine FDTD-Simulation verwendet. Linear polarisiertes Licht in Form von ebenen Wellen propagiert dabei durch ein System aus strukturierten PDMS und Glas. auf der anderen Seite des Systems werden Querschnitte aufgenommen und anhand dieser die Umverteilung analysiert. Das Ergebnis dieser Auswertung zeigt, dass Besselstrukturen dazu neigen das Licht ähnlich einem Fresnel-Axicon zu fokussieren. Im Gegensatz dazu verteilen die übrigen Strukturen das Licht recht gut um. Wenn die Modulationstiefe vergrößert und gleichzeitig der Strukturabstand verkleinert wird, werden die auftretenden Effekte (Fokussierung durch die Besselstruktur und Umverteilung durch den Rest) noch einmal deutlich verstärkt. Da die Besselstruktur das Licht in diesem Fall extrem fokussiert, wird sie gleichzeitig zu einem Kandidaten für die Anwendung in sogenannten Konzentratorsolarzellen. Im Gegensatz dazu fügen die anderen Strukturen den beteiligten Vektoren des elektrischen Feldes eine mehr oder weniger homogen verteilte Verkippung zu. Aus diesem Grund sind sie prinzipiell für dei Anwendung auf konventionellen (organisch und anorganisch) Solarzellen geeignet. Natürlich müssen Strukturabstand sowie Modulationshöhe den jeweiligen Bedürfnissen angepasst werden.

Perspektiven zu Teil II

Alle vorgestellten Anwendungen von organischen Materialien besitzen eine vielfältige Zukunft. Bis heute benötigen die meisten photorefraktiven Komposite starke elektrische Felder, weisen eine geringen Langzeitstabilität auf und besitzen eher geringe Schaltraten. Falls diese Nachteile überwunden werden, gibt es eine reale Chance für die Kompositpolymere in Massenmarktanwendungen eingesetzt zu werden. Zu diesen gehören neben optischen Schaltern auch 3D-Displays, wie sie von Blanche et al. [4] im Jahr 2010 vorgestellt worden sind. Wie bereits zuvor erwähnt haben die genannten Limitierungen ihren Ursprung in unterschiedlichen den Komponenten. Daher ist eine bessere Abstimmung der Materialien aufeinander notwendig, damit die gewünschten Eigenschaften des Komposits erreicht werden. Diese Optimierungen beinhalten neben der Schaltgeschwindigkeiten der elektrooptischen Komponenten auch effizienten Ladungstransport kombiniert mit ausreichend vielen Fallenzuständen [247]. Diese Vorgehen sollte auch zu großen Verstärkungskoeffizienten führen. Daher müssen entweder weitere Dotierungen vorgenommen oder neue Materialien maßgeschneidert werden.

Perspektiven zu Teil III

Vor ein paar Jahren haben die organischen Solarzellen einen großen Wettbewerber bekommen – Perowskitsolarzellen. Dieser neuen Typ kann als Abwandlung der bekannten Farbstoffsolarzellen betrachtet werden. Es handelt sich somit um eine Hybridsystem, das teilweise organisch und anorganisch ist. Derzeit erreichen PSCs viel höhere Effizienzen als typische organische Solarzellen (vgl. Abbildung 7.1). Außerdem sind PSCs einfach in großem Maßstab herstellbar, sie sind leicht und teilweise bezüglich des Absorptionsbereich einstellbar. Letzteres hängt von der Wahl eines geeigneten Farbstoffs oder einer Modifikation des Perowskitmaterials ab. Aufgrund dieser Fähigkeiten und Möglichkeiten ist die organische Solarzelle zu einem gewissen Grad rückständig, da es eine Alternative gibt, die die gleichen Eigenschaften mitbringt und außerdem wesentlich effizienter ist. Dennoch besitzt auch die Perowskitzelle Probleme bezüglich der Langzeitstabilität und enthält zudem noch Blei. Gerade ist aus diesem Grund ist die PSC noch weit davon entfernt als umweltfreundlich bezeichnet zu werden. Das trifft momentan zwar auch noch auf die organische Solarzelle zu, aber es gibt hier bereits größere Anstrengungen Materialien zu finden, die mit harmlosen Lösungsmitteln verarbeitet werden können [248] und zudem noch noch biologisch abbaubar oder vollständig recyclebar sind [249]. Dieser Ansatz ist ein großer Schritt in Richtung wirklich „grüner" Energiegewinnung. Im Gegensatz dazu kann die Entwicklung neuer Donator und Akzeptormaterialien, die nicht umweltfreundlich sind, ein totes Ende sein. Die Grund für diese Annahme liegt in dem enormen Fortschritt und dem weiteren Wachstumspotenzial der Perowskitzellen.

Perspektiven zu Teil IV

Die Erzeugung von strukturierten Azopolymerfilmen mit Licht hat sich als leistungsfähiges Werkzeug für die Vorlagenherstellung im Zuge des Rapid-Prototyping von komplexen Strukturen und die Kleinserienproduktion gezeigt. Der Nachteil dieser Technik ist die relativ kleine Fläche die in einem Schritt strukturiert werden kann wenn kleine Abstände benötigt werden. Aus diesem Grund ist entweder sequentielles Schreiben der Muster notwendig oder es werden kostspielige, hochauflösende Modulatoren benötigt. Genügt im Gegensatz dazu auch eine kleine strukturierte Fläche, können Abstände in den Mustern noch weiter durch optische Verkleinerung reduziert werden. Generell ist das Beugungslimit eine untere Grenze für die Strukturgröße. Letztendlich erlaubt der vorgestellte Ansatz das Schreiben von Mustern in weiche Materialien mit einer lateralen Abständen im Submikrometerbereich, wohingegen die Höhenmodulation Werte von 200 nm und mehr erreichen kann.

Die eingesetzte FDTD-Simulation ist bislang auf senkrechten Einfall des Lichts limitiert. Um auch geneigten Einfall mit Winkeln größer als ein paar weniger Grad simulieren zu können, müssen Reflexionen von der Eintrittsfläche und von den Seiten des Simulationsvolumens stärker berücksichtigt werden. An dieser Stelle müssen die Randbedingungen mit Vorsicht bedacht werden, da der Winkel zwischen Licht und Wänden des Volumens nicht länger näherungsweise parallel oder senkrecht ist. Daher ist mit dem Aufkommen mit Nebeneffekten zu rechnen. Um diese zu vermeiden könnten komplexere Randbedingungen, zum Beispiel periodische, eingesetzt oder das Simulationsvolumen vergrößert werden. Let-

zteres sollte in alle Richtungen erweitert werden. Durch die laterale Erweiterung wird die Wirkung des Musters noch deutlicher, wohingegen eine längere Propagationslänge näher an das reale System kommt und somit genauere Daten erlaubt. Bis jetzt ist das Glas viel dünner als ein reales Substrat und auch der PDMS-Film ist in einem realistischerem Szenario viel dicker. Die Kosten für ein vergrößertes Simulationsvolumen bestehen finden sich im Bedürfnis für höhere Rechenleistung und Speicher der verwendeten Computer wieder. Besonders wenn das Simulationsvolumen zusätzlich noch feiner gegliedert werden soll um die Genauigkeit der Ergebnisse zu steigern, steigt der Speicherbedarf exorbitant an. Aus diesem Grund sollte dann der Einsatz von Hochleistungsrechnern in Betracht bezogen werden. Außerdem erlaubt der Einsatz eines solchen Systems die Variation der verwendeten Strukturen in kleineren Schritten, da die Berechnungen wesentlich schneller ablaufen. Mehr Daten erzeugen ein wesentlich detailierteres Bild der Lichtumverteilung und helfen somit einer optimierte Mustergeometrie zu finden.

Lebenslauf (Curriculum Vitae)